



Universidad de Oviedo

Programa de Doctorado en Materiales

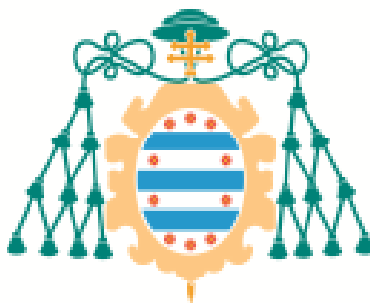
SÍNTESIS DE MATERIALES BIDIMENSIONALES MEDIANTE EXFOLIACIÓN ELECTROQUÍMICA PARA ALMACENAMIENTO DE ENERGÍA

*SYNTHESIS OF TWO-DIMENSIONAL MATERIALS THROUGH
ELECTROCHEMICAL EXFOLIATION FOR ENERGY STORAGE*

Doctorando:

Daniel Fernández Carrasco

Oviedo, noviembre 2024



Universidad de Oviedo

Departamento de Ciencia de los Materiales e Ingeniería Metalúrgica

Programa de Doctorado en Materiales

SÍNTESIS DE MATERIALES BIDIMENSIONALES MEDIANTE EXFOLIACIÓN ELECTROQUÍMICA PARA ALMACENAMIENTO DE ENERGÍA

*SYNTHESIS OF TWO-DIMENSIONAL MATERIALS THROUGH
ELECTROCHEMICAL EXFOLIATION FOR ENERGY STORAGE*

Doctorando:

Daniel Fernández Carrasco

Directores:

Dr. D. Juan Ignacio Paredes Nachón

Dr. D. Fabián Suárez García

Oviedo, noviembre 2024



RESUMEN DEL CONTENIDO DE TESIS DOCTORAL

1.- Título de la Tesis	
Español: Síntesis de materiales bidimensionales mediante exfoliación electroquímica para almacenamiento de energía.	Inglés: Synthesis of two-dimensional materials through electrochemical exfoliation for energy storage.
2.- Autor	
Nombre: Daniel Fernández Carrasco	
Programa de Doctorado: Materiales	
Órgano responsable: Centro Internacional de Postgrado	

RESUMEN (en español)

La presente tesis doctoral se centra en la preparación, caracterización y aplicaciones de materiales bidimensionales (2D) en almacenamiento electroquímico de energía, en particular grafeno oxidado y diseleniuro de niobio (NbSe_2). Se presentan nuevas estrategias de exfoliación y funcionalización de los correspondientes materiales laminares bulk, destacando el potencial de los materiales 2D obtenidos como electrodos en supercondensadores, condensadores híbridos de ion zinc acuoso y en almacenamiento de litio.

En el ámbito del grafeno, una de las principales contribuciones de esta tesis es la investigación de una estrategia novedosa basada en exfoliación anódica para obtener grafeno altamente oxidado, la cual constituye una alternativa muy atractiva por su simplicidad y rapidez a los métodos convencionales de obtención de grafeno muy oxidado (óxido de grafeno preparado, por ejemplo, por el método de Hummers). La ruta anódica permite además obtener grafeno oxidado de calidad estructural relativamente alta, caracterizado por dominios oxidados densos y pequeños entremezclados con dominios aromáticos relativamente extensos. Esto lo convierte en un precursor idóneo para la generación de grafeno poroso, en donde los poros generados mediante ataque selectivo de los dominios oxidados presentan dimensiones pequeñas (unos pocos nanómetros) y una distribución espacial muy uniforme. Todo ello se traduce en grafenos con mejor rendimiento electroquímico cuando se usan como material activo en supercondensadores, presentando mayor capacidad de almacenamiento de carga y mayor densidad de energía en comparación con materiales similares derivados de óxido de grafeno estándar.

Asimismo, se ha explorado una estrategia de exfoliación anódica que permite un cierto control de las poblaciones de grupos funcionales oxigenados presentes en los grafenos resultantes. Concretamente, se demuestra que es posible ajustar el tipo y la cantidad relativa de los grupos oxigenados mediante una elección adecuada de la composición del electrolito acuoso en el que se lleva a cabo la exfoliación anódica. Ello permite obtener grafeno con mayores cantidades de grupos carboxilo, los que mejora algunas de sus propiedades (por ejemplo, la mojabilidad) y se traduce en una mayor capacidad de almacenamiento de carga en condensadores híbridos de ion zinc acuoso. Asimismo, las prestaciones de electrodos basados en este tipo de grafeno se han potenciado mediante la inclusión de moléculas con actividad redox, como el mononucléotido de flavina. También se ha demostrado que el recubrimiento de electrodos de zinc con grafeno Enriquecido en grupos carboxilo mejora su ciclabilidad y estabilidad al evitar la formación de dendritas, problema que limita la aplicabilidad de baterías y condensadores que usan zinc metálico como ánodo.

Por último, se ha investigado la exfoliación catódica en medio acuoso como método eficiente para la obtención de dicalcogenuros de metales de transición de carácter metálico, principalmente NbSe_2 pero también NbS_2 y VSe_2 , con control sobre la morfología final del material (nanorollo, nanolámina). Dicho control morfológico permite obtener electrodos con distinto comportamiento en almacenamiento electroquímico de litio. De esta manera, los electrodos basados en nanorollos de NbSe_2 presentan una mayor capacidad de almacenamiento que las nanoláminas, atribuible a un empaquetamiento menos compacto del



Universidad de Oviedo

electrodo con los primeros que facilita un mejor acceso del electrolito. Asimismo, se demuestra que el mecanismo de la exfoliación catódica de estos dicalcogenuros desarrollada en el presente trabajo es completamente diferente al que tiene lugar en procesos comunes de exfoliación electroquímica (catódica o anódica) de materiales laminares.

RESUMEN (en Inglés)

This doctoral thesis focuses on the preparation, characterization, and applications of two-dimensional (2D) materials in electrochemical energy storage, specifically oxidized graphene and niobium diselenide (NbSe_2). New exfoliation and functionalization strategies of the corresponding bulk layered materials are presented, highlighting the potential of the resulting 2D materials as electrodes in supercapacitors, hybrid aqueous zinc-ion capacitors, and lithium storage.

In the field of graphene, one of the main contributions of this thesis is the investigation of a novel strategy based on anodic exfoliation to obtain highly oxidized graphene, which represents a very attractive alternative due to its simplicity and speed compared to conventional methods for obtaining highly oxidized graphene (such as graphene oxide prepared by the Hummers method). The anodic route also allows for obtaining oxidized graphene with relatively high structural quality, characterized by dense and small oxidized domains interspersed with relatively extensive aromatic domains. This makes it an ideal precursor for the generation of porous graphene, where the pores generated through the selective attack of the oxidized domains present small dimensions (a few nanometers) and a very uniform spatial distribution. All this translates into graphenes with improved electrochemical performance when used as active materials in supercapacitors, showing higher charge storage capacity and energy density compared to similar materials derived from standard graphene oxide.

Moreover, an anodic exfoliation strategy has been explored that allows some control over the populations of oxygenated functional groups present in the resulting graphenes. Specifically, it is demonstrated that it is possible to adjust the type and relative amount of oxygenated groups through an appropriate choice of the aqueous electrolyte composition in which the anodic exfoliation is carried out. This allows for obtaining graphene with higher amounts of carboxyl groups, which improves some of its properties (such as wettability) and results in a higher charge storage capacity in aqueous zinc-ion hybrid capacitors. Furthermore, the performance of electrodes based on this type of graphene has been enhanced by incorporating redox-active molecules like flavin mononucleotide. It has also been shown that coating zinc electrodes with carboxyl-enriched graphene improves their cyclability and stability by preventing dendrite formation, a problem that limits the applicability of batteries and capacitors using metallic zinc as the anode.

Finally, cathodic exfoliation in an aqueous medium has been investigated as an efficient method for obtaining transition metal dichalcogenides with metallic character, mainly NbSe_2 , but also NbS_2 and VSe_2 , with control over the material's final morphology (nanoroll, nanosheet). This morphological control allows for obtaining electrodes with different behaviors in electrochemical lithium storage. Thus, electrodes based on NbSe_2 nanorolls exhibit a higher storage capacity than nanosheets, attributable to the less compact packing of the electrode with the former, which facilitates a better electrolyte access. Furthermore, it is demonstrated that the mechanism of cathodic exfoliation of these metal dichalcogenides is entirely different from that occurring in common electrochemical (cathodic or anodic) exfoliation processes of layered materials.

SR. PRESIDENTE DE LA COMISIÓN ACADÉMICA DEL PROGRAMA DE DOCTORADO EN MATERIALES

Tabla de contenido

INDICE	1
RESUMEN.....	3
LISTA DE ACRÓNIMOS.....	7
1. INTRODUCCIÓN	9
1.1. Nanomateriales 2D.....	11
1.1.1. Grafeno	13
1.1.2. Diseleniuro de Niobio (NbSe_2)	19
1.2. Métodos de obtención de materiales 2D	22
1.2.1. Métodos bottom-up o ascendentes	23
1.2.2. Métodos top-down o descendentes	26
1.3. Materiales 2D para almacenamiento electroquímico de energía	36
1.4. Procesos de almacenamiento de energía.....	39
1.4.1. Procesos no faradaicos: doble capa eléctrica	39
1.4.2. Procesos faradaicos: pseudocapacitancia y comportamiento tipo batería	41
1.5. Dispositivos de almacenamiento de energía electroquímica	43
1.6. Referencias.....	47
2. OBJETIVOS Y PLANTEAMIENTO DE LA MEMORIA	59
2.1. Objetivos.....	61
2.2. Organización de la memoria	63
3. TÉCNICAS DE CARACTERIZACIÓN	65
3.1. Espectroscopías.....	67
3.1.1. Espectroscopia de absorción ultravioleta-vis (UV-vis).....	67
3.1.2. Espectroscopía Raman	71
3.1.3. Espectroscopía fotoelectrónica de rayos X	74
3.2. Microscopías.....	76
3.2.1. Microscopía electrónica de transmisión.....	76
3.2.2. Microscopía electrónica de barrido.....	77
3.2.3. Microscopía de fuerza atómica	80
3.3. Técnicas electroquímicas	82
3.3.1. Espectroscopía de impedancia electroquímica.....	82
3.3.2. Voltamperometría	85
3.3.3. Cronopotenciometría galvanostática	86

Tabla de contenido

3.4. Otras técnicas de caracterización	89
3.4.1. Método de cuatro puntas para la medida de conductividad eléctrica.....	89
3.4.2. Dispersión dinámica de la luz	89
3.4.3. Potencial Z	90
3.4.4. Difracción de rayos X.....	92
3.5. Referencias.....	94
4. MATERIALES Y MÉTODOS	97
4.1. Obtención de grafeno poroso	99
4.1.1. Obtención de grafeno altamente oxidado mediante intercalación y exfoliación anódica de grafito	99
4.1.2. Obtención de grafeno oxidado mediante reducción parcial de óxido de grafeno (GO)	100
4.1.3. Obtención de grafeno poroso mediante ataque oxidativo en medio líquido.....	101
4.1.4. Obtención de grafeno poroso mediante ataque oxidativo en aire.....	102
4.2. Obtención de grafenos químicamente modulables mediante exfoliación anódica.....	102
4.3. Obtención de diseleniuro de niobio (NbSe_2) exfoliado.....	103
4.4. Preparación de electrodos para caracterización electroquímica	105
4.4.1. Electrodos de grafeno poroso	105
4.4.2. Electrodos de grafeno anódico de química modulable	106
4.4.3. Electrodos de NbSe_2 exfoliado	107
5. RESÚMENES Y ARTÍCULOS	109
5.1. Obtención de grafeno mediante exfoliación electroquímica anódica.....	111
5.2. Obtención de dicalcogenuros de metales de transición mediante exfoliación electroquímica catódica.....	241
6. CONCLUSIONES.....	303
ANEXOS	307
Anexo I	309

Resumen

La presente tesis doctoral se centra en la preparación, caracterización y aplicaciones de materiales bidimensionales (2D) en almacenamiento electroquímico de energía, en particular grafeno oxidado y diseleniuro de niobio (NbSe_2). Se presentan nuevas estrategias de exfoliación y funcionalización de los correspondientes materiales laminares *bulk*, destacando el potencial de los materiales 2D obtenidos como electrodos en supercondensadores, condensadores híbridos de ion zinc acuoso y en almacenamiento de litio.

En el ámbito del grafeno, una de las principales contribuciones de esta tesis es la investigación de una estrategia novedosa basada en exfoliación anódica para obtener grafeno altamente oxidado, la cual constituye una alternativa muy atractiva por su simplicidad y rapidez a los métodos convencionales de obtención de grafeno muy oxidado (óxido de grafeno preparado, por ejemplo, por el método de Hummers). La ruta anódica permite además obtener grafeno oxidado de calidad estructural relativamente alta, caracterizado por dominios oxidados densos y pequeños entremezclados con dominios aromáticos relativamente extensos. Esto lo convierte en un precursor idóneo para la generación de grafeno poroso, en donde los poros generados mediante ataque selectivo de los dominios oxidados presentan dimensiones pequeñas (unos pocos nanómetros) y una distribución espacial muy uniforme. Todo ello se traduce en grafenos con mejor rendimiento electroquímico cuando se usan como material activo en supercondensadores, presentando mayor capacidad de almacenamiento de carga y mayor densidad de energía en comparación con materiales similares derivados de óxido de grafeno estándar.

Asimismo, se ha explorado una estrategia de exfoliación anódica que permite un cierto control de las poblaciones de grupos funcionales oxigenados presentes en los grafenos resultantes. Concretamente, se demuestra que es posible

Resumen

ajustar el tipo y la cantidad relativa de los grupos oxigenados mediante una elección adecuada de la composición del electrolito acuoso en el que se lleva a cabo la exfoliación anódica. Ello permite obtener grafeno con mayores cantidades de grupos carboxilo, los que mejora algunas de sus propiedades (por ejemplo, la mojabilidad) y se traduce en una mayor capacidad de almacenamiento de carga en condensadores híbridos de ion zinc acuoso. Asimismo, las prestaciones de electrodos basados en este tipo de grafeno se han potenciado mediante la inclusión de moléculas con actividad redox, como el mononucléotido de flavina. También se ha demostrado que el recubrimiento de electrodos de zinc con grafeno enriquecido en grupos carboxilo mejora su ciclabilidad y estabilidad al evitar la formación de dendritas, problema que limita la aplicabilidad de baterías y condensadores que usan zinc metálico como ánodo.

Por último, se ha investigado la exfoliación catódica en medio acuoso como método eficiente para la obtención de dicalcogenuros de metales de transición de carácter metálico, principalmente NbSe_2 pero también NbS_2 y VSe_2 , con control sobre la morfología final del material (nanorollo, nanolámina). Dicho control morfológico permite obtener electrodos con distinto comportamiento en almacenamiento electroquímico de litio. De esta manera, los electrodos basados en nanorollos de NbSe_2 presentan una mayor capacidad de almacenamiento que las nanoláminas, atribuible a un empaquetamiento menos compacto del electrodo con los primeros que facilita un mejor acceso del electrolito. Asimismo, se demuestra que el mecanismo de la exfoliación catódica de estos dicalcogenuros desarrollada en el presente trabajo es completamente diferente al que tiene lugar en procesos comunes de exfoliación electroquímica (catódica o anódica) de materiales laminares.

Abstract

This doctoral thesis focuses on the preparation, characterization, and applications of two-dimensional (2D) materials in electrochemical energy storage, specifically oxidized graphene and niobium diselenide (NbSe_2). New exfoliation and functionalization strategies of the corresponding bulk layered materials are presented, highlighting the potential of the resulting 2D materials as electrodes in supercapacitors, aqueous zinc-ion hybrid capacitors, and lithium storage.

In the field of graphene, one of the main contributions of this thesis is the investigation of a novel strategy based on anodic exfoliation to obtain highly oxidized graphene, which represents a very attractive alternative due to its simplicity and speed compared to conventional methods for obtaining highly oxidized graphene (such as graphene oxide prepared by the Hummers method). The anodic route also allows for obtaining oxidized graphene with relatively high structural quality, characterized by dense and small oxidized domains interspersed with relatively extensive aromatic domains. This makes it an ideal precursor for the generation of porous graphene, where the pores generated through the selective attack of the oxidized domains present small dimensions (a few nanometers) and a very uniform spatial distribution. All this translates into graphenes with improved electrochemical performance when used as active materials in supercapacitors, showing higher charge storage capacity and energy density compared to similar materials derived from standard graphene oxide.

Moreover, an anodic exfoliation strategy has been explored that allows some control over the populations of oxygenated functional groups present in the resulting graphenes. Specifically, it is demonstrated that it is possible to adjust the type and relative amount of oxygenated groups through an appropriate choice of the aqueous electrolyte composition in which the anodic exfoliation is carried out.

Abstract

This allows for obtaining graphene with higher amounts of carboxyl groups, which improves some of its properties (such as wettability) and results in a higher charge storage capacity in hybrid aqueous zinc-ion capacitors. Furthermore, the performance of electrodes based on this type of graphene has been enhanced by incorporating redox-active molecules like flavin mononucleotide. It has also been shown that coating zinc electrodes with carboxyl-enriched graphene improves their cyclability and stability by preventing dendrite formation, a problem that limits the applicability of batteries and capacitors using metallic zinc as the anode.

Finally, cathodic exfoliation in an aqueous medium has been investigated as an efficient method for obtaining transition metal dichalcogenides with metallic character, mainly NbSe₂, but also NbS₂ and VSe₂, with control over the material's final morphology (nanoroll, nanosheet). This morphological control allows for obtaining electrodes with different behaviors in electrochemical lithium storage. Thus, electrodes based on NbSe₂ nanorolls exhibit a higher storage capacity than nanosheets, attributable to the less compact packing of the electrode with the former, which facilitates a better electrolyte access. Furthermore, it is demonstrated that the mechanism of cathodic exfoliation of these metal dichalcogenides is entirely different from that occurring in common electrochemical (cathodic or anodic) exfoliation processes of layered materials

Lista de acrónimos

- **AFM:** Atomic Force Microscopy (Microscopía de fuerza atómica)
- **ASCs:** Asymmetric Supercapacitors (Supercondensadores asimétricos)
- **AZICs:** Aqueous Zinc-Ion Capacitors (Condensadores híbridos de ion zinc)
- **BE:** Binding Energy (Energía de ligadura)
- **CNT:** Carbon Nanotubes (Nanotubos de carbono)
- **DLS:** Dynamic Light Scattering (Dispersión dinámica de la luz)
- **DMF:** N,N-dimetilformamida
- **EDLCs:** Electrical Double Layer Capacitors (Supercondensadores de doble capa eléctrica)
- **EIS:** Electrochemical Impedance Spectroscopy (Espectroscopía de impedancia electroquímica)
- **E.O.:** Estado de oxidación
- **EOG:** Electrochemically oxidized graphene (grafeno oxidado electroquímicamente)
- **ESR:** Equivalent Series Resistance (Resistencia en serie equivalente)
- **FWHM:** Full Width at Half Maximum (Anchura a media altura)
- **GO:** Graphene Oxide (Óxido de grafeno)
- **H₂O₂:** Peróxido de hidrógeno
- **H₂SO₄:** Ácido sulfúrico
- **Hg/HgO:** Electrodos de mercurio/óxido de mercurio
- **HOPG:** Highly Oriented Pyrolytic Graphite (Grafito pirolítico altamente orientado)
- **HR-TEM:** High Resolution TEM (Microscopía electrónica de transmisión de alta resolución)
- **HSC:** Hybrid Supercapacitor (Supercondensador híbrido)
- **IHP:** Inner Helmholtz Plane (Plano interno de Helmholtz)
- **KNO₃:** Nitrato de potasio
- **KOH:** Hidróxido de potasio
- **LIBs:** Lithium-Ion Batteries (Baterías de ion litio)
- **LiPF₆:** Hexafluorofosfato de litio
- **LP30:** Solución de 1 M LiPF₆ en una mezcla de carbonato de etileno/carbonato de dimetilo
- **Na₂SO₄:** Sulfato de sodio
- **NaCl:** Cloruro de sodio

Lista de acrónimos

- **NaOH:** Hidróxido de sodio
- **NbSe₂:** Diseleniuro de niobio
- **NMP:** N-metil-2-pirrolidona
- **OHP:** Outer Helmholtz Plane (Plano externo de Helmholtz)
- **PCs:** Pseudocapacitors (Pseudocondensadores)
- **PTFE:** Politetrafluoroetileno
- **PVDF:** Fluoruro de polivinilideno
- **SEM:** Scanning Electron Microscopy (Microscopía electrónica de barrido)
- **SPM:** Scanning Probe Microscopy (Microscopía de campo cercano o de proximidad)
- **STEM:** Scanning Transmission Electron Microscopy (Microscopía electrónica de barrido por transmisión)
- **TEM:** Transmission Electron Microscopy (Microscopía electrónica de transmisión)
- **TMDs:** Transition Metal Dichalcogenides (Dicalcogenuros de Metales de Transición)
- **TMOs:** Transition metal oxides (Óxidos de metales de transición)
- **UV-Vis:** Espectroscopía ultravioleta-visible
- **XPS:** X-ray photoelectron spectroscopy (Espectroscopía fotoelectrónica de rayos X)
- **XRD:** X-ray Diffraction (Difracción de rayos X)
- **ZICs:** Zinc-Ion Capacitors (Condensadores de ion zinc)
- **ZnSO₄:** Sulfato de zinc

1. INTRODUCCIÓN

1 Introducción

1.1 Nanomateriales 2D

En las últimas décadas, los nanomateriales o materiales nanométricos o nanoestructurados han irrumpido con fuerza en la ciencia de materiales y la tecnología moderna, transformando la forma en que concebimos, diseñamos y aplicamos materiales en distintos campos. Los nanomateriales se caracterizan por morfologías en las que al menos una de sus dimensiones espaciales se encuentra comprendida entre 1 y 100 nanómetros [1], y se clasifican en función del número de dimensiones espaciales que presenten dentro de la escala nanométrica. Así, podemos encontrar materiales de dimensionalidad 0 (0D), que presentan todas sus dimensiones en nanoescala (puntos cuánticos, nanopartículas); unidimensionales (1D), que presentan dos dimensiones dentro de la nanoescala (hilos cuánticos, nanotubos, nanobarras, nanocables); y bidimensionales (2D), que presentan una sola dimensión dentro de la nanoescala (pozos cuánticos, nanoláminas, nanoplacas) [2,3]. La principal relevancia de los nanomateriales radica en sus propiedades y funcionalidades únicas, que no están disponibles generalmente en versiones no nanométricas de los mismos. Esto se ejemplifica claramente en el caso de los materiales de carbono con hibridación sp^2 , donde el grafeno, material 2D formado por una única monocapa de grafito, posee propiedades electrónicas, ópticas, térmicas, etc., diferenciadas de las de su equivalente 3D bulk.

El aislamiento de monocapas y mult capas (<10) de grafito para dar lugar a grafeno se realizó por primera vez en 2004 de la mano de los físicos Andre Geim y Konstantin Novoselov. Ello supuso el hito fundacional del campo de los materiales 2D y dio lugar a líneas de investigación centradas en la obtención de estos materiales por medio de distintas metodologías, así como la exploración de sus usos prácticos. Muchos de los materiales 2D más relevantes están directamente

Introducción

relacionados con los materiales laminares. Éstos últimos son sólidos macroscópicos formados por láminas de grosor atómico apiladas unas sobre otras, que están unidas entre sí por fuerzas débiles de tipo Van der Waals [4]. La estructura de monocapas débilmente interactuantes característica de los materiales laminares hace que la obtención de sus equivalentes 2D sea relativamente sencilla, en base a metodologías que van desde la síntesis a partir de precursores moleculares (estrategias ascendentes o *bottom-up*) a la exfoliación del material laminar *bulk* (estrategias descendentes o *top-down*). Tras dos décadas de investigación, se han obtenido gran cantidad de materiales 2D, como son el grafeno y sus derivados, materiales 2D monoelementales (fosforeno, aseneno, etc), dicalcogenuros de metales de transición (TMDs), MXenos o los óxidos de metales de transición (TMOs), entre otros.

Pese a presentar propiedades únicas, surgidas del confinamiento de los electrones en dos dimensiones y de la alta proporción superficie/volumen, la estabilidad de los materiales 2D es un factor crítico a la hora de su aplicabilidad. En la Figura 1 se puede observar la estabilidad relativa de alguno de los materiales 2D más relevantes en condiciones ambientales, donde los materiales destacados en azul son estables de manera indefinida, los destacados en verde son estables en períodos relativamente largos, mientras que los destacados en rosa son materiales 2D inestables. Los materiales destacados en gris han sido preparados en forma 2D, pero aún no se dispone de información concluyente sobre su estabilidad [2,5,6]. Cabe destacar que recientes estudios han demostrado que los materiales laminares tipo perovskita podrían presentar cierta estabilidad en condiciones ambientales tras modificación estructural [7,8].

Familia del grafeno	Grafeno	hBN	BCN	Fluorografeno	Oxido de grafeno
Calcogenuros 2D	MoS ₂ , WS ₂ , MoSe ₂ , WSe ₂ , WSe ₂		Dicalcogenuros semiconductores: MoTe ₂ , WTe ₂ , ZrS ₂ , ZrSe ₂ , etc.	Dicalcogenuros metálicos: NbSe ₂ , NbS ₂ , TaS ₂ , TiS ₂ , NiSe ₂ , etc.	Semiconductores laminares: GaSe, GaTe, InSe, Bi ₂ Se ₃ , etc.
Oxidos 2D	Micas, BSCCO	MoO ₃ , WO ₃		Tipo Perovskita: LaNb ₂ O ₇ , (Ca,Sr) ₂	Hidróxidos: Ni(OH) ₂ , Eu(OH) ₂ , etc.
	Oxidos de Cu laminares	TiO ₂ , MnO ₂ , V ₂ O ₅ , TaO ₃ , RuO ₂ , etc.		Nb ₃ O ₁₀ , Bi ₄ Ti ₃ O ₁₂ , Ca ₂ Ta ₂ TiO ₁₀ , etc.	Otros

Figura 1. Tipos de materiales 2D obtenidos a partir de materiales 3D laminares y su estabilidad en condiciones ambientales. Adaptado de [5].

Esta tesis se ha desarrollado dentro del marco de síntesis y estudio de aplicaciones de materiales 2D, concretamente grafeno y dicalcogenuros metálicos.

1.1.1 Grafeno.

Estrictamente hablando, el grafeno es una forma alotrópica del carbono formado por una única monocapa de átomos de carbono con hibridación sp^2 , donde se encuentran enlazados covalentemente en una estructura hexagonal [9]. Por lo tanto, el grafeno también se puede definir como una monocapa de grafito. Sin embargo, el término grafeno también se usa para designar nanoláminas de grafito formadas por varias monoláminas, típicamente entre 2 y 10. Por encima de 10

Introducción

monocapas, el material se considera como filme delgado de grafito, pero no grafeno, debido a que sus propiedades son ya esencialmente indistinguibles de las del grafito *bulk*. Las propiedades electrónicas, térmicas, ópticas, mecánicas y químicas diferenciadas de las del grafito confieren un interés destacado al grafeno en gran número de aplicaciones.

Las **propiedades electrónicas** del grafeno derivan de la combinación de su estructura (átomos de carbono con hibridación sp^2) y su morfología 2D. En la hibridación sp^2 , el orbital s y dos orbitales p (p_x y p_y) del carbono se combinan para dar lugar a 3 orbitales híbridos sp^2 , que se disponen en un plano formando ángulos de 120° grados. Un orbital p sin hibridar (orbital p_z) permite formar enlaces dobles con átomos de carbono contiguos, conjugándose a lo largo de toda la estructura en forma de nube electrónica deslocalizada a ambos lados del plano basal (electrones π , Figura 3a). Los electrones π deslocalizados dotan de una gran movilidad electrónica al grafeno ($> 200000 \text{ cm}^2\text{V}^{-1}\text{s}^{-1}$ a densidades de electrones de $2 \times 10^{11} \text{ cm}^{-2}$) [10-13]. Esta alta movilidad está asociada con la estructura de bandas del grafeno, que forma conos que se tocan en puntos específicos del espacio recíproco, conocidos como puntos de Dirac, donde los estados excitados y no excitados confluyen (Figura 3b) [14]. Los puntos de Dirac dan lugar a propiedades electrónicas únicas, como la presencia de fermiones de Dirac y la ausencia de *gap* de banda (el grafeno monocapa es un semiconductor de *gap* de banda cero).

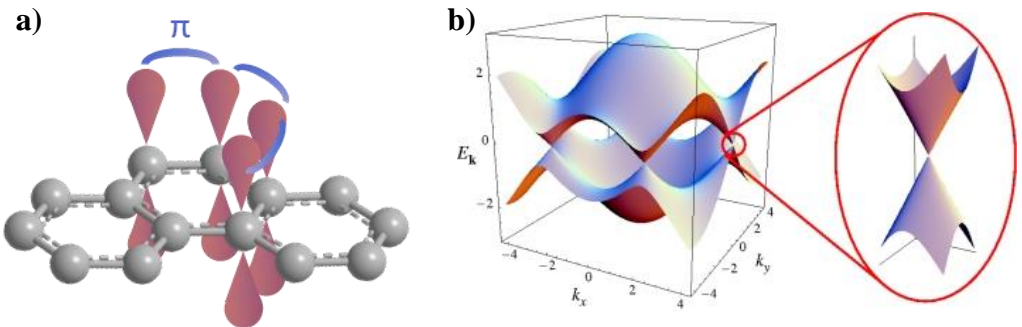


Figura 2. a) Orbitales π del grafeno provenientes de orbitales p_z del carbono, b) Conos de Dirac. Adaptado de [15].

Otra propiedad del grafeno asociada a su naturaleza 2D es el efecto Hall cuántico fraccionario. Este efecto se produce cuando los portadores de carga (principalmente electrones) están confinados en un espacio 2D y son atravesados perpendicularmente por un campo magnético. Como resultado de las fuertes interacciones entre los electrones, estos portadores de carga se comportan como cuasipartículas, con una carga efectiva que es una fracción de la de un electrón [16-18]. Se ha observado que el efecto Hall cuántico fraccionario puede ocurrir en el grafeno a temperaturas más altas (hasta 20 K) que en otros materiales[16]. Por otro lado, se ha observado que la iluminación de una lámina de grafeno con luz polarizada circularmente de alta intensidad puede inducir el efecto Hall cuántico (efecto hall cuántico inducido por luz), lo que se traduce en aplicaciones potenciales para el grafeno como material topológico [19].

En cuanto a sus **propiedades ópticas**, el grafeno monocapa posee una transmitancia del 97.7% en la zona del visible, así como fuerte absorción en la región del ultravioleta cercano, presentando una banda de absorción característica en torno a 265-270 nm asociada a transiciones $\pi \rightarrow \pi^*$ [20]. La elevada transparencia en el rango óptico junto con la alta conductividad eléctrica hacen que el grafeno y

Introducción

algunos de sus derivados sean muy atractivos como sustitutos de los actuales conductores transparentes [óxidos de indio y estaño (ITO)] [21]. Por otro lado, el grafeno presenta efectos ópticos no lineales, que pueden ser potenciados por campos eléctricos. Este fenómeno, conocido como generación de armónicos ópticos, permite al grafeno capturar fotones, combinarlos y generar un haz óptico más potente.

Otra propiedad óptica destacable de ciertos derivados del grafeno es la fotoluminiscencia, que puede ser inducida mediante la creación de un *gap* de banda finito adecuado. Existen dos estrategias principales para abrir un *gap* de banda y, por tanto, conseguir fotoluminiscencia en grafenos. Una consiste en reducir la dimensionalidad de la estructura 2D a estructuras 1D (nanocintas de grafeno) o 0D (puntos cuánticos de grafeno). La otra se basa en tratamientos químicos o físicos que reduzcan la extensión y la conectividad de los dominios electrónicamente conjugados (electrones π) del material [20]. Una combinación de capas alternativas fotoluminiscentes y conductoras de grafeno se podría utilizar para generar diodos tipo sándwich [22,23].

El grafeno posee excepcionales **propiedades mecánicas**, al tratarse de uno de los materiales más duros y resistentes que se conocen (superia la dureza del diamante y es unas 200 veces más resistente que el acero). Se ha determinado que el grafeno tiene una resistencia a la tracción de aproximadamente 130 GPa y un módulo de Young de alrededor de 1 TPa, lo que lo hace sumamente elástico y capaz de soportar grandes presiones sin sufrir ruptura [24]. Estas propiedades mecánicas excepcionales lo hacen adecuado para su uso en una gran variedad de aplicaciones, por ejemplo, como refuerzo en materiales compuestos o en la fabricación de dispositivos electrónicos para la industria aeroespacial y automotriz[25].

En cuanto a sus **propiedades térmicas**, cabe destacar que la conductividad térmica del grafeno a temperatura ambiente se encuentra generalmente entre 2000

y 4000 W mK^{-1} para muestras suspendidas [9,26,27]. No obstante, se han observado valores de hasta 4419 W mK^{-1} para muestras purificadas isotópicamente (0,01% de ^{13}C en lugar de 1,1% de abundancia natural de este isótopo) con tamaños de dominio grandes [28] e incluso en recientes estudios se han llegado a medir valores de conductividad térmica de hasta 5.300 W mK^{-1} para una única lámina aislada de grafeno suspendida sobre espacios generados en un sustrato de SiO_2 [29], lo que supone una valor hasta 10 veces mayor que el del cobre (400 W mK^{-1}). Pese a que, a priori, estos valores indican que el grafeno podría ser un buen sustituto del cobre en dispositivos termoeléctricos, en el procesado para su utilización en dispositivos reales, la tendencia al reapilamiento de las láminas da lugar a valores de conductividad térmica menores. Por ello, para su utilización en dispositivos reales, se combina con nanotubos de carbono dando lugar a estructuras 3D con funcionalidad termomecánica ajustable [30].

Las **propiedades químicas** del grafeno también son relevantes. Debido a su elevada área superficial accesible, el grafeno es un material que se puede modificar extensamente por medios químicos, por ejemplo, para introducirle grupos funcionales adecuados que faciliten su utilización en diversas aplicaciones. La modificación química del grafeno se puede llevar a cabo mediante dos metodologías, a saber, covalente y no covalente [31].

La funcionalización covalente consiste en la introducción de heteroátomos o grupos moleculares funcionales en la superficie del grafeno mediante la formación de fuertes enlaces covalentes y conlleva una alteración de la red atómica carbonosa en forma de defectos sustitucionales, generación de hibridación sp^3 , etc [31,32]. Por otro lado, los métodos no covalentes de funcionalización se basan en interacciones débiles (ion- π , Vander Waals, $\pi-\pi$, hidrófobas) para anclar especies moleculares en la superficie del grafeno. Éstos últimos permiten modular las propiedades del grafeno (p.ej., alterar su estructura electrónica por transferencia de

Introducción

carga o su hidrofilia) sin necesidad de introducir defectos en su red cristalina (Figura 3) [33].

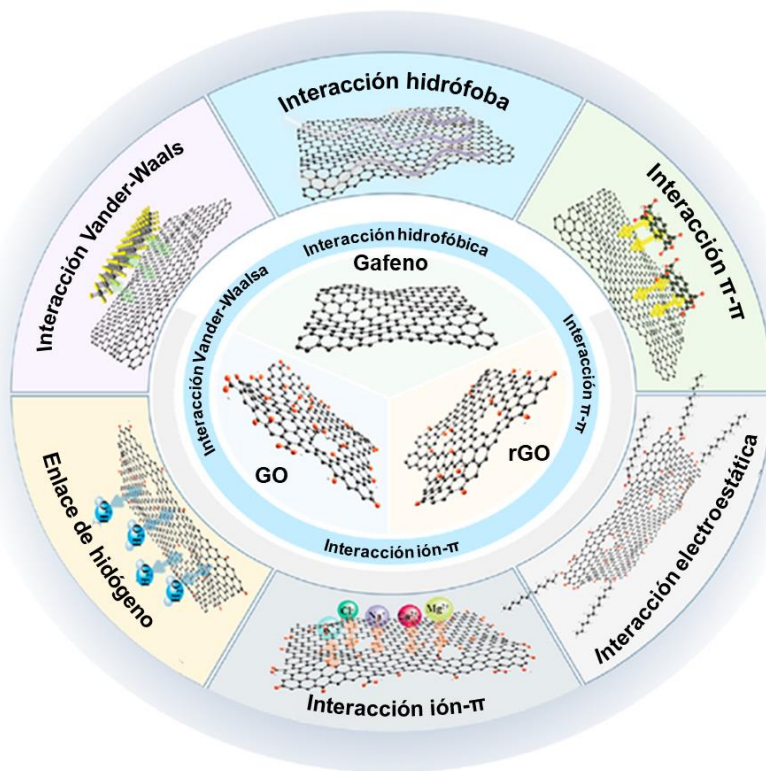


Figura 3. Interacciones no covalentes del grafeno. Adaptado de [33].

La funcionalización de grafeno con grupos moleculares permite, entre otros usos relevantes, mejorar su estabilidad coloidal en medio líquido, particularmente en agua. El grafeno prístico es hidrófobo y, por tanto, no dispersa bien en medio acuoso por sí solo. Sin embargo, el anclaje de grupos hidrófilos en su superficie, ya sea por métodos covalentes o no covalentes (surfactantes y otras moléculas anfifílicas) [34-36], permite obtener dispersiones coloidales estables y facilita con

ello su posterior procesado para la obtención de materiales compuestos [37], catalíticos [38], biomédicos [39] o dispositivos electrónicos [40].

1.1.2 Diseleniuro de niobio (NbSe_2)

El diseleniuro de niobio (NbSe_2) es un sólido que pertenece a la familia de los dicalcogenuros de metales de transición (TMDs, de *transition metal dichalcogenides*). Los TMDs atienden a una formula general MX_2 , donde M es un metal de transición (Mo, W, V, Nb, Ta, etc) y X es un calcógeno (S, Se, Te). En su mayoría se caracterizan por tener una estructura laminar, con láminas formadas por una monocapa de átomos del metal embebida entre dos monocapas atómicas del calcógeno, en las que los primeros están enlazados covalentemente a los segundos. A su vez, estas láminas se apilan unas sobre otras, manteniéndose unidas entre sí por interacciones débiles tipo van der Waals. Por tanto, a diferencia de lo que ocurre en el caso del grafeno (monocapa atómica), cada lámina de un TMD laminar es una tricapa atómica.

Los TMDs laminares pueden presentarse en varias fases estructurales que resultan de los distintos tipos de coordinación del metal con el calcógeno y del orden de apilamiento de unas láminas sobre otras. Las dos fases más comunes son la 1T (coordinación octaédrica y apilamiento AbC AbC, donde las letras mayúsculas denotan al calcógeno y las minúsculas al metal) y la 2H (coordinación trigonal prismática, apilamiento AbA BaB) (Figura 4). Dependiendo de la combinación concreta de metal y calcógeno, la fase termodinámicamente estable suele ser una de estas dos, mientras que la otra aparece como fase metaestable [41]. En los últimos años, los TMDs laminares en forma 2D han sido objeto de gran interés, tanto desde un punto de vista de ciencia fundamental como aplicado, debido a sus

Introducción

propiedades electrónicas, ópticas, mecánicas y químicas diferenciadas de las de sus equivalentes *bulk*. En esta tesis se ha seleccionado NbSe₂ como objeto de estudio debido a que, a diferencia de los TMDs laminares más estudiados, como MoS₂, WS₂ o MoSe₂, que poseen un carácter semiconductor, el NbSe₂-2H (fase 2Dtermodinámicamente estable) presenta un carácter metálico que lo hace más atractivo para determinadas aplicaciones [42].

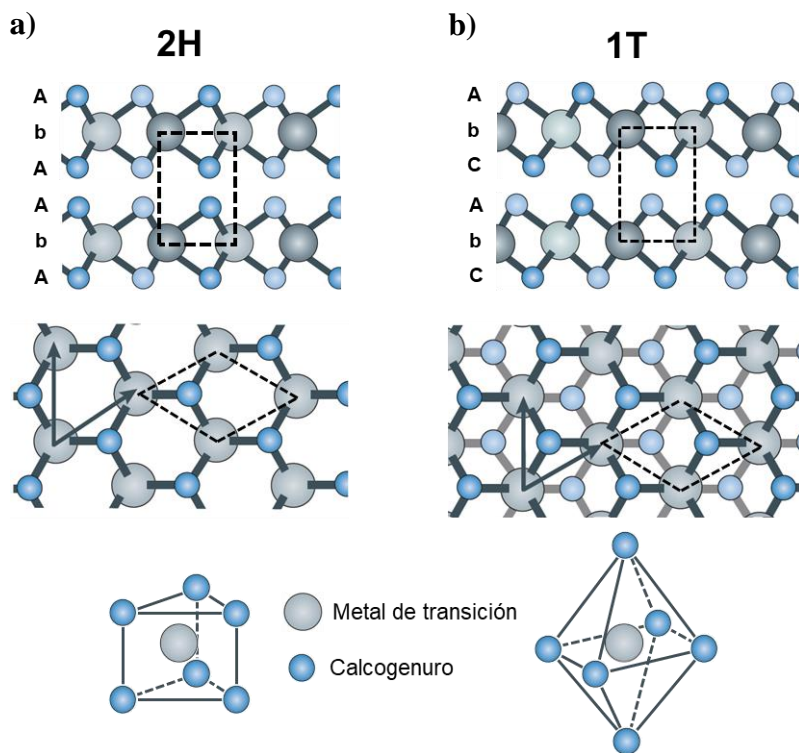


Figura 4. Fase (a) 2H (trigonal prismática) y (b) 1T (octaédrica) del NbSe₂. Adaptado de [41].

La combinación de electrones *d* de valencia, la coordinación del metal de transición con el calcógeno y el apilamiento de las capas son los factores determinantes de las propiedades de los TMDs [43,44]. Una de los rasgos más relevantes que presenta el NbSe₂ es la **onda de densidad de carga** (CDW, *charge*

density wave). Ésta aparece en materiales con estructuras de bandas electrónicas altamente anisótropas, donde las interacciones electrón-fonón llevan a un tipo de estado en el que la densidad de electrones se encuentra modulada periódicamente [45]. Ello permite alterar las propiedades electrónicas y químicas de los materiales que cuentan con esta característica, lo que facilita la utilización del NbSe₂ en catálisis heterogénea o nanoelectrónica [46].

Por otro lado, todos los materiales que muestran un estado CDW en su diagrama de fases también exhiben **superconductividad**, y de hecho ambas coexisten en el 2H-NbSe₂ [41]. Aquí, cabe destacar que la superconductividad está generalmente relacionada con el grosor del material, donde la tendencia habitual, es que, a medida que disminuye el grosor, disminuye la temperatura crítica a la que se alcanza el estado superconductor. Por ejemplo, para el 2H-NbSe₂ obtenido mediante exfoliación mecánica (Scotch tape), la temperatura crítica, pasa de un valor inicial de 7.2 K para el bulk a 2.5 K para láminas de unas pocas monocapas [47]. Sin embargo, estudios recientes también han determinado el comportamiento opuesto, probablemente ligado a la metodología de obtención del material en condiciones ambientales, que implica su oxidación parcial durante el proceso de exfoliación [48,49].

Las **propiedades electrónicas y químicas** de los TMDs se pueden controlar mediante dopaje, bien por sustitución, bien por intercalación. El dopaje por sustitución consiste en reemplazar el metal o el calcógeno por otro elemento diferente. En el caso del NbSe₂, se han desarrollado sustituciones del Nb por W ($W_xNb_{1-x}Se_2$) para su utilización en dispositivos electrónicos, así como del Se por S o Si (NbS_xSe_{2-x}), logrando con ello modular la densidad de estados cerca del nivel de Fermi y, por tanto, modificando su conductividad eléctrica y magnetismo [50]. El dopaje por intercalación permite introducir átomos de los mismos u otros elementos (p.ej., metales alcalinos [51,52] metales de transición [53-55] y metales

Introducción

del bloque p [56]) en los espacios interlaminares, modulando las propiedades del TMD sin alterar su estructura. Por ejemplo, la intercalación de Mg en 2H-NbSe₂ da lugar a una disminución de su temperatura crítica de superconductividad (T_c) [57].

1.2 Métodos de obtención de materiales 2D

Como se ha indicado anteriormente, uno de los factores determinantes de las propiedades de los materiales es su dimensionalidad. En los materiales nanoestructurados (0D, 1D, 2D), el tamaño concreto a lo largo de las dimensiones nanométricas puede influir de manera importante en sus propiedades. Por ejemplo, en los materiales 2D el grosor (o el número de monocapas de que constan, si provienen de un material bulk laminar) suele determinar sus características electrónicas, ópticas, mecánicas y otras, con lo que resulta determinante controlar dicho parámetro durante su preparación.

En las últimas dos décadas se han desarrollado distintas metodologías de síntesis/preparación de materiales 2D. Estas metodologías tienen en cuenta no solo la obtención de materiales 2D con grosores adecuados, sino también aspectos como la rapidez, eficiencia, coste, rendimiento, control de otras características (grado de oxidación, funcionalización, defectos, etc.) o sostenibilidad ambiental del proceso. Al igual que ocurre con los métodos de preparación de materiales nanoestructurados en general, los métodos de obtención de materiales 2D se engloban en dos grandes categorías: métodos *bottom-up* o ascendentes y métodos *top-down* o descendentes.

1.2.1 Métodos *bottom-up* o ascendentes

En ellos, los materiales 2D se obtienen mediante el ensamblaje de sus componentes más básicos, ya sea a nivel atómico o molecular. Algunas metodologías *bottom-up* comúnmente utilizadas en la síntesis de grafeno y TMDs son las siguientes:

a. Depósito químico en fase vapor

El método de depósito químico en fase vapor o CVD (*chemical vapor deposition*) es una técnica de síntesis donde una película fina de un determinado material se deposita sobre un sustrato. Para ello, en una cámara de reacción se introducen distintos gases (precursores, portadores del gas y, en algunos casos, gases de activación). Los gases precursores (en algunos casos solo hay uno) se descomponen a altas temperaturas y las especies resultantes reaccionan sobre el sustrato, que actúa como catalizador, generándose un depósito de un material monoelemental (p.ej., grafeno) o de un compuesto (p.ej., TMDs) de grosor generalmente uniforme [58,59].

Se han propuesto diversas rutas para la síntesis de grafeno por CVD en base a diferentes precursores que van incluso más allá del uso de gases, incluyendo distintos tipos de sólidos, líquidos y materiales de desecho ricos en carbono. Además, se han explorado diversos sustratos de crecimiento, como níquel, cobre, platino, germanio y aleaciones de cobre-níquel, siendo el cobre y el níquel los más utilizados [60,61]. En el caso de los TMDs, se ha conseguido modular las características del material (morfología, fase, tamaño de dominios, número de monocapas, calidad estructural) controlando los parámetros de crecimiento (temperatura, gas portador, precursores y sus proporciones, presión, tiempo de crecimiento) [62].

b. Crecimiento epitaxial

Esta técnica se basa en el crecimiento de un sólido cristalino como continuación de la red cristalina de un sustrato que actúa como plantilla. Se ha empleado dicho método, por ejemplo, para generar filmes de grafeno sobre sustratos de carburo de silicio (SiC) monocrystalino. El material 2D obtenido suele tener una alta calidad estructural, pero el proceso tiene limitaciones inherentes, como las altas temperaturas requeridas o la dificultad para transferir el grafeno resultante a otros sustratos de interés tecnológico [63,64].

c. Métodos basados en tratamientos láser

Es posible obtener filmes de grafeno mediante tratamiento de precursores adecuados con un haz láser. En esta categoría, existen dos enfoques principales. El primero, denominado técnica de grafeno inducido por láser (LIG, *laser-induced graphene*) se caracteriza por la preparación de grafeno en una morfología 3D y se basa en la exposición de un precursor orgánico a un haz láser infrarrojo, que se transforma en un material carbonoso basado en grafeno [65]. El segundo enfoque, denominado ablación por láser (LAG, *laser-ablated graphene*) se basa en irradiar un precursor de carbono (p.ej., grafito) típicamente mediante un láser pulsado de alta potencia, lo que provoca su evaporación y la formación de un plasma, que finalmente condensa para formar capas delgadas de grafeno [66].

d. Metodologías de descarga eléctrica (flash graphene)

Una metodología desarrollada en años recientes para preparar grafeno es la denominada de descarga eléctrica (*flash graphene*), que utiliza el calentamiento por destello Joule para convertir diversas fuentes de carbono en grafeno con un bajo

grado de defectos. Esta estrategia conlleva someter precursores de carbono sólidos, como carbono coque de petróleo, a una descarga eléctrica intensa. El proceso, llevado a cabo en un tubo cerámico entre dos electrodos, alcanza temperaturas de hasta 2700 °C durante breves períodos de tiempo (menos de 100 ms), lo que contribuye a la buena calidad estructural de los productos obtenidos [67].

e. Método de síntesis hidrotérmica

Este método, muy utilizado en la síntesis de TMDs, se lleva a cabo en autoclaves en los que especies precursoras se solubilizan total o parcialmente en medio acuoso y se someten a temperaturas moderadas (150-250 °C) y presión normalmente autogenerada. La reacción transcurre en tres etapas, a saber, nucleación, crecimiento y modulación de Ostwald (Figura 6), obteniéndose finalmente el TMD deseado [68,69].

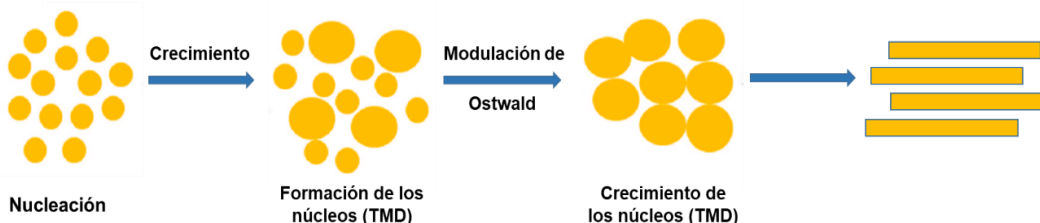


Figura 5. Metodología hidrotérmica de obtención de TMDs. Adaptado de [68].

Esta estrategia permite modular distintas variables, tales como la relación molar de precursores, presión, temperatura o tiempo de reacción, lo que se traduce en un control sobre la morfología del material 2D resultante [70]. Asimismo, mediante la adición de surfactantes al medio de reacción, es posible modular no

solo la morfología, sino también el número de monocapas por lámina e incluso la fase estructural [71].

1.2.2 Métodos *top-down* o descendentes

Estos métodos persiguen la obtención de materiales 2D mediante la exfoliación a láminas monocapa o de unas pocas o varias monocapas de un material de partida *bulk* de estructura laminar. La estrategia se aprovecha del hecho de que, en los materiales laminares, unas láminas monocapa se encuentran unidas a otras por fuerzas débiles tipo Vander Waals. Dichas fuerzas son proporcionales a $1/d^6$ (dónde d es la distancia interlaminar) y se consideran despreciables a partir de distancias de varios angstroms ($> 5 \text{ \AA}$) [72]. De esta manera, es posible deslaminar (exfoliar) el material laminar utilizando fuerzas o estímulos externos que, al mismo tiempo, sean suficientemente débiles como para evitar la ruptura de los enlaces covalentes que mantienen cohesionados a los átomos dentro de cada monocapa. En función de la estrategia concreta utilizada para deslaminar el material, existen distintos tipos de exfoliación, como la exfoliación por ultrasonidos, exfoliación por fuerzas de cizalla o exfoliación electroquímica, entre otras.

El primer método *top-down* desarrollado para la obtención de materiales 2D fue el método de **exfoliación micromecánica** con cinta adhesiva (Scotch tape), introducido por Andre Geim y Konstantin Novoselov en 2004 [73]. En este caso, la exfoliación se consigue despegando con la cinta adhesiva fragmentos cada vez más delgados de grafito a partir de una pieza de grafito pirolítico altamente orientado (HOPG, *highly oriented pyrolytic graphite*), hasta un punto en el que se obtienen fragmentos lo suficientemente delgados como para ser considerados grafeno. Esta metodología permite preparar láminas de grafeno de alta calidad estructural, muy

útiles para la realización de estudios fundamentales, y se puede aplicar también en la obtención de otros materiales 2D laminares, como el nitruro de boro hexagonal (h-BN), dicalcogenuros de metales de transición (MoS_2 , WS_2 , NbSe_2 , etc.) y óxidos complejos ($\text{Bi}_2\text{SrCaCu}_2\text{O}_x$) [74], aunque en estos dos últimos casos la exfoliación también se puede realizar por fricción de los cristales de partida sobre una superficie sólida. Sin embargo, el rendimiento de este método es muy bajo (genera sólo unas pocas láminas 2D entre un gran número de objetos de mayor grosor), lo que motivó el desarrollo de estrategias de exfoliación alternativas capaces de producir mayor cantidad de material 2D con mayores rendimientos. En la actualidad, los métodos de exfoliación más habituales son los que se llevan a cabo en fase líquida, ya que facilitan la obtención de grafeno y otros materiales 2D en grandes cantidades y, en muchos casos, con buena calidad estructural alta y a bajo coste [75]. En función de los estímulos usados para inducir la exfoliación, se puede hablar de distintas metodologías, entre las que destacan la exfoliación por ultrasonidos y fuerzas de cizalla, la exfoliación química (p.ej., ruta del óxido de grafito) y la exfoliación electroquímica.

a. Exfoliación por ultrasonidos y por fuerzas de cizalla

Constituye una de las rutas de preparación de materiales 2D más utilizadas. Se fundamenta en la aplicación, en medio líquido, de fuerzas laterales y verticales a los planos basales de materiales *bulk* laminares, que provocan la separación de capas del sólido y, por tanto, su exfoliación a láminas 2D [76]. Las fuerzas pueden proceder de ondas de choque en el caso de la exfoliación por ultrasonidos o del propio movimiento del fluido en el caso de la exfoliación por fuerzas de cizalla. En el primer caso, la deslaminación se genera por la implosión de burbujas de cavitación generadas por los ultrasonidos, que provoca que las resultantes ondas de choque incidan perpendicular y paralelamente a la superficie del material laminar.

Introducción

En el segundo caso, el paso del material laminar suspendido en el líquido a gran velocidad entre los componentes (rotor y estator) de un mezclador de alta cizalla (*high shear mixer*) genera una serie de fuerzas asociadas a la dinámica de fluidos (no solo de cizalla, sino también de cuña), que inducen la exfoliación del sólido [77,78] (Figura 6).



Figura 6. Mecanismo de exfoliación por ultrasonidos. Adaptado de [79].

Es importante resaltar que los disolventes más adecuados para la exfoliación y consiguiente dispersión coloidal de materiales 2D son aquellos que poseen una energía superficial similar a la del plano basal del material laminar a exfoliar. Ello es debido a que la similitud de energías superficiales permite minimizar la energía requerida para la solvatación de las láminas 2D. Algunos de los disolventes apropiados para la exfoliación y dispersión de grafeno y TMDs laminares son compuestos orgánicos como la *N*-metil-2-pirrolidona (NMP), el isopropanol (IPA) y la *N,N*-dimetilformamida (DMF) [76],[78]. De manera alternativa, es posible exfoliar y estabilizar coloidalmente materiales 2D en medio acuoso utilizando

surfactantes y otras moléculas anfifílicas adecuadas (polímeros, biomoléculas, etc.), o bien mezclas de agua con determinados disolventes orgánicos (p.ej., etanol). El medio de dispersión acuoso es particularmente atractivo desde un punto de vista medioambiental o con vistas a determinados usos (p.ej., biomedicina) [80-83]. Sin embargo, aunque estos disolventes orgánicos y mezclas agua-estabilizante han demostrado ser efectivos en la preparación de dispersiones coloidales de láminas 2D, el rendimiento de exfoliación asociado a los procesos de ultrasonidos y cizalla con los mismos es generalmente bajo (< 1%) [78]. Por otro lado, una de las principales ventajas de esta metodología reside en el hecho de que los materiales 2D obtenidos suelen tener una alta calidad estructural, ya que el proceso no implica el uso de especies químicas ni tratamientos agresivos que alteren el material. Además, el hecho de generar dispersiones estables permite que éstas se puedan procesar posteriormente por distintas técnicas para dar lugar a una variedad de materiales de distintas morfologías (fibras, filmes, geles, etc) con utilidad en distintos campos, como el de los materiales compuestos [84], almacenamiento de energía [85] o protección de superficies [86].

b. Ruta del óxido de grafito

Una estrategia para la obtención de materiales 2D se basa en llevar a cabo una modificación por métodos químicos del material laminar *bulk* de partida que facilite su posterior exfoliación. Como consecuencia de dicho proceso, las láminas 2D resultantes pueden tener una composición química diferente de la que se pretendía en un principio para el material 2D objetivo, en cuyo caso se haría necesario un posterior tratamiento para revertir la modificación química realizada. El ejemplo más conocido de esta estrategia es el de la preparación de grafeno mediante la ruta del óxido de grafito. En esta ruta, un grafito en polvo es oxidado de manera agresiva mediante una mezcla de oxidantes y ácidos fuertes.

Introducción

Dependiendo de los oxidantes y ácidos concretos utilizados, los métodos de preparación de óxido de grafito reciben distintos nombres: métodos de Brodie, Staudenmaier, Hofmann, Hummers, Tour o modificaciones de estos [87-90]. Este tratamiento de oxidación introduce grupos funcionales oxigenados en los planos basales y bordes de grano del grafito, lo que conlleva un aumento del espaciado interlaminar y, por tanto, una disminución de las fuerzas interlaminares atractivas, lo que facilita la exfoliación del material. Asimismo, algunos de estos grupos oxigenados son fácilmente ionizables (desprotonables), lo que facilita la exfoliación del óxido de grafito y la estabilización coloidal de las láminas resultantes de óxido de grafeno (GO, *graphene oxide*) en medio acuoso. Dicha exfoliación se consigue de manera muy efectiva, es decir, con muy altos rendimientos ($> 80\%$), mediante la aplicación de ultrasonidos o fuerzas de cizalla. También es posible exfoliar y estabilizar coloidalmente láminas de GO en determinados disolventes orgánicos [91,92].

El GO es un grafeno fuertemente oxidado y, por tanto, muchas de sus características (conductividad eléctrica y térmica, resistencia mecánica, reactividad química, etc) difieren drásticamente de las observadas en el grafeno prístino. Presenta relaciones atómicas O/C en torno a 0.40-0.50 y posee una variedad de grupos funcionales oxigenados (hidroxilos, epoxis, carbonilos, carboxilos) decorando ambas caras de las láminas, que normalmente son monocapa. Además, también posee defectos estructurales (vacantes atómicas, bordes internos) inducidos por el tratamiento oxidativo. Para recuperar en la medida de lo posible las características del grafeno prístino, es necesario eliminar los grupos oxigenados. Esto se puede llevar a cabo por medio de distintos agentes reductores, como hidracina [93], vitamina C [94], hidrógeno [95] o determinadas biomoléculas [96], así como mediante otros procesos de reducción, como reducción térmica [97], electroquímica [98], fotoquímica [99], hidrotérmica [100] o por microondas [101]. Las láminas reducidas obtenidas se denominan óxido de grafeno reducido (rGO,

reduced graphene oxide). Es importante destacar que la calidad estructural del rGO es, en la inmensa mayoría de los casos, inferior a la del grafeno prístino, ya que los métodos de reducción no tienen por lo general una eficacia absoluta. Sin embargo, la ruta del óxido de grafito presenta la ventaja de tratarse de un método sencillo, económico, rápido y que proporciona muy buenos rendimientos.

c. Exfoliación por intercalación iónica

La exfoliación por intercalación iónica es otro método muy utilizado que se basa en la inserción de especies iónicas en el espacio interlaminar de un material *bulk* laminar. Esta intercalación induce un aumento de la distancia interlaminar y, por tanto, facilita la posterior deslaminación del sólido. Además, el proceso de exfoliación puede verse favorecido por la co-intercalación de moléculas de disolvente, cuya descomposición por reacciones redox con el material laminar genera gases que contribuyen a la expansión del material laminar. Factores termodinámicos y cinéticos influyen en la eficiencia de la intercalación iónica, que a su vez vienen dictados por características como los centros donde ocurre la intercalación, el tamaño y carga del ion intercalante el espacio interlaminar efectivo disponible [102].

La intercalación iónica puede llevarse a cabo por métodos químicos y electroquímicos. De los métodos químicos, el más conocido para la preparación de láminas 2D es el usado para exfoliar TMDs en base a la reacción con reactivos de organolitio, en particular con *n*-butil-litio (Figura 7). Por ejemplo, en el caso del NbSe₂, la reacción con *n*-butil-litio da lugar a la intercalación de iones Li⁺, generando el compuesto Li_xNbSe₂ [103]. Dicho compuesto reacciona fácilmente con agua, generando H₂ que fuerza la separación de unas láminas de otras, así como LiOH. Las láminas exfoliadas resultantes retienen una carga negativa residual del

Introducción

proceso de intercalación, que contribuye a su estabilización coloidal en el medio acuoso [104].

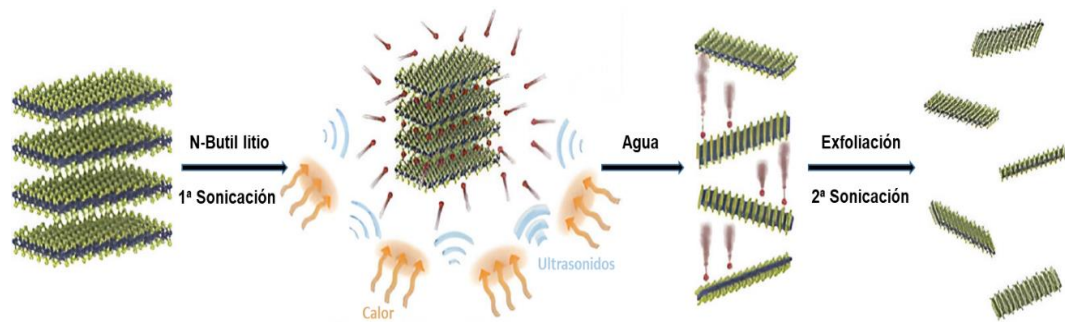


Figura 7. Mecanismo de exfoliación por intercalación iónica química. Adaptado de [104].

Mención aparte merecen los métodos electroquímicos de intercalación iónica para la exfoliación de materiales laminares. Estos métodos, denominados de manera más concisa métodos de exfoliación electroquímica (Figura 8), utilizan corrientes eléctricas como fuerzas inductoras de la exfoliación. Para ello, se aplica una diferencia de potencial entre dos electrodos, un electrodo de trabajo (WE, *working electrode*), que está hecho del material laminar a exfoliar, y un contraelectrodo (CE, *counter electrode*), hecho de un material inerte (p.ej., platino), sumergidos en un electrolito. La diferencia de potencial induce una migración de cargas iónicas del electrolito hacia la superficie y su posterior intercalación en los espacios interlaminares del material laminar que compone el WE. Esta intercalación iónica puede tener lugar con el ión totalmente desolvatado, parcialmente desolvatado o totalmente solvatado. En estos dos últimos casos, se produce por tanto una co-intercalación del disolvente, que puede participar en procesos redox y favorecer así la expansión del material laminar y/o su funcionalización. Tanto la concentración y tipo de electrolito, la presencia de aditivos en el electrolito, el potencial aplicado, la temperatura y la distancia de separación entre los electrodos

son factores determinantes en el grado de deslaminación y en las características fisicoquímicas del material exfoliado, lo que hace de la metodología electroquímica una estrategia muy versátil para la obtención de materiales 2D. Sin embargo, una cierta limitación de la técnica de exfoliación electroquímica es que se sólo se puede aplicar a materiales laminares que posean una cierta conductividad eléctrica, lo que en la práctica significa que sólo los materiales de naturaleza metálica y semiconductor son susceptibles de exfoliarse por esta vía.

Se pueden distinguir dos tipos de exfoliación electroquímica según la polaridad del voltaje que se aplique al WE: **exfoliación anódica**, cuando el potencial aplicado es positivo, y **exfoliación catódica** cuando se aplica un potencial negativo (Figura 8).

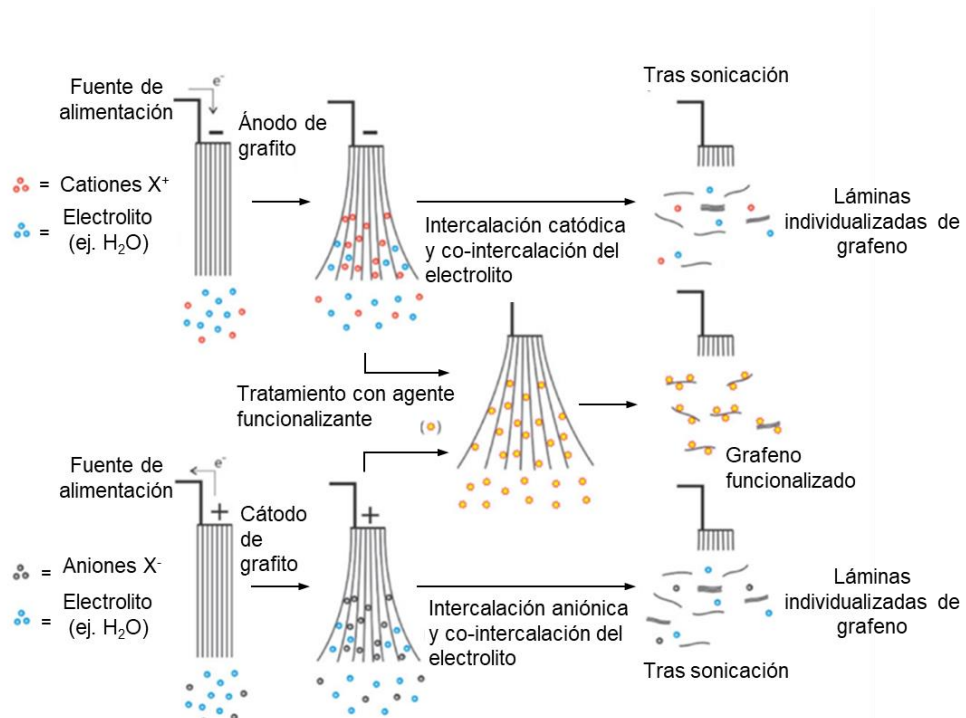


Figura 8. Mecanismos de exfoliación (a) catódica y (b) anódica. Adaptado de [105].

Exfoliación catódica

En la exfoliación catódica el WE se somete a un potencial negativo respecto al CE, lo que induce la intercalación de cationes del electrolito en el material laminar. Suele llevarse a cabo con sales de litio, alquilamonio o líquidos iónicos como electrolitos en disolventes orgánicos como dimetilsulfóxido, DMF o carbonato de propileno [106-109]. Esta metodología generalmente proporciona rendimientos y grados de exfoliación menores que los que se obtienen mediante exfoliación anódica, aunque tiene la ventaja de que es menos propensa a inducir modificaciones en la estructura y química del material 2D obtenido (p.ej., evita su oxidación) [110],[111]. Sin embargo, en el caso de los TMDs una intercalación excesiva, que se puede dar fácilmente con iones de pequeño tamaño (p.ej., Li^+), es susceptible de inducir una transformación de fase en el material laminar debido a la carga electrónica en exceso que adquiere el TMD. Esto ocurre, por ejemplo, en la intercalación de MoS_2 por litio, tanto por métodos electroquímicos como químico. El MoS_2 intercalado sufre una transformación desde su fase 2H semiconductor original a la fase 1T metálica [111-113]. Los materiales 2D obtenidos por exfoliación catódica se investigan en diversas aplicaciones, como almacenamiento y conversión electroquímicos de energía, sensores o celdas solares [114],[115].

Exfoliación anódica

En la exfoliación anódica, se aplica un potencial positivo al WE respecto al CE, lo que induce la intercalación de aniones en los espacios interlaminares del primero. En este caso, los electrolitos más usados son de tipo acuoso, con iones formados por ácidos, bases y sales inorgánicas, aunque también se han empleado sales orgánicas y líquidos iónicos [116-120]. En el caso del grafito, el mecanismo de exfoliación comienza con un proceso de oxidación local de su estructura en

límites de grano, bordes y otros defectos estructurales. Ello induce una expansión local de la distancia interlaminar que favorece la intercalación de aniones, con posible co-intercalación de moléculas de agua. El hecho de que los potenciales aplicados sean muy superiores al potencial de oxidación del agua da lugar a la descomposición de ésta y a la formación de especies de oxígeno reactivas, principalmente radicales hidroxilo ($\cdot\text{OH}$), que atacarán al grafito en expansión, provocando su oxidación [121]. La oxidación electroquímica del agua también llegará a dar su producto final, es decir, O_2 , que contribuirá a la expansión y deslaminación del grafito por efecto de las fuerzas de presión del gas [122]. La eficiencia de exfoliación anódica de grafito a grafeno suele ser bastante alta, obteniéndose láminas muy delgadas (monocapa y de unas pocas monocapas) con rendimientos elevados (por encima del 50% en muchos casos). Sin embargo, los procesos oxidativos asociados al proceso anódico en medio acuoso hacen que dichas láminas de grafeno presenten grados de oxidación significativos, típicamente con relaciones atómicas O/C entre 0.10 y 0.20 cuando se usan electrolitos comunes basados en sales de sulfatos [p.ej., Na_2SO_4 o $(\text{NH}_4)_2\text{SO}_4$] [123].

No obstante, la versatilidad del método electroquímico permite que el grado de modificación química del grafeno anódico (oxidativa o de otro tipo) se pueda modular en un rango bastante amplio. Esto se consigue normalmente usando electrolitos y/o aditivos de electrolito apropiados, que pueden tener dos efectos diferentes: **(1) Disminución del grado de oxidación del material 2D.** Ello se logra incluyendo en el electrolito sustancias de naturaleza antioxidante que tienden a reducir a las especies de oxígeno reactivas, evitando así que ataquen al grafeno y, por tanto, su oxidación. Dichas sustancias antioxidantes pueden ser los propios aniones intercalantes del proceso electroquímico (p.ej., determinados hidrocarburos aromáticos sulfonados) o aditivos que acompañan al anión intercalante [p.ej., melamina, TEMPO (2,2,6,6-tetrametilpiperidin-1-il)oxil] o benzoato de sodio]. En estos casos, los grafenos resultantes suelen poseer relaciones atómicas O/C en torno

a 0.05 [122],[124],[125]. **(2) Funcionalización del grafeno con otras especies químicas.** Esta funcionalización puede ser no covalente (fisisorción de moléculas presentes en el electrolito, p.ej., por interacción π - π) o covalente (p.ej., introducción de heteroátomos y determinados grupos moleculares) [117],[126-128].

La estrategia de exfoliación anódica no es muy utilizada para la obtención de láminas 2D de TMDs debido a la fuerte tendencia a la oxidación que presentan estos compuestos. Así, aunque existen estudios sobre la obtención anódica de láminas 2D de MoS₂, éstas presentan un porcentaje alto (> 20%) de molibdeno oxidado (Mo⁵⁺ y Mo⁶⁺) [129,130].

1.3 Materiales 2D para almacenamiento electroquímico de energía

Como se ha indicado anteriormente, los materiales 2D son potencialmente relevantes en el campo del almacenamiento y conversión de energía. Concretamente, los materiales obtenidos en esta tesis han sido estudiados como electrodos para distintos dispositivos de almacenamiento electroquímico de energía (EES, *electrochemical energy storage*), como supercondensadores, condensadores híbridos y baterías. Atendiendo al diagrama de Ragone (Figura 9), se observa que las baterías son dispositivos que poseen una elevada densidad gravimétrica de energía (es decir, acumulan una gran cantidad de energía por unidad de masa), pero adolecen de bajas densidades de potencia. Por el contrario, los condensadores y supercondensadores (simétricos, asimétricos) presentan generalmente altas densidades de potencia (capacidad de liberar y captar energía de forma rápida) combinadas con densidades de energía limitadas. En un término medio se encontrarían los sistemas híbridos condensador-batería, que poseen densidades de

energía y potencia significativas, aunque normalmente sin llegar a los valores alcanzados por las baterías en cuanto a energía específica.

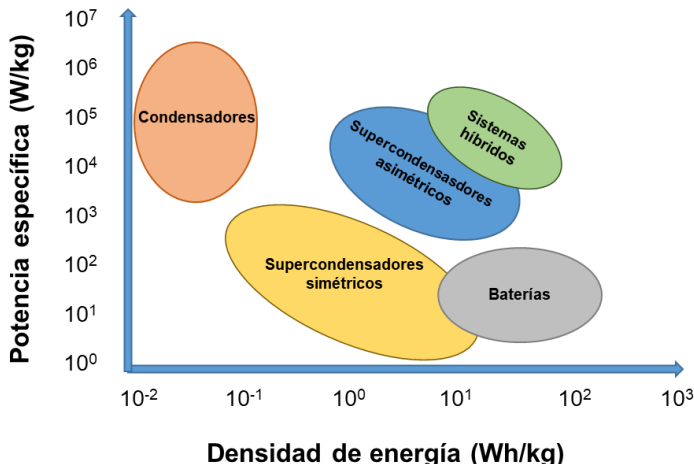


Figura 9. Diagrama de Ragone.

La arquitectura general de los dispositivos de almacenamiento electroquímico de energía consiste en un conjunto de celdas conectadas en serie o en paralelo, donde cada una de ellas se compone de dos electrodos (ánodo y cátodo) separados por una membrana porosa (separador) que permite la migración de iones del electrolito entre ambos (Figura 10) [131].

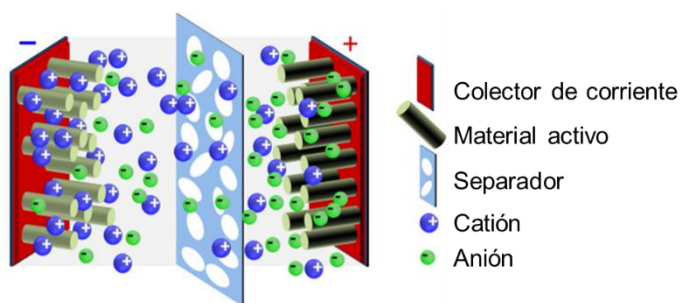


Figura 10. Esquema general de un dispositivo de EES. Adaptado de [131].

Introducción

El carácter más escorado hacia batería o condensador de un determinado tipo de dispositivo de EES viene determinado por los mecanismos de almacenamiento de energía que tienen lugar en dicho dispositivo. Es más, en un mismo dispositivo e incluso en un mismo electrodo del dispositivo pueden coexistir varios mecanismos de almacenamiento, aunque uno de ellos pueda ser el dominante. Los mecanismos de almacenamiento se pueden clasificar como: (a) procesos puramente capacitivos, no faradaicos, asociados a la formación de la capa doble eléctrica en la interfaz entre el electrodo y el electrolito; (b) procesos faradaicos, que implican algún tipo de reacción con el electrodo, como reacciones de intercalación iónica, reacciones redox o reacciones de conversión [132]. Los procesos puramente capacitivos tienen lugar exclusivamente en la superficie del electrodo y, por tanto, no están limitados por la difusión de especies iónicas en el interior del sólido. Por otro lado, los procesos faradaicos pueden tener lugar mayoritariamente en la superficie o muy cerca de la superficie del electrodo, en cuyo caso tampoco estarán limitados por difusión en el sólido, recibiendo el nombre de procesos pseudocapacitivos. Sin embargo, cuando los procesos faradaicos tienen lugar mayoritariamente en el interior del electrodo y están limitados por difusión, el electrodo mostrará un comportamiento tipo batería. Por tanto, los procesos capacitivos y pseudocapacitivos de almacenamiento de carga se caracterizan por ser cinéticamente rápidos, mientras que los procesos tipo batería, por su propia naturaleza, tienden a ser cinéticamente lentos [133].

1.4 Procesos de almacenamiento de energía

1.4.1 Procesos no faradaicos: doble capa eléctrica

El almacenamiento de carga eléctrica por formación de la doble capa eléctrica es un mecanismo superficial puramente electrostático que no implica reacciones redox o de otro tipo y cuya cinética no está controlada por la difusión del electrolito en el electrodo. El concepto de la doble capa eléctrica nació de la mano de Helmholtz en 1879, y consideraba que cuando se aplica un potencial eléctrico a un sólido conductor sumergido en un electrolito, cargas puntuales (iones) de signo opuesto se posicionan sobre su superficie para contrarrestar la carga que dicha superficie acumula, formando la denominada doble capa eléctrica [134].

No obstante, este modelo considera las cargas eléctricas de la superficie como cargas puntuales y estáticas, por lo que la capacidad dependería únicamente del potencial aplicado y no de la concentración y otras características del electrolito. Sin embargo, se observó que de hecho existe una dependencia con la concentración del electrolito. Para explicar esta dependencia, Gouy-Chapman propuso una modificación del modelo de Helmholtz, considerando que la doble capa no es rígida, sino difusa. Este nuevo modelo explicaba el comportamiento de la capacidad respecto a la concentración del electrolito a concentraciones y potenciales bajos, aunque a concentraciones altas del electrolito el comportamiento de la doble capa se explicaba mejor por el modelo de Helmholtz. Por ello, en 1923 Stern propuso un modelo que combinaba los modelos de Helmholtz y de Gouy-Chapman y que suponía la formación de una capa rígida de iones directamente sobre el electrodo y otra capa difusa en contacto con el electrolito. Refinamientos posteriores de este modelo, como el desarrollado por Grahame, dejaron atrás la representación de los iones como cargas puntuales y, en su lugar, consideraban a éstos como objetos de

Introducción

dimensiones finitas con su esfera de solvatación, lo que implicaba la imposición de límites a la distancia de aproximación del ion solvatado a la superficie del electrodo [135] (Figura 11). El modelo de Grahame propone la existencia de diversos planos/capas de especies iónicas en el entorno de la superficie del electrodo: (a) Plano interno de Helmholtz (IHP, *inner Helmholtz plane*), que corresponde a la capa de iones y moléculas de disolvente en contacto directo con el electrodo; estos iones, que se encuentran desolvatados, son denominados iones adsorbidos de manera específica. (b) Plano externo de Helmholtz (OHP, *outer Helmholtz plane*), formado por iones solvatados situados a la menor distancia posible a la superficie del electrodo. (c) Capa difusa de iones solvatados situada más allá del OHP [135].

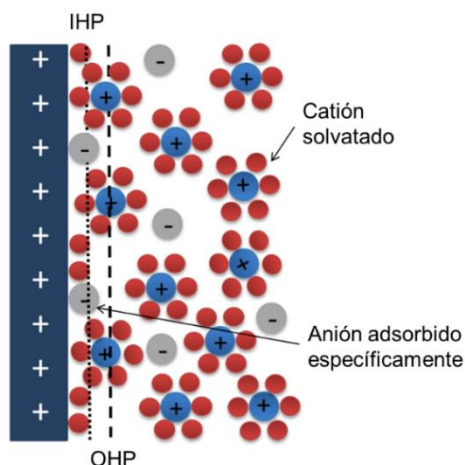


Figura 11. Esquema del modelo de Grahame.

1.4.2 Procesos faradaicos: pseudocapacitancia y comportamiento tipo batería

En los procesos pseudocapacitivos de almacenamiento de carga tienen lugar reacciones faradaicas en la superficie o en regiones muy próximas a la superficie del electrodo. Precisamente debido a ello, dichos procesos no están limitados por la difusión de especies iónicas al interior del electrodo y, por tanto, suelen ser cinéticamente rápidos. El término pseudocapacitancia fue definido por Conway para describir sistemas que comparten respuestas electroquímicas similares a las de sistemas capacitivos (p.ej., voltamogramas cílicos rectangulares, dependencia lineal de la densidad de corriente con el voltaje), pero en los que el almacenamiento de carga no tiene lugar por formación de doble capa eléctrica, sino por mecanismos faradaicos. Entre estos procesos faradaicos destacan la pseudocapacitancia redox y la pseudocapacitancia por intercalación [136]. La primera se refiere a los procesos de oxidación y reducción que tienen lugar en especies moleculares presentes en la superficie del electrodo o en especies iónicas que se adsorben sobre la superficie del mismo y que poseen actividad redox. La segunda añe a la inserción y extracción de iones en regiones muy cercanas a la superficie de electrodos que presentan túneles o galerías que favorecen su tránsito, en los que dicha inserción no conlleva cambios estructurales del material [137],[138].

Por otro lado, hay procesos faradaicos (p.ej., intercalación, conversión) que están controlados por la difusión de las especies iónicas en el interior del electrodo. Estos son procesos tipo batería, que poseen cinéticas generalmente lentas. El carácter controlado por difusión (tipo batería) o no (tipo condensador) del almacenamiento de carga de un sistema se puede determinar estudiando la relación entre la intensidad de corriente y la velocidad de barrido de potencial obtenidos en voltamperogramas cílicos, siendo la intensidad de corriente total la suma de las

Introducción

intensidades de corriente controladas por superficie ($i_{capacitiva}$) y por difusión ($i_{difusión}$), ecuación (1)

$$i = i_{capacitiva} + i_{difusión} = a \cdot v^b \quad (1)$$

, donde i es la corriente, v es la velocidad de barrido de potencial, y a y b son parámetros ajustables. El valor de b está comprendido entre 0.5 y 1. Un valor de 0.5 indica que la cinética está totalmente controlada por difusión, con lo que el almacenamiento de carga es el típico de una batería. Un valor de b de 1 indica un proceso exclusivamente superficial, que corresponde al comportamiento típico de un condensador [139]. Sin embargo, la mayoría de los sistemas electroquímicos presentan valores de b intermedios entre 0.5 y 1, lo que suele indicar la existencia de una combinación de procesos y cinéticas diferentes con distintas prevalencias.

En los condensadores de doble capa eléctrica (EDLCs, *electrical double layer capacitors*), en los que el almacenamiento de carga sólo implica procesos superficiales no faradaicos, los voltamperogramas cíclicos obtenidos se caracterizan por un perfil esencialmente cuadrado y una dependencia lineal de la corriente eléctrica con la velocidad de barrido del potencial. Asimismo, los perfiles de carga y descarga galvanostáticos muestran una dependencia casi perfectamente lineal del voltaje medido en función del tiempo. Por otro lado, en las baterías, cuyo comportamiento se encuentra dominado por procesos faradaicos limitados por la difusión del electrolito en el interior del electrodo, los voltamperogramas suelen mostrar picos redox claramente definidos y una dependencia de la corriente eléctrica con la velocidad de barrido de potencial tipo raíz cuadrada, junto con perfiles de carga y descarga galvanostáticos caracterizados por mesetas de potencial casi constante [140],[141].

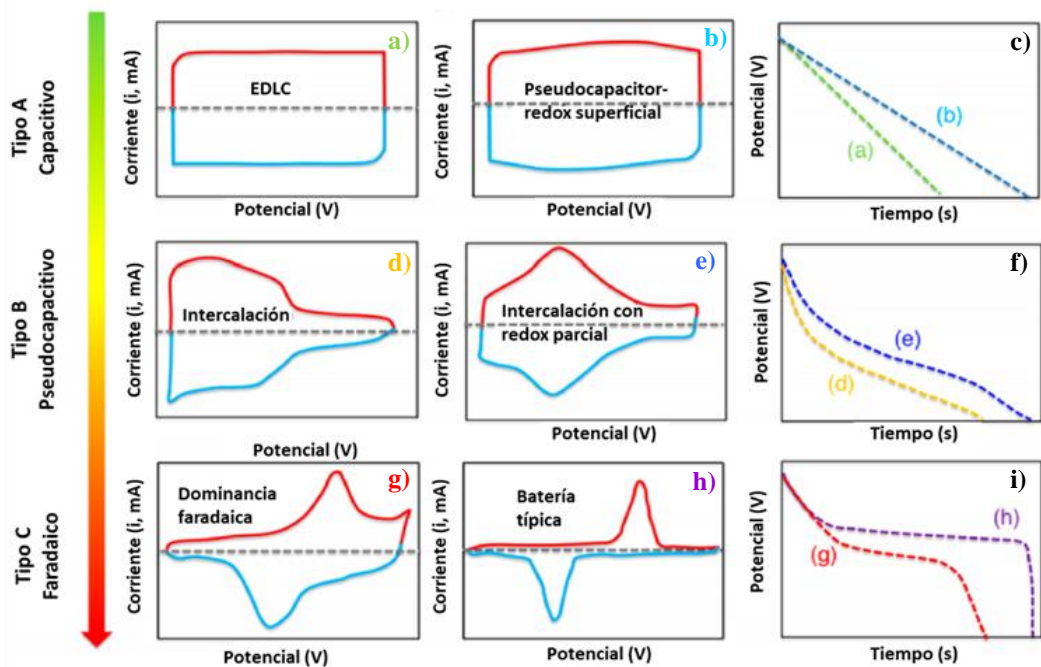


Figura 12. Esquema de voltamperogramas cíclicos (a, b, d, e, g, h) y de ciclos de descargas galvanostáticas (c, i, f) de materiales con distintos procesos de almacenamiento de energía. Adaptación de [140].

1.5 Dispositivos de almacenamiento de energía electroquímica

La familia de los dispositivos de almacenamiento electroquímico de energía engloba mayormente a los supercondensadores (SCs, *supercapacitors*) y a las baterías recargables. A su vez, en función del mecanismo de almacenamiento, los SCs se pueden clasificar en: (i) supercondensadores de doble capa eléctrica (EDLCs), (ii) pseudocondensadores (PCs, *pseudocapacitors*) y (iii) supercondensadores asimétricos (ASCs, *asimétrico supercapacitors*), que están formados por una combinación de un electrodo tipo EDLC y otro electrodo tipo PC, aunque también pueden estar constituidos por dos electrodos de la misma naturaleza (EDLC o PC) pero que trabajan en distintos rangos de potencial. Un tipo

Introducción

relativamente nuevo de dispositivo tipo supercondensador es el denominado supercondensador híbrido (HSC, *hybrid supercapacitor*), que es aquel formado por un electrodo tipo batería y un electrodo tipo condensador (EDLC o PC) [142]. Éste último tipo cubre en cierta medida el *gap* de prestaciones existente entre los supercondensadores y las baterías, ya que permite combinar altas densidades de energía próximas a las que poseen las baterías con la potencia y ciclabilidad típicas de los supercondensadores.

En los EDLCs, los materiales de electrodo más utilizados son materiales de carbono de alta área superficial, por ejemplo, carbón activado, aerogeles de carbono, grafeno y nanotubos de carbono [143],[144]. Ello es debido a que son eléctricamente conductores, químicamente inertes y, al menos en el caso de los carbonos activados, económicamente asequibles. Respecto a los PCs, algunos ejemplos de materiales de electrodo incluyen óxidos metálicos (IrO_2 , RuO_2 , Fe_3O_4 , MnO_2 , NiO , V_2O_5), dicalcogenuros metálicos (MoS_2 , WS_2 , FeS_2) y polímeros conductores (polianilina, polipirrol, etc), entre otros [145-147].

En el ámbito de los **HSCs**, los condensadores híbridos acuosos de ion zinc (AZICs, *aqueous zinc-ion hybrid capacitors*) presentan especial relevancia para esta tesis. Estos dispositivos están constituidos por un ánodo de zinc metálico combinado con un cátodo de un material capacitivo o pseudocapacitivo. El almacenamiento de carga en el ánodo se produce mediante depósito y extracción de zinc (*plating/stripping*) (Figura 13). Los materiales de cátodo comúnmente usados son aquellos típicos de los EDLCs y PCs, es decir, principalmente materiales de carbono de alta área superficial, algunos óxidos metálicos y MXenos. Como electrolitos acuosos, se emplean distintas sales de zinc, mayormente sulfato y triflato de zinc [ZnSO_4 , $\text{Zn}(\text{CF}_3\text{SO}_3)_2$], pero también cloruro y perclorato de zinc (ZnCl_2 , ZnClO_4)[148],[149]. La combinación del ánodo tipo batería y cátodo tipo condensador que operan en rangos de potencial diferentes se traduce en dispositivos

AZIC que trabajan a voltajes mayores que los que proporcionan los supercondensadores estándar, lo que a su vez se traduce en densidades de energía mayores que las de éstos, junto con densidades de potencia y estabilidades cíclicas superiores a las de la mayor parte de las baterías típicas [150].

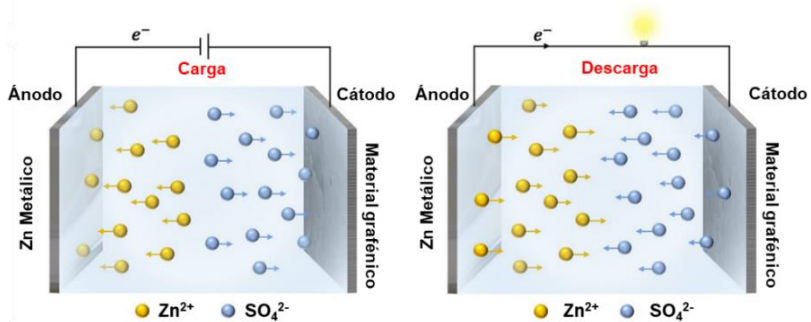


Figura 13. Proceso de carga/descarga para ZICs. Adaptación de [147].

Por último, en lo que respecta a las baterías recargables, aunque se están investigando y existen comercialmente distintos tipos, las más comunes son las baterías de ion metálico y, en particular, las baterías de ion litio (LIBs, *lithium ion batteries*) (Figura 14). En éstas últimas, el almacenamiento de carga eléctrica se basa en procesos de inserción/intercalación iónica tanto en el ánodo como en el cátodo [151],[152]. Los materiales de ánodo más comúnmente usados son el grafito y otros materiales de carbono, aunque también se emplean titanatos de litio ($Li_4Ti_5O_{12}$) o aleaciones Sn/Co. Otros muchos sólidos, incluidos los TMDs, se están explorando a nivel de laboratorio como ánodos. Como materiales de cátodo, se emplean frecuentemente determinados óxidos mixtos de litio (p.ej., $LiCoO_2$, $LiNi_xMn_yCo_zO_2$, $LiMn_2O_4$), pero también fosfatos de litio ($LiFePO_4$), entre otros [153-155]. Los electrolitos de las LIBs suelen ser sales de litio (típicamente $LiPF_6$) disueltos en disolventes orgánicos, entre los cuales las mezclas de carbonatos orgánicos son los más usados (p.ej., mezclas de carbonato de etileno y propileno).

Introducción

En la actualidad, se investigan intensamente LIBs de estado sólido, en las que el electrolito orgánico líquido es reemplazado por un electrolito sólido (conductor iónico), generalmente hecho de determinados materiales cerámicos, poliméricos o mezclas de ambos [156]. Aunque las LIBs son muy usadas en la actualidad en distintos ámbitos prácticos (dispositivos electrónicos portátiles, vehículos eléctricos, almacenamiento estacionario de energía) y se prevé que su uso siga aumentando muy rápidamente en los próximos años, estos dispositivos no están exentos de limitaciones y problemas. Por ejemplo, presentan riesgos de seguridad y toxicidad asociados al uso de los electrolitos orgánicos, así como perspectivas de implementación futura a muy gran escala complicadas por la previsible escasez de determinadas materias primas críticas (litio, cobalto, etc). Por esta razón, en los últimos tiempos se está haciendo mucho hincapié en investigar y desarrollar químicas de batería alternativas, entre las que se encuentran las baterías de ion sodio, baterías metal-calcógeno y metal-aire, o baterías de ion multivalente, algunas de las cuales permiten trabajar con electrolitos acuosos [157-159].

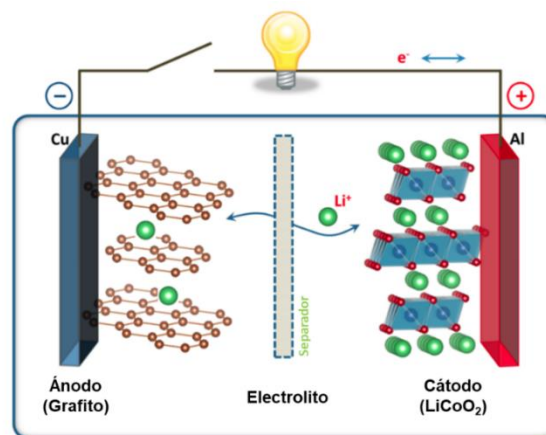


Figura 14. Esquema representativo de una batería ion-litio. Adaptada de [152].

1.6 Referencias

- [1] Q. Lu, X. Wang, Recent progress of sub-nanometric materials in photothermal energy conversion, *Advanced Science* 9 (2022), 2104225.
- [2] S. Singh, K. Verma, C. Prakash, Advanced applications of 2D nanostructures *Emerging Research and Opportunities*, 2021.
- [3] M. Byakodi, N.S. Shrikrishna, R. Sharma, S. Bhansali, Y. Mishra, A. Kaushik, S. Gandhi, Emerging 0D, 1D, 2D, and 3D nanostructures for efficient point-of-care biosensing, *Biosensors and Bioelectronics: X* 12 (2022), 100284.
- [4] A.J. Mannix, B. Kiraly, M.C. Hersam, N.P. Guisinger, Synthesis and chemistry of elemental 2D materials, *Nature Reviews Chemistry* 1 (2017), 0014.
- [5] A. Gupta, T. Sakthivel, S. Seal, Recent development in 2D materials beyond graphene, *Progress in Materials Science* 73 (2015), 44–126.
- [6] A.K. Geim, I. V. Grigorieva, Van der Waals heterostructures, *Nature* 499 (2013), 419-425.
- [7] T.A. Chowdhury, M.A. Bin Zafar, M. Sajjad-Ul Islam, M. Shahinuzzaman, M.A. Islam, M.U. Khandaker, Stability of perovskite solar cells: issues and prospects, *RSC Advances* 13 (2023), 1787-1810.
- [8] B. Wang, J. Iocozzia, M. Zhang, M. Ye, S. Yan, H. Jin, S. Wang, Z. Zou, Z. Lin, The charge carrier dynamics, efficiency and stability of two-dimensional material-based perovskite solar cells, *Chemical Society Reviews* 48 (2019), 4854–4891.
- [9] E. Pop, V. Varshney, A.K. Roy, Thermal properties of graphene: fundamentals and applications, *MRS Bulletin* 37 (2012), 1273–1281.
- [10] I.A. Popov, K. V Bozhenko, A.I. Boldyrev, Is Graphene aromatic?, *Nano Research* 5 (2012), 117–123.
- [11] S. Unarunotai, Y. Murata, C.E. Chialvo, N. Mason, I. Petrov, R.G. Nuzzo, J.S. Moore, J.A. Rogers, Conjugated carbon monolayer membranes: methods for synthesis and integration, *Advanced Materials* 22 (2010), 1072-1077.
- [12] K.I. Bolotin, K.J. Sikes, Z. Jiang, M. Klima, G. Fudenberg, J. Hone, P. Kim, H.L. Stormer, Ultrahigh electron mobility in suspended graphene, *Solid State Communications* 146 (2008), 351–355.
- [13] S. V. Morozov, K.S. Novoselov, M.I. Katsnelson, F. Schedin, D.C. Elias, J.A. Jaszczak, A.K. Geim, Giant intrinsic carrier mobilities in graphene and its bilayer, *Physical Review Letters* 100 (2008), 11–14.
- [14] S.M. Young, C.L. Kane, Dirac semimetals in two dimensions, *Physical Review Letters* 115 (2015), 1–5.
- [15] P. Recher and B. Trauzettel, *Physics* 4 (2011), 25.
- [16] A.F. Morpurgo, Dirac electrons broken to pieces, *Nature* 462 (2009), 170–171.

Introducción

- [17] X. Du, I. Skachko, F. Duerr, A. Luican, E.Y. Andrei, Fractional quantum Hall effect and insulating phase of Dirac electrons in graphene, *Nature* 462 (2009), 192–195.
- [18] K.I. Bolotin, F. Ghahari, M.D. Shulman, H.L. Stormer, P. Kim, Observation of the fractional quantum Hall effect in graphene, *Nature*, 462 (2009), 196–199.
- [19] J.W. McIver, B. Schulte, F.U. Stein, T. Matsuyama, G. Jotzu, G. Meier, A. Cavalleri, Light-induced anomalous Hall effect in graphene, *Nature Physics* 16 (2020), 38–41
- [20] F. Bonaccorso, Z. Sun, T. Hasan, A.C. Ferrari, Graphene photonics and optoelectronics, *Nature Photonics* 4 (2010), 611–622.
- [21] J.K. Wassei, R.B. Kaner, Graphene , a promising, *Materialstoday* 13 (2010), 52–59.
- [22] Y. Han, L. Zhang, X. Zhang, K. Ruan, L. Cui, Y. Wang, L. Liao, Z. Wang, J. Jie, Clean surface transfer of graphene films via an effective sandwich method for organic light-emitting diode applications, *Journal of Materials Chemistry C* 2 (2014), 201–207.
- [23] J.X. Ran, B.Y. Liu, X.L. Ji, A. Fariza, Z.T. Liu, J.X. Wang, P. Gao, T.B. Wei, Impact of graphene interlayer on performance parameters of sandwich structure Pt/GaN Schottky barrier diodes, *Journal of Physics D: Applied Physics* 53 (2020), 404003.
- [24] C. Lee, X. Wei, J.W. Kysar, J. Hone, Measurement of the elastic properties and intrinsic strength of monolayer graphene, *Science* 321 (2008), 385–388.
- [25] H.G. Prashantha Kumar, M. Anthony Xavior, Graphene reinforced metal matrix composite (GRMMC): a review, *Procedia Engineering* 97 (2014), 1033–1040.
- [26] S. Chen, A.L. Moore, W. Cai, J.W. Suk, J. An, C. Mishra, C. Amos, C.W. Magnuson, J. Kang, L. Shi, R.S. Ruoff, Raman measurements of thermal transport in suspended monolayer graphene of variable sizes in vacuum and gaseous environments, *ACS Nano* 5 (2011), 321–328.
- [27] A.A. Balandin, Thermal properties of graphene and nanostructured carbon materials, *Nature Materials* 10 (2011), 569–581.
- [28] S. Chen, Q. Wu, C. Mishra, J. Kang, H. Zhang, K. Cho, W. Cai, A.A. Balandin, R.S. Ruoff, Thermal conductivity of isotopically modified, *Nature Materials* 11 (2012), 203-207.
- [29] A.A. Balandin, S. Ghosh, W. Bao, I. Calizo, D. Teweldebrhan, F. Miao, C.N. Lau, Superior thermal conductivity of single-layer graphene, *Nano Letters* 8 (2008), 902–907.
- [30] L. Li, T. Sun, S. Lu, Z. Chen, S. Xu, M. Jian, J. Zhang, Graphene interlocking carbon nanotubes for high-strength and high-conductivity fibers, *ACS Applied Materials & Interfaces* 15 (2023), 5701–5708.
- [31] J. Liu, J. Tang, J.J. Gooding, Strategies for chemical modification of graphene and applications of chemically modified graphene, *Journal of Materials Chemistry* 22 (2012), 12435–12452.
- [32] H. Lee, K. Paeng, I.S. Kim, A review of doping modulation in graphene, *Synthetic Metals* 244 (2018), 36–47.
- [33] J. Zhan, Z. Lei, Y. Zhang, Non-covalent interactions of graphene surface: Mechanisms and applications, *Chem* 8 (2022), 947–979.
- [34] S. Kashyap, S. Mishra, S.K. Behera, Aqueous colloidal stability of graphene oxide and chemically converted graphene, *Journal of Nanoparticles Research* 14 (2014), 1–6.

-
- [35] B. Nazari, Z. Ranjbar, R.R. Hashjin, A. Rezvani Moghaddam, G. Momen, B. Ranjbar, Dispersing graphene in aqueous media: investigating the effect of different surfactants, *Colloids and Surfaces A: Physicochemical and Engineering Aspects*, 582 (2019), 123870.
 - [36] J.I. Paredes, S. Villar-Rodil, Biomolecule-assisted exfoliation and dispersion of graphene and other two-dimensional materials: A review of recent progress and applications, *Nanoscale* 8 (2016), 15389–15413.
 - [37] C. Liu, X. Huang, Y.Y. Wu, X. Deng, Z. Zheng, Z. Xu, D. Hui, Advance on the dispersion treatment of graphene oxide and the graphene oxide modified cement-based materials, *Nanotechnology Reviews* 10 (2021), 34–49.
 - [38] M. Ayán-Varela, R. Ruiz-Rosas, S. Villar-Rodil, J.I. Paredes, D. Cazorla-Amorós, E. Morallón, A. Martínez-Alonso, J.M.D. Tascon, Efficient Pt electrocatalysts supported onto flavin mononucleotide-exfoliated pristine graphene for the methanol oxidation reaction, *Electrochimica Acta* 231 (2017), 386–395.
 - [39] S. Ahadian, M. Estili, V.J. Surya, J. Ramón-Azcón, X. Liang, H. Shiku, M. Ramalingam, T. Matsue, Y. Sakka, H. Bae, K. Nakajima, Y. Kawazoe, A. Khademhosseini, Facile and green production of aqueous graphene dispersions for biomedical applications, *Nanoscale* 7 (2015), 6436–6443.
 - [40] P.J.M. Swinkels, Z. Gong, S. Sacanna, E.G. Noya, P. Schall, Visualizing defect dynamics by assembling the colloidal graphene lattice, *Nature Communications* 14 (2023), 1–9.
 - [41] S. Manzeli, D. Ovchinnikov, D. Pasquier, O. V. Yazyev, A. Kis, 2D transition metal dichalcogenides, *Nature Review Materials* 2 (2017), 17033.
 - [42] B. Zhao, D. Chen, Z. Zhang, P. Lu, M. Hossain, J. Li, B. Li, X. Duan, B. Zhao, D.Y. Shen, Z.C. Zhang, P. Lu, M. Hossain, J. Li, B. Li, X.D. Duan, 2D metallic transition-metal dichalcogenides: structures, synthesis, properties, and applications, *Advanced Functional Materials* 31 (2021), 2105132.
 - [43] X. Wang, J. Lin, Y. Zhu, C. Luo, K. Suenaga, C. Cai, L. Xie, Chemical vapor deposition of trigonal prismatic NbS₂ monolayers and 3R-polytype few-layers, *Nanoscale* 9 (2017), 16607.
 - [44] A. Coogan, Y.K. Gun'ko, Solution-based “bottom-up” synthesis of group VI transition metal dichalcogenides and their applications, *Materials Advances* 2 (2021), 146.
 - [45] G. Grüner, The dynamics of charge-density waves, *Reviews of Modern Physics* 60 (1988), 1129–1181.
 - [46] H. Feng, Z. Xu, J. Zhuang, L. Wang, Y. Liu, X. Xu, L. Song, W. Hao, Y. Du, role of charge density wave in monatomic assembly in transition metal dichalcogenides, *Advanced Function Materials* 29 (2019), 1900367.
 - [47] N. E. Staley, J. Wu, P. Eklund, Y. Liu, Electric field effect on superconductivity in atomically thin flakes of NbSe₂, *Physical Review B* 80 (2009), 184505.
 - [48] R. Yan, G. Khalsa, B.T. Schaefer, A. Jarjour, S. Rouvimov, K.C. Nowack, H.G. Xing, D. Jena, Thickness dependence of superconductivity in ultrathin NbS₂, *Applied Physics Express* 12 (2019), 023008.

Introducción

- [49] M.S. El-Bana, D. Wolverson, S. Russo, G. Balakrishnan, D.M.K. Paul, S.J. Bending, Superconductivity in two-dimensional NbSe₂ field effect transistors, *Superconductor Science and Technology* 26 (2013), 125020.
- [50] D. Wickramaratne, I.I. Mazin, Effect of alloying in monolayer niobium dichalcogenide superconductors, *Nature Communications* 13 (2022), 2376.
- [51] X. Fan, H. Chen, L. Zhao, S. Jin, G. Wang, Quick suppression of superconductivity of NbSe₂ by Rb intercalation, *Solid State Communications* 297 (2019), 6–10.
- [52] C.S. McEwen, D.J. St Julien, M.J. Sienko, P.P. Edwards, Structure and superconductivity in lithium-intercalated niobium dichalcogenides, *Inorganic Chemistry Frontiers* 24 (1985), 1656–1660.
- [53] N.M. Toporova, E.M. Sherokalova, N. V. Selezneva, V. V. Ogloblichev, N. V. Baranov, Crystal structure, properties and griffiths-like phase in niobium diselenide intercalated with chromium, *Journal of Alloys Compounds* 848 (2020), 156534.
- [54] R. Pervin, M. Krishnan, S. Arumugam, P.M. Shirage, Second magnetization peak effect and the vortex phase diagram of V0.0015NbSe₂ single crystal, *Journal of Magnetism and Magnetic Materials* 507 (2020), 166817.
- [55] H. Luo, J. Strychalska-Nowak, J. Li, J. Tao, T. Klimczuk, R.J. Cava, S-shaped suppression of the superconducting transition temperature in Cu-intercalated NbSe₂, *Chemistry of Materials* 29 (2017), 3704–3712.
- [56] J.M.V. Van Den Berg, On the ternary phases Al_xNbSe₂ and Cu_xNbSe₂, *Journal of the Less Common Metals* 26 (1972), 399–402.
- [57] S. Naik, S. Kalaiarasan, R.C. Nath, S.N. Sarangi, A.K. Sahu, D. Samal, H.S. Biswal, S.L. Samal, Nominal effect of mg intercalation on the superconducting properties of 2H-NbSe₂, *Inorganic Chemistry* 60 (2021), 4588–4598.
- [58] R. Muñoz, C. Gómez-Aleixandre, Review of CVD synthesis of graphene, *Chemical Vapor Deposition* 19 (2013), 297–322.
- [59] Q. Deng, Z. Li, R. Huang, P. Li, H. Gomaa, S. Wu, C. An, N. Hu, Research progress of transition-metal dichalcogenides for the hydrogen evolution reaction, *Journal of Materials Chemistry A* 11 (2023), 24434–24453.
- [60] S. Xu, L. Zhang, B. Wang, R.S. Ruoff, Chemical vapor deposition of graphene on thin-metal films, *Cell Reports Physical Science* 2 (2021), 10372.
- [61] Peter M. Martin, Handbook ok deposition technologies for films and coatings, 2000.
- [62] H. Zeng, Y. Wen, L. Yin, R. Cheng, H. Wang, C. Liu, J. He, Recent developments in CVD growth and applications of 2D transition metal dichalcogenides, *Frontiers of Physics* 18 (2023), 53603.
- [63] M.S.A. Bhuyan, M.N. Uddin, M.M. Islam, F.A. Bipasha, S.S. Hossain, Synthesis of graphene, *International Nano Letters* 6 (2016), 65–83.
- [64] A. Gutiérrez-Cruz, A.R. Ruiz-Hernández, J.F. Vega-Clemente, D.G. Luna-Gazcón, J. Campos-Delgado, A review of top-down and bottom-up synthesis methods for the production of graphene, graphene oxide and reduced graphene oxide, *Journal of Materials Science* 57 (2022), 14543–14578.

-
- [65] R. Ye, D.K. James, J.M. Tour, Laser-induced graphene, *Accounts of Chemical Research* 51 (2018), 1609–1620.
 - [66] R. Kumar, R.K. Singh, D.P. Singh, E. Joanni, R.M. Yadav, S.A. Moshkalev, Laser-assisted synthesis, reduction and micro-patterning of graphene: Recent progress and applications, *Coordination Chemistry Reviews* 342 (2017), 34–79.
 - [67] D.X. Luong, K. V. Bets, W.A. Algozeen, M.G. Stanford, C. Kittrell, W. Chen, R. V. Salvatierra, M. Ren, E.A. McHugh, P.A. Advincula, Z. Wang, M. Bhatt, H. Guo, V. Mancevski, R. Shahsavari, B.I. Yakobson, J.M. Tour, Gram-scale bottom-up flash graphene synthesis, *Nature* 577 (2020), 647–651.
 - [68] S. Rani, M. Sharma, D. Verma, A. Ghanghass, R. Bhatia, I. Sameera, Two-dimensional transition metal dichalcogenides and their heterostructures: Role of process parameters in top-down and bottom-up synthesis approaches, *Materials Science in Semiconductor Processing* 139 (2022), 106313.
 - [69] N.T.K. Thanh, N. Maclean, S. Mahiddine, Mechanisms of nucleation and growth of nanoparticles in solution, *Chemical Reviews* 114 (2014), 7610–7630.
 - [70] L. Luo, M. Shi, S. Zhao, W. Tan, X. Lin, H. Wang, F. Jiang, Hydrothermal synthesis of MoS₂ with controllable morphologies and its adsorption properties for bisphenol A, *Journal of Saudi Chemical Society* 23 (2019), 762–773.
 - [71] G. Tang, H. Tang, C. Li, W. Li, X. Ji, Surfactant-assisted hydrothermal synthesis and characterization of WS₂ nanorods, *Materials Letters* 65 (2011), 3457–3460.
 - [72] W. Du, X. Jiang, L. Zhu, From graphite to graphene: Direct liquid-phase exfoliation of graphite to produce single- and few-layered pristine graphene, *Journal of Materials Chemistry A* 1 (2013), 10592–10606.
 - [73] K.S. Novoselov, A.K. Geim, S. V Morozov, D. Jiang, Electric field effect in atomically thin carbon films, *Physicals Review Letters* 306 (2004), 666–669.
 - [74] K.S. Novoselov, D. Jiang, F. Schedin, T.J. Booth, V. V. Khotkevich, S. V. Morozov, A.K. Geim, Two-dimensional atomic crystals, *Proceeding of National Academy of Science U. S. A.* 102 (2005), 10451–10453.
 - [75] Z. Li, R.J. Young, C. Backes, W. Zhao, X. Zhang, A.A. Zhukov, E. Tillotson, A.P. Conlan, F. Ding, S.J. Haigh, K.S. Novoselov, J.N. Coleman, Mechanisms of liquid-phase exfoliation for the production of graphene, *American Chemical Society Nano* 14 (2020), 10976–10985.
 - [76] J.N. Coleman, M. Lotya, A. O'Neill, S.D. Bergin, P.J. King, U. Khan, K. Young, A. Gaucher, S. De, R.J. Smith, I. V. Shvets, S.K. Arora, G. Stanton, H.Y. Kim, K. Lee, G.T. Kim, G.S. Duesberg, T. Hallam, J.J. Boland, J.J. Wang, J.F. Donegan, J.C. Grunlan, G. Moriarty, A. Shmeliov, R.J. Nicholls, J.M. Perkins, E.M. Grieveson, K. Theuwissen, D.W. McComb, P.D. Nellist, V. Nicolosi, Two-dimensional nanosheets produced by liquid exfoliation of layered materials, *Science* 331 (2011), 568–571.
 - [77] M. Yi, Z. Shen, A review on mechanical exfoliation for the scalable production of graphene, *Journal of Materials Chemistry A* 3 (2015), 11700–11715.

Introducción

- [78] Y. Hernandez, V. Nicolosi, M. Lotya, F.M. Blighe, Z. Sun, S. De, I.T. McGovern, B. Holland, M. Byrne, Y.K. Gun'ko, J.J. Boland, P. Niraj, G. Duesberg, S. Krishnamurthy, R. Goodhue, J. Hutchison, V. Scardaci, A.C. Ferrari, J.N. Coleman, High-yield production of graphene by liquid-phase exfoliation of graphite, *Nature Nanotechnology* 3 (2008) 563–568.
- [79] K. Edward, K. Mamun, S. Narayan, M. Assaf, D. Rohindra, U. Rathnayake, State-of-the-art graphene synthesis methods and environmental concerns, *Applied and Environmental Soil Science* 1 (2023), 8475504.
- [80] U. Halim, C.R. Zheng, Y. Chen, Z. Lin, S. Jiang, R. Cheng, Y. Huang, X. Duan, A rational design of cosolvent exfoliation of layered materials by directly probing liquid-solid interaction, *Nature Communications* 4 (2013), 2213.
- [81] M. Lotya, Y. Hernandez, P.J. King, R.J. Smith, V. Nicolosi, L.S. Karlsson, F.M. Blighe, S. De, W. Zhiming, I.T. McGovern, G.S. Duesberg, J.N. Coleman, Liquid phase production of graphene by exfoliation of graphite in surfactant/water solutions, *Journal of American Chemical Society* 131 (2009), 3611–3620.
- [82] A.B. Bourlinos, V. Georgakilas, R. Zboril, T.A. Steriotis, A.K. Stubos, C. Trapalis, Aqueous-phase exfoliation of graphite in the presence of polyvinylpyrrolidone for the production of water-soluble graphenes, *Solid State Communications* 149 (2009), 2172–2176.
- [83] B. Caridad, J.I. Paredes, O. Pérez-Vidal, S. Villar-Rodil, A. Pagán, J.L. Cenis, A. Martínez-Alonso, J.M.D. Tascón, A biosupramolecular approach to graphene: Complementary nucleotide-nucleobase combinations as enhanced stabilizers towards aqueous-phase exfoliation and functional graphene-nucleotide hydrogels, *Carbon* 129 (2018), 321–334.
- [84] K.M.F. Shahil, A.A. Balandin, Graphene-multilayer graphene nanocomposites as highly efficient thermal interface materials, *Nano Letters* 12 (2012), 861–867.
- [85] A.A. Pirzado, F. Le Normand, T. Romero, S. Paszkiewicz, V. Papaefthimiou, D. Ihiawakrim, I. Janowska, Few-layer graphene from mechanical exfoliation of graphite-based materials: structure-dependent characteristics, *Chemical Engineering Journal* 3 (2019), 37.
- [86] Y. Zhang, J. Sun, X. Xiao, N. Wang, G. Meng, L. Gu, Graphene-like two-dimensional nanosheets-based anticorrosive coatings: A review, *Journal of Materials Science & Technology* 129 (2022), 139–162.
- [87] B.C. Brodie, On the atomic weight of graphite, *Philosophical Transaction of the Royal Society A*, 1859 p. 249.
- [88] D.C. Marcano, D. V. Kosynkin, J.M. Berlin, A. Sinitskii, Z. Sun, A. Slesarev, L.B. Alemany, W. Lu, J.M. Tour, Improved synthesis of graphene oxide, *American Chemical Society Nano* 4 (2010), 4806–4814.
- [89] E.K. Ulrich Hofmann, Untersuchungen über Graphitoxid, *Z. Anorg. u. Allg. Chem* 234 (1937), 311–336.
- [90] W.S. Hummers, R.E. Offeman, Preparation of graphitic oxide, *Journal of American Chemical Society* 80 (1958), 1339–1339.
- [91] Y. Zhu, S. Murali, W. Cai, X. Li, J.W. Suk, J.R. Potts, R.S. Ruoff, Graphene and graphene oxide: synthesis, properties, and applications, *Advanced Materials* 22 (2010), 3906–3924.

- [92] J.I. Paredes, S. Villar-Rodil, A. Martínez-Alonso, J.M.D. Tascón, Graphene oxide dispersions in organic solvents, *Langmuir* 24 (2008), 10560–10564.
- [93] S. Stankovich, D.A. Dikin, R.D. Piner, K.A. Kohlhaas, A. Kleinhammes, Y. Jia, Y. Wu, S.B.T. Nguyen, R.S. Ruoff, Synthesis of graphene-based nanosheets via chemical reduction of exfoliated graphite oxide, *Carbon* 45 (2007), 1558–1565.
- [94] M.J. Fernández-Merino, L. Guardia, J.I. Paredes, S. Villar-Rodil, P. Solís-Fernández, A. Martínez-Alonso, J.M.D. Tascón, Vitamin C is an ideal substitute for hydrazine in the reduction of graphene oxide suspensions, *Journal o Physical Chemistry C* 114 (2010), 6426–6432.
- [95] V.H. Pham, H.D. Pham, T.T. Dang, S.H. Hur, E.J. Kim, B.S. Kong, S. Kim, J.S. Chung, Chemical reduction of an aqueous suspension of graphene oxide by nascent hydrogen, *Journal of Materials Chemistry A* 22 (2012), 10530.
- [96] M.T.H. Aunkor, I.M. Mahbubul, R. Saidur, H.S.C. Metselaar, The green reduction of graphene oxide, *RCS Advances* 6 (2016), 27807-27828.
- [97] M. Acik, G. Lee, C. Mattevi, A. Pirkle, R.M. Wallace, M. Chhowalla, K. Cho, Y. Chabal, The role of oxygen during thermal reduction of graphene oxide studied by infrared absorption spectroscopy, *Journal o Physical Chemistry C* 115 (2011), 19761-19781.
- [98] H.L. Guo, X.F. Wang, Q.Y. Qian, F. Bin Wang, X.H. Xia, A green approach to the synthesis of graphene nanosheets, *ACS Nanomaterials* 3 (2009), 2653–2659.
- [99] L. Guardia, S. Villar-Rodil, J.I. Paredes, R. Rozada, A. Martínez-Alonso, J.M.D. Tascón, UV light exposure of aqueous graphene oxide suspensions to promote their direct reduction, formation of graphene–metal nanoparticle hybrids and dye degradation, *Carbon* 3 (2012), 1014–1024.
- [100] H.-H. Huang, K. Kanishka, H. De Silva, G.R.A. Kumara, M. Yoshimura, Structural evolution of hydrothermally derived reduced graphene oxide, *Nature* 8 (2018), 6849.
- [101] R. Jakhar, J.E. Yap, R. Joshi, Microwave reduction of graphene oxide, *Carbon* 170 (2020), 277–293.
- [102] Q. Zhang, L. Mei, X. Cao, Y. Tang, Z. Zeng, Intercalation and exfoliation chemistries of transition metal dichalcogenides, *Journal of Materials Chemistry A* 8 (2020), 15417–15444.
- [103] H. Park, J.Y. Kim, J.Y. Oh, T. Il Lee, Long-term stable NbSe₂ nanosheet aqueous ink for printable electronics, *Applied Surfaces Science* 504 (2020), 144342.
- [104] B.H. Kang, D.K. Lee, D. sik Kim, O.N. Hur, C.S. Lee, J. Bae, S.H. Park, High-yield exfoliation of NbSe₂ through optimized lithium-ion intercalation and its application in electromagnetic-interference shielding, *Applied Surfaces Science* 637 (2023), 157954.
- [105] N. Kumar, R. Salehiyan, V. Chauke, O. Joseph Botlhoko, K. Setshedi, M. Scriba, M. Masukume, S. Sinha Ray, Top-down synthesis of graphene: a comprehensive review, *FlatChem* 27 (2021), 100224.
- [106] Y. Yang, F. Lu, Z. Zhou, W. Song, Q. Chen, X. Ji, Electrochemically cathodic exfoliation of graphene sheets in room temperature ionic liquids N-butyl, methylpyrrolidinium bis(trifluoromethylsulfonyl)imide and their electrochemical properties, *Electrochimica Acta*, 113 (2013) 9–16.

Introducción

- [107] A.J. Cooper, N.R. Wilson, I.A. Kinloch, R.A.W. Dryfe, Single stage electrochemical exfoliation method for the production of few-layer graphene via intercalation of tetraalkylammonium cations, *Carbon* 66 (2014), 340–350.
- [108] A.J. Cooper, M. Velický, I.A. Kinloch, R.A.W. Dryfe, On the controlled electrochemical preparation of R4N⁺ graphite intercalation compounds and their host structural deformation effects, *Journal of Electroanalytical Chemistry* 730 (2014), 34–40.
- [109] J. Wang, K.K. Manga, Q. Bao, K.P. Loh, High-yield synthesis of few-layer graphene flakes through electrochemical expansion of graphite in propylene carbonate electrolyte, *Journal of American Chemical Society* 133 (2011), 8888–8891.
- [110] P. Yu, S.E. Lowe, G.P. Simon, Y.L. Zhong, Electrochemical exfoliation of graphite and production of functional graphene, *Current Opinion in Colloid & Interface Science* 20 (2015), 329–338.
- [111] M.A. Py, R.R. Haering, Structural destabilization induced by lithium intercalation in MoS₂ and related compous, *Current Opinion in Colloid & Interface Science* 61 (1983), 76–84.
- [112] M.A. Lukowski, A.S. Daniel, F. Meng, A. Forticaux, L. Li, S. Jin, Enhanced hydrogen evolution catalysis from chemically exfoliated metallic MoS₂ nanosheets, *Journal of American Chemical Society* 135 (2013), 10274–10277.
- [113] Y. Yang, H. Hou, G. Zou, W. Shi, H. Shuai, J. Li, X. Ji, Electrochemical exfoliation of graphene-like two-dimensional nanomaterials, *Nano* 11 (2019), 16-33.
- [114] C.T.J. Low, F.C. Walsh, M.H. Chakrabarti, M.A. Hashim, M.A. Hussain, Electrochemical approaches to the production of graphene flakes and their potential applications, *Carbon* 54 (2012), 1-21.
- [115] Y. Fang, X. Li, J. Li, C. Yao, C. Hui, Y. Hoh, X. Hai, J. Lu, C. Su, Janus electrochemical exfoliation of two-dimensional materials, *Journal of Materials Chemistry A* 7 (2019), 25691–25711.
- [116] N. Liu, F. Luo, H. Wu, Y. Liu, C. Zhang, J. Chen, One-step ionic-liquid-assisted electrochemical synthesis of ionic-liquid-functionalized graphene sheets directly from graphite, *Advanced Functional Materials* 18 (2008,) 1518–1525.
- [117] M. Alanyalioğlu, J.J. Segura, J. Oró-Sol, N. Casañ-Pastor, The synthesis of graphene sheets with controlled thickness and order using surfactant-assisted electrochemical processes, *Carbon* 50 (2012), 142–152.
- [118] K. Parvez, Z.S. Wu, R. Li, X. Liu, R. Graf, X. Feng, K. Müllen, Exfoliation of graphite into graphene in aqueous solutions of inorganic salts, *Journal of American Chemical Society* 136 (2014), 6083–6091.
- [119] J. Liu, H. Yang, S.G. Zhen, C.K. Poh, A. Chaurasia, J. Luo, X. Wu, E.K.L. Yeow, N.G. Sahoo, J. Lin, Z. Shen, A green approach to the synthesis of high-quality graphene oxide flakes via electrochemical exfoliation of pencil core, *RSC Advances* 3 (2013), 11745–11750.
- [120] K. Parvez, R. Li, S.R. Puniredd, Y. Hernandez, F. Hinkel, S. Wang, X. Feng, K. Müllen, Electrochemically exfoliated graphene as solution-processable, highly conductive electrodes for organic electronics, *ACS Nano* 7 (2013), 3598–3606.
- [121] W.-W. Liu, A. Aziz, Review on the effects of electrochemical exfoliation parameters on the yield of graphene oxide, *ACS Omega* 7 (2022), 33719-33731.

-
- [122] S. Yang, S. Brüller, Z.S. Wu, Z. Liu, K. Parvez, R. Dong, F. Richard, P. Samori, X. Feng, K. Müllen, Organic radical-assisted electrochemical exfoliation for the scalable production of high-quality graphene, *Journal of American Chemical Society* 137 (2015), 13927–13932.
 - [123] S. Yang, M.R. Lohe, K. Müllen, X. Feng, New-Generation graphene from electrochemical approaches: production and applications, *Advanced Materials* 28 (2016), 6213–6221.
 - [124] Y.I. Kurys, O.O. Ustavytska, V.G. Koshechko, V.D. Pokhodenko, Structure and electrochemical properties of multilayer graphene prepared by electrochemical exfoliation of graphite in the presence of benzoate ions, *RSC Advances* 6 (2016), 36050–36057.
 - [125] C.H. Chen, S.W. Yang, M.C. Chuang, W.Y. Woon, C.Y. Su, Towards the continuous production of high crystallinity graphene via electrochemical exfoliation with molecular in situ encapsulation, *Nanoscale* 7 (2015), 15362–15373.
 - [126] K. Parvez, R.A. Rincón, N.E. Weber, K.C. Cha, S.S. Venkataraman, One-step electrochemical synthesis of nitrogen and sulfur co-doped, high-quality graphene oxide, *Chemical Communicantions* 52 (2016), 5714–5717.
 - [127] N. Parveen, M.O. Ansari, S.A. Ansari, M.H. Cho, Simultaneous sulfur doping and exfoliation of graphene from graphite using an electrochemical method for supercapacitor electrode materials, *Journal of Materials Chemistry A* 4 (2015), 233–240.
 - [128] Y. Yang, W. Shi, R. Zhang, C. Luan, Q. Zeng, C. Wang, S. Li, Z. Huang, H. Liao, X. Ji, Electrochemical exfoliation of graphite into nitrogen-doped graphene in glycine solution and its energy storage properties, *Electrochimica Acta*, 204 (2016), 100–107.
 - [129] N. Liu, P. Kim, J.H. Kim, J.H. Ye, S. Kim, C.J. Lee, Large-area atomically thin MoS₂ nanosheets prepared using electrochemical exfoliation, *ACS Nano* 8 (2014), 6902–6910.
 - [130] M. Zhao, C. Casiraghi, K. Parvez, Electrochemical exfoliation of 2D materials beyond graphene, *Chemical Society Reviews* 53 (2024), 3036–3064.
 - [131] T. Wang, H.C. Chen, F. Yu, X.S. Zhao, H. Wang, Boosting the cycling stability of transition metal compounds-based supercapacitors, *Energy Storage Materials* 16 (2019), 545–573.
 - [132] T.S. Mathis, N. Kurra, X. Wang, D. Pinto, P. Simon, Y. Gogotsi, Energy storage data reporting in perspective-guidelines for interpreting the performance of electrochemical energy storage systems, *Advanced Energy Materials* 9 (2019), 1902007.
 - [133] S. Ardizzone, G. Fregonara, S. Trasatti, “Inner” and “outer” active surface of RuO₂ electrodes, *Electrochimica Acta* 35 (1990), 263–267.
 - [134] B.B. Damaskin, O.A. Petrii, Historical development of theories of the electrochemical double layer, *Journal of Solid State Electrochemistry* 15 (2011), 1317–1334.
 - [135] L.M. Da Silva, R. Cesar, C.M.R. Moreira, J.H.M. Santos, L.G. De Souza, B.M. Pires, R. Vicentini, W. Nunes, H. Zanin, Reviewing the fundamentals of supercapacitors and the difficulties involving the analysis of the electrochemical findings obtained for porous electrode materials, *Energy Storage Materials* 27 (2020), 555–590.
 - [136] B.E. Conway, Electrochemical supercapacitors-scientific fundamentals and technological applications, 1999.

Introducción

- [137] D. Rochefort, A.L. Pont, Pseudocapacitive behaviour of RuO₂ in a proton exchange ionic liquid, *Electrochemistry Communications* 8 (2006), 1539–1543.
- [138] Y. Liu, S.P. Jiang, Z. Shao, Intercalation pseudocapacitance in electrochemical energy storage: recent advances in fundamental understanding and materials development, *Materials Today Advances* 7 (2020), 100072.
- [139] F.L.R. Bard A. J., *Electrochemical methods: fundamentals and applications*, 2001.
- [140] Y. Gogotsi, R.M. Penner, Energy storage in nanomaterials - capacitive, pseudocapacitive, or battery-like?, *ACS Nano* 12 (2018), 2081–2083.
- [141] P. Simon, Y. Gogotsi, B. Dunn, Where do batteries end and supercapacitors begin?, *Science*, 43 (2014), 1210–1211.
- [142] S. Rudra, H.W. Seo, S. Sarker, D.M. Kim, Supercapacitors as hybrid electrochemical energy storage devices: current status and future prospects, *Molecules* 29 (2024), 243.
- [143] M. Enterriá, A. Castro-Muñiz, F. Suárez-García, A. Martínez-Alonso, J.M.D. Tascon, T. Kyotani, Effects of the mesostructural order on the electrochemical performance of hierarchical micro–mesoporous carbons, *Journal of Materials Chemistry A* 2 (2014), 12023–12030.
- [144] A.M. Abdelkader, D.J. Fray, Controlled electrochemical doping of graphene-based 3D nanoarchitecture electrodes for supercapacitors and capacitive deionisation, *Nanoscale* 9 (2017), 14548–14557.
- [145] V. Augustyn, P. Simon, B. Dunn, Pseudocapacitive oxide materials for high-rate electrochemical energy storage, *Energy & Environmental Science* 7 (2014), 1597–1614.
- [146] R. Barik, P.P. Ingole, Challenges and prospects of metal sulfide materials for supercapacitors, *Current Opinion in Electrochemistry* 21 (2020), 327–334.
- [147] H.W. Park, K.C. Roh, Recent advances in and perspectives on pseudocapacitive materials for Supercapacitors—A review, *Journal of Power Sources* 557 (2023), 232558.
- [148] L. Zhang, D. Wu, G. Wang, Y. Xu, H. Li, X. Yan, An aqueous zinc-ion hybrid supercapacitor for achieving ultrahigh-volumetric energy density, *Chinese Chemical Letters* 32 (2021), 926–931.
- [149] D. Zhang, L. Li, Y. Gao, Y. Wu, J. Deng, Carbon-based materials for a new type of Zinc-Ion Capacitor, *ChemElectroChem* 8 (2021), 1541–1557.
- [150] L. Dong, X. Ma, Y. Li, L. Zhao, W. Liu, J. Cheng, C. Xu, B. Li, Q.H. Yang, F. Kang, Extremely safe, high-rate and ultralong-life zinc-ion hybrid supercapacitors, *Energy Storage Materials* 13 (2018), 96–102.
- [151] Q. Liu, H. Wang, C. Jiang, Y. Tang, Multi-ion strategies towards emerging rechargeable batteries with high performance, *Energy Storage Materials* 23 (2019), 566–586.
- [152] J.B. Goodenough, K.S. Park, The Li-ion rechargeable battery: A perspective, *Journal of the American Chemical Society* 135 (2013), 1167–1176.
- [153] R. Sahoo, M. Singh, T.N. Rao, A review on the current progress and challenges of 2D layered transition metal dichalcogenides as Li/Na-ion battery anodes, *ChemElectroChem* 8 (2021), 2358–2396.

- [154] Y.P. Wu, E. Rahm, R. Holze, Carbon anode materials for lithium ion batteries, *Journal of Power Sources* 114 (2003), 228–236.
- [155] B. Xu, D. Qian, Z. Wang, Y.S. Meng, Recent progress in cathode materials research for advanced lithium ion batteries, *Materials Science And Engineering* 73 (2012), 51-65.
- [156] J. Janek, W.G. Zeier, A solid future for battery development, *Nature Energy* 1 (2016) 16141.
- [157] A.G. Olabi, E.T. Sayed, T. Wilberforce, A. Jamal, A.H. Alami, K. Elsaid, S.M.A. Rahman, S.K. Shah, M.A. Abdelkareem, Metal-Air Batteries—A Review, *Energies* 14 (2021), 7373.
- [158] Y. Boyjoo, H. Shi, Q. Tian, S. Liu, J. Liang, Z.S. Wu, M. Jaroniec, J. Liu, Engineering nanoreactors for metal–chalcogen batteries, *Energy & Environmental Science* 14 (2021), 540–575.
- [159] X. Li, X. Sun, X. Hu, F. Fan, S. Cai, C. Zheng, G.D. Stucky, Review on comprehending and enhancing the initial Coulombic efficiency of anode materials in lithium-ion/sodium-ion batteries, *Nano Energy* 77 (2020), 105143.

2. OBJETIVOS

2 Objetivos y planteamiento de la memoria

2.1 Objetivos

La presente tesis tiene como objetivo general la obtención de materiales bidimensionales, en particular grafeno y dicalcogenuros de metales de transición, mediante procesos de exfoliación en fase líquida, para su utilización como materiales en dispositivos de almacenamiento electroquímico de energía. Concretamente, el trabajo se centra en la exfoliación electroquímica en medio acuoso, ya que representa una alternativa prometedora en términos de eficiencia, simplicidad y versatilidad a los métodos de exfoliación de materiales laminares más comúnmente utilizados. En el caso de los materiales grafénicos, se han investigado estrategias de exfoliación anódica, ya que permiten un alto grado de control sobre la química final del material. Por otro lado, se han estudiado estrategias de exfoliación catódica para obtener nanoláminas de dicalcogenuros de metales de transición de carácter metálico, limitando así la conversión de los materiales a óxidos metálicos asociada a su fuerte tendencia a la oxidación.

Para la consecución de este objetivo general, en la tesis se han planteado los objetivos específicos que se detallan a continuación:

- Obtención de grafeno altamente oxidado y, al mismo tiempo, de calidad estructural relativamente alta mediante exfoliación anódica de grafito, para su utilización como precursor en la preparación de grafeno poroso en sustitución del óxido de grafeno convencional.
- Obtención de grafeno poroso de calidad estructural relativamente alta y distribución estrecha de tamaño de poro en el rango de unos pocos nanómetros, para su utilización en almacenamiento electroquímico de energía (supercondensadores).

Objetivos

- Obtención de grafeno por exfoliación anódica de grafito en medio acuoso con control sobre las proporciones relativas de grupos funcionales oxigenados.
- Exploración de las prestaciones de grafeno anódico con grupos funcionales oxigenados modulables en aplicaciones de almacenamiento electroquímico de energía basado en zinc (condensadores híbridos y baterías de ion zinc acuoso).
- Obtención de nanoláminas de NbSe₂ y otros dicalcogenuros de carácter metálico mediante exfoliación catódica en medio acuoso, con control sobre la morfología del producto exfoliado.
- Evaluación de las prestaciones de NbSe₂ exfoliado en almacenamiento electroquímico de litio.

2.2 Organización de la memoria

En el primer capítulo de la tesis, denominado como introducción, se describen de forma general los materiales bidimensionales (2D) y de forma más detallada los que han sido objeto de estudio en la tesis presente, grafeno y dicalcogenuros de metales de transición (concretamente NbSe₂), así como los principales métodos de preparación de estos materiales y sus aplicaciones, centrándose en el almacenamiento de energía como aplicación principal. En el capítulo presente, se describen los objetivos y la organización de la memoria. El tercer capítulo se compone de la recopilación de los fundamentos de las técnicas de caracterización empleadas. En el cuarto capítulo se recogen los métodos de preparación y caracterización de los materiales estudiados en la tesis. En el quinto capítulo se recopilan los resultados de la tesis en forma de artículos publicados, precedidos en cada bloque de resúmenes detallados de cada uno de los artículos. Las publicaciones se han agrupado en dos bloques, coincidiendo con la naturaleza química de los dos tipos de materiales estudiados. Un bloque de grafeno con dos publicaciones y un segundo bloque para el NbSe₂, con un artículo. Finalmente, el capítulo sexto, recoge las conclusiones de esta tesis y se ha incluido un anexo que recoge las publicaciones relacionadas que no pertenecen a la tesis, así como una compilación de las comunicaciones a congresos.

3. TÉCNICAS DE CARACTERIZACIÓN

3 Técnicas de caracterización

3.1 Espectroscopías

A lo largo de la tesis, se han caracterizado varios de los materiales mediante técnicas espectroscópicas. Estas técnicas se fundamentan en la absorción, emisión o dispersión de radiación electromagnética por parte de la materia. Debido a que los niveles energéticos en la materia están cuantizados, la materia solo puede absorber o emitir radiación con valores de energía específicos, como se expresa en la ecuación de Planck –Einstein.

$$E_{superior} - E_{inferior} = \Delta E = h \cdot v \quad (2)$$

Donde **$E_{superior}$** es la energía del estado más alto, **$E_{inferior}$** es la del estado mas bajo, **h** es la constantes de Plank y **v** es la frecuencia de la radiación emitida o absorbida. Esta frecuencia de radiación corresponde a una diferencia energética característica del material; la medición de esta diferencia energética es el fundamento de las técnicas espectroscópicas. Dependiendo del tipo concreto de interacción entre la materia y la radiación electromagnética, se pueden distinguir varias técnicas.

3.1.1 Espectroscopia de absorción ultravioleta-vis (UV-vis)

La absorción de radiación de un material en dispersión coloidal o especie molecular en disolución, a cualquier frecuencia dada se puede relacionar con su concentración en el medio según la ley de Lambert-Beer.

$$A = \varepsilon \cdot l \cdot c \quad (3)$$

Donde A es la absorbancia a una determinada frecuencia o longitud de onda (λ), ϵ es el coeficiente de extinción a dicha longitud de onda, l la longitud del paso óptico de la cubeta y c la concentración. De esta forma, se puede determinar la concentración de una especie en dispersión en función de su absorbancia a una longitud de onda específica siempre y cuando la medida se realice dentro del rango lineal de aplicación de la ecuación (3).

La caracterización mediante espectroscopía UV-Vis realizada durante la tesis se ha llevado a cabo con un espectrofotómetro Thermo Scientific UV-Visible GENESYS 180, cuyo esquema se puede observar en la figura 15.

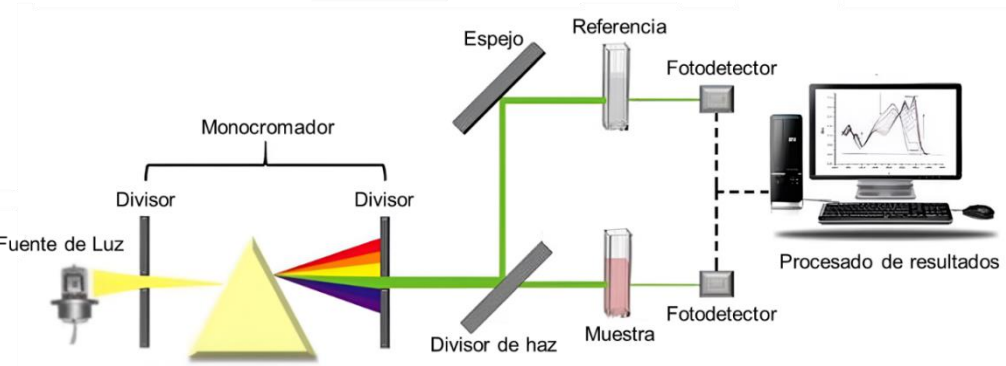


Figura 15. Esquema de un equipo de UV-Vis. Adaptado de [1]

El funcionamiento de este equipo se basa en medir al mismo tiempo la intensidad de un haz que atraviesa la muestra (P) y el que traviesa la cubeta de referencia (P_0), obteniéndose la absorbancia mediante la ecuación:

$$A = -\log P/P_0 \quad (4)$$

Las dispersiones o disoluciones deben de estar suficientemente diluidas con el fin de permitir medidas de absorbancia dentro del rango lineal de la ecuación de Lambert-Beer.

Este tipo de instrumentos trabaja en un rango de radiación correspondiente al espectro del visible, parte del ultravioleta y parte del infrarrojo (entre 200 nm y 1100 nm), lo que supone energías entre 1 y 6 eV, que causan transiciones electrónicas entre niveles de energía como $\sigma \rightarrow \sigma^*$, $n \rightarrow \sigma^*$, $n \rightarrow \pi$ y $\pi \rightarrow \pi^*$ (Figura 16) [2].

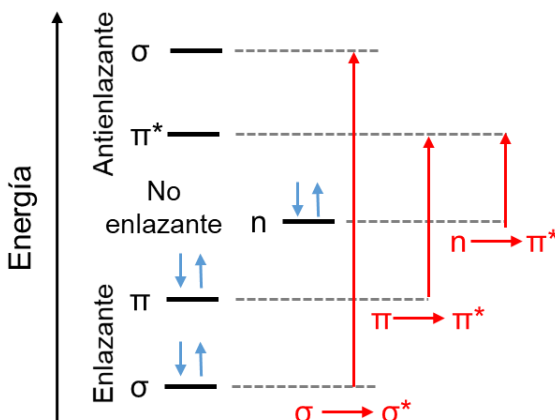


Figura 16. Transiciones electrónicas típicas entre niveles energéticos de los orbitales moleculares.

Estos niveles energéticos electrónicos a su vez se combinan con estados vibracionales y rotacionales, dando lugar a ensanchamientos en los espectros obtenidos. Además, cuando se realizan medidas espectroscópicas UV-Vis a dispersiones coloidalmente estables de materiales, se debe tener en cuenta que también la interacción entre los materiales y los disolventes da lugar a modificaciones en los estados energéticos, ensanchando nuevamente las señales

[3,4]. No obstante, pese a sus limitaciones, es una técnica ampliamente utilizada y muy útil, ya que proporciona información sobre la muestra de forma sencilla y rápida. Durante el desarrollo de la tesis, esta técnica se ha utilizado para:

- Determinar el cambio de posición de la banda de absorbancia del óxido de grafeno (Hummers) desde 231 nm hacia valores más próximos a 270 nm. Esta banda se asocia a la transición $\pi \rightarrow \pi^*$ de los dominios electrónicamente conjugados de grafenos/grafitos, y la variación de su posición está relacionada con variaciones en el tamaño de tales dominios [5,6]. El tamaño de estos dominios aromáticos, a su vez, se relaciona inversamente con el grado de oxidación del material para grafenos reducidos a partir de GO (Hummers) [7].
- Determinar el rasgo característico de absorción a 300 nm correspondiente a la transición $n \rightarrow \pi^*$ de los enlaces C=O, lo que se asocia a dominios oxidados bien definidos presentes en grafenos anódicos, en comparación con grafenos reducidos obtenidos a partir de métodos convencionales (Figura 17).
- Determinar de forma cuantitativa la concentración de dispersiones coloidales de materiales mediante la aplicación de la ley de Lambert-Beer para su posterior utilización en diferentes preparaciones de muestras.

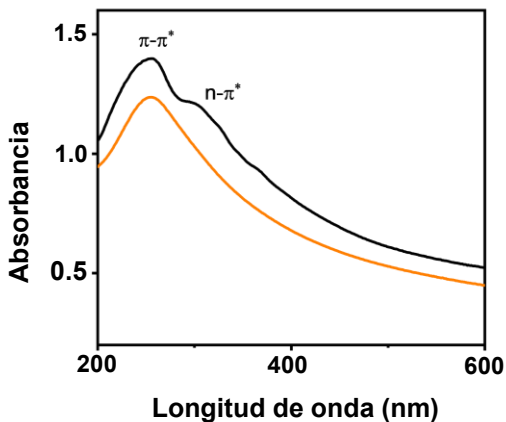


Figura 17. Espectros UV-Vis de grafeno anódico altamente oxidado (negro) y grafeno reducido obtenido a partir de óxido de grafeno Hummer's (naranja).

3.1.2 Espectroscopía Raman

La espectroscopía Raman se fundamenta en el análisis de las transiciones vibracionales en la materia [3,4,8]. Para ello, se hace incidir un haz de luz monocromática sobre una muestra donde la mayor parte de la luz se dispersa con la misma energía (dispersión elástica) que la del haz incidente (Rayleigh). Sin embargo, una pequeña fracción de la luz incidente se dispersará con cambios en su energía (dispersión inelástica). Si los fotones de haz dispersado tienen mayor energía (menor longitud de onda) que los del haz incidente, se denomina dispersión Raman anti-Stokes. Por otro lado, si tienen menor energía que los del haz incidente, se obtiene la radiación denominada Raman Stokes. Estos cambios en la energía se asocian a transiciones entre estados vibracionales de la muestra (Figura 18) [8].

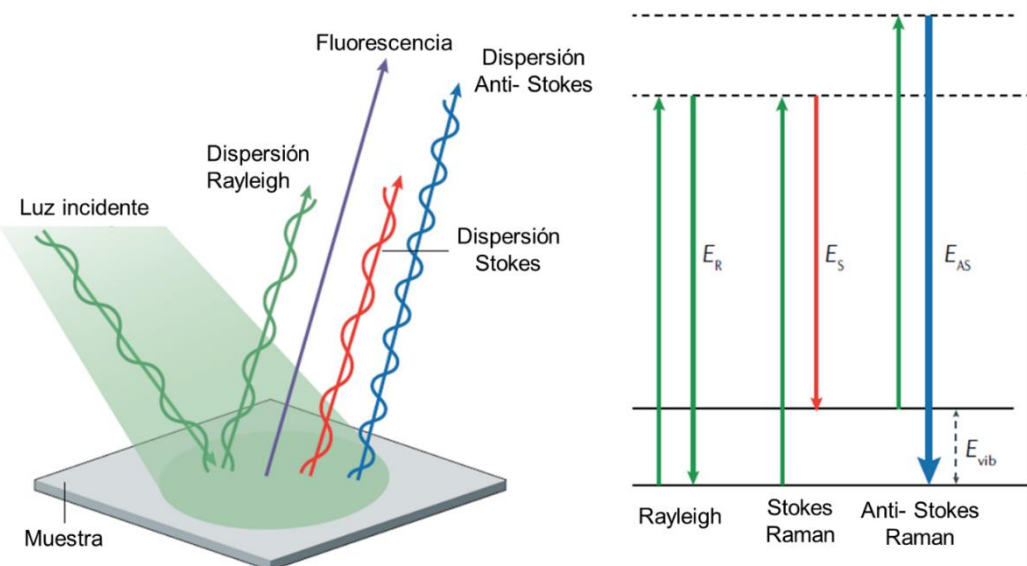


Figura 18. Dispersión Raman. Transiciones entre niveles energéticos que dan lugar a fenómenos Rayleigh, Stokes y anti-Stokes. E_R es la energía de fotones Rayleigh, E_S la energía de los fotones Stokes, E_{AS} la energía fotones anti-Stokes y E_{vib} es la energía de transición vibracional de un modo específico de la materia. Esquema adaptado de [9].

Esta técnica se utiliza habitualmente para caracterizar propiedades estructurales de sólidos incluyendo materiales carbonosos y materiales bidimensionales (grafeno o dicalcogenuros de metales de transición) [10].

Las medidas espectroscópicas realizadas en esta tesis fueron llevadas a cabo en un espectrómetro Renishaw inVia Qontor con radiación incidente generada por una fuente láser de 532 nm (láser verde), y una potencia incidente inferior a 0.5 mW para todas las muestras, con el fin de minimizar los daños. Los espectros registrados corresponden a transiciones Stokes y fueron obtenidos:

- Como pastilla, en el caso del NbSe₂.

- Como muestra depositada a partir de dispersiones coloidalmente estables, mediante depósito sobre disco de acero de 12 mm y posterior evaporación del disolvente a 50-60 °C, en caso de grafenos.

Los espectros de Raman obtenidos en esta tesis se han utilizado para:

- Comparar la calidad estructural de grafenos altamente oxidados preparados por dos vías distintas, para su utilización como precursores en la síntesis de grafeno poroso. En este caso, la comparación se realiza en base a la anchura de las bandas D y G a media altura (FWHM, *full width at half maximum*), cuyos valores se asocian a regímenes de nanocrystalización o amorfización del material [11,12].
- Evaluar la calidad estructural de las láminas de grafeno, midiendo la relación de intensidades integradas de las bandas denominadas G (1582 cm^{-1}) y D (1348 cm^{-1}) (Figura 19a) [13].
- Estudio de la calidad estructural del NbSe_2 (bulk y exfoliado), así como determinación de la presencia de oxidación parcial en el material exfoliado, debido a la alteración de la banda vibracional A_{1g} (asociada a la presencia de t-Se) y modificación de la relación de los picos E^{1g}/A_{1g} , (Figura 19b) [14].

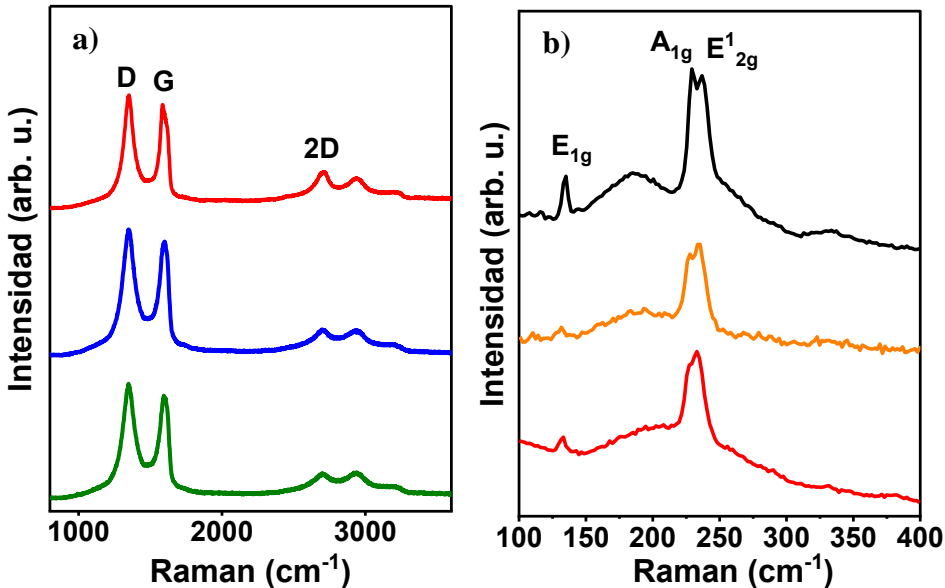


Figura 19. Espectros de Raman de (a) grafeno anódico obtenido por exfoliación electroquímica con Na_2SO_4 0.1 M (rojo), Na_2SO_4 0.1 M + NaOH 0.1 M (azul) y Na_2SO_4 0.1 M + NaOH 0.1 M + NaCl 0.1 M (verde) como electrolito, y (b) NbSe_2 bulk sin exfoliar (negro), NbSe_2 exfoliado catódicamente y dispersado en agua (naranja) y en isopropanol (rojo).

3.1.3 Espectroscopía fotoelectrónica de rayos X

La espectroscopía fotoelectrónica de rayos X (XPS, *X-ray photoelectron spectroscopy*) difiere de otros tipos de espectroscopías ya que estudia las transiciones de electrones desde niveles internos del átomo hacia el continuo de energía, es decir, se basa en arrancar electrones de orbitales internos del átomo mediante el efecto fotoeléctrico. Para que este efecto ocurra, es necesario irradiar la muestra con fotones de mayor energía que la suma de la energía de ligadura del electrón al átomo (binding energy, *BE*) y la función de trabajo del equipo (Φ , la energía necesaria para llevar un electrón al nivel de Fermi del vacío cercano a la muestra). La energía restante de la radiación incidente se transfiere al electrón

extraído como energía cinética (Kinetic energy, **KE**), lo que permite escribir la ecuación de Planck-Einstein de la siguiente manera:

$$\Delta E = h \cdot v = BE + \phi + KE \quad (5)$$

En esta técnica, se emplean rayos X para expulsar electrones de las capas internas de los átomos de la muestra a analizar, y su energía de ligadura se determina a través de la medición de su energía cinética. El espectro XPS representa la intensidad de la señal (número de electrones emitidos) en función de la energía de ligadura. Sin embargo, sólo los electrones procedentes de átomos situados en las capas más superficiales de la muestra pueden escapar y ser detectados, ya que los generados a profundidades mayores son reabsorbidos por la muestra tras colisiones inelásticas. Por lo tanto, los espectros de XPS ofrecen información exclusivamente de la superficie de la muestra, con un espesor típico de unos pocos nanómetros (<10 nm). Mediante XPS es posible detectar todos los elementos excepto H y He, lo que permite obtener la composición superficial de una muestra. Además, la energía de ligadura de los electrones internos se ve influenciada por el entorno químico de los átomos, lo que posibilita obtener información, por ejemplo, sobre los estados de oxidación y los enlaces entre átomos a partir de la forma detallada del espectro correspondiente a cada elemento (espectros de alta resolución) [3,4,15].

El equipo utilizado para la caracterización de las muestras mediante XPS es un espectrómetro de la casa SPECS equipado con un analizador de energía de electrones hemisférico Phoibos 100, que utiliza como fuente de rayos X la radiación monocromática Al K_α monocromática. El equipo opera a ultraaltovacío (10^{-7} Pa).

Las muestras se preparan por depósito de dispersiones coloidalmente estables sobre un disco de acero de 12 mm, evaporando el disolvente a 50-60 °C.

En esta tesis se ha empleado XPS para:

- Estudiar las distintas poblaciones de grupos funcionales oxigenados en los grafenos obtenidos por exfoliación electroquímica. La presencia de distintos componentes en el espectro del carbono 1s (C1s) indica distintos estados de oxidación (E.O.) de este elemento [(286.5- 287.1 eV C (E.O +1) y 287.0- 289.0 eV C (E.O. +2/+3)] y, por lo tanto, la existencia de distintos tipos de grupos funcionales en los grafenos [16].
- Determinar la cantidad relativa de oxígeno en base a la relación O/C de los materiales obtenidos.
- Estudiar la oxidación superficial de NbSe₂ tanto bulk como exfoliado. Mediante XPS se puede observar la presencia de óxidos de niobio, así como de selenio elemental [17,18].

3.2 Microscopías

3.2.1 Microscopía electrónica de transmisión

Los materiales nanoestructurados no pueden ser estudiados a escalas relevantes mediante microscopía óptica debido a sus limitaciones de resolución determinada por la longitud de onda de la luz visible (~unos pocos centenares de nanómetros). Esto lleva a la utilización de microscópios en los que se sustituyen los fotones por electrones como elementos que interactúan con la muestra. Los electrones presentan un comportamiento similar a los fotones cuando son emitidos por un filamento y son acelerados por un campo electromagnético (voltajes comprendidos entre ~100 kV y 1000 kV). En la microscopía de transmisión (TEM, *transmission electron microscopy*), los electrones inciden sobre la muestra y la atraviesan, siendo recogidos posteriormente por un detector [19]. En esta tesis, el equipo utilizado es un microscopio de alta resolución (HR-TEM, High resolution

TEM) JEM-2100F (JEOL) con un voltaje de 200 kV, y que trabaja a temperatura ambiente o a temperatura del N₂ líquido.

Para realizar las medidas, las muestras se prepararon depositando 20 µL de una dispersión del material a estudiar en agua o agua/etanol sobre una rejilla de cobre recubierta de *lacey carbon*, dejando evaporar el disolvente a temperatura ambiente.

Esta técnica se utilizó en la tesis para observar la porosidad generada en láminas de grafeno altamente oxidado, dónde se pueden diferenciar desde agujeros de 200 nm de grosor hasta agujeros comprendidos entre 4 y 8 nm (Figura 20).

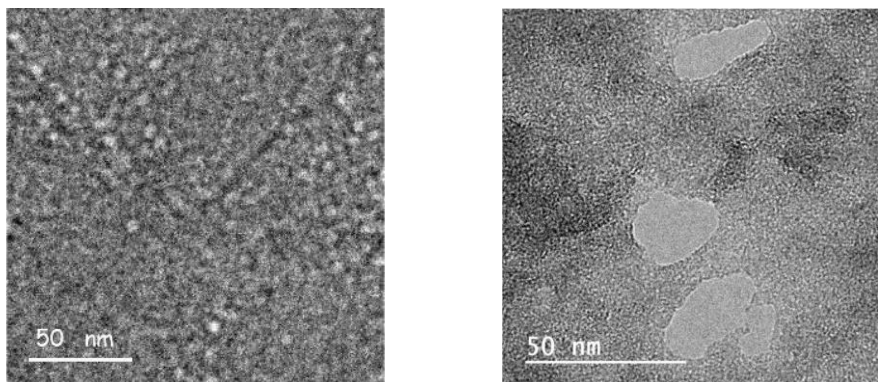


Figura 20. Imágenes de TEM de grafenos con distinta porosidad.

3.2.2 Microscopía electrónica de barrido

El fundamento de la microscopía electrónica de barrido (SEM, *scanning electron microscopy*) es similar al del TEM, aunque en este caso los electrones son generados en una fuente de menor voltaje (~20-40 kV) y se concentran mediante la utilización de lentes electromagnéticas sobre la muestra. A diferencia del TEM, los electrones incidentes no atraviesan la muestra, si no que experimentan otros procesos [3,20].

En el caso de que los electrones sufran choques elásticos al incidir con la muestra, es decir, que sean dispersados por la muestra sin perder energía, éstos se denominan **electrones retrodispersados**. Por otro lado, cuando los electrones incidentes interaccionan con electrones de valencia de la muestra, estos últimos son arrancados, obteniéndose un flujo de los denominados **electrones secundarios**, de menor energía que los retrodispersados. Los electrones secundarios se generan en capas internas de la muestra, pero pierden energía debido a los choques inelásticos, con lo que en la práctica los que se detectan por el microscopio son superficiales, en consecuencia, los electrones secundarios se utilizan para obtener imágenes de la superficie de la muestra. Por último, los electrones incidentes pueden dar lugar a la expulsión de electrones de capas internas de los átomos, dando lugar a la emisión de rayos X por la relajación de electrones de las capas exteriores del átomo a los niveles internos dejados libres por los electrones eyectados [19,20] (Figura 21).

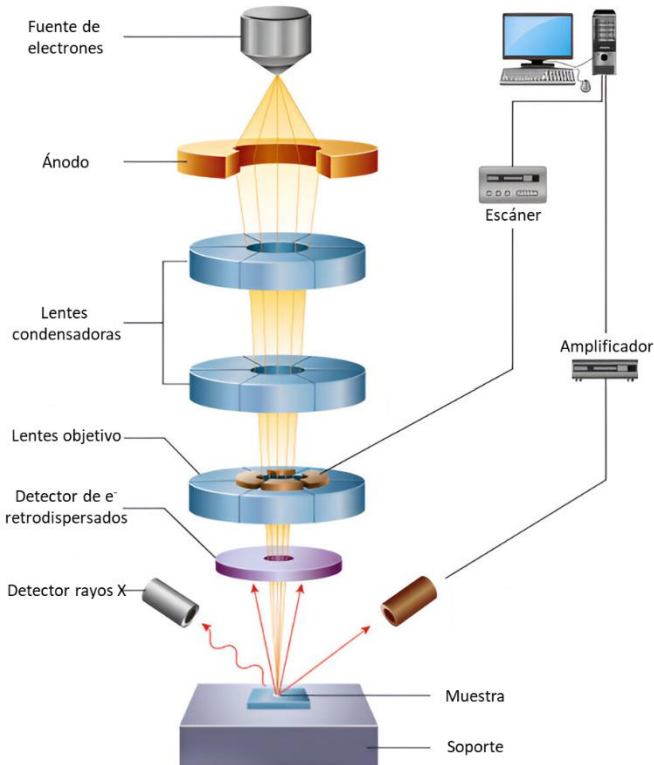


Figura 21. Esquema de un microscopio electrónico de barrido (SEM) y los diferentes tipos de emisión al hacer incidir un haz de electrones sobre la superficie de la muestra. Adaptado de [21].

En esta tesis las imágenes de SEM se han tomado con un microscopio Quanta FEG 650 (FEI Company), operado a 25 kV y utilizando la señal de electrones secundarios, que se ha utilizado principalmente para el estudio de la morfología de:

- Grafeno altamente oxidado obtenido mediante exfoliación electroquímica anódica utilizado como precursor de grafeno poroso.
- Material bulk de NbSe₂ utilizado como material de partida en la exfoliación catódica y residuo bulk generado post exfoliación.
- Electrodos de grafeno anódico depositados como filmes sobre papel de carbono.

- Ánodos de zinc recubiertos de grafeno anódico como protección de electrodos en dispositivos AZIC.

Si el equipo de SEM incorpora un detector de electrones situado debajo de la muestra y esta es suficientemente delgada como para permitir el paso de los electrones (p.ej., caso de nanoláminas bidimensionales), se pueden registrar imágenes de microscopía electrónica de barrido por transmisión (STEM, *scanning transmission electron microscopy*) con mayor resolución que la obtenida con los electrones secundarios [22]. El microscopio utilizado para llevar a cabo las medidas de SEM de las muestras de la tesis permitió realizar también medidas de STEM, que se utilizaron para estudiar la morfología de los materiales exfoliados catódicamente a partir de NbSe₂ *bulk* y de las nanoláminas de grafeno obtenidas por exfoliación anódica.

3.2.3 Microscopía de fuerza atómica

La microscopía de fuerza atómica es un tipo de microscopía que pertenece a las microscopias de campo cercano o de proximidad (SPM, *Scanning probe microscopy*). Dichas microscopías son un tipo de técnicas de análisis superficial que se desarrollaron a partir de la invención del microscopio de efecto túnel [23]. Concretamente, la microscopía de fuerza atómica (AFM, *atomic force microscopy*) se fundamenta en cuantificar y controlar las fuerzas generadas entre la superficie de la muestra y una punta colocada sobre un extremo de un material flexible (cantilever) acoplado a un material piezoelectrónico. En función de las interacciones establecidas entre la punta y la muestra, así como de la respuesta del cantiléver a estas interacciones, existen diferentes modos de medida [24] (Figura 22). Durante esta tesis se realizaron medidas de AFM en modo tapping o de contacto intermitente. Este modo se basa en aplicar un voltaje sinusoidal al material

piezoeléctrico, lo que hace que el cantiléver oscile a su frecuencia de resonancia natural y a una determinada amplitud en su estado libre (i.e., sin interacción entre la punta y la muestra) [25,26]. Cuando la punta se acerca a la muestra y se establece una interacción entre ambos, tiene lugar un cambio en la amplitud de oscilación del cantilever debido a que la interacción punta-muestra resta energía a su oscilación. Este cambio en la amplitud de oscilación del cantiléver al interactuar con la superficie de la muestra, tanto mayor cuanto mayor sea la interacción (mayor proximidad entre punta y muestra), se utiliza como señal para obtener imágenes topográficas de la superficie de la muestra. La amplitud y frecuencia de oscilación del cantiléver se cuantifica en base al comportamiento de un haz láser que se hace incidir sobre un fotodetector, después de reflejar sobre el cantiléver (Figura 22).

Para la obtención de imágenes de AFM en modo tapping, en esta tesis se ha utilizado un microscopio Nanoscope IIIa Multimode de Veeco Instruments, utilizando cantilévers de silicio de constante de fuerza $\sim 40 \text{ N m}^{-1}$ y frecuencias de resonancia $\sim 250\text{--}300 \text{ kHz}$ (Bruker Corporation). Para preparar las muestras a medir, se depositaron pequeños volúmenes ($10 \mu\text{L}$) de una dispersión acuosa diluida ($\sim 0.05 \text{ mg mL}^{-1}$) del material en cuestión sobre un sustrato de grafito pirolítico altamente orientado (HOPG) o mica precalentado a $60\text{--}80^\circ\text{C}$.

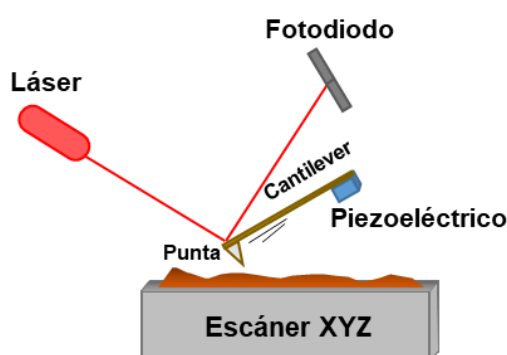


Figura 22. Esquema de operación de un microscopio de AFM en modo tapping.

En esta tesis se ha utilizado el AFM para obtener imágenes de nanoláminas (NbSe_2 y grafeno) y nanotubos (NbSe_2) de materiales bidimensionales depositadas de dispersión coloidal, para de esta manera determinar sus dimensiones (grosor, tamaño lateral y longitud) (Figura 23).

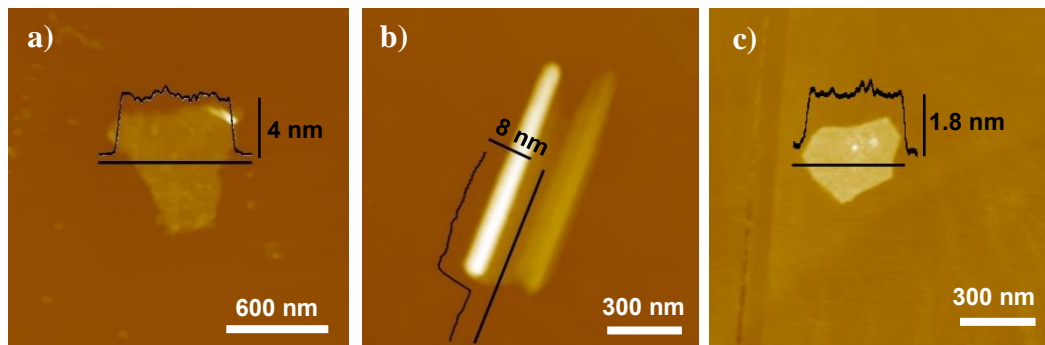


Figura 23. Imágenes de AFM de (a) NbSe_2 laminar, (b) NbSe_2 nanotubular y (c) grafeno anódico.

3.3 Técnicas electroquímicas

3.3.1 Espectroscopía de impedancia electroquímica

La espectroscopía de impedancia electroquímica (EIS, *electrochemical impedance spectroscopy*) es una técnica electroquímica que se fundamenta en la aplicación de un pulso de voltaje sinusoidal a un sistema, que genera una respuesta en forma de corriente alterna que se recoge y se analiza [27].

La impedancia, $Z(f)$, es una magnitud vectorial que se define como la relación entre la señal de potencial aplicado y la intensidad de corriente de respuesta del sistema (I), y viene dada por la ecuación:

$$Z(f) = \frac{V(t)}{I(t)} \quad (6)$$

Al tratarse de una magnitud vectorial, se expresa en forma de números complejos, siendo Z' la parte real y Z'' la parte imaginaria. Si se representa gráficamente la parte real frente a la parte imaginaria, se obtiene el conocido diagrama de Nyquist. Esta representación gráfica permite asociar regiones del diagrama con comportamientos del sistema, obteniéndose información sobre los procesos de transferencia de carga y masa que puedan tener lugar en el electrodo [27].

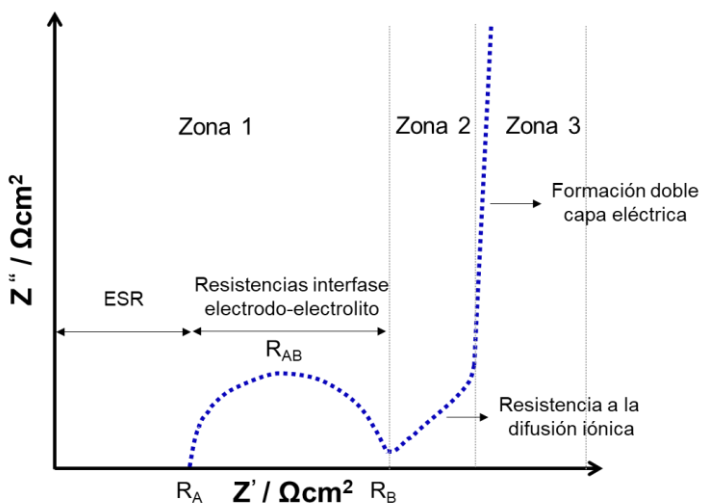


Figura 24. Diagrama de Nyquist de un material grafénico como electrodo de trabajo en supercondensadores.

El diagrama de Nyquist que se observa en la figura 24 es un diagrama ideal de materiales grafénicos, y en él se pueden apreciar 3 zonas distintas:

Zona 1: Esta zona (media-alta frecuencia), se compone de la suma de R_A y R_{AB} , donde R_{AB} , también denominada como resistencia a la transferencia de carga

[28,29], se asocia con la resistencia correspondiente a los procesos que tienen lugar en la interfase electrodo-electrolito, concretamente la resistencia a la transferencia de carga [30-34,35]. Por otro lado, la intersección del diagrama con la parte real (eje X), representada como R_A y denominada como resistencia en serie equivalente (ESR, *equivalent series resistance*), se asocia con la suma de las resistencias en serie del electrolito, electrodo y resistencia del contacto electrodo-colector de corriente [28,30,31,33].

Zona 2: (zona de Warburg). Esta contiene información sobre los procesos difusivos de los iones del electrolito a través del electrodo. La mayor o menor verticalidad de ésta se asocia con una mayor o menor resistencia a la difusión iónica [34,36].

Zona 3: (bajas frecuencias). Esta zona se asocia al comportamiento capacitivo del electrodo. Para tal comportamiento ideal, se obtendría una recta completamente vertical. Sin embargo, en los sistemas reales ese tramo suele representar una cierta inclinación, lo que se asocia a una dificultad en la formación de la doble capa eléctrica [37].

En esta tesis se utilizó la EIS de manera complementaria para caracterizar los materiales preparados como electrodos de trabajo. Las medidas se llevaron a cabo en un potenciómetro VSP, de Bio-Logic Science Instruments, en el potencial de circuito abierto con un intervalo de frecuencias entre 10 mHz y 100 kHz, con una amplitud de voltaje de $\pm 10\text{mV}$ en configuración de celda de tres electrodos y dos electrodos (simétrica y asimétrica).

Las medidas de EIS realizadas a las muestras de esta tesis se utilizaron para comparar el comportamiento de dos grafenos como electrodos de trabajo en sistemas de ion zinc y en supercondensadores (Figura 25).

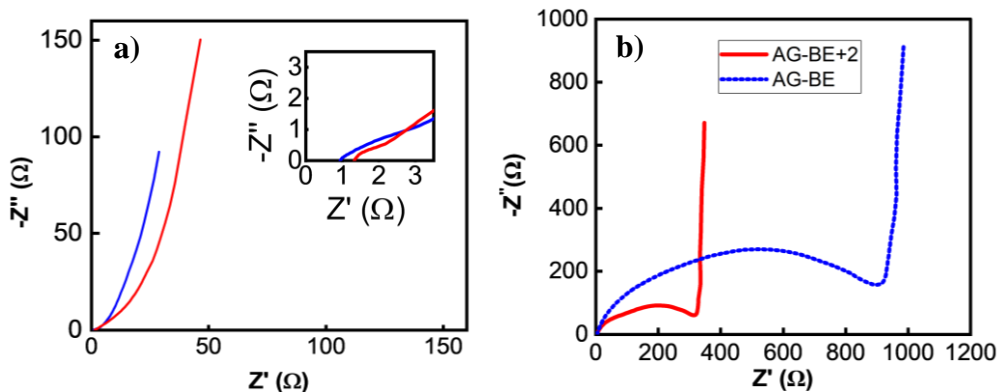


Figura 25. Diagramas de Nyquist de (a) grafenos anódicos altamente oxidados y (b) grafenos anódicos de química modulable.

3.3.2 Voltamperometría

Esta técnica se fundamenta en aplicar un voltaje (V) variable a una velocidad constante de barrido (v) entre el electrodo de trabajo y el electrodo de referencia. Este voltaje aplicado genera una intensidad de corriente (I) como respuesta, la cual se mide y se representa frente al voltaje en un diagrama denominado voltamperograma [27].

Si el barrido se realiza en una única dirección, la medida llevada a cabo se denomina voltamperometría lineal. Si el barrido se realiza en ambas direcciones de forma cíclica, se denomina voltamperometría cíclica. Esta técnica es la base del análisis electroquímico, ya que muestra información sobre procesos redox, de adsorción e intercalación, catálisis y mecanismos de almacenamiento de energía.

Además, permite conocer el rango de trabajo estable del sistema (ventana de potencial) y procesos de descomposición del electrolito o de transformación del electrodo [38,39].

Las medidas de voltamperometría cíclica se realizaron en un potenciómetro VSP, de Bio-Logic Science Instruments.

En esta tesis, la voltamperometría cíclica se utilizó para caracterizar el comportamiento de los electrodos de trabajo en dispositivos de almacenamiento tipo supercondensador, batería de ion litio y condensadores híbridos de ion zinc. Además, se utilizó para estudiar cuantitativamente el comportamiento cinético de los cátodos de estos últimos (Figura 26).

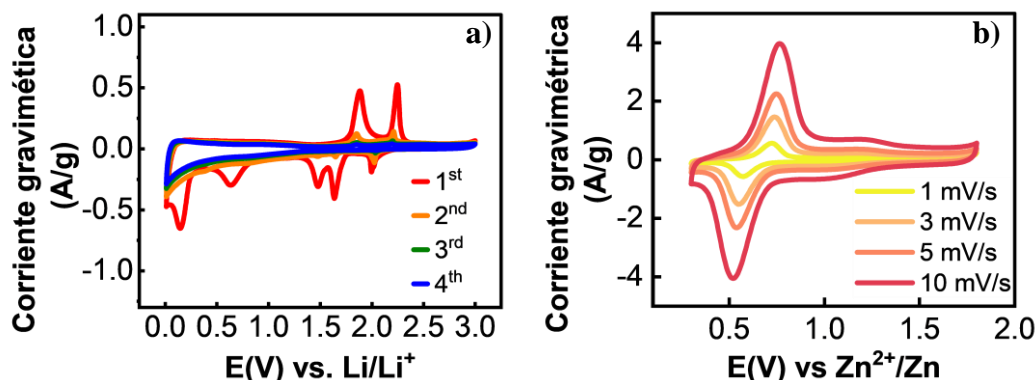


Figura 26. Voltamperogramas cíclicos de (a) nanorrollos de NbSe₂ a 0.1 mV s⁻¹ y (b) grafeno anódico de química modular con FMN (3:6) entre 1 mV s⁻¹ y 10 mV s⁻¹.

3.3.3 Cronopotenciometría galvanostática

La cronopotenciometría galvanostática es una técnica fundamentada en la medición del potencial (V) en función del tiempo durante la aplicación de una intensidad de corriente constante (I). La representación gráfica del voltaje medido en función del tiempo para una intensidad dada, se denomina curva de carga-

descarga. Cuando el almacenamiento de carga en el sistema electroquímico implica la formación de una doble capa eléctrica, el cronopotenciograma presenta una forma triangular característica (p.ej., Figura 27a) [40]. En estos sistemas, al aplicar una intensidad de corriente constante, el voltaje de la celda varía de forma lineal con el tiempo, por lo que la capacidad del sistema se puede calcular atendiendo a la siguiente fórmula.

$$C = \frac{I \Delta t}{m \Delta V} \quad (7)$$

Donde C (F g^{-1}) es la capacitancia, I (A) es la intensidad de corriente aplicada, Δt (s) es el tiempo total correspondiente a la descarga, m (g) es la masa del material activo del electrodo de trabajo (WE) en un sistema a tres electrodos y de los dos electrodos en un sistema a dos electrodos para la presente tesis, y ΔV (V) es la variación del voltaje durante la descarga.

A partir de la capacitancia obtenida para sistemas de dos electrodos, también se pueden determinar la densidad de energía (E) y de potencia (P) a través de las siguientes ecuaciones:

$$E = \frac{C \Delta V^2}{2} \quad (8)$$

$$P = \frac{E}{\Delta t} \quad (9)$$

Por otro lado, cuando el cronopotenciograma se aleja de la linealidad, presentando hombros o mesetas (p.ej., Figura 27b), no es pertinente caracterizar el almacenamiento de carga en términos de capacitancia [41]. En este caso, el almacenamiento de carga se expresa simplemente en términos de capacidad, es decir, como la cantidad de carga (Q) almacenada durante un tiempo (t) a una intensidad de corriente determinada (I), y se puede expresar como:

$$Q = I \Delta t \quad (10)$$

Por otro lado, además de los valores de capacidad o capacitancia, también se suelen obtener otros datos de los ciclos de carga-descarga, como por ejemplo valores de retención de capacidad tras un número elevado de ciclos consecutivos de carga y descarga.

En esta tesis, las medidas de cronopotencimetría galvanostática se realizaron con el mismo equipo que las EIS y las voltamperometrías cíclicas, y se utilizaron para caracterizar el comportamiento de grafenos porosos como electrodos de trabajo en supercondensadores, nanotubos y nanoláminas de NbSe₂ como electrodos de almacenamiento de litio y grafenos anódicos como cátodos en condensadores híbridos de ion zinc.

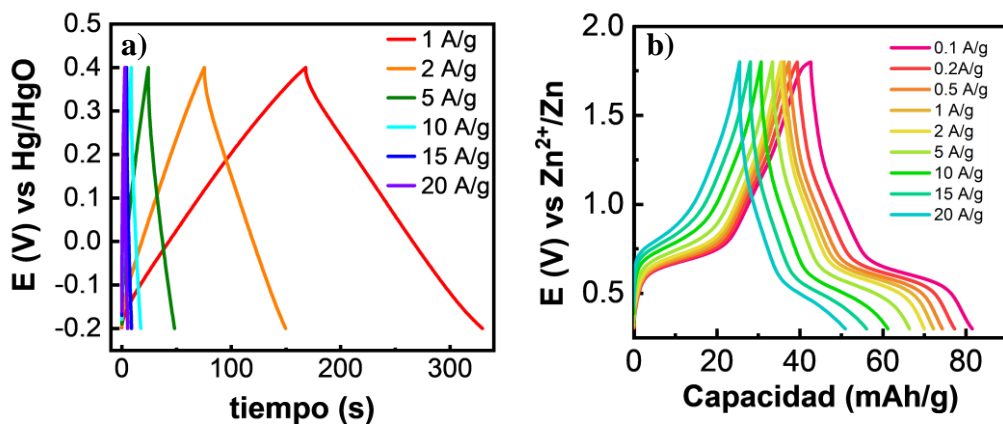


Figura 27. Perfiles de descarga de (a) grafeno poroso obtenido a partir de óxido de grafeno reducido (b) grafeno anódico de química modular híbrido con la molécula redox mononucleótido de flavina.

3.4 Otras técnicas de caracterización

3.4.1 Método de cuatro puntas para la medida de conductividad eléctrica

Las medidas de conductividad eléctrica de los materiales se llevaron a cabo sobre el material depositado en forma de filme. Para tal fin, se hace circular un flujo de electrones entre dos puntos del material depositado y se mide la resistencia correspondiente al paso de electrones entre dos puntos, lo que se relaciona con la conductividad eléctrica del material. Este método permite eliminar de la medida la resistencia asociada al contacto de las puntas con el material y la propia resistencia asociada al equipo de trabajo.

Para realizar las medidas de conductividad eléctrica de grafenos, se prepararon filmes mediante filtración de dispersiones (0.1 mg mL^{-1} , 250 mL) sobre filtros de PTFE hidrófilo. Su grosor se determinó con un micrómetro digital.

En esta tesis, se midió la conductividad eléctrica con el fin de comparar la conductividad eléctrica de grafenos anódicos con distinta calidad estructural.

3.4.2 Dispersión dinámica de la luz

La dispersión dinámica de la luz (DLS, *dynamic light scattering*) es una técnica utilizada para medir el tamaño de partículas suspendidas en un medio líquido y se fundamenta en las fluctuaciones temporales de la intensidad del haz dispersado cuando un haz incidente monocromático interacciona con partículas en movimiento browniano [42]. Para ello, se genera luz con un haz láser, que incide sobre la superficie de las partículas. Estas partículas dispersan la luz en todas las direcciones. Sin embargo, ésta se recoge a un ángulo determinado, ya que, de esta manera, la intensidad de la luz dispersada depende únicamente de la velocidad de

Técnicas de caracterización

difusión de las partículas (partículas más grandes tendrán movimientos más lentos). Recogiendo la fluctuación de la intensidad del haz dispersado a lo largo del tiempo se obtienen datos, que se ajustan con una función de correlación para dar lugar a la denominada constante de decaimiento. Posteriormente, a partir del valor de esta constante, se obtiene el radio hidrodinámico de las partículas y la distribución de tamaños de las partículas en dispersión [42,43].

Las medidas de DLS se realizaron con un equipo Litesizer 500 de Anton Paar, equipado con un láser de longitud de onda de 658 nm. Las medidas se tomaron a un ángulo fijo de 90° y se llevaron a cabo para complementar la información de tamaños laterales de lámina determinados previamente mediante AFM (Figura 28).

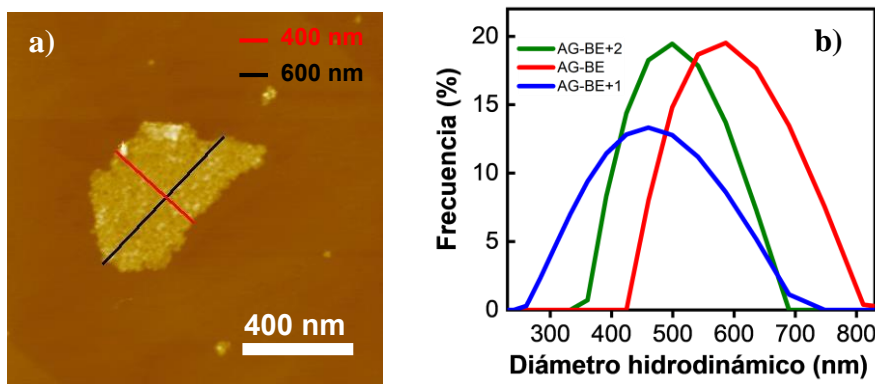


Figura 28. (a) Imagen de AFM de AGBE+2 y (b) distribución ponderada en número de los diámetros hidrodinámicos de dispersiones acuosas de diferentes grafenos anódicos.

3.4.3 Potencial Z

El potencial Z es el potencial eléctrico en el plano de desplazamiento de una partícula. Se genera en la doble capa, en el límite con la capa difusa, es decir, debido a la diferencia de potencial generada en la interfase sólido-líquido. Este parámetro

electrostático se utiliza habitualmente como un indicador coloidal de partículas debido a su carga eléctrica superficial [44,45].

Para realizar la medida del potencial Z, se hace incidir un haz láser de forma continua sobre una dispersión coloidal diluida del material a estudiar. Paralelamente, se aplica una diferencia de potencial entre dos electrodos situados en los extremos de la celda. Esta diferencia de potencial da lugar a que las partículas eléctricamente cargadas sean atraídas hacia el electrodo de carga opuesta. El movimiento electroforético de las partículas causa una fluctuación de la intensidad de luz dispersada con una frecuencia que se correlaciona con la velocidad de las partículas en movimiento.

El potencial Z (ζ) está relacionado con la movilidad electroforética (U_E) por la ecuación de Henry:

$$U_E = \frac{2\epsilon\zeta f(kr)}{3\eta} \quad (11)$$

, donde $f(kr)$ representa la denominada función de Henry, siendo κ la longitud de Debye-Hückel (inversa del grosor de la doble capa) y “ r ” el radio de la partícula. El término $f(kr)$ representa la relación entre el tamaño de la partícula y el espesor de la doble capa eléctrica. En este caso, se tomó un valor de $f(kr)$ de 1.5, que corresponde a la aproximación de Smoluchowski [46], aconsejable en medio acuoso y a concentración moderada del material. En esta tesis, las medidas de potencial Z se han llevado a cabo en un equipo Litesizer 500 de Anton Paar equipado con una lámpara 658 nm, a un ángulo fijo de 15°. Las medidas se han utilizado para estudiar la estabilidad coloidal a distintos valores de pH de grafenos anódicos.

3.4.4 Difracción de rayos X

La técnica de difracción de rayos X (XRD, *X-ray diffraction*) es ampliamente utilizada para el estudio de estructuras cristalinas, incluidas estructuras cristalinas laminares [3]. Esta técnica se fundamenta en el fenómeno de difracción de rayos X por los distintos planos cristalinos de un sólido. Cuando la radiación interacciona con la muestra, tiene lugar una reflexión de una parte de la misma por parte de la red de átomos del sólido. Esta reflexión ocurre con un desfase debido a la distinta posición espacial de los átomos, fenómenos de interferencia en función del ángulo de incidencia de los rayos X.

La relación entre el ángulo de la radiación incidente que genera interferencia constructiva y la separación entre los planos cristalinos viene dada por la ley de Bragg:

$$2d \operatorname{sen} (\theta) = n\lambda \quad (12)$$

Donde d es la distancia entre planos cristalinos, θ el ángulo entre la dirección de la radiación incidente y el plano, n un número entero positivo y λ la longitud de onda de la radiación incidente.

Al hacer incidir la radiación sobre la muestra en un rango de ángulos θ , se obtiene un patrón de difracción, que puede ser transformado en difractograma al representar la intensidad de la radiación reflejada en función del ángulo. En el difractograma se observan picos generados por los fenómenos de interferencia constructiva, que aportan información de las distancias entre planos cristalinos y por lo tanto información sobre la estructura del sólido.

En esta tesis se utilizó un equipo de difracción Bruker D8 Advance, con la radiación de Cu K α ($\lambda=0.154$ nm) como fuente de rayos X, para determinar la presencia de polimorfos en MoS₂ y NbSe₂, así como de especies de óxidos de Nb y de Se en materiales derivados de este último (p.ej., Figura 29).

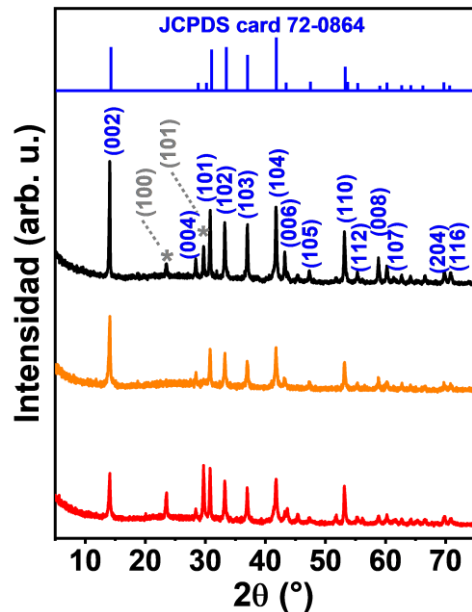


Figura 29. Diffractograma de NbSe₂ bulk (negro), exfoliado con morfología de nanorollos (naranja) y nanolaminas (rojo).

3.5 Referencias

- [1] M.S. Braga, O.F. Gomes, R.F.V.V. Jaimes, E.R. Braga, W. Borysow, W.J. Salcedo, Multispectral colorimetric portable system for detecting metal ions in liquid media, INSCIT 2019 - 4th International Symposium on Instrumentation Systems, Circuits Transducers (INSCIT), 2019, 1-6.
- [2] M. Picollo, M. Aceto, T. Vitorino, UV-Vis spectroscopy, *Physical Science Reviews* 4 (2019), 20180008.
- [3] C. Faraldo, M.; Goberna, Técnicas de análisis y caracterización de materiales, *Madrid: Consejo Superior de Investigaciones Científicas* 2011.
- [4] D.A. Skoog, S.R. Chourch, F.J. Holler, Principles of instrumental analysis, 6th ed. Thomson Brooks/Cole 2007.
- [5] J. Hu, H. Zeng, C. Wang, Z. Li, C. Kan, Y. Liu, Interband π plasmon of graphene: strong small-size and field-enhancement effects, *Physical Science Reviews* 16 (2014) 23483–23491.
- [6] D. Li, M.B. Müller, S. Gilje, R.B. Kaner, G.G. Wallace, Processable aqueous dispersions of graphene nanosheets, *Nature Nanotechnology* 3 (2008), 101–105.
- [7] M.J. Fernández-Merino, L. Guardia, J.I. Paredes, S. Villar-Rodil, P. Solís-Fernández, A. Martínez-Alonso, J.M.D. Tascón, Vitamin C is an ideal substitute for hydrazine in the reduction of graphene oxide suspensions, *Journal of Physical Chemistry C* 114 (2010), 6426–6432.
- [8] E. Smith, G. Dent, Modern Raman Spectroscopy: A Practical Approach, John Wiley & Sons 2004.
- [9] S. Mosca, C. Conti, N. Stone, P. Matousek, Spatially offset Raman spectroscopy, *Nature Reviews Methods Primers* 1 (2021), 2662-8449.
- [10] S. Zhang, N. Zhang, Y. Zhao, T. Cheng, X. Li, R. Feng, H. Xu, Z. Liu, J. Zhang, L. Tong, Spotting the differences in two-dimensional materials – the Raman scattering perspective, *Chemical Society Reviews* 47 (2018), 3217–3240.
- [11] P. Yu, Z. Xiong, H. Zhan, K. Xie, Y.L. Zhong, G.P. Simon, D. Li, Electrochemically-derived graphene oxide membranes with high stability and superior ionic sieving, *Chemical Communications* 55 (2019), 4075–4078
- [12] L.G. Cançado, A. Jorio, E.H.M. Ferreira, F. Stavale, C.A. Achete, R.B. Capaz, M.V.O. Moutinho, A. Lombardo, T.S. Kulmala, A.C. Ferrari, Quantifying defects in graphene via Raman spectroscopy at different excitation energies, *Nano Letters* 11 (2011), 3190–3196.
- [13] M.A. Pimenta, G. Dresselhaus, M.S. Dresselhaus, L.G. Cançado, A. Jorio, R. Saito, Studying disorder in graphite-based systems by Raman spectroscopy, *Physical Chemistry Chemical Physics* 9 (2007), 1276–1290.
- [14] G.E. Myers, G.L. Montet, Light-induced oxidation of NbSe₂ single crystals, *Journal of Physics and Chemistry Solids* 32 (1971), 2645–2646.

- [15] V. der Heide, X-Ray photoelectron spectroscopy: an introduction to the principles and practices, John Wiley & Sons Ltd, New York, 2012.
- [16] I. Ferrari, A. Motta, R. Zanoni, F.A. Scaramuzzo, F. Amato, E.A. Dalchiele, A.G. Marrani, Understanding the nature of graphene oxide functional groups by modulation of the electrochemical reduction: A combined experimental and theoretical approach, *Carbon* 203 (2023), 29–38.
- [17] Z. Zeng, T. Sun, J. Zhu, X. Huang, Z. Yin, G. Lu, Z. Fan, Q. Yan, H.H. Hng, H. Zhang, An effective method for the fabrication of few-layer-thick inorganic nanosheets, *Angewandte Chemie International Edition* 51 (2012), 9052–9056.
- [18] M.J. Park, H.Y. Asl, A. Manthiram, M.J. Park, H.Y. Asl, A. Manthiram, Understanding zinon insertion chemistry through nonaqueous electrochemical investigation of 2H-NbSe₂, *Advanced Materials Interfaces* 8 (2021), 2100878.
- [19] Transmission Electron Microscopy: Fundamentals of Methods and Instrumentation, Electron Microscopy of Polymers Springer Laboratory (2008), 15–51.
- [20] J.C.H. Spence, High-Resolution Electron Microscopy, Oxford, 2014.
- [21] R. Shahadev, B.K. saikia, 18-Advanced micro-and nanoscale characterization techniques for carbonaceous aerosols, Handbook of Nanomaterials in Analytical Chemistry, (2020) 449-472.
- [22] R.F. Egerton, Physical principles of electron microscopy, Springer, 2005.
- [23] G. Binnig, H. Rohrer, C. Gerber, E. Weibel, Surface studies by scanning tunneling microscopy, *Physical Review Letters* 49 (1982), 57-61.
- [24] G. Binnig, C.F. Quate, C. Gerber, Atomic force microscope, *Physical Review Letters* 56 (1986), 930–933.
- [25] J.I. Paredes, S. Villar-Rodil, P. Solís-Fernández, A. Martínez-Alonso, J.M.D. Tascón, Atomic force and scanning tunneling microscopy imaging of graphene nanosheets derived from graphite oxide, *Langmuir* 25 (2009), 5957–5968.
- [26] G. Haugstad, Atomic Force Microscopy: Understanding Basic Modes and Advanced Applications, John Wiley and Sons, 2012
- [27] L.R.F. Allen J. Bard, Electrochemical methods: Fundamentals and applications, 2nd ed., John Wiley & Sons Ltd, Austin, Texas.
- [28] I. Yang, S.G. Kim, S.H. Kwon, M.S. Kim, J.C. Jung, Relationships between pore size and charge transfer resistance of carbon aerogels for organic electric double-layer capacitor electrodes, *Electrochimica Acta* 223 (2017), 21–30.
- [29] C. Lei, F. Markoulidis, Z. Ashitaka, C. Lekakou, Reduction of porous carbon/Al contact resistance for an electric double-layer capacitor (EDLC), *Electrochimica Acta* 92 (2013), 183–187.
- [30] Y.R. Nian, H. Teng, Influence of surface oxides on the impedance behavior of carbon-based electrochemical capacitors, *Journal of Electroanalytical Chemistry* 540 (2003), 119–127.
- [31] C.L. Liu, W.S. Dong, G.P. Cao, J.R. Song, L. Liu, Y.S. Yang, Influence of KOH followed by oxidation pretreatment on the electrochemical performance of phenolic based activated carbon fibers, *Journal of Electroanalytical Chemistry* 611 (2007), 225–231.

Materiales y métodos

- [32] K.H. An, W.S. Kim, Y.S. Park, J. Moon, D.J. Bae, S.C. Lim, Y.S. Lee, Y.H. Lee, Electrochemical properties of high-power supercapacitors using single-walled carbon nanotube electrodes, *Advanced Functional Materials*, 11 (2001), 387–392.
- [33] B. Fang, L. Binder, A modified activated carbon aerogel for high energy storage in electric double layer capacitors, *Journal of Power Sources* 163 (2006) 616–622.
- [34] R. de Levie, On porous electrodes in electrolyte solutions: I. Capacitance effects, *Electrochimica Acta* 8 (1963), 751–780.
- [35] B.E. Conway, Electrochemical supercapacitors _scientific fundamentals and technological applications, 1st ed. Springer 1999.
- [36] A. Noori, M.F. El-Kady, M.S. Rahmanifar, R.B. Kaner, M.F. Mousavi, Towards establishing standard performance metrics for batteries, supercapacitors and beyond, *Chemical Society Reviews* 48 (2019), 1272–1341.
- [37] M. Toupin, D. Bélanger, I.R. Hill, D. Quinn, Performance of experimental carbon blacks in aqueous supercapacitors, *Journal of Power Sources* 140 (2005), 203–210.
- [38] D. Mandler, Electroanalytical methods: guide to experiments and applications, 2nd ed. Springer 2010.
- [39] C.G. Zoski, Handbook of Electrochemistry, Elsevier (2007).
- [40] S. Shiraishi, H. Kurihara, A. Oya, Preparation and Electric Double Layer Capacitance of Mesoporous Carbon, *Carbon Letters* 1 (2001), 133–137.
- [41] T.S. Mathis, N. Kurra, X. Wang, D. Pinto, P. Simon, Y. Gogotsi, energy storage data reporting in perspective-guidelines for interpreting the performance of electrochemical energy storage systems, *Advanced Energy Materials* 9 (2019), 1902007.
- [42] X. Feng, G. Huang, J. Qiu, L. Peng, K. Luo, D. Liu, P. Han, Dynamic light scattering in flowing dispersion, *Optics Communications* 531 (2023), 129225.
- [43] ISO 22412:2017 - Particle size analysis— Dynamic light scattering (DLS), 2nd ed. 2017 .
- [44] J.Y. Kim, J.J. Sansalone, Zeta potential of clay-size particles in urban rainfall–runoff during hydrologic transport, *Journal of Hydrology* 356 (2008), 163–173.
- [45] K. Furusawa, K. Uchiyama, Collaborative studies of zeta-potential measurements and electrophoretic measurements using reference sample, *Colloids Surfaces A: Physicochemical and Engineering Aspects* 140 (1998), 217–226.
- [46] M. von Smoluchowski, E. E. und Strömungsströme, Handbuch der Elektrizität und des Magnetismus, Band II, Leipzig (1921), 366–428.

4. MATERIALES Y MÉTODOS

4 Materiales y métodos

4.1 Obtención de grafeno poroso

4.1.1 Obtención de grafeno altamente oxidado mediante intercalación y exfoliación anódica de grafito

El grafito altamente oxidado se obtuvo mediante un tratamiento anódico de una lámina de grafito (graphite foil) en una configuración de dos electrodos, mediante un proceso de dos pasos que se basa en: (1) intercalación del ánodo de grafito con ácido sulfúrico (H_2SO_4) altamente concentrado y (2) deslaminación y oxidación simultáneas de la lámina de grafito expandida en una disolución diluida de ácido sulfúrico. Para ello, inicialmente se introdujo una lámina de grafito (Papyex 1980, Mersen de dimensiones laterales $50 \times 25 \text{ mm}^2$) como electrodo de trabajo (ánodo) y una lámina de platino como contraelectrodo (cátodo) en 80 mL de ácido sulfúrico 98 % en peso enfrentados en disposición paralela con una separación de 2 cm entre ambos. Posteriormente se aplicó una diferencia de potencial de 3 V entre ambos electrodos, con el grafito a voltaje positivo respecto al platino, durante 20 minutos con una fuente de alimentación (E3633A, Keysight Technologies) (Figura 30). Durante esta etapa, se observó que la lámina de grafito (ánodo) adquiría un tono azulado y se hinchaba en pequeña medida, lo que indicó una intercalación del material por aniones del electrolito (SO_4^{2-}).

En un segundo paso, el electrolito de ácido sulfúrico concentrado fue sustituido por una disolución de ácido sulfúrico 50 % en peso ($\approx 7.1 \text{ M}$) y se aplicó de nuevo un voltaje positivo de 3 V al electrodo previamente intercalado durante otros 20 minutos. Este tratamiento condujo a una expansión rápida y vigorosa de la pieza de grafito intercalado, con el desprendimiento de algunas partículas

Materiales y métodos

expandidas del ánodo que se acumularon en la superficie del electrolito. Tras finalizar esta etapa, se recogió el material expandido (tanto los fragmentos sueltos como la pieza completamente expandida, a excepción de la parte emergida del electrolito), que se lavó con abundante agua en filtro de celulosa y finalmente se secó a vacío durante 18 horas a temperatura ambiente. El producto resultante fue denominado EOG (*electrochemically oxidized graphene*) y se almacenó en un desecador.

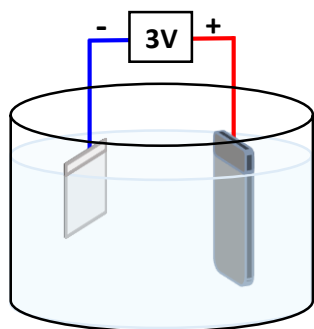


Figura 30. Esquema general de una celda electroquímica para la preparación de grafeno altamente oxidado

4.1.2 Obtención de grafeno oxidado mediante reducción parcial de óxido de grafeno (GO).

Para obtener un grafeno con un grado de oxidación similar al del grafeno anódico obtenido en la sección 4.1.1, partiendo para ello de un GO estándar obtenido por el método de Hummers, este último fue sometido a una reducción hidrotérmica suave en medio básico. Para ello, se preparó una dispersión estable de GO mediante sonicación de óxido de grafito en polvo durante 3 horas en agua milli-Q. A dispersiones del GO con una concentración de 1 mg mL^{-1} se añadió amoniaco ($2 \mu\text{L}$ de una disolución de amoniaco al 25 % por cada mililitro de dispersión), que fue calentada a 95°C durante 5 horas. El material resultante se lavó mediante ciclos

de centrifugación (2000 g, 10 minutos) hasta que el sobrenadante presentó un pH de 5-6. Posteriormente, el sólido decantado se secó mediante liofilización (equipo Cryodos, de Telstar).

La concentración de GO en dispersión se determinó mediante espectroscopía UV-Vis usando la ley de Lambert-Beer [ecuación (3) en sección 3], usando para ello un coeficiente de extinción de $40.082 \text{ mL mg}^{-1} \text{ cm}^{-1}$ a una longitud de onda de medida de 231 nm.

4.1.3 Obtención de grafeno poroso mediante ataque oxidativo en medio líquido

Para obtener grafeno poroso, los grafenos oxidados obtenidos de la exfoliación anódica y mediante reducción de GO se sometieron a tratamiento químico con peróxido de hidrógeno a temperatura moderada. El proceso típico consistió en introducir 36 mg de grafeno oxidado en un recipiente de teflón de 40 mL de volumen junto con 36 mL de una disolución de peróxido de hidrógeno al 0.92 % en peso (1 mL de una disolución de H_2O_2 al 30 % en peso en 35 mL de agua). Posteriormente, el recipiente de teflón se introdujo en un autoclave de tapa roscada de acero inoxidable, que se calentó a 100 °C durante 10 horas con una rampa de calentamiento de 1°C min^{-1} en un horno (Thermolyne de ThermoScientific). El producto obtenido se lavó con abundante agua en filtro de celulosa y se secó a vacío durante 12 horas a temperatura ambiente.

Con el fin de obtener materiales con distintos desarrollos de porosidad, la metodología anterior se aplicó al grafeno anódico usando cantidades de peróxido de hidrógeno: 0.18, 0.37, 0.55, 1.84 y 4.55 % en peso, lo que equivale a 0.2, 0.4, 0.6, 2 y 5 mL de peróxido de hidrógeno al 30 % en peso en 35.8, 35.6, 35.4, 34 y 31 mL de agua, respectivamente.

4.1.4 Obtención de grafeno poroso mediante ataque oxidativo en aire

El grafeno oxidado obtenido mediante exfoliación anódica se sometió a un tratamiento térmico en atmósfera de aire para generar también porosidad. El proceso consistió en tratar 10 mg del grafeno sobre en una naveccilla de cuarzo en un horno (Thermolyne, de ThermoScientific) precalentado previamente a la temperatura deseada. El tiempo de permanencia en el horno a la temperatura objetivo fue de 30 minutos. Las temperaturas investigadas fueron 400, 450, 500, 550 y 600 °C.

4.2 Obtención de grafenos químicamente modulables mediante exfoliación anódica

Los grafenos anódicos de química modular se obtuvieron mediante exfoliación de barra de grafito. Para ello, dos barras de grafito de 5 cm de longitud se introdujeron verticalmente (80 % de longitud) en 80 mL de una disolución acuosa de NaOH, NaCl y Na₂SO₄ en concentraciones variables, con una distancia de separación entre ambas barras de ~2 cm, que se conectan mediante dos pinzas tipo cocodrilo a una fuente de corriente (E3633A, de Keysight Technologies) (Figura 31). Al aplicarse una diferencia de potencial de 10 V entre las barras, se observó el desprendimiento de fragmentos de pequeño tamaño del ánodo, que quedaron suspendidos en el electrolito. Tras una hora de tratamiento, se recuperó el material suspendido mediante filtración a través de filtro de celulosa. El material retenido se lavó con 1 L de agua, hasta un pH 6-7. Para preparar dispersiones coloidalmente estables del material, este se sonicó en agua durante 3 horas en baño de ultrasonidos.

Finalmente, para obtener láminas suspendidas individuales, se centrifugó la dispersión a 200 g durante 20 min, reteniéndose el sobrenadante.

La concentración del grafeno en dispersión se determinó mediante espectroscopia UV-Vis usando la ley de Lambert-Beer, con un coeficiente de extinción a 267 nm de $64.84 \text{ mL mg}^{-1} \text{ cm}^{-1}$.

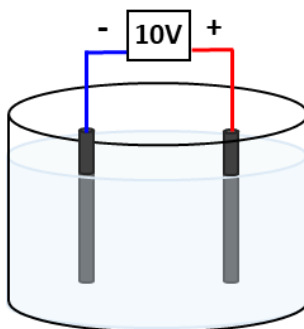


Figura 31. Esquema representativo de una celda electroquímica para la preparación de grafeno anódico de química modular.

4.3 Obtención de diseleniuro de niobio (NbSe_2) exfoliado.

La obtención de NbSe_2 exfoliado se llevó a cabo mediante un proceso catódico en electrolito acuoso. Para ello, inicialmente se prensaron 100 mg de NbSe_2 en polvo sobre un disco de grafito flexible (Papyex I980, Mersen) de 10 mm de diámetro y 0.5 mm de grosor con una fuerza de 5 toneladas durante 1 minuto. El electrodo resultante y una lámina de platino ($25 \times 25 \times 0.025 \text{ mm}^3$) se sumergieron, en disposición paralela, en 25 mL de una disolución de KNO_3 0.3 M a una distancia de ~2 cm entre ambos, y se conectaron a una fuente de corriente mediante unas pinzas tipo cocodrilo (Figura 32).

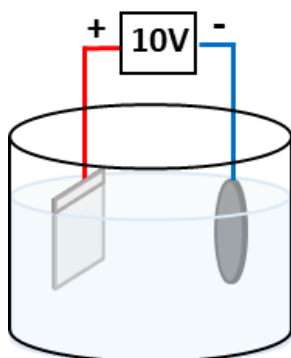


Figura 32. Esquema representativo de una celda electroquímica para la obtención de dicalcogenuros de metales de transición.

Al aplicarse un voltaje negativo sobre el NbSe_2 (-10 V), se observó la formación de un sólido en suspensión marrón-rojizo. A su vez, se desprendieron partículas grises de NbSe_2 de gran tamaño que precipitaban en el fondo del electrolito. Después de 1-2 minutos de tratamiento, la intensidad de corriente medida disminuyó drásticamente, indicando la terminación del proceso. Seguidamente, se retiró el sobrenadante con el sólido rojizo en suspensión, procediendo a su lavado con agua mediante decantación del material, bien dejándolo reposar durante 12 horas, bien mediante centrifugación en viales de vidrio de 10 mL a 100 g durante 10 minutos, repitiendo el proceso 3 veces. La centrifugación se realizó introduciendo los viales de vidrio dentro de tubos de polipropileno de 50 mL, ya que el material exfoliado se adhería fuertemente a la superficie del polímero del tubo. En ambos casos, el material en proceso de lavado se resuspendía a con unos segundos de tratamiento con un agitador de vórtice. Finalmente, el material exfoliado se sedimentó, se retiró el sobrenadante y se secó a vacío durante 12 horas a temperatura ambiente. Las dispersiones de este material para su posterior estudio, se prepararon a partir del sólido seco en el disolvente deseado (isopropanol o agua), sonicando durante 1-2 minutos.

4.4 Preparación de electrodos para caracterización electroquímica

4.4.1 Electrodos de grafeno poroso

La preparación de los electrodos de trabajo para su caracterización electroquímica se llevó a cabo con grafeno poroso obtenido por los tratamientos térmicos y químicos descritos anteriormente (sección 4.1), sin tratamientos posteriores.

Para las medidas a tres electrodos, los electrodos de trabajo se prepararon prensando unos 0.78 mg del grafeno con una fuerza de una tonelada durante 1 minuto sobre un disco de grafito flexible (Papyex I980, Mersen) de 10 mm de diámetro (0.78 cm^2), obteniéndose un electrodo con una carga de material activo de $\sim 1 \text{ mg cm}^{-2}$. Como contraelectrodo se utilizaron 7 mg de una mezcla en forma de pasta de negro de carbono como aditivo conductor (Cabot), carbón activado comercial como material activo (YP50F) y politetrafluoroetileno (PTFE) como aglomerante, en una relación mísica de 90:5:5 (carbón activado: negro de carbono: PTFE). Los electrodos se montaron en una celda tipo Swagelok centrados cara a cara, separados por una membrana de nylon (0.45 μm de tamaño de poro, de Whatman), con barras de grafito como colectores de corriente conectados al potenciómetro (Biologic VSP). Como electrodo de referencia, se utilizó un electrodo de Hg/HgO (1 M NaOH) y como electrolito se usó KOH 6 M.

Las medidas a dos electrodos se llevaron a cabo en una celda de configuración simétrica, donde ambos electrodos se prepararon por prensado del grafeno seco sobre disco de grafito flexible, tal y como se indicó en el párrafo anterior. Los electrodos se montaron en una celda tipo Swagelok (Figura 33) centrados cara a cara, separados por una membrana de nylon (0.4 μm de tamaño de

Materiales y métodos

poro, utilizando barras de grafito como colectores de corriente). Como electrolito se usaron KOH 6 M, y NaClO₄ 14 M.

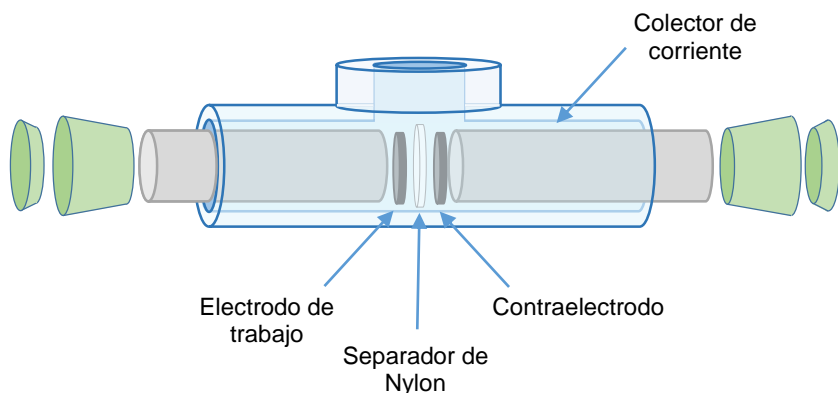


Figura 33. Esquema de una celda Swagelok.

4.4.2 Electrodos de grafeno anódico de química modular

El estudio electroquímico de los grafenos anódicos como cátodo en condensadores híbridos de ion zinc acuoso se llevó a cabo en una celda tipo Swagelok en configuración de dos electrodos, donde el cátodo se preparó en forma de película delegada sobre papel de carbono. Para ello, se preparó una dispersión de grafeno a una concentración entre 1 y 2 mg mL⁻¹ sonicando durante tres horas el producto obtenido de la exfoliación electroquímica. Seguidamente, la dispersión se depositó por goteo (200 µL) sobre una pieza de papel de carbono de 10 mm de diámetro y masa conocida, se dejó secar a 50-60 °C y se determinó por diferencia de pesada la masa del electrodo hasta obtener (0.8-0.9 mg, aproximadamente). Como ánodo se utilizó una lámina de zinc metálico troquelada a discos de 10 mm de diámetro que fueron pulidos hasta un acabado tipo espejo con tres lijas de diferente grano (P1200, P2500 y P4000).

Ambos electrodos se sumergen 24 horas en el electrolito (ZnSO_4 2 M) previamente al ensamblaje de la celda. Para el ensamblaje de la celda tipo Swagelok, los electrodos de colocan en disposición paralela enfrentados cara a cara y separados por un separador poroso de Nylon (13 mm de diámetro), se utilizan como colectores de corriente dos barras de acero inoxidable, como electrolito una disolución acuosa comercial de ZnSO_4 2 M (10 mL aproximadamente) y como electrodo de referencia el propio zinc metálico.

El estudio de grafenos anódicos como revestimiento protector para el electrodo de zinc metálico se realizará en una celda simétrica tipo Swagelok con dos electrodos de Zn recubiertos con una película delgada de grafeno anódico obtenida por deposición controlada. Para ello, una dispersión estable del material grafénico de concentración 1 mg mL⁻¹ preparada por sonicación se deposita por goteo (2 gotas, 400 μL) sobre un disco de Zinc de 10 mm de diámetro pulido a espejo. Ambos electrodos se separan por un disco de nilón de 13 mm de diámetro y se utiliza una disolución de ZnSO_4 2 M como electrolito.

4.4.3 Electrodos de NbSe_2 exfoliado

Los materiales de NbSe_2 delaminados catódicamente se estudiaron como electrodos para almacenamiento de litio en una celda tipo pila de botón (Figura 34). Para ello, el electrodo de trabajo se preparó mezclando 54 % en peso del material activo (NbSe_2), 16 % en peso de nanotubos de carbono (CNT, *carbon nanotubes*), y 20 % en peso de Super C65 (negro de carbono) como aditivos conductores, así como 10 % de PVDF como aglomerante, en una pequeña cantidad de NMP con un mezclador de cizalla hasta obtener una suspensión homogénea densa. La suspensión generada se extendió sobre una lámina de cobre metálico (24 cm^2) y se secó a 120 °C durante 3 horas. Una vez seco el depósito, se troquelaron discos circulares de 10

Materiales y métodos

mm de diámetro, en los que la carga total de la mezcla (NbSe_2 , CNTs, Super C65 y PVDF) fue de $0.65 \pm 0.03 \text{ mg cm}^{-2}$. La lámina de cobre recubierta se colocó en disposición paralela a un disco de litio (electrodo de referencia y contraelectrodo), estando separados por dos separadores de fibra de vidrio. Como electrolito se utilizó el LP30 (LiPF_6 1 M en carbonato de etileno/carbonato de dimetilo).



Figura 34. Esquema de una pila de botón.

5. RESÚMENES Y ARTÍCULOS

5. Resúmenes y artículos

5.1 Obtención de grafeno mediante exfoliación electroquímica anódica

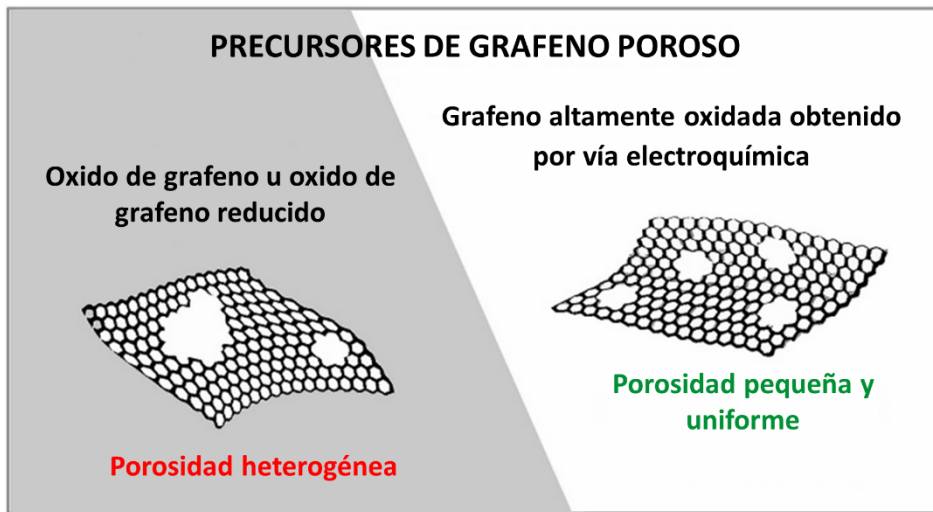
Artículo I

An electrochemical route to holey graphene nanosheets for charge storage applications, Daniel Fernández Carrasco, Juan Ignacio Paredes, Silvia Villar-Rodil, Fabián Suárez-García, Amelia Martínez-Alonso, Juan Manuel Diez Tascón, *Carbon* 195 (2022), 57-68.

Artículo II

Chemically tuning graphene via anodic exfoliation for enhanced performance in aqueous zinc-based electrochemical energy storage applications, Daniel Fernández Carrasco, Enrique Álvarez Rubiera, Silvia Villar Rodil, Alberto Martinez Jódar Juan Manuel Diez Tascón, Fabián Suárez García, Juan Ignacio Paredes, *Carbon* 228 (2024), 119293.

Resumen artículo I



Entre las aplicaciones anteriormente citadas para el grafeno y sus derivados, está su uso como electrodo en dispositivos de almacenamiento electroquímico de energía (baterías, supercondensadores). Sin embargo, a pesar de que las prestaciones de los grafenos en tales usos son muy prometedoras, en la práctica surgen dificultades derivadas en gran medida del ensamblaje de los electrodos. Por ejemplo, el reapilamiento de las láminas puede reducir considerablemente la fracción de material accesible al electrolito, lo que se traduce en una disminución significativa de su capacidad de almacenamiento de carga. Con el fin de subsanar esta limitación, se han desarrollado diferentes estrategias que reducen el grado de apilamiento o sus efectos, entre las que cabe destacar la generación de porosidad de dimensiones nanométricas en las láminas de grafeno. Estos poros pueden facilitar la movilidad iónica en la dirección perpendicular a la lámina sin comprometer excesivamente su conductividad eléctrica.

Tradicionalmente, la síntesis de grafeno poroso hace uso de óxido de grafito convencional (por ejemplo, el preparado por el método de Hummers) como

precursor. Sin embargo, las características estructurales del óxido de grafeno convencional no tienen por qué ser las óptimas para este fin. Por ello, en el trabajo presentado en el **Artículo I** se plantea por primera vez la utilización de grafeno altamente oxidado preparado por exfoliación electroquímica anódica como alternativa al óxido de grafeno convencional. El primero presenta a priori ciertas ventajas respecto al segundo, como son el distinto tamaño de los dominios electrónicamente conjugados y oxidados, su menor coste de preparación, el uso de reactivos menos agresivos con el medio ambiente o un tiempo de síntesis reducido.

En este trabajo se llevó a cabo la síntesis de grafeno altamente oxidado mediante exfoliación anódica en un proceso que consta de dos etapas, una de intercalación en ácido sulfúrico concentrado y otra de exfoliación en ácido sulfúrico más diluido. Una vez obtenido este material (denominado EOG), se comparó con un óxido de grafeno convencional sometido a un ligero tratamiento de reducción por vía hidrotérmica (denominado MRGO), con el fin de obtener dos materiales de partida con el mismo grado de oxidación, pero estructuralmente diferentes.

Como se pudo constatar mediante análisis elemental, EOG y MRGO presentaban grados de oxidación muy similares. Sin embargo, rasgos específicos observados en sus espectros de absorbancia UV-vis sugirieron tamaños de dominios electrónicamente conjugados diferentes (mayores y/o más conectados para EOG). Los resultados obtenidos por XPS y espectroscopía Raman confirmaron que el grafeno anódico presentaba dominios conjugados más extensos y abundantes que su homólogo MRGO, lo que se tradujo en propiedades macroscópicas diferentes, tales como una mayor conductividad eléctrica de EOG (50 frente a 0.09 mS cm^{-1} de MRGO).

La hipótesis de que grafenos con un nivel de oxidación similar, pero estructuralmente diferentes en cuanto a las dimensiones de sus dominios conjugados y oxidados, darían lugar a grafenos con diferente desarrollo de

Resumen Artículo I

porosidad se confirmó cuando EOG y MRGO se sometieron a procesos de oxidación con peróxido de hidrógeno. Mediante TEM se pudo observar que el tamaño de los poros era claramente diferente entre ambos materiales: poros más pequeños y de tamaños más similares entre sí para el grafeno anódico (EOG-H) y de mayores dimensiones, pero con una distribución mucho más ancha de tamaños para el derivado de óxido de grafeno (MROG-H). En ambos casos, se dedujo mediante caracterización fisicoquímica que la estructura conjugada de partida se mantuvo esencialmente inalterada y sólo los dominios fuertemente oxidados, mucho más reactivos, fueron eliminados por el tratamiento oxidativo con peróxido de hidrógeno. Se observó también un aumento de la superficie específica del material poroso respecto al material de partida, en base a medidas de fisisorción de nitrógeno.

La mayor superficie activa, la estructura conjugada inalterada y la generación de porosidad sugiere que los grafenos porosos deberán tener un mejor desempeño como electrodos en supercondensadores. Dicho comportamiento se estudió para ambos materiales porosos (EOG-H y MRGO-H) y para sus respectivos precursores (EOG y MRGO) en una celda tipo Swagelok utilizando como electrolito KOH 6M. Se obtuvieron mayores densidades de corriente gravimétricas en las ciclovoltamperometrías para los grafenos porosos frente a sus precursores, corroborando así que la generación de poros favorece el almacenamiento de energía. Esta conclusión se apoyó también en resultados de espectroscopía de impedancia electroquímica, técnica mediante la que se pudo observar una menor resistencia a la difusión del electrolito además de una menor resistencia interna para los grafenos porosos.

Por otro lado, el grafeno poroso obtenido a partir de grafeno anódico (EOG-H) mostró una ventana de potencial de trabajo algo más ancha que la obtenida con el grafeno MRGO-H. Esto se atribuyó a la mayor calidad estructural del primero

(menor concentración de defectos estructurales como bordes internos, vacantes, etc), lo que se tradujo en una menor actividad como catalizador de la descomposición de moléculas de agua del electrolito y por tanto una ventana de potencial efectiva más ancha.

En conclusión, el grafeno oxidado obtenido mediante exfoliación electroquímica anódica constituye una alternativa viable y atractiva a las metodologías convencionales de obtención de óxido de grafeno para distintos usos, no solo por su mayor calidad estructural, sino también por su simplicidad de preparación. Este enfoque puede permitir un control preciso sobre el grado de oxidación del grafeno y, por consiguiente, sobre la homogeneidad y tamaño de los poros generados, lo que ofrece ventajas significativas en su uso como electrodo en almacenamiento electroquímico de energía, o como precursor en la preparación de diversos materiales que tradicionalmente se han obtenido a partir de óxidos de grafeno convencionales

ARTÍCULO I

An electrochemical route to holey graphene nanosheets for charge storage applications

D.F. Carrasco, J.I. Paredes*, S. Villar-Rodil*, F. Suárez-García, A. Martínez-Alonso, J.M.D. Tascón

*Instituto de Ciencia y Tecnología del Carbono, INCAR-CSIC,
C/Francisco Pintado Fe 26, 33011 Oviedo, Spain*

*Corresponding authors.

E-mail address: paredes@incar.csic.es (J. I. Paredes),

E-mail address: silvia@incar.csic.es (S. Villar-Rodil).

Abstract

Holey graphene nanosheets are potentially useful in several relevant technological applications, including electrochemical energy storage and molecular separation. Access to this material is mostly accomplished by resorting to standard graphene oxides obtained by common routes (e.g., the Hummers method). However, such a type of highly oxidized graphenes may not be the best option as a precursor to holey graphene on account of their chemical/structural heterogeneity and harsh synthesis conditions. Here, we report the use of highly oxidized graphene nanosheets derived by an electrochemical exfoliation/oxidation strategy as an alternative precursor to holey graphene. Compared to a standard graphene oxide with the same extent of oxidation, the electrochemically derived precursor exhibited larger aromatic domains, which provided a structural basis for its higher electrical conductivity, as well as smaller and denser oxidized regions, associated to a higher chemical homogeneity and lability of its oxygen-containing functional groups. Through selective chemical etching of the oxidized domains, the latter feature was exploited to afford holey graphene nanosheets having smaller and more uniform holes. When used as an electrode material for electrochemical charge storage, the electrochemically derived holey graphene outperformed its standard graphene oxide-based counterpart in terms of capacity and energy density. Overall, boasting distinct structural and chemical characteristics, highly oxidized graphene obtained by electrochemical means can be regarded as a prospective advantageous precursor to many graphene-based materials whose preparation has traditionally relied on the processing of graphene oxides.

Keywords: holey graphene, anodic exfoliation, capacitive energy storage

1. Introduction

The advent of graphene and its derivatives, more than a decade ago, as experimentally available two-dimensional (2D) materials has fueled intensive research efforts worldwide aimed at exploiting their many appealing characteristics in a variety of technological applications [1,2]. One such application realm is that of electrochemical energy storage, where different types of graphenes can be used either as the active material or in a supporting role (e.g., as a conductive additive) for electrodes of supercapacitors and batteries [3-7]. The main rationale for the attraction of graphene in electrochemical energy storage lies in a number of relevant features that this 2D carbon material exhibits, including high electrical conductivity, chemical and mechanical stability, and large specific surface area [3,5]. However, these attributes are mostly associated to stand-alone graphene nanosheets (NSs) in pristine form, but in practice they tend to be degraded to some extent during the fabrication and/or processing of the 2D material. Particularly, the reduction of accessible surface area due to NS re-stacking is a serious issue that can readily occur when initially well-exfoliated graphenes are processed into electrodes. Such a re-stacking inevitably leads to a much impeded transport of ions within the electrode and, therefore, to a poor charge storage performance of the latter [3,8].

Over the years, different strategies have been devised to directly prevent nanosheet re-stacking or to counteract its negative consequences in graphene electrodes. These strategies mostly rely on the generation of some kind of porosity in the electrodes, which can be categorized as interlayer and in-plane porosity [8-10]. The former involves the creation of micrometer- to nanometer-sized voids between neighboring graphene NSs, for example, through their assembly into aerogels. In-plane porosity, on the other hand, relates to the presence of nanometer-sized holes within the NSs, which can be produced by either physical or chemical means and give rise to what is usually referred to as holey graphene [11-14]. Even

with substantial nanosheet re-stacking, mass/ion transport through an electrode made up of holey graphene can still be allowed to a substantial extent by the presence of in-plane porosity [12,15].

Many of the approaches developed so far to access holey graphene in considerable quantities make use of graphene oxide as the starting material [11,14]. As both experimental observation [16,17] and theoretical modeling [18] have revealed, from a structural point of view graphene oxide is a patchwork of heavily oxidized graphene domains a few to several nanometers in size interspersed with essentially pristine domains. Due to their much higher chemical reactivity and structural instability, the oxidized domains can be selectively etched away by means of, e.g., oxidative and/or heat treatments, thus leaving behind holes encircled by the largely unreactive, pristine graphene domains of the NSs. Nonetheless, while standard graphene oxide, i.e., that obtained from the oxidation of graphite by the Hummers or Brodie methods, is widely used as a precursor to holey graphene, such a type of oxidized graphene may not be the best option as a starting material, and instead other oxidation routes could potentially offer some advantages for this purpose. For example, the oxidized and pristine domains of standard graphene oxide tend to be very small (typically 1-3 nm) [16]. As a result, the percolated carbon network in the corresponding holey NSs could be dominated by narrow graphene constrictions, which act as a barrier to the flow of electrical charge and thus could impair the overall electrical conductivity of the material. Furthermore, graphene oxides prepared by the Hummers and Brodie methods require the use of harsh acids and oxidants, making such methods unattractive from an environmental and practical standpoint. It is thus clear that resorting to highly oxidized graphene NSs obtained by proper alternative routes (i.e., routes other than those typical of standard graphene oxide) as a precursor to holey graphene could positively impact the use of the latter as an electrode material and also in other applications. However, to the best of our knowledge this issue has not yet been addressed.

As a prospective replacement for standard graphene oxide, we have turned our attention to oxidized graphene obtained by electrochemical exfoliation of graphite, particularly aqueous anodic exfoliation. The electrolytic route to graphene has been shown to be fast, easy to implement, efficient, potentially scalable at low cost [19,20], as well as versatile enough to afford NSs with controllable degrees of oxidation [21,22], including highly oxidized NSs that could be suitable as a precursor to holey graphene [23-25]. Because the oxidizing conditions are generated by the application of an anodic potential in aqueous electrolyte that obviates the need of strong chemical oxidants, the preparation of highly oxidized graphene by electrochemical exfoliation can be regarded as more environmentally friendly than the traditional routes based on chemical oxidation [25]. Moreover, some experimental evidence suggests the electrical conductivity and overall structural quality of electrochemically derived, oxidized graphene NSs to be higher than those of their (reduced) standard graphene oxide counterparts of similar oxidation degree [26-28], thus hinting at the idea that the former possess larger pristine graphene domains.

Here, oxidized anodic graphene is used for the first time as precursor of holey graphene and proved to be an advantageous alternative to standard graphene oxide in such role. Moreover, when used as an electrode material for supercapacitors, the holey NSs prepared from anodic graphene are shown to possess improved performance compared to that of their counterpart stemming from traditional graphene oxide, which can be put down to the superior electrical and structural characteristics of the former. Overall, the present work introduces a new-generation holey graphene as an advantageous electrode material that could be used in a variety of electrochemical energy storage applications, e.g., either as the active material or as a support for the active material in different types of supercapacitor and battery devices.

2. Experimental section

2.1. Materials and reagents

High purity graphite foil with a thickness of 0.5 mm (Papyex I980) was purchased from Mersen. Highly concentrated sulfuric acid (H_2SO_4 , 95-97 wt%), hydrogen peroxide (H_2O_2 , 30 wt% solution), potassium hydroxide (KOH, powder form) and platinum foil (dimensions: $25 \times 25 \times 0.025$ mm³) were obtained from Sigma-Aldrich and used as received. Ultrapure deionized water (resistivity: 18.2 MΩ·cm; Milli-Q Reference water purification system, from Millipore Corporation) was used throughout the experiments.

2.2. Preparation of highly oxidized graphene by anodic intercalation and exfoliation of graphite

Highly oxidized graphene was obtained by anodic treatment of graphite foil in a two-electrode set-up via a two-step process previously described elsewhere [25] that comprised (1) intercalation of the graphite anode in highly concentrated sulfuric acid and (2) delamination and oxidation of the intercalated anode in a more diluted solution of the same acid as the electrolyte. To this end, a piece of graphite foil (lateral dimensions: 25×50 mm², with (only 25×40 mm² immersed in the electrolytic medium) as the working electrode (anode) and platinum foil as the counter electrode were first immersed in 80 mL of concentrated sulfuric acid in a face-to-face configuration at a distance of ~2 cm from each other, and then a bias voltage of +3 V was applied to the graphite electrode for 20 min by means of a power supply (E3633A apparatus, from Keysight Technologies). During this stage, the graphite foil anode was seen to acquire a bluish tone and swell to a small extent, which was indicative of its extensive intercalation by sulfate anions. Subsequently, the electrolytic medium of the cell was changed to 50 wt% (≈ 7.1 M) sulfuric acid

solution and a bias voltage of +3 V was applied to the intercalated electrode for another 20 min. Such a treatment led to a fast and very pronounced expansion of the graphite foil piece, with some small expanded fragments even detaching from the anode and building up on the surface of the electrolytic solution. Upon completion of this step, the expanded material (both the detached fragments and the expanded fraction remaining on the anode) was collected, extensively washed with water and finally dried under a vacuum overnight at room temperature. The resulting dried product was then stored for further use and is henceforth denoted as EOG.

2.3. Preparation of holey graphene by treatment of electrochemically derived, highly oxidized graphene

To obtain holey graphene, the highly oxidized graphene product derived from the electrochemical process was subjected to chemical treatment with hydrogen peroxide at a moderate temperature. In a typical standard procedure, 36 mg of highly oxidized graphene were added to 36 mL of an aqueous 0.92 wt% hydrogen peroxide solution (i.e., 1 mL of 30 wt% H₂O₂ solution mixed with 35 mL of deionized water) in a Teflon-lined autoclave, which was heated at 100 °C for 10 h (heating ramp of 1 °C min⁻¹). The hydrogen peroxide-treated product was then collected, washed with water and dried under a vacuum overnight at room temperature. This material is henceforth designated as EOG-H. For comparison purposes, samples were also prepared by treating the highly oxidized graphene material with hydrogen peroxide solutions of different concentrations, namely, 0.18, 0.37, 0.55, 1.84 and 4.55 wt%, which amounted to adding 0.2, 0.4, 0.6, 2 and 5 mL of 30 wt% H₂O₂ solution to 35.8, 35.6, 35.4, 34 and 31 mL of deionized water, respectively (the density of 30 wt% H₂O₂ solution was taken as 1.11 g mL⁻¹). Also for comparison, the highly oxidized graphene material was subjected to thermal

treatment under air atmosphere. To this end, 10 mg of the oxidized graphene were placed on a ceramic boat and introduced into a furnace (Thermolyne from ThermoScientific) that had been pre-heated to a given temperature. The dwelling time in the furnace was 30 min. Different heat treatment temperatures, namely, 400, 450, 500, 550 and 600 °C, were tested.

2.4. Characterization techniques

The morphological, structural, thermal and chemical characteristics of the materials were investigated by field emission scanning electron microscopy (FE-SEM), transmission electron microscopy (TEM), atomic force microscopy (AFM), Raman spectroscopy, elemental analysis, UV-Vis absorption spectroscopy, X-ray photoelectron spectroscopy (XPS), temperature-programmed desorption (TPD) and nitrogen physisorption. FE-SEM images were recorded with a Quanta FEG apparatus (FEI Company) operated at 25 kV. TEM measurements were carried out in a JEOL JEM 2100F microscope at an acceleration voltage of 200 kV, with specimens prepared by drop-casting 20 µL of a dispersion of the sample (0.01 mg mL⁻¹) in water or a water/ethanol mixture onto a copper grid (200 square mesh) covered with a lacey carbon film and allowing it to dry at room temperature. AFM imaging was performed in a Nanoscope IIIa Multimode system in the tapping mode of operation and using rectangular silicon cantilevers with resonance frequencies of 250-300 kHz and nominal spring constant of 40 N m⁻¹. Specimens for AFM were prepared by drop-casting small volumes (~20 µL) of an aqueous dispersion of the graphene sample (~0.01 mg mL⁻¹) onto freshly cleaved highly oriented pyrolytic graphite substrates that were pre-heated to 50-60 °C. Raman spectra were obtained with a Renishaw inVia Qontor instrument, using a green laser excitation line (532 nm) at an incident power below 0.5 mW. For elemental analysis, the measurement of carbon and hydrogen was done in a LECO CHN-2000 instrument, whereas

oxygen and sulfur were measured with a LECO Truspec Micro O accessory and a LECO S632 analyzer, respectively. Carbon, hydrogen and sulfur were determined, respectively, from the amount of CO₂, H₂O and SO₂ generated upon combustion of the sample, and oxygen was inferred from the amount of CO and CO₂ produced upon pyrolysis of the sample at high temperature. UV-vis absorption spectra of graphene dispersions were recorded with a double-beam Genesys 180 spectrophotometer (Thermo Fisher Scientific). XPS analysis was performed in a SPECS instrument, working at a pressure of 10⁻⁷ Pa with a monochromatic Al K_α X-ray source (14 kV, 175 W). TPD measurements were carried out with an Autochem II chemisorption analyzer (Micromeritics) under argon flow (50 mL min⁻¹) at a heating rate of 10 °C min⁻¹. A mass spectrometer (Omnistar apparatus, from Pfeiffer Vacuum) was used to measure the amount of H₂O, CO and CO₂ released from the sample during the heating cycle, by determining the intensity of the *m/z* = 18, 28 and 44 signals, respectively. The electrical conductivity of paper-like graphene films was also evaluated. To this end, graphene papers were first prepared by vacuum filtration of aqueous graphene suspensions (250 mL, ~0.1 mg mL⁻¹) through polycarbonate membrane filters (47 mm in diameter, 0.2 µm of pore size, from Whatman). Rectangular strips (0.5 cm in width and about 3 cm in length) were then cut from the papers and their electrical resistivity was measured at different fixed distances by means of a hand-held digital multimeter (Fluke 45). These data, together with the thickness of the graphene paper (estimated with a Mitutoyo digital micrometer), were used to calculate the electrical conductivity of the films. Nitrogen adsorption isotherms were recorded at -196 °C in an ASAP 2420 volumetric apparatus (Micromeritics), after degassing overnight the samples under vacuum at 110 °C. The specific surface areas (S_{BET}) were obtained from the adsorption branch of the nitrogen isotherms by the standard Brunauer-Emmett-Teller (BET) method in the relative pressure range from 0.06–0.30.

2.5. Electrochemical measurements

The electrochemically derived, holey graphene materials were tested as electrodes for electrochemical charge storage in three- and two-electrode cell configurations. The tests were carried out with a BioLogic VSP potentiostat in Swagelok-type cells, recording cyclic voltammograms at different potential scan rates and galvanostatic charge-discharge (GCD) profiles at different current densities, as well as electrochemical impedance spectroscopy (EIS) data. For the three-electrode cells, holey graphene and a commercial activated carbon (YP-50F, from Kuraray) were used as the active material for the working electrode and counter electrode, respectively, whereas Hg/HgO (1 M NaOH) was used as the reference electrode in aqueous 6 M KOH electrolyte. To prepare the working electrodes, an amount of holey graphene sample was placed on a circular piece of graphite foil at a typical mass loading of ~1 mg cm⁻² and pressed under 1 ton for a few seconds with a hydraulic press. The counter electrodes were obtained in the form of a paste by mixing the commercial activated carbon, carbon black (acquired from Cabot) as a conductive additive and polytetrafluoroethylene (PTFE; powder form, from Aldrich) as a binder in a mortar. The weight ratio of these components in the paste was 90:5:5 (activated carbon:carbon black:PTFE). For the two-electrode cells, a symmetric configuration was employed, whereby the abovementioned pressed holey graphene served as both the positive and negative electrode. In this case, in addition to the aqueous 6 M KOH electrolyte, a water-in-salt electrolyte, namely 14 m NaClO₄, was also tested. Two stacked pieces of nylon membrane filter (0.45 µm of pore size, from Whatman) were used as electrode separator in all cases. Gravimetric capacitance values were derived from the GCD profiles according to the following equation:

$$C = I \cdot \Delta t / m \cdot \Delta V \quad (1)$$

where C (F g^{-1}) is the gravimetric capacitance, I (A) is the current intensity, Δt (s) is the discharge time, m (g) is the mass of holey graphene in the electrode (only the mass of the working electrode for the three-electrode cell and the mass of the two symmetric electrodes for the two-electrode cell) and ΔV (V) is the potential window. Gravimetric energy (E) and power (P) densities were calculated for the two-electrode cells from the following equations:

$$E = C \cdot \Delta V^2 / 2 \quad (2)$$

$$P = E / \Delta t \quad (3)$$

Volumetric values of these parameters were also estimated by taking into account the density of holey graphene in the electrodes. To determine such a density, circular pellets (12 mm in diameter) were prepared by pressing a given amount of holey graphene sample under the same conditions as those used for electrode preparation (i.e., 1 ton for a few seconds in the hydraulic press). Then, from the known weight and dimensions of the pellet (the thickness was estimated with a digital multimeter), its density could be ascertained. Typical values were around 1.6 g cm^{-3} .

3. Results and discussion

3.1. Structural and chemical characteristics of the electrochemically derived, highly oxidized graphene

Our aim was to prepare holey graphene from an alternative precursor that offered advantages with respect to the typically used standard graphene oxide. As mentioned above, oxidized graphenes obtained by electrochemical exfoliation of graphite have been found to possess higher electrical conductivity and overall structural quality than those of their (reduced) standard graphene oxide counterparts of similar oxidation degree. This fact pointed to the presence of larger aromatic domains in the former material, which for a similar oxidation degree, would imply smaller, denser oxidized domains than in standard graphene oxide. As the starting point for this work, we hypothesized that selective etching of the oxidized domains in both types of materials would yield holey graphenes with distinct porosities. Specifically, holey graphene with smaller and more uniform porosity would be expected when using the structurally and chemically more homogeneous electrochemically-derived material as precursor. Fig. 1 illustrates the central idea of this work.

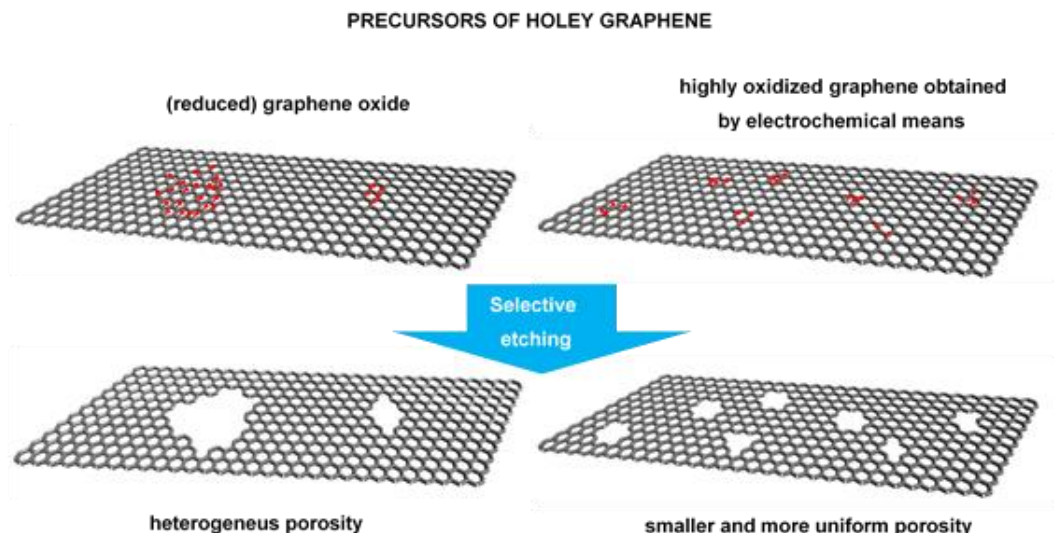


Figure 1. Schematic of the preparation of holey graphene from structurally/chemically different precursors.

Highly oxidized graphene was obtained from graphite foil by way of an electrolytic process carried out in two sequential steps, namely, (1) anodic intercalation of the graphite foil in highly concentrated sulfuric acid and (2) anodic delamination and oxidation of the intercalated graphite in a more diluted sulfuric acid solution (see Experimental section for details) [25]. After a washing and drying work-up procedure, this electrolytic treatment yielded a loose, fluffy powder as the primary product, which was made up of highly expanded and elongated particles, as noticed from field emission scanning electron microscopy (FE-SEM) imaging (Fig. 2a). Closer inspection of the particles (Fig. 2b) revealed them to be comprised of very thin, rippled/wrinkled sheets separated by micrometer- and submicrometer-sized voids. Such a morphology was very similar to that seen in efficient, single-step processes of anodic exfoliation of graphite to give graphene with aqueous electrolytes (e.g., sulfate-based salts), which do not include an anodic intercalation

<step in concentrated acid [29,30]. This indicated that a successful delamination was also attained in the present case, as will be shown below.

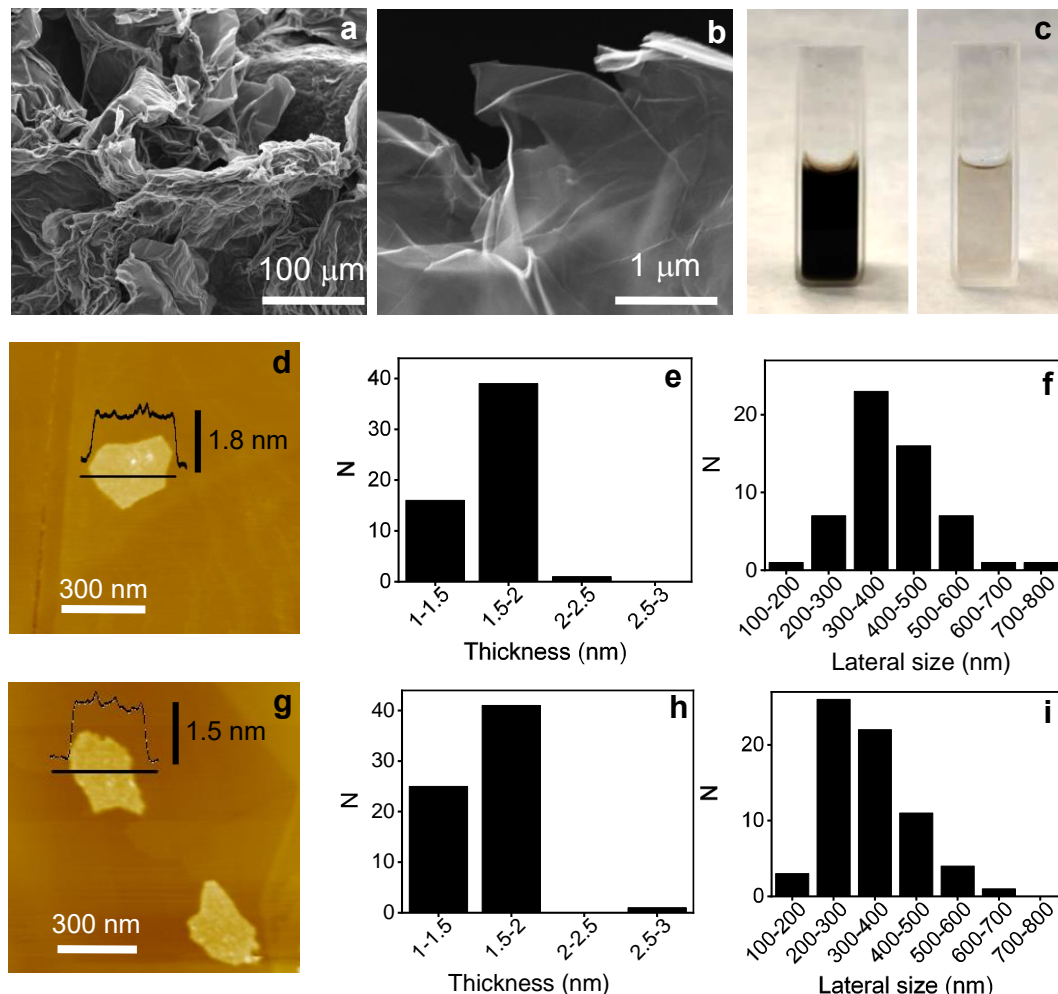


Figure 2. Microscopic characterization of different holey graphene precursors. (a-b) Representative field emission scanning electron microscopy (FE-SEM) images of the dry powder of electrochemically derived, highly oxidized graphene. **(c)** Digital pictures of the previous material in concentrated (left) and diluted (right) aqueous suspension upon ultrasonication. **(d)** Representative atomic force microscopy (AFM) image of a nanosheet of anodic graphene and histograms of **(e)** thickness and **(f)** lateral size. **(g)** AFM image and histograms of **(h)** thickness and **(i)** lateral size for mildly reduced graphene oxide. The histograms were measured on ~60 objects from the AFM images.

For single-step processes of anodic exfoliation, individual single/few-layer graphene NSs can be readily extracted from the primary product and colloidally dispersed in certain organic solvents and water/surfactant solutions with the aid of sonication or shear forces, but usually not in pure water [29,31,32]. The latter can be ascribed to the relatively limited extent of oxidation (typical O/C atomic ratios $\sim 0.10\text{--}0.20$), and thus limited hydrophilicity and ionizability, of the graphene product. On the other hand, stable colloidal suspensions of well-exfoliated NSs could be easily obtained in neat water, i.e., in the absence of any dispersant, from the product of the present two-step protocol. A digital picture of the suspension (both concentrated and diluted) and an atomic force microscopy (AFM) image of the corresponding NSs are shown in Fig. 2c and d, respectively, as well as thickness (Fig. 2e) and lateral size (Fig. 2f) histograms derived from the AFM images. The colloidal stability of the material in water strongly suggested that the present product was, as anticipated, substantially more oxidized than common anodic graphenes derived from single-step processes. Indeed, elemental analysis of our product yielded an O/C atomic ratio of ~ 0.31 [composition in at%: 65.1 (C), 13.0 (H), 20.2 (O), 0.1 (N) and 1.6 (S)], which was comparable to values typical of just slightly reduced graphene oxides obtained from standard protocols (e.g., Hummers method) [26,33,34]. To facilitate comparisons with the latter, more common type of highly oxidized graphenes, we prepared a Hummers-based mildly reduced graphene oxide (MRGO) having the same O/C ratio as that of the electrochemically derived oxidized graphene (referred to as EOG). The elemental composition of MRGO (in at%) was the following: 58.0 (C), 20.4 (H), 17.9 (O), 3.6 (N) and 0.1 (S). Details of the preparation of MRGO are given in the Electronic Supplementary Material (ESM), together with digital photographs of the corresponding aqueous suspension (both concentrated and diluted, Fig. S1). An AFM image of the MRGO NSs, together with thickness and lateral size histograms derived from the AFM images, are shown in Fig. 2g, h and i, respectively.

Fig. 3a shows the UV-Vis absorption spectrum of EOG (black trace), which featured a prominent peak centered at a wavelength of 256 nm in combination with decreasing but still strong absorbance at longer wavelengths up to 1000 nm. This absorption peak arises from $\pi\rightarrow\pi^*$ transitions in the aromatic, electronically conjugated domains of graphenic and other sp²-based carbon materials, and its position is known to red-shift with the size of the domains [35,36]. For example, it is located at ~230 nm in unreduced graphene oxides, which only possess extremely small (~1-3 nm) aromatic domains, but shifts to ~270 nm for well-reduced graphene oxides, which exhibit larger domains, as well as for pristine graphene (indefinitely large domains) [26,35,37]. Consistent with the substantial degree of oxidation of the present electrochemically derived graphene, the absorption peak of EOG lay in-between these two extremes at a similar position to that of MRGO (see Fig. 3a, orange trace). More significantly, a shoulder around 300 nm, which is assigned to $n\rightarrow\pi^*$ transitions of C=O bonds also appeared for EOG but was absent for MRGO. Thus, even though the overall oxidation level of EOG and MRGO was very much the same, the oxidized domains were more noticeable in the former graphene.

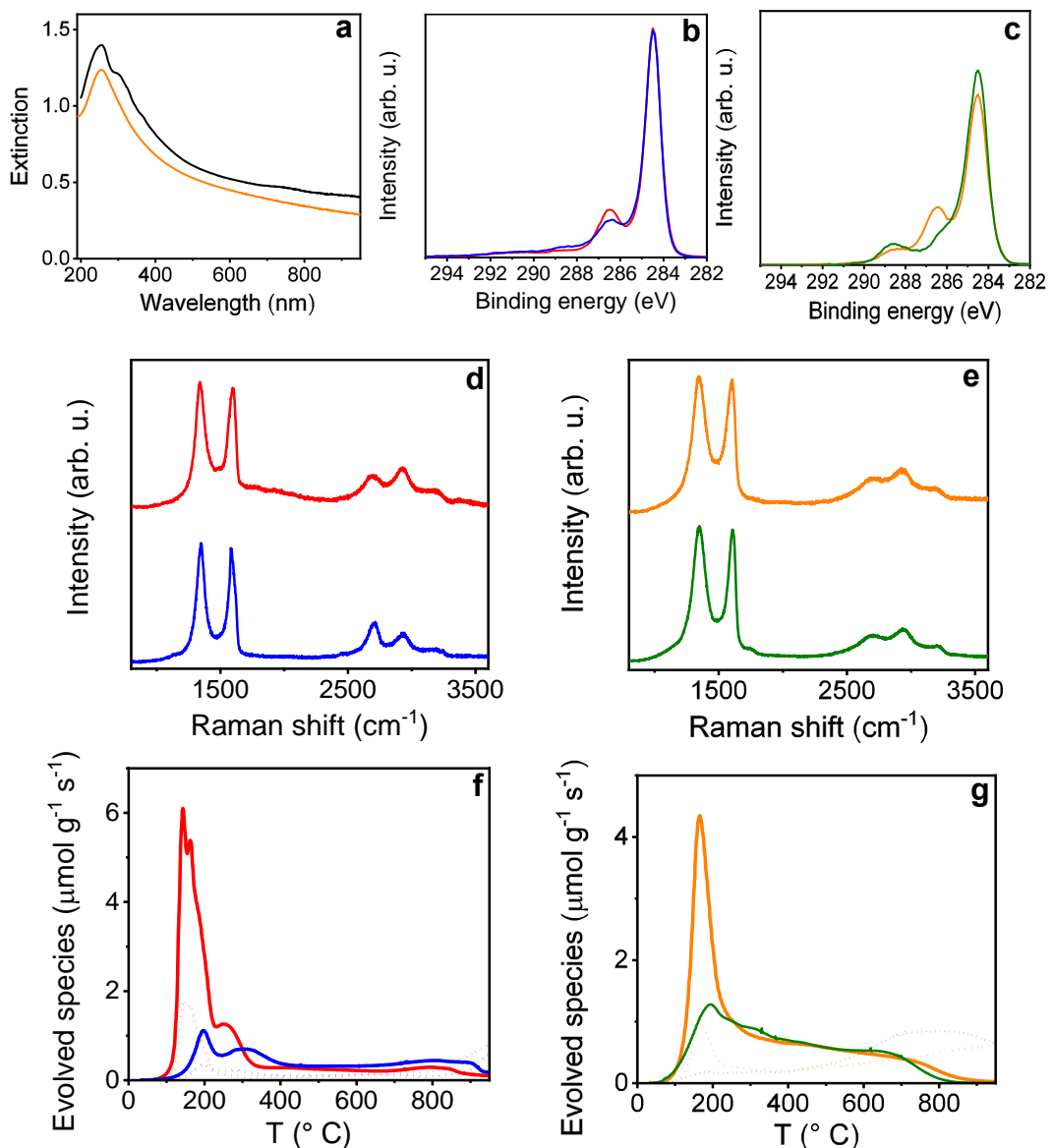


Figure 3. Spectroscopic characterization of different precursors and the holey graphenes derived from them. (a) UV-Vis absorption/extinction spectra of electrochemically derived, highly oxidized graphene (black trace) and mildly reduced graphene oxide (orange trace). High resolution C 1s XPS of (b) EOG (red trace) and EOG-H (blue trace); (c) MRGO (orange trace) and MRGO-H (green trace). Raman spectra of (d) EOG (red trace) and EOG-H (blue trace); (e) MRGO (orange trace) and MRGO-H (green trace). TPD profiles for (f) EOG (CO₂: red solid trace; CO: red dotted trace) and EOG-H (CO₂: blue solid traces; CO: blue dotted traces); (g) MRGO (CO₂: orange solid trace; CO: orange dotted trace) and MRGO-H (CO₂: green solid trace; CO: green dotted trace).

Further evidence in support of this conclusion was collected from the observation of the π plasmon band in EOG by X-ray photoelectron spectroscopy (XPS). As expected, the high resolution C 1s XPS envelope of EOG (Fig. 3b, red trace) was dominated by a component located at \sim 284.6 eV, arising from sp^2 -based carbon atoms in unaltered aromatic structures. A strong component at \sim 286.5 eV associated to carbon atoms in an oxidation state of +1 (e.g., in hydroxyl and/or epoxy groups) was also present [23,25], in agreement with the high oxygen content of this graphene. In addition, a broad, very weak but nonetheless discernible component above \sim 291 eV could be seen in the C 1s envelope of EOG. This feature corresponds to the well-known $\pi \rightarrow \pi^*$ shake-up satellite band characteristic of delocalized electrons in sp^2 -hybridized carbon structures [38], and its presence was a clear indication of (at least) a relatively well developed aromatic character in the carbon material. Notably, the C 1s spectrum of MRGO lacked such a satellite peak, i. e., no intensity was detected above 291 eV (Fig. 3c, orange trace). This result implied that EOG boasted more abundant, larger aromatic domains compared to those of MRGO, despite their having the same extent of oxidation.

The Raman spectrum of EOG (Fig. 3d, red trace) displayed the typical features of graphite/graphene materials, namely, the D and G bands in the first-order region ($1100\text{-}1700\text{ cm}^{-1}$) at 1344 and 1590 cm^{-1} , respectively, together with some additional bands in the second-order region ($2300\text{-}3500\text{ cm}^{-1}$), most notably the 2D band ($\sim 2690\text{ cm}^{-1}$) [39,40]. The G band is due to in-plane bond-stretching motions (E_{2g} mode) of sp^2 -hybridized carbon atoms, whether they are in aromatic or aliphatic structures, whereas the D band arises from breathing vibrations (A_{1g} mode) of six-fold aromatic rings lying in close proximity to any defect or discontinuity that breaks the ideal periodicity of the graphite/graphene lattice [41,42]. For this reason, the intensity ratio of the D and G bands (I_D/I_G ratio) is sensitive to the average lateral size of the crystallites/aromatic domains, L_a , present in such materials. More to the point, as L_a progressively decreases across the

nanometer size regime (i.e., from several hundred down to just very few nanometers), I_D/I_G increases as $I_D/I_G \propto 1/L_a$ (nanocrystallization regime). However, upon further reducing L_a the overall number of six-fold aromatic rings that contribute to the D band starts to decrease, so that I_D/I_G decreases as $I_D/I_G \propto L_a^2$ (amorphization regime) [41]. The I_D/I_G ratio for EOG was measured to be 1.04 ± 0.02 . Coincidentally, a very similar value was obtained in the case of MRGO (1.070 ± 0.003 ; see Fig. 3e, orange trace). At first sight this result seemed to imply that the average size of the aromatic domains in EOG and MRGO was essentially the same. Nevertheless, we note that the full width at half maximum (FWHM) values of their respective D and G bands were substantially different, indicating that the two graphenes should be structurally dissimilar. Specifically, the Raman bands of MRGO were broader than those of EOG [FWHM values of 80 ± 1 (G) and 138 ± 2 (D) cm^{-1} for MRGO vs. 72 ± 3 (G) and 97 ± 5 (D) cm^{-1} for EOG], which pointed to a more disordered lattice in the former graphene. Indeed, the FWHM of the G band can be taken as a proxy to discriminate between samples belonging to the nanocrystallization and amorphization regimes, even though they may exhibit the same I_D/I_G value [28,43]. Along this line, it can be concluded that the structure of EOG belongs to the nanocrystallization regime, while that of MRGO belongs to the amorphization one, and therefore that the aromatic domains are larger in the electrochemically derived graphene.

The previous spectroscopic data collectively indicated that the aromatic domains of a highly oxidized graphene obtained by the electrochemical route tend to be larger than those of a counterpart derived from standard graphene oxide, even though both exhibit the same overall degree of oxidation. Such a subtle difference in their microscopic structure can be expected, however, to translate into distinct macroscopic properties for materials prepared from the two graphenes [28]. This should be particularly the case of the electrical conductivity. Because the electrical

transport in graphite/graphene materials is made possible by delocalized π states associated to their extended aromatic character, an oxidized graphene having larger aromatic domains should be electrically more conductive than another graphene with smaller domains [44,45]. We measured the electrical conductivity of thin paper-like films of EOG and MRGO obtained by vacuum filtration of their respective aqueous dispersions. As expected, the value determined for the EOG film was considerably larger than that of its MRGO counterpart (50 vs. 0.09 mS cm⁻¹), which lent further support to the idea of the structural differences discussed above.

3.2. Electrochemically derived holey graphene: role of labile groups

To be useful as precursors to holey graphene, oxidized graphenes should possess a significant amount of labile oxygen groups that can be easily removed in the form of CO and CO₂ molecules by, e.g., chemical or thermal treatment. To probe the presence of such labile groups in EOG, the sample was analyzed by temperature-programmed desorption (TPD) under a flowing argon atmosphere, whereby the amount of released CO and CO₂ was measured as a function of heating temperature in the 30-950 °C range. Fig. 3f shows the corresponding TPD profiles (CO₂: red solid trace; CO: red dotted trace), which revealed that a large fraction of the carbon oxides were released at rather low temperatures (~100-300 °C, with maxima below 200 °C). This low-temperature behavior is quite atypical in carbon materials (except maybe for the evolution of carboxylic acid groups as CO₂) [46-48], although it has been previously observed in standard graphene oxides [49-51], and is a clear sign of the abundant presence of readily removable, hole-forming oxygen groups. Extensive theoretical work on graphene oxide has identified the latter as mainly epoxide and hydroxyl moieties bound to the basal plane, rather than to edges, of the NSs and lying in close proximity to each other [52-55], which is the expected configuration of the highly oxidized domains in graphene oxides [18].

Accordingly, the present XPS results (Fig. 3b, red trace) indicated that epoxides and/or hydroxyls are the dominant oxygen-containing groups also in EOG. Furthermore, qualitatively similar TPD profiles were recorded in the case of MRGO (see Fig. 3g; CO₂: orange solid trace; CO: orange dotted trace). Indeed, the overall evolution of oxygen in the form of CO and CO₂ was very similar for both oxidized graphenes, i.e., 9617 (EOG) vs. 9707 (MRGO) $\mu\text{mol g}^{-1}$, in agreement with the fact that they exhibited the same level of oxidation.

However, some differences between the TPD profiles of EOG and MRGO were also apparent. First, the amount of carbon oxides released in the lower temperature range (100-300 °C) was somewhat larger in the EOG sample [2931 (CO₂) and 748 (CO) $\mu\text{mol g}^{-1}$ vs. 2144 (CO₂) and 508 (CO) $\mu\text{mol g}^{-1}$ for MRGO], whereas the opposite was the case at higher temperatures [985 (CO₂) and 1000 (CO) $\mu\text{mol g}^{-1}$ vs. 1633 (CO₂) and 1590 (CO) $\mu\text{mol g}^{-1}$ for MRGO]. Second, the evolution of both CO₂ and CO in the 100-300 °C range peaked at a noticeably lower temperature (~30-40 °C lower) in EOG compared to MRGO. These results implied that the oxygen groups in EOG tend to be more labile than those in MRGO. As a plausible hypothesis to account for such a difference, we propose that the density of oxygen groups in the highly oxidized domains of EOG is, on average, higher than that of MRGO. Because the lability of such groups, at least in terms of evolving carbon oxides, is directly related to their spatial proximity to each other on the graphene lattice [53,55], higher oxygen group densities should lead to higher labilities for these groups. At the same time, having denser oxidized domains in EOG implies that its NSs should bear larger fractions of non-oxidized areas compared to the case of MRGO, since both samples possess the same overall level of oxidation. Hence, the aromatic domains of the former graphene should be larger than those of the latter, which would be consistent with the spectroscopic results discussed above.

To obtain holey graphene from EOG, the material was subjected to hydrothermal treatment at 100 °C in a Teflon-lined autoclave in the presence of a small amount of hydrogen peroxide (see Experimental section for details). In standard graphene oxides, this type of treatment is known to etch away their highly reactive, heavily oxidized domains, leaving behind nanometer-sized holes in the NSs [11-15]. Fig. 4 shows transmission electron microscopy (TEM) images of the starting EOG NSs (a and b) and their hydrogen peroxide-treated counterpart (c and d; sample EOG-H). Different from the starting graphene, the EOG-H NSs were decorated with a moderate density of small holes typically between 4 and 8 nm in diameter, suggesting that this chemical etching treatment was effective on the electrochemically derived graphene. By contrast, the same treatment applied to MRGO (Fig. 4e and f) led to much more extensively etched NSs (Fig. 4g and h, sample denoted as MRGO-H). In this case, a high density of relatively large holes (up to 125 nm in size) was generated. The distinct evolution of EOG and MRGO upon chemical etching generally agreed with their structural differences as highlighted above. Specifically, the higher fraction of aromatic areas in EOG should make this graphene less reactive overall towards hydrogen peroxide etching than MRGO, because such areas are expected to exhibit a relatively low reactivity compared with that of the heavily oxidized, structurally defective domains [56,57]. Consequently, etched NSs with smaller and/or less abundant holes should be expected in the case of EOG, as it was indeed observed (see Fig. S2 in the ESM for a comparison of the hole size distribution for the two materials). Performing the hydrothermal treatment in the presence of a higher concentration of hydrogen peroxide led to the generation of larger holes than using the standard procedure (see Fig. S4 of the ESM), but still far below the sizes attained for MRGO-H. The heterogeneity of the hole size distribution is also half way between that for EOG-H and MRGO-H. We note that no damage artifactual leading to pore generation was induced by TEM imaging of the samples. Indeed, the starting graphene materials

(EOG and MRGO) did not show any porosity even after repeatedly imaging the same zone to magnify certain areas. Neither did any of the graphene materials (whether precursors or holey graphenes derived from them) vary in any detectable way after repeated imaging of the same area.

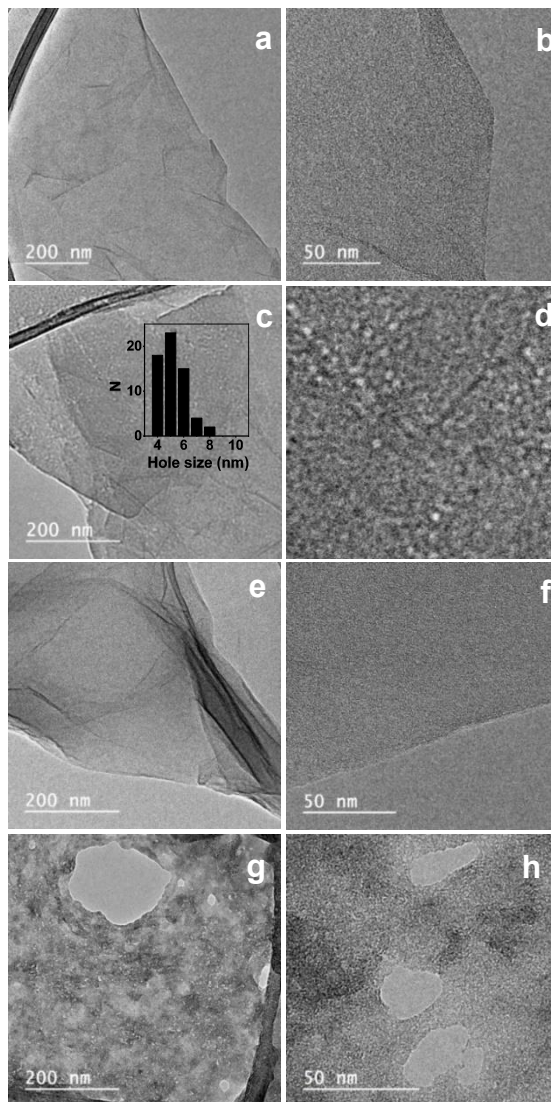


Figure 4. Transmission electron microscopy (TEM) images of (a,b) the starting EOG nanosheets and (c,d) their hydrogen peroxide-treated counterpart, EOG-H, as well as (e,f) the MRGO and (g,h) MRGO-H nanosheets. Inset to c: hole size histogram determined from the TEM images.

The physicochemical characteristics of the holey products were consistent with the TEM observations and the expected etching behavior of their precursors. More to the point, after the etching process the components of the high resolution C 1s core level band associated to graphitic carbon, i. e., both the most intense component centered at ~284.6 eV and the $\pi \rightarrow \pi^*$ satellite band, were left unchanged (Fig. 3b), indicating that the aromatic domains in the precursor graphene NSs were not altered for the most part during the etching process, as anticipated. Only subtle changes were noticed in the C 1s XPS spectrum of EOG following hydrogen peroxide treatment (Fig. 3b, blue trace), namely, (1) the component located at a binding energy of 286.5 eV became somewhat weaker, and (2) a faint but nonetheless discernible component developed at a binding energy of 288.5 eV. In EOG, the former component (carbon atoms in an oxidation state of +1, i.e., single-bonded to oxygen) can be mostly ascribed to hydroxyl and epoxide groups bound to the basal plane in the highly oxidized domains of the graphene lattice [23,25]. These groups are expected to be largely removed upon etching with hydrogen peroxide, thus contributing to a reduction in the 286.5 eV component, but the holes generated in the etched NSs also provided new edge sites where oxygen atoms in other C-O configurations could be stabilized (e.g., phenol-type hydroxyls and ethers). For this reason, the component at 286.5 eV cannot be expected to vanish in the holey graphene products, even if all the original oxygen groups were abstracted during the etching process.

On the other hand, the C 1s component located at 288.5 eV was attributed to carboxylic acid groups, which are normally found at edge sites of sp²-based carbon materials [23,47]. Therefore, the rise of this component in EOG-H could be correlated with the creation of new (internal) edges in the holey graphene NSs. We also note that the π plasmon band of EOG (component centered at ~291 eV) remained unchanged after the chemical treatment, further corroborating the idea that the electronically conjugated, aromatic areas of the material were not affected

by such a treatment to a large extent. A similar evolution was observed for MRGO-H relative to its precursor (see Fig. 3c, green trace), i.e., a decrease and an increase of the 286.5 and 288.5 eV components, respectively. However, in this case the changes were somewhat more apparent, especially for the 286.5 eV component, which could be attributed to the more extensive perforation of the MRGO NSs upon treatment with hydrogen peroxide. It is also worth noting that the 288.5 eV component was already present in the starting MRGO sample (Fig. 3c, orange trace), whereas it was not in its EOG counterpart (Fig. 3b, red trace). This observation was in line with previous reports [24] and suggested that (1) contrary to the case of standard graphene oxides, oxidation of the graphite anode during the electrochemical exfoliation and subsequent work-up processes did not trigger any substantial cleavage of C-C bonds within the sp²-hybridized lattice, where carboxylic acid groups could have been accommodated, and (2) as-prepared EOG is chemically more homogeneous overall than MRGO.

The Raman spectra of EOG-H (Fig. 3d, blue trace) and MRGO-H (Fig. 3e, green trace) were not substantially different to those of their respective precursors (red traces). In particular, the measured I_D/I_G ratios (1.18 ± 0.08 for EOG-H and 1.042 ± 0.003 for MRGO-H) were similar to the values determined for their corresponding precursor graphenes, again suggesting that the aromatic areas of the NSs were not altered to a large extent during the hydrogen peroxide etching. On the other hand, significant changes were observed in the TPD profiles of the holey products relative to those of their parent materials, as shown in Fig. 3f for EOG-H (CO_2 : blue solid traces; CO: blue dotted traces) and Fig. 3g for MRGO-H (CO_2 : green solid traces; CO: green dotted traces). In all cases, the intense evolution of carbon oxides at low temperatures (100-300 °C), which was characteristic of the starting graphenes, was drastically reduced after the hydrogen peroxide treatment. This result corroborated that etching by hydrogen peroxide preferentially removed the most labile and reactive oxygen groups from both types of graphene. By

contrast, the evolution of CO₂ and CO was not seen to decrease for the most part at higher temperatures, or even increased somewhat in the case of CO for MRGO-H. The release of carbon oxides from sp²-based carbon materials at such high temperatures is usually associated to stable oxygen groups bound to edges, and not basal planes, of the carbon lattice (e.g., phenols, ethers or carbonyls) [47]. Therefore, the creation of holes, and thus of internal edges, should promote the presence of such stable oxygen groups in the hydrogen peroxide-treated NSs, which in turn should contribute to the persistence of carbon oxide evolution in the TPD profiles at these high temperatures.

Another expected effect of the generation of holes in graphene is the enhancement of specific surface area [58]. Indeed, nitrogen physisorption isotherms revealed a development of porosity upon hydrogen peroxide treatment (Fig. S3), which led to an increase in the specific surface area from 6 m² g⁻¹ (EOG) to 107 m² g⁻¹ (EOG-H).

3.3. Electrochemical charge storage behavior of the holey graphenes

The introduction of holes in graphene enhances the specific surface area and introduces channels for ion transport, which is expected to be beneficial for its use in electrochemical charge storage applications [58]. The holey graphene materials were tested as electrodes for electrochemical charge storage in a three-electrode configuration using aqueous 6 M KOH as the electrolyte (see Experimental section for details). Fig. 5a shows cyclic voltammograms recorded at a potential scan rate of 10 mV s⁻¹ for the EOG (red trace) and EOG-H (blue trace) samples, where it can be seen that substantially higher gravimetric current densities were measured for the latter. The enhanced ability of EOG-H to store electrical charge relative to EOG could be reasonably ascribed to a better access of the electrolyte due to the presence of nanometer-sized openings within the holey graphene NSs, affording

comparatively faster ionic diffusion in the holey graphene electrode, which in turn would be afforded by shorter ion transport channels associated to the holes in the NSs [12,15]. Indeed, the EOG-H voltammograms showed rectangular shape (Fig. 5a) except for the highest potential scan rates (see Fig. 5b; voltammograms for EOG at different scan rates are also shown in Fig. 5c). Additional support for this conclusion was obtained from electrochemical impedance spectroscopy (EIS) measurements. Fig. 5d shows Nyquist plots for EOG (red trace) and EOG-H (blue trace). Although the overall appearance of such plots was similar, that of EOG-H displayed a more vertical profile in the medium-low frequency range, including the Warburg region, indicative of a lower resistance to electrolyte diffusion compared to the case of EOG (shorter ion diffusion lengths) [59,60]. As for the high frequency range of the plots (see inset to Fig. 5d), EOG-H showed a lower intercept with the real part of the impedance axis than EOG. Such intercept values is interpreted as the ohmnic resistance of the solution and separator, and any internal resistance of the electrode material [61]. As the two former factors are equivalent for both electrodes, this observation points to a lower internal resistance of porous EOG-H. The characteristic relaxation time of the electrochemical cell derived from the EIS data, t_0 , determined as $t_0 = 1/f_0$, where f_0 is the frequency at which the imaginary part of the capacitance reaches its maximum value [62,63] (see corresponding plots in Fig. 5e), was calculated to be 31 s both for EOG and EOG-H, respectively. However, the latter showed a complex profile resulting from convolution of two Gaussian bands, which is indicative of two underlying phenomena, the resulting relaxation times being ~ 82 and ~ 6 s. The shorter relaxation time measured with EOG-H revealed a faster response of the holey graphene-based electrode, which again pointed to an improved accessibility of this material by the electrolyte, relative to that of EOG.

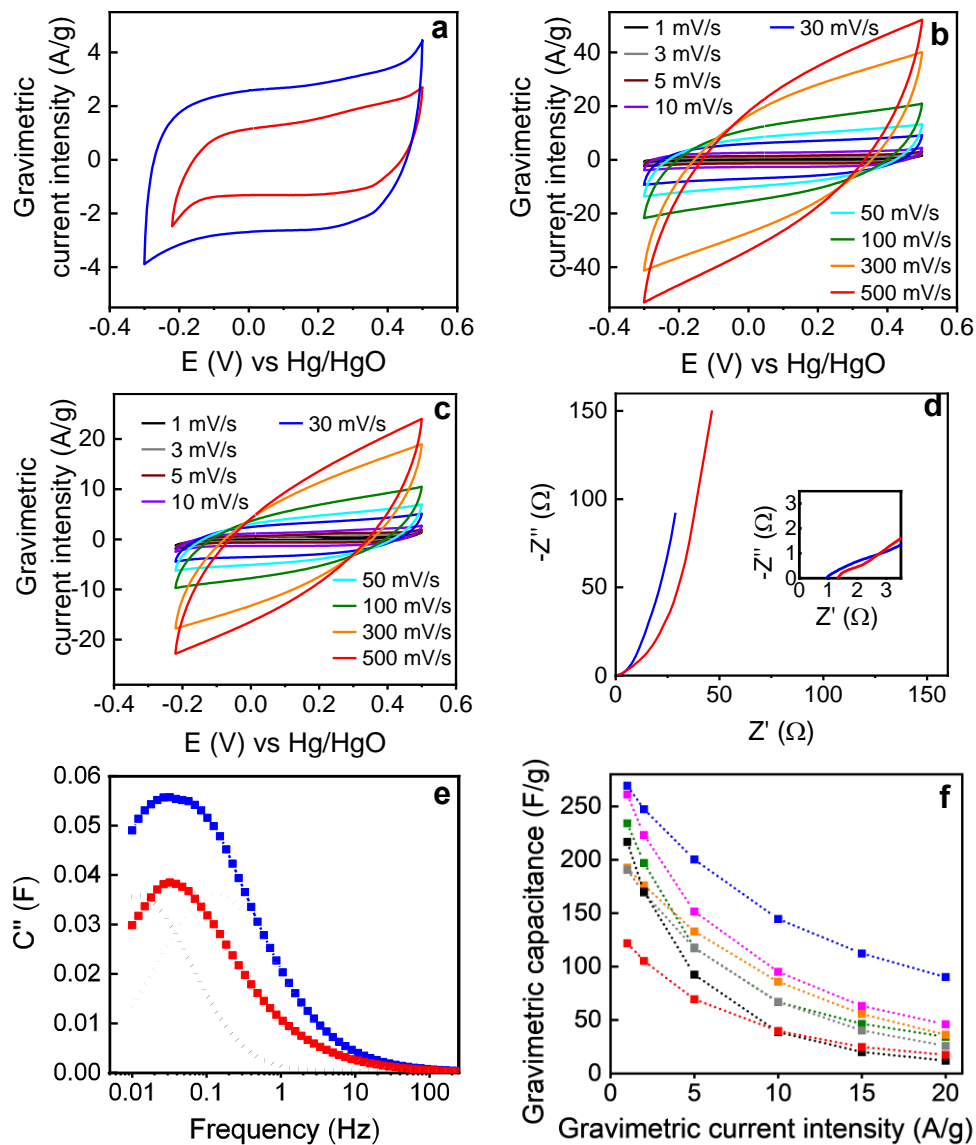


Figure 5. (a) Cyclic voltammograms recorded at a potential scan rate of 10 mV s⁻¹ for the EOG (red trace) and EOG-H (blue trace). (b,c) Cyclic voltammograms recorded at different potential scan rates for (b) EOG-H and (c) EOG. (d) Nyquist plots for EOG (red trace) and EOG-H (blue trace). The inset shows a detailed view of the high frequency region of the plots. (e) Imaginary part of the capacitance versus frequency for EOG (red trace) and EOG-H (blue trace). The black and gray dotted lines correspond to the deconvolution of EOG-H profile into two components. (f) Capacitance values measured at different current densities for EOG-H (blue symbols), EOG-H (red symbols) and for electrodes prepared from EOG treated with different amounts of the etchant, namely, 0.18 (orange symbols), 0.37 (green), 0.55 (cyan), 1.84 (gray) and 4.55 wt% (black).

For comparison purposes, the corresponding voltammetric and EIS data recorded for the Hummers-derived graphenes (MRGO and MRGO-H samples) are shown in Fig. S5 of the ESM. As expected, in this case the obtained results were also consistent with a faster diffusion of the electrolyte throughout the holey graphene electrode, i.e., MRGO-H yielded a more vertical Nyquist plot profile and a shorter relaxation time than those of MRGO (~68 s vs. ~82 s; if the former is deconvoluted into two components, it yields ~82 and ~6 s). More significantly, comparison of the electrochemical- and Hummers-derived holey graphenes (i.e., EOG-H vs. MRGO-H) tended to favor the former material. Specifically, although EOG-H showed a similar relaxation time to that of MRGO-H (both materials being porous), it boasted a somewhat broader voltage window (~0.7 vs. 0.5 V; see, e.g., corresponding voltammograms in Figs. 5a and S5a). When the voltage window of MRGO-H was extended above (below) 0.4 (-0.1) V vs. the Hg/HgO reference electrode, sharp increases in the measured current were observed, indicative of substantial water electrolysis taking place in the cell. By contrast, the same effect was noticed in EOG-H only above (below) 0.5 (-0.2) V vs. Hg/HgO. Water electrolysis and other electro-induced reactions are known to be catalyzed by different types of active (defect) sites present in sp^2 -based carbon materials, in particular carbon edges saturated by heteroatoms (oxygen, nitrogen, etc) [64,65]. Exhibiting a larger fraction of holes and, thus, of oxygen-decorated internal edges, MRGO-H was expected to be electrocatalytically more active overall towards water splitting than EOG-H. Such a higher activity implied lower overpotentials for the hydrogen and oxygen evolution reactions and, consequently, a narrower operating voltage window when MRGO-H was used as an electrode for charge storage, as it was indeed observed.

Fig. 5f shows the capacitance values for the EOG-H (blue symbols) and EOG electrodes (red features) calculated from their galvanostatic charge-discharge profiles recorded at different current densities between 1 and 20 A g⁻¹ (shown in

Fig. S6 in the ESM). As could be anticipated from the results presented above, EOG-H featured substantially larger capacitance values and a better rate capability compared to the case of EOG, e.g., a capacitance of 269 F g^{-1} (EOG-H) vs. 122 F g^{-1} (EOG) was measured at a gravimetric current intensity of 1 A g^{-1} , together with a capacitance retention of 14% (EOG-H) vs. 33% (EOG) at 20 A g^{-1} . The positive effect brought about by generating holes within the EOG NSs via hydrogen peroxide etching was made more apparent by investigating samples treated with different amounts of the etchant, the capacitance values of which are given in Fig. 5f. Using both higher and lower amounts of hydrogen peroxide than that of the benchmark EOG-H material (0.92 wt% H_2O_2 ; see Experimental section for details) led in all cases to graphene electrodes with clearly better electrochemical performance than that of the non-etched EOG product. However, the best overall results in terms of combined capacitance and rate capability were obtained with the benchmark EOG-H material, and etching with other amounts of hydrogen peroxide was not able to improve on the values attained with EOG-H to any significant extent (except for EOG etched with 1.84 wt% H_2O_2 when measured at the lowest current intensities). Table S1 of the ESM compares capacitance values measured for the present EOG-H material with those of other holey graphenes previously reported in the literature (mostly obtained from standard graphene oxides), where it is noticed that a competitive performance was achieved with the electrochemically derived holey graphene. We note that, even in cases where EOG-H loses out in the comparison of capacitance values, it is still advantageous from the point of view of its simpler, less time-consuming and more environmentally friendly preparation process. The galvanostatic profiles measured at different current densities for MRGO-H and MRGO are presented in the ESM (Figs. S7a and b, respectively) together with their corresponding capacitances (Fig. S7c). It is worth noting that while the capacitance values of MRGO-H were similar to those of its EOG-H counterpart (also shown in Fig. S7c for a better comparison), the total charges stored

by the latter (i.e., the capacity values) were substantially larger on account of its wider operating voltage window. This point is illustrated in Fig. S7d, which compares the capacities of the EOG, EOG-H, MRGO and MRGO-H samples and highlights the advantage of using the holey graphene derived by electrochemical means.

Thermal annealing under air atmosphere, which is known to be another effective method to create holes in both standard graphene oxide [11,12] and reduced graphene oxide [66], was also investigated on the EOG material (see Experimental section for details). The capacitance values measured at different current intensities for electrodes prepared from EOG annealed at temperatures ranging between 400 and 650 °C are presented in Fig. S5f. In this case, while the thermal treatments were generally seen to boost the electrochemical behavior of EOG, the performance of the annealed samples tended to be lower than that of their hydrogen peroxide-etched counterparts. This result can be tentatively ascribed to a more indiscriminate attack of the carbon lattice in the oxidized graphenes by molecular oxygen at high temperatures compared to the etching attained with hydrogen peroxide at a moderate temperature (100 °C). Such an aggressive attack by molecular oxygen was expected to not only remove the highly oxidized domains of the NSs, but also much of their pristine, aromatic areas via edge recession. In fact, it is well documented from past studies that even the edges of highly crystalline graphites recede at a fast rate (affording CO and CO₂ molecules) upon exposure to air at temperatures of 500 °C and above [67,68]. Evidence for the extensive abstraction of carbon atoms from the EOG NSs by this type of treatment was obtained by measuring their product yields, which were as low as ~15 wt% after thermal annealing at 650 °C. For comparison, typical product yields for hydrogen peroxide etching were ~ 72 wt%. This result was further supported by the observation of very irregular, jagged edge profiles in the annealed NSs (see Fig. S8

of the ESM). Such irregular profiles were a clear sign of extensive edge recession and were not seen in the hydrogen peroxide-etched EOG NSs.

Finally, the holey graphene materials were also tested as electrodes in a two-electrode, symmetric supercapacitor configuration. Fig. S9 of the ESM shows cyclic voltammograms (a,c) and galvanostatic charge-discharge profiles (b,d) for EOG-H (a,b) and MRGO-H (c,d) symmetric devices in 6 M KOH electrolyte. Similar to the situation noted above for the three-electrode measurements, a wider operating voltage window could be used with the electrochemically derived holey graphene, i.e., 1.2 V for EOG-H vs. 0.6 V for MRGO-H. Such a difference was translated into a better performance of the former in terms of energy and power densities, as can be noticed in the Ragone plots of Fig. 6, based on gravimetric values (orange symbols for EOG-H, green for MRGO-H). For instance, the EOG-H device delivered a gravimetric energy density of $\sim 8.7 \text{ Wh kg}^{-1}$ at a power density of $\sim 600 \text{ W kg}^{-1}$, to be compared with 0.46 Wh kg^{-1} at 600 W kg^{-1} for the MRGO-H device. These figures were relatively modest in the context of carbon-based aqueous supercapacitors [69-71]. Furthermore, in both cases the energy density fell sharply with increasing power density in the $10^3\text{-}10^4 \text{ W kg}^{-1}$ range. Likewise, using a concentrated water-in-salt electrolyte for EOG-H (14 m NaClO₄ [72]) to broaden the operating voltage window (up to 2.4 V) was only able to marginally improve the device performance (gray symbols in Fig. 6). For example, the water-in-salt device delivered an energy density of 9.4 Wh kg^{-1} at a power density of $\sim 600 \text{ W kg}^{-1}$ (see corresponding cyclic voltammograms and galvanostatic profiles in Fig. S10). This behavior was most likely due to the particular electrode configuration used for the present measurements, in which the holey graphene materials were heavily compacted under high pressure to a density of $\sim 1.6 \text{ g cm}^{-3}$. Such an extensive compaction acts as a barrier to the transport of ions within the electrode, even in the presence of holes in the NSs, thus yielding limited performance metrics. Still, the benefits of using the electrochemically derived holey graphene over its Hummers-

based counterpart were made apparent even with this electrode configuration. Future work in our laboratory will focus on exploiting such benefits for the development of high performance electrodes, e.g., by processing the electrochemical holey graphene into lower density, three-dimensional aerogels.

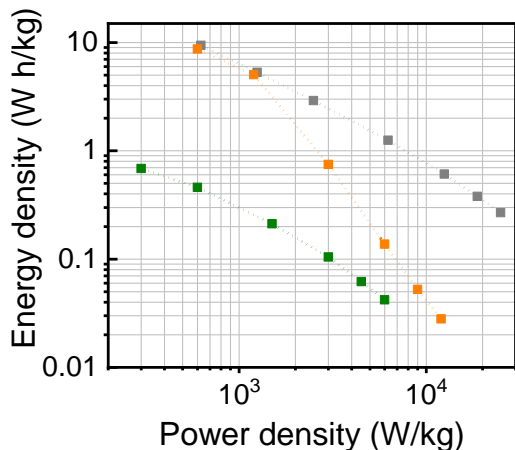


Figure 6. Ragone plots, based on gravimetric values, for EOG-H (orange symbols), MRGO-H (green) symmetric devices in 6 M KOH electrolyte, as well as for EOG-H using 14 M NaClO₄ water in salt electrolyte (gray symbols).

4. Conclusions

For the first time, highly oxidized graphene obtained by an electrochemical exfoliation approach was shown to be a convenient alternative to the more prevalent standard graphene oxides derived from common oxidation strategies (e.g., Hummers method) as a precursor for the preparation of holey graphene NSs. Comparison of two different highly oxidized graphenes, made by the electrochemical and Hummers routes but having the same extent of oxidation, revealed the former route to afford NSs with larger aromatic areas and, consequently, with smaller and denser oxidized domains. When these two graphenes were used to generate holey NSs based on the selective etching of their

oxidized domains, such structural differences led to holey products with distinct characteristics, namely, the created holes tended to be smaller and more uniform in the electrochemically derived material. As an electrode for electrochemical charge storage, this new type of holey graphene exhibited some advantages relative to its standard graphene oxide-based counterpart, which translated into improved capacity and energy density values. Finally, it is anticipated that applications other than electrochemical charge storage can benefit from the present electrochemically derived holey graphene. For example, the ability to generate holes in the NSs with more uniform dimensions could be exploited in (bio)molecular separation membranes that outperform those based on standard graphene oxides.

Electronic Supplementary Material. The Supplementary Material is available free of charge on the Elsevier website at <https://doi.org/10.1016/j.carbon.2022.04.003>.

Preparation of MRGO through the Hummers method. Additional characterization of the materials. Effect of the use of a higher concentration of hydrogen peroxide in the hydrothermal treatment of EOG on the size of the holes generated. Testing of EOG, EOG-H, MRGO and MRGO-H as electrodes for electrochemical charge storage in three-electrode cell configurations. Thermal annealing of EOG. Testing of EOG-H and MRGO-H as electrodes for electrochemical charge storage in two-electrode symmetric cell configurations.

Acknowledgements. Funding by the Spanish Ministerio de Ciencia, Innovación y Universidades (MICINN), Agencia Estatal de Investigación (AEI) and the European Regional Development Fund (ERDF) through project RTI2018-100832-B-I00, as well as Plan de Ciencia, Tecnología e Innovación (PCTI) 2013-2017 and 2018-2022 del Principado de Asturias and the ERDF (projects IDI/2018/000233 and IDI/2021/000037, respectively) is gratefully acknowledged.

References

- [1] A. C. Ferrari, F. Bonaccorso, V. I. Fal'ko, K. S. Novoselov, S. Roche, P. Bøggild, S. Borini, F. Koppens, V. Palermo, N. Pugno, J. A. Garrido, R. Sordan, A. Bianco, L. Ballerini, M. Prato, E. Lidorikis, J. Kivioja, C. Marinelli, T. Ryhänen, A. Morpurgo, J. N. Coleman, V. Nicolosi, L. Colombo, A. Fert, M. Garcia-Hernandez, A. Bachtold, G. F. Schneider, F. Guinea, C. Dekker, M. Barbone, C. Gallois, A. Grigorenko, G. Konstantatos, A. Kis, M. Katsnelson, C. W. J. Beenakker, L. Vandersypen, A. Loiseau, V. Morandi, D. Neumaier, E. Treossi, V. Pellegrini, M. Polini, A. Tredicucci, G. M. Williams, B. H. Hong, J. H. Ahn, J. M. Kim, H. Zirath, B. J. van Wees, H. van der Zant, L. Occhipinti, A. Di Matteo, I. A. Kinloch, T. Seyller, E. Quesnel, X. Feng, K. Teo, N. Rupasinghe, P. Hakonen, S. R. T. Neil, Q. Tannock, T. Löfwander, J. Kinaret, Science and technology roadmap for graphene, related two-dimensional crystals, and hybrid systems, *Nanoscale* 7 (2015), 4598-4810.
- [2] W. Kong, H. Kum, S.-H. Bae, J. Shim, H. Kim, L. Kong, Y. Meng, K. Wang, C. Kim, J. Kim, Path towards graphene commercialization from lab to market, *Nature Nanotechnology* 14 (2019), 927-938.
- [3] R. Raccichini, A. Varzi, S. Passerini, B. Scrosati, The role of graphene for electrochemical energy storage, *Nature Materials* 14 (2015), 271-279.
- [4] M.F. El-Kady, Y. Shao, R.B. Kaner, Graphene for batteries, supercapacitors and beyond, *Nature Reviews Materials* 1 (2016), 16033.
- [5] T. Wang, Q. Zhang, J. Zhong, M. Chen, H. Deng, J. Cao, L. Wang, L. Peng, J. Zhu, B. Lu, 3D holey graphene/polyacrylonitrile sulfur composite architecture for high loading lithium sulfur batteries, *Advanced Energy Materials* 11 (2021), 2100448.
- [6]. Li, J. Cao, T. Wang, L. Wang, H. Deng, Q. Zhang, Y. Cheng, J. Zhu, B. Lu, Intercalation and covalent bonding strategies for constructing a stable cathode for high-energy density and long-cycling potassium-organic batteries, *Chemical Engineering Journal* 431 (2022), 133215.
- [7] B. Wang, T. Ruan, Y. Chen, F. Jin, L. Peng, Y. Zhou, D. Wang, S. Dou, Graphene-based composites for electrochemical energy storage, *Energy Storage Materials* 24 (2020), 22-51.
- [8] K. Chen, S. Song, F. Liu, D. Xue, Structural design of graphene for use in electrochemical energy storage devices, *Chemical Society Reviews* 44 (2015), 6230-6257.
- [9] T. Yang, H. Lin, X. Zheng, K.P. Loh, B. Jia, Tailoring pores in graphene-based materials: from generation to applications, *Journal of Materials Chemistry A* 5 (2017), 16537-16558.
- [10] Y. Zhang, Q. Wan, N. Yang, Recent advances of porous graphene: synthesis, functionalization, and electrochemical applications, *Small* 15 (2019), 1903780.
- [11] A.C. Lokhande, I.A. Qattan, C.D. Lokhande, S.P. Patole, Holey graphene: an emerging versatile material, *Journal of Materials Chemistry A* 8 (2020), 918-977.
- [12] T. Liu, L. Zhang, B. Cheng, X. Hu, J. Yu, Holey graphene for electrochemical energy storage, *Cell Reports Physical Science* 1 (2020), 100215.

- [13] Y. Lin, Y. Liao, Z. Chen, J. W. Connell, Holey graphene: a unique structural derivative of graphene, *Materials Research Letters* 5 (2017), 209-234.
- [14] N. S. Rajput, S. Al Zadjali, M. Gutierrez, A. M. K. Esawi, M. Al Teneiji, Synthesis of holey graphene for advanced nanotechnological applications, *RSC Advances* 11 (2021), 27381–27405.
- [15] Y. Xu, Z. Lin, X. Zhong, X. Huang, N.O. Weiss, Y. Huang, X. Duan, Holey graphene frameworks for highly efficient capacitive energy storage, *Nature Communications* 5 (2014), 4554.
- [16] K. Erickson, R. Erni, Z. Lee, N. Alem, W. Gannett, A. Zettl, Determination of the local chemical structure of graphene oxide and reduced graphene oxide, *Advanced Materials* 22 (2010), 4467-4472.
- [17] S.H. Dave, C. Gong, A.W. Robertson, J.H. Warner, J.C. Grossman, Chemistry and structure of graphene oxide via direct imaging, *ACS Nano* 10 (2016), 7515-7522.
- [18] F. Mouhat, F. X. Coudert, M.-L. Bocquet, Structure and chemistry of graphene oxide in liquid water from first principles, *Nature Communications* 11 (2020), 1566.
- [19] A. M. Abdelkader, A. J. Cooper, R. A. W. Dryfe, I. A. Kinloch, How to get between the sheets: a review of recent works on the electrochemical exfoliation of graphene materials from bulk graphite, *Nanoscale* 7 (2015), 6944-6956.
- [20] S. Fang, Y. Lin, Y. H. Hu, Recent advances in green, safe, and fast production of graphene oxide via electrochemical approaches, *ACS Sustainable Chemistry & Engineering Journal* 7 (2019), 12671-12681.
- [21] S. Yang, M.R. Lohe, K. Müllen, X. Feng, New-generation graphene from electrochemical approaches: production and applications, *Advanced Materials* 28 (2016), 6213-6221.
- [22] J.I. Paredes, J.M. Munuera, Recent advances and energy-related applications of high quality/chemically doped graphenes obtained by electrochemical exfoliation methods, *Journal of Materials Chemistry A* 5 (2017), 7228-7242.
- [23] Z. Tian, P. Yu, S.E. Lowe, A.G. Pandolfo, T.R. Gengenbach, K.M. Laird, J. Song, X. Wang, Y.L. Zhong, D. Li, Facile electrochemical approach for the production of graphite oxide with tunable chemistry, *Carbon* 112 (2017), 185-191.
- [24] J. Cao, P. He, M.A. Mohammed, X. Zhao, R.J. Young, B. Derby, I.A. Kinloch, R.A.W. Dryfe, Two-step electrochemical intercalation and oxidation of graphite for the mass production of graphene oxide, *Journal of the American Chemical Society* 139 (2017), 17446-17456.
- [25] S. Pei, Q. Wei, K. Huang, H. M. Cheng, W. Ren, Green synthesis of graphene oxide by seconds timescale water electrolytic oxidation, *Nature Communications* 9 (2018), 145.
- [26] M.J. Fernández-Merino, L. Guardia, J.I. Paredes, S. Villar-Rodil, P. Solís-Fernández, A. Martínez-Alonso, J.M.D. Tascón, Vitamin C is an ideal substitute for hydrazine in the reduction of graphene oxide suspensions, *Journal of Physical Chemistry C* 114 (2010), 6426-6432.
- [27] J.M. Munuera, J.I. Paredes, S. Villar-Rodil, A. Martínez-Alonso, J.M.D. Tascón, A simple strategy to improve the yield of graphene nanosheets in the anodic exfoliation of graphite foil, *Carbon* 115 (2017), 625-628.

- [28] P. Yu, Z. Xiong, H. Zhan, K. Xie, Y.L. Zhong, G.P. Simon, D. Li, Electrochemically-derived graphene oxide membranes with high stability and superior ionic sieving, *Chemical Communications* 55 (2019), 4075-4078.
- [29] K. Parvez, Z. S. Wu, R. Li, X. Liu, R. Graf, X. Feng, K. Müllen, Exfoliation of graphite into graphene in aqueous solutions of inorganic salts, *Journal of the American Chemical Society* 136 (2014), 6083-6091.
- [30] B. Ossonon, D. Bélanger, Functionalization of graphene sheets by the diazonium chemistry during electrochemical exfoliation of graphite, *Carbon* 111 (2017), 83-93.
- [31] J.M. Munuera, J.I. Paredes, S. Villar-Rodil, M. Ayán-Varela, A. Martínez-Alonso, J.M.D. Tascón, Electrolytic exfoliation of graphite in water with multifunctional electrolytes: en route towards high quality, oxide-free graphene flakes, *Nanoscale* 8 (2016), 2982-2998.
- [32] D. Parviz, F. Irin, S.A. Shah, S. Das, C.B. Sweeney, M.J. Green, Challenges in liquid-phase exfoliation, processing, and assembly of pristine graphene, *Advanced Materials* 28 (2016), 8796-8818.
- [33] S. Pei, H. M. Cheng, The reduction of graphene oxide, *Carbon* 50 (2012), 3210-3228.
- [34] P.P. Brisebois, M. Siaj, Harvesting graphene oxide – years 1859 to 2019: a review of its structure, synthesis, properties and exfoliation, *Journal of Materials Chemistry C* 8 (2020), 1517-1547.
- [35] D. Li, M.B. Müller, S. Gilje, R.B. Kaner, G.G. Wallace, Processable aqueous dispersions of graphene nanosheets, *Nature Nanotechnology* 3 (2008), 101-105.
- [36] J. Hu, H. Zeng, C. Wang, Z. Li, C. Kan, Y. Liu, Interband π plasmon of graphene: strong small-size and field-enhancement effects, *Physical Chemistry Chemical Physics* 16 (2014), 23483-23491.
- [37] J. W.T. Seo, A.A. Green, A.L. Antaris, M.C. Hersam, High-concentration aqueous dispersions of graphene using nonionic, biocompatible block copolymers, *Journal of Physical Chemistry Letters* 2 (2011), 1004-1008.
- [38] D. Briggs, M. P Seah. Practical Surface Analysis. Vol 1: Auger and X-Ray Photoelectron Spectroscopy. 2nd ed.; John Wiley & Sons, 1990; pp. 131 and 448.
- [39] M.A. Pimenta, G. Dresselhaus, M.S. Dresselhaus, L.G. Cançado, A. Jorio, R. Saito, Studying disorder in graphite-based systems by Raman spectroscopy, *Physical Chemistry Chemical Physics* 9 (2007), 1276-1290.
- [40] J. B. Wu, M. L. Lin, X. Cong, H. N. Liu, P. H. Tan, Raman spectroscopy of graphene-based materials and its applications in related devices, *Chemical Society Reviews* 47 (2018), 1822-1873.
- [41] A.C. Ferrari, J. Robertson, Interpretation of Raman spectra of disordered and amorphous carbon, *Physical Review B* 61 (2000), 14095-14107.
- [42] A.C. Ferrari, D.M. Basko, Raman spectroscopy as a versatile tool for studying the properties of graphene, *Nature Nanotechnology* 8 (2013), 235-246.
- [43] L.G. Cançado, A. Jorio, E.H.M. Ferreira, F. Stavale, C.A. Achete, R.B. Capaz, M.V.O. Moutinho, A. Lombardo, T.S. Kulmala, A.C. Ferrari, Quantifying defects in graphene via Raman spectroscopy at different excitation energies, *Nano Letters* 11 (2011), 3190-3196.

- [44] C. Mattevi, G. Eda, S. Agnoli, S. Miller, K.A. Mkhoyan, O. Celik, D. Mastrogiovanni, G. Granozzi, E. Garfunkel, M. Chhowalla, Evolution of electrical, chemical, and structural properties of transparent and conducting chemically derived graphene thin films, *Advanced Functional Materials* 19 (2009), 2577-2583.
- [45] J.S. Roh, H.W. Yoon, L. Zhang, J.-Y. Kim, J. Guo, H.W. Kim, Carbon lattice structures in nitrogen-doped reduced graphene oxide: implications for carbon-based electrical conductivity, *ACS Applied Nano Materials* 4 (2021), 7897-7904
- [46] U. Zielke, K.J. Hüttlinger, W.P. Hoffman, Surface-oxidized carbon fibers: I. Surface structure and chemistry, *Carbon* 34 (1996), 983-998.
- [47] J.L. Figueiredo, M.F.R. Pereira, M.M.A. Freitas, J.J.M. Órfão, Modification of the surface chemistry of activated carbons, *Carbon* 37 (1999), 1379-1389.
- [48] A. Sánchez-Sánchez, F. Suárez-García, A. Martínez-Alonso, J.M.D. Tascón. Surface modification of nanocast ordered mesoporous carbons through a wet oxidation method, *Carbon* 62 (2013), 193-203.
- [49] I. Jung, D.A. Field, N.J. Clark, Y. Zhu, D. Yang, R.D. Piner, S. Stankovich, D.A. Dikin, H. Geisler, C.A. Ventrice, R.S. Ruoff, Reduction kinetics of graphene oxide determined by electrical transport measurements and temperature programmed desorption, *Journal of Physical Chemistry C* 113 (2009), 18480-18486.
- [50] P. Solís-Fernández, R. Rozada, J.I. Paredes, S. Villar-Rodil, M.J. Fernández-Merino, L. Guardia, A. Martínez-Alonso, J.M.D. Tascón, Chemical and microscopic analysis of graphene prepared by different reduction degrees of graphene oxide, *Journal of Alloys and Compounds* 536S (2012), S532-S537.
- [51] A. Lipatov, M.J.-F. Guinel, D.S. Muratov, V.O. Vanyushin, P.M. Wilson, A. Kolmakov, A. Sinitskii, Low-temperature thermal reduction of graphene oxide: in situ correlative structural, thermal desorption, and electrical transport measurements, *Applied Physics Letters* 112 (2018), 053103.
- [52] A. Bagri, C. Mattevi, M. Acik, Y.J. Chabal, M. Chhowalla, V.B. Shenoy, Structural evolution during the reduction of chemically derived graphene oxide, *Nature Chemistry* 2 (2010), 581-587.
- [53] T. Sun, S. Fabris, S. Baroni, Surface precursors and reaction mechanisms for the thermal reduction of graphene basal surfaces oxidized by atomic oxygen, *Journal of Physical Chemistry C* 115 (2011), 4730-4737.
- [54] R. Larciprete, S. Fabris, T. Sun, P. Lacovic, A. Baraldi, S. Lizzit, Dual path mechanism in the thermal reduction of graphene oxide, *Journal of the American Chemical Society* 133 (2011), 17315-17321.
- [55] F. Raffone, F. Savazzi, G. Cicero, Molecular dynamics study of the pore formation in single layer graphene oxide by a thermal reduction process, *Physical Chemistry Chemical Physics* 23 (2021), 11831-11836.
- [56] D. Wang, R. Dai, X. Zhang, L. Liu, H. Zhuang, Y. Lu, Y. Wang, Y. Liao, Q. Nian, Scalable and controlled creation of nanoholes in graphene by microwave-assisted chemical etching for improved electrochemical properties, *Carbon* 161 (2020), 880-891.
- [57] A. Vittore, M.R. Acocella, G. Guerra, Edge-oxidation of graphites by hydrogen peroxide, *Langmuir* 35 (2019), 2244-2250.

- [58] V.D. Nithya, A review on holey graphene electrode for supercapacitor, *Journal of Energy Storage* 44 (2021), 103380.
- [59] B.A. Mei, O. Munteşari, J. Lau, B. Dunn, L. Pilon, Physical interpretations of Nyquist plots for EDLC electrodes and devices, *Journal of Physical Chemistry C* 122 (2018), 194-206.
- [60] A. Noori, M.F. El-Kady, M.S. Rahmanifar, R.B. Kaner, M.F. Mousavi, Towards establishing standard performance metrics for batteries, supercapacitors and beyond, *Chemical Society Reviews* 48 (2019), 1272-1341.
- [61] B. E. Conway “Electrochemical Supercapacitors. Scientific fundamentals and technological Applications. Kluwer Academic/Plenum Publishers, New York, 1999, p. 493.
- [62] J. Zhang, X.S. Zhao, On the configuration of supercapacitors for maximizing electrochemical performance, *ChemSusChem* 5 (2012), 818-841.
- [63] S. Zhang, N. Pan, Supercapacitors performance evaluation, *Advanced Energy Materials* 5 (2015), 1401401.
- [64] S. Zhao, D.W. Wang, R. Amal, L. Dai, Carbon-based metal-free catalysts for key reactions involved in energy conversion and storage, *Advanced Materials* 31 (2019), 1801526.
- [65] J. Ortiz-Medina, Z. Wang, R. Cruz-Silva, A. Morelos-Gomez, F. Wang, X. Yao, M. Terrones, M. Endo, Defect engineering and surface functionalization of nanocarbons for metal-free catalysis, *Advanced Materials* 31 (2019), 1805717.
- [66] P. Solís-Fernández, J. I. Paredes, S. Villar-Rodil, L. Guardia, M. J. Fernández-Merino, G. Dobrik, L. P. Biró, A. Martínez-Alonso, J. M. D. Tascón, Global and local oxidation behavior of reduced graphene oxide. *Journal of Physical Chemistry C* 115 (2011), 7956–7966.
- [67] H. Chang, A.J. Bard, Scanning tunneling microscopy studies of carbon-oxygen reactions on highly oriented pyrolytic graphite, *Journal of the American Chemical Society* 113 (1991), 5588-5596.
- [68] F. Stevens, L.A. Kolodny, T.P. Beebe, Kinetics of graphite oxidation: monolayer and multilayer etch pits in HOPG studied by STM, *Journal of Physical Chemistry B* 102 (1998), 10799-10804.
- [69] L.L. Zhang, X.S. Zhao, Carbon-based materials as supercapacitor electrodes, *Chemical Society Reviews* 38 (2009), 2520-2531.
- [70] J.M. Baptista, J.S. Sagu, U. Wijayantha, K. Lobato, State-of-the-art materials for high power and high energy supercapacitors: performance metrics and obstacles for the transition from lab to industrial scale – a critical approach, *Chemical Engineering Journal* 374 (2019), 1153-1179.
- [71] Z. Song, L. Miao, L. Li, D. Zhu, Y. Lv, W. Xiong, H. Duan, Z. Wang, L. Gan, M. Liu, A universal strategy to obtain highly redox-active porous carbons for efficient energy storage, *Journal of Materials Chemistry A* 8 (2020), 3717-3725.
- [72] X. Bu, L. Su, Q. Dou, S. Lei, X. Yan, A low cost “water-in-salt” electrolyte for a 2.3 V high-rate carbon-based supercapacitor, *Journal of Materials Chemistry A* 7 (2019), 7541-7547.

Electronic Supplementary Material for

**An electrochemical route to holey graphene nanosheets for charge storage
applications**

D.F. Carrasco, J.I. Paredes*, S. Villar-Rodil*, F. Suárez-García,
A. Martínez-Alonso, J.M.D. Tascón

*Instituto de Ciencia y Tecnología del Carbono, INCAR-CSIC,
Francisco Pintado Fe 26, 33011 Oviedo, Spain*

*Corresponding authors' e-mail addresses: paredes@incar.csic.es (J. I. Paredes),
silvia@incar.csic.es (S. Villar-Rodil).

S1. Preparation of mildly reduced graphene oxide (MRGO)

MRGO was obtained via the Hummers route following a previously documented protocol with some minor variations [1]. Briefly, graphite oxide was first prepared from graphite powder by the Hummers method and then exfoliated into individual graphene oxide nanosheets (NSs) in deionized water by sonication. The concentration of the ensuing aqueous graphene oxide dispersion (typically a few milligrams per milliliter) was estimated by UV-vis absorption spectroscopy according to a procedure reported elsewhere [2]. When starting from dilute graphene oxide, a 1 mg mL^{-1} suspension was obtained by dilution and slightly reduced by heating at 95°C for 5 h in the presence of a small amount of ammonia ($\sim 2 \mu\text{L}$ of 25% ammonia solution per milliliter of dispersion). The resulting MRGO suspension was colloidally stable at least for several weeks, but could be recovered in the form of a solid product by sedimentation via high-speed centrifugation (after slight acidification with sulfuric acid to neutral pH), followed by extensive washing and drying of the sediment. However, when starting from concentrated graphene oxide ($\sim 5 \text{ mg mL}^{-1}$), the correspondingly more concentrated MRGO could be aggregated by centrifugation. After discarding the supernatant, the resulting slurry was freeze-dried using a Telstar Cryodos apparatus.

S2. Additional characterization of the materials

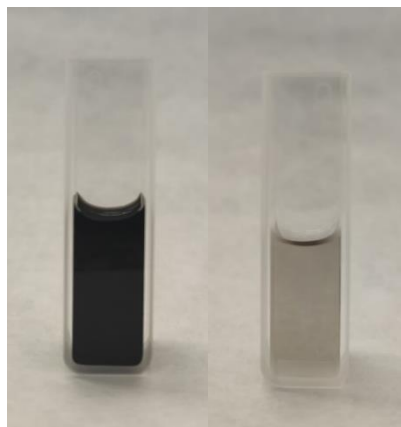


Figure S1. Digital photograph of MRGO in concentrated (left) and diluted (right) aqueous suspension.

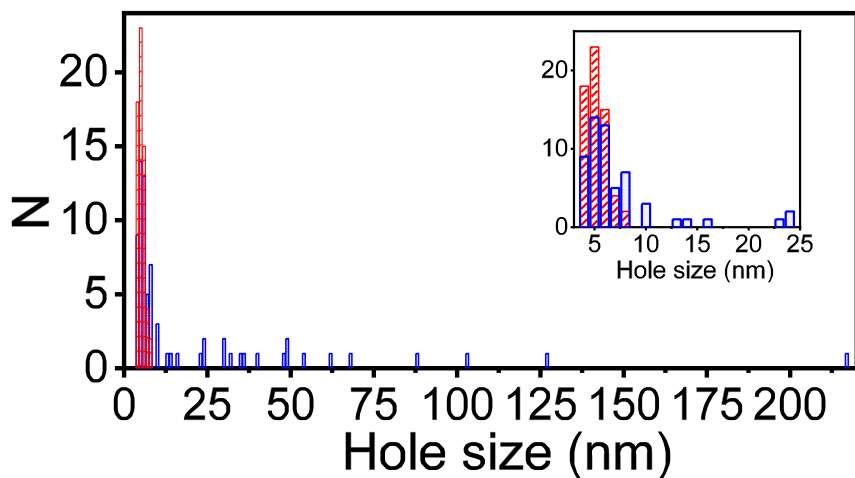


Figure S2. Hole size histograms determined from TEM images for EOG-H (red bars) and MRGO-H (blue bars). The lowest hole size range is magnified in the inset for clarity.

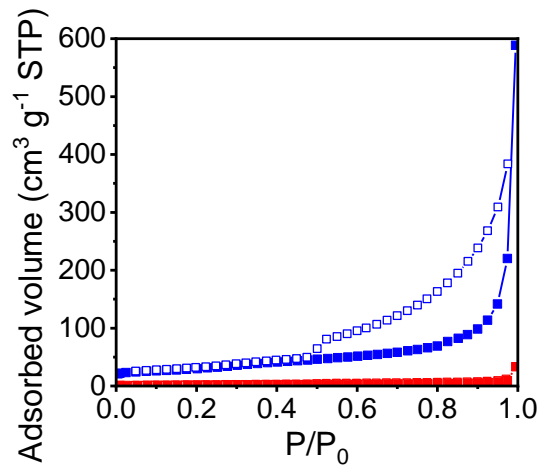


Figure S3. Nitrogen adsorption (filled squares) and desorption (empty squares) isotherms for EOG-H (red symbols) and EOG-H (blue symbols).

S3. Effect of the use of a higher concentration of hydrogen peroxide in the hydrothermal treatment of EOG on the size of the holes generated

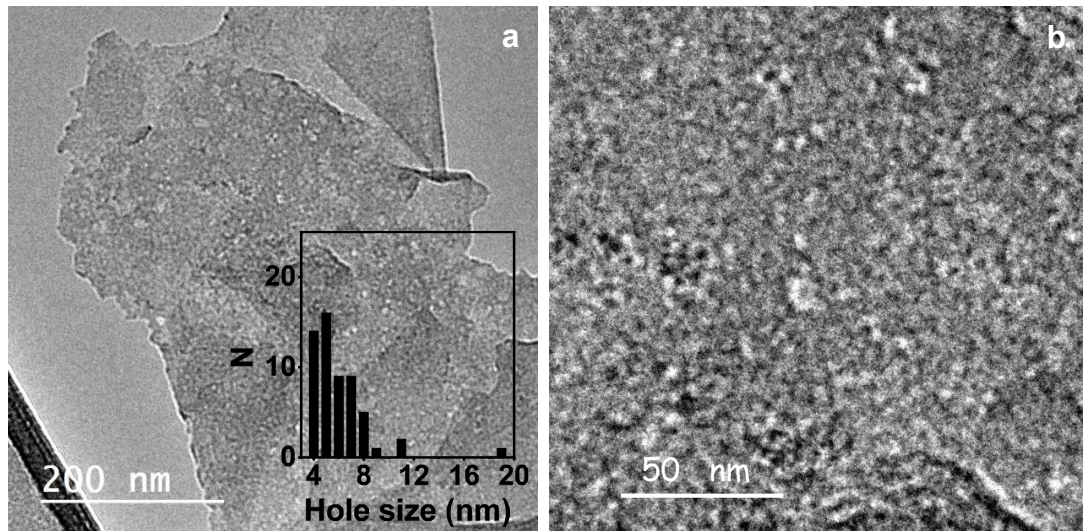


Figure S4. Representative TEM images obtained at different magnifications of holey graphene obtained from electrochemically-derived highly oxidized graphene through chemical treatment with aqueous 4.55 wt% hydrogen peroxide solution (versus 0.9 wt% used in the standard procedure). Inset to c: hole size distribution.

S4. Testing of EOG, EOG-H, MRGO and MRGO-H as electrodes for electrochemical charge storage in three-electrode cell configurations

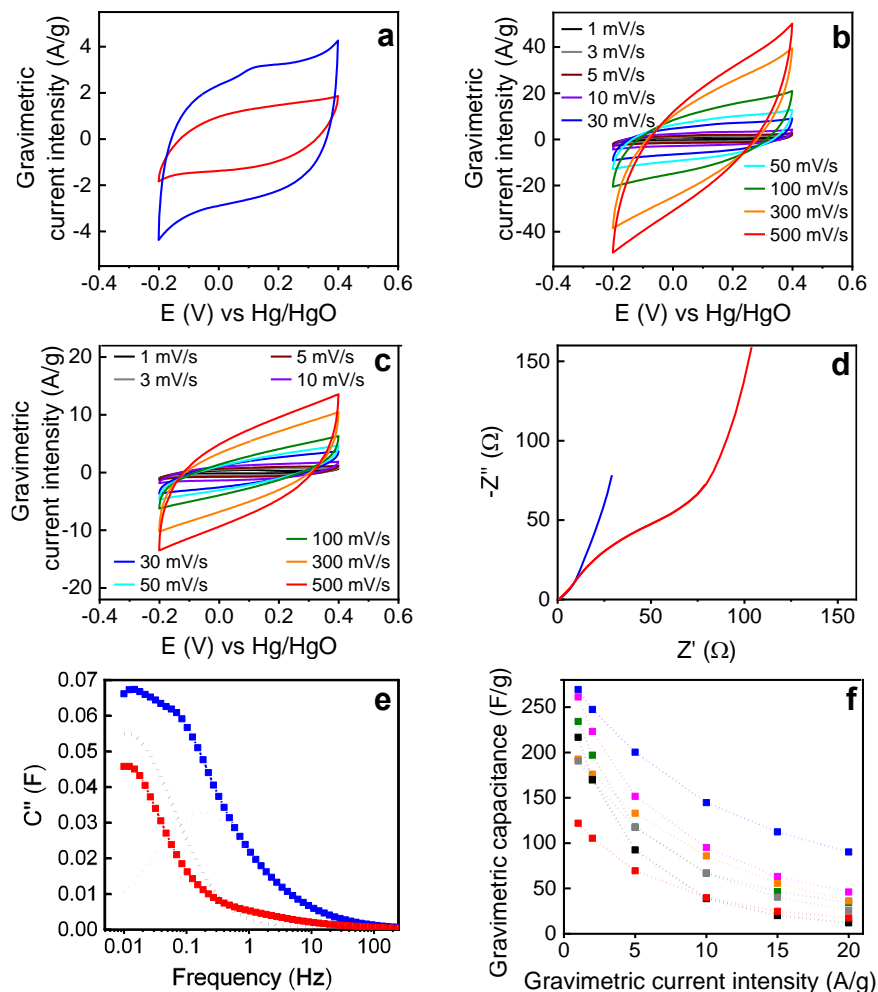


Figure S5. (a) Cyclic voltammograms recorded at a potential scan rate of 10 mV s⁻¹ MRGO (red trace) and MRGO-H (blue trace). (b,c) Cyclic voltammograms recorded at different potential scan rates for (b) MRGO-H and (c) MRGO. (d) Nyquist plots for MRGO (red trace) and MRGO-H (blue trace). (e) Imaginary part of the capacitance versus frequency for MRGO (red trace) and MRGO-H (blue trace). The black and gray dotted lines correspond to the deconvolution of EOG-H profile into two components. (f) Capacitance values measured at different current densities for EOG-H (blue symbols), EOG-H (red symbols) and for electrodes prepared from EOG annealed at temperatures of 400 (green symbols), 450 (orange), 500 (magenta), 550 (gray) and 600 °C (black).

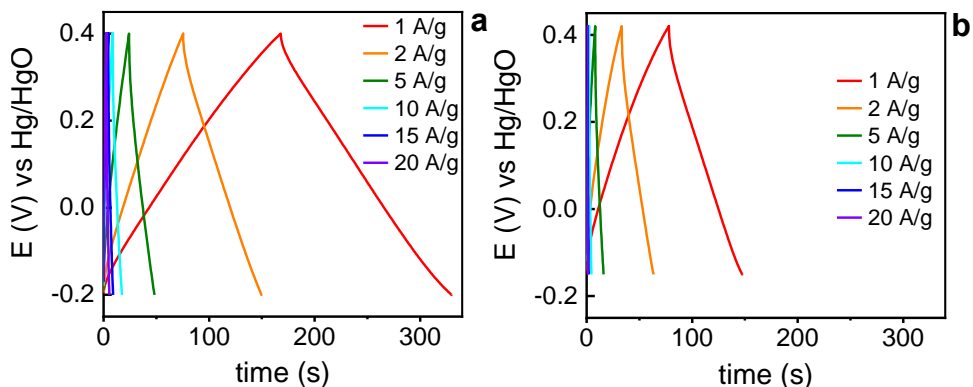


Figure S6. Typical galvanostatic charge-discharge profiles recorded at different current densities between 1 and 20 A g⁻¹ for (a) the EOG-H and (b) EOG electrodes.

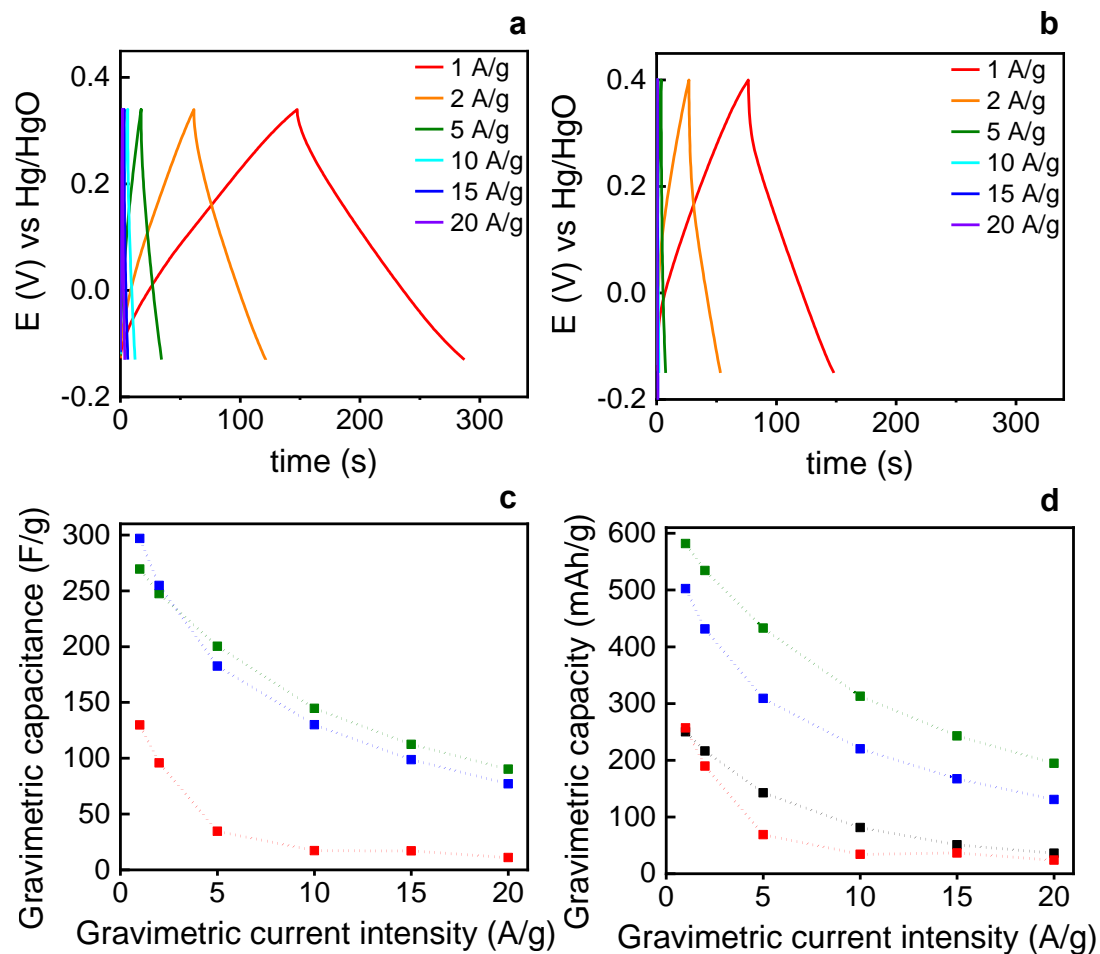


Figure S7. Galvanostatic profiles measured at different current densities for (a) MRGO-H and (b) MRGO. (c) Capacitances for MRGO-H (blue trace), MRGO (red trace) and EOG-H (green trace). (d) Capacity values for EOG (black trace), EOG-H (green trace), MRGO (red trace) and MRGO-H (blue trace).

Table S1. A comparison of the gravimetric capacitance values measured for holey graphene electrodes reported in the literature, mostly obtained from standard graphene oxides (GO), with indication of the applied gravimetric current density (except in the cases where the gravimetric capacitance has been calculated by integration of the CVs, where the potential scan rate is indicated instead).

Electrode material	Electrolyte	Gravimetric capacitance (F g ⁻¹) / gravimetric current density (A g ⁻¹)	Ref.
Chemically-etched, highly oxidized anodically exfoliated graphene	6 M KOH	269/1	Present work
NSs obtained by pyrolysis of Bougainvillea flower powder	1 M Na ₂ SO ₄	458/2.28	3
NSs synthesized through simultaneous activation-graphitization of coconut shell	6 M KOH	268/1	4
Activated carbon	6 M KOH	374/0.5	5
3D assembly of activated rGO NSs	6 M KOH	442/2	6
3D Na ₂ MoO ₄ /rGO hydrogel	1 M KOH	473/10 mV s ⁻¹	7
3D assembly of rGO NSs	6 M KOH	176/0.1	8
rGO NSs	butylmethylpyrrolidinium–dicyanamide ionic liquid	330/5 mV s ⁻¹	9
rGO hydrogel	1 M H ₂ SO ₄ 2.0 M 1-ethyl-3-methylimidazolium tetrafluoroborate in acetonitrile	283/1	10
rGO oxidized in air	6 M KOH	102/0.1; 81/1	11
calcinated GO/ZnO composite	6 M KOH	306/1	12
KOH-activated rGO	6 M KOH	225/1	13
Nitrogen-doped holey graphene	6 M KOH	250/0.5	14
Reduced, chemically-edged GO	6 M KOH	251/1	15
Thermally treated rGO		350/0.1; 197/1	16
rGO NSs	1M H ₂ SO ₄	250/0.5	17

S5. Thermal annealing of EOG

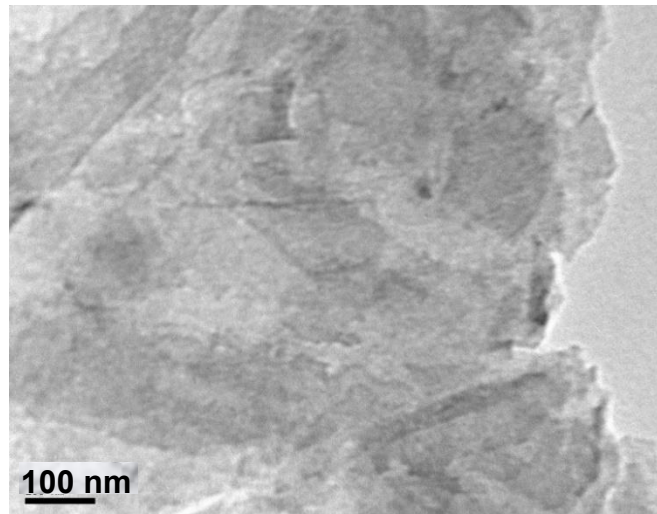


Figure S8. Representative TEM image of EOG thermally annealed at 600 °C.

S6. Testing of EOG-H and MRGO-H as electrodes for electrochemical charge storage in two-electrode symmetric cell configurations

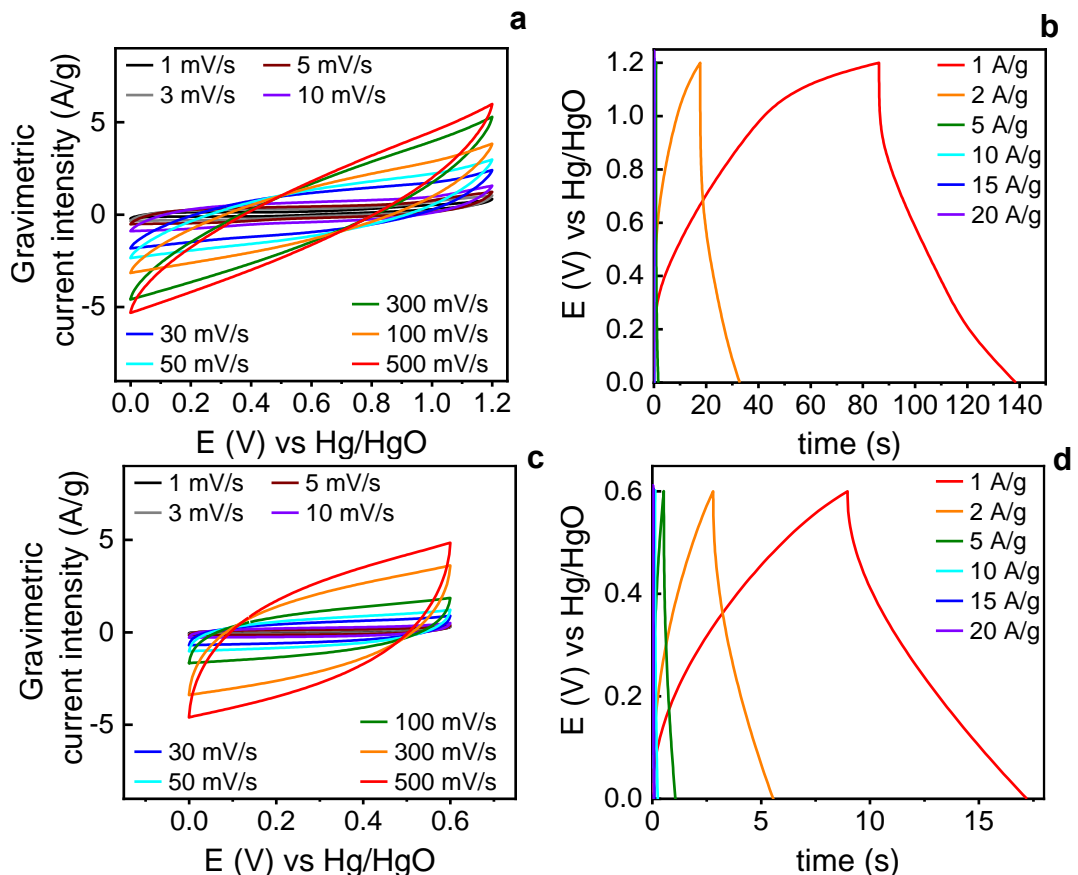


Figure S9. (a,c) Cyclic voltammograms and (b,d) galvanostatic charge-discharge profiles for EOG-H (a,b) and MRGO-H (c,d) symmetric devices in 6 M KOH electrolyte.

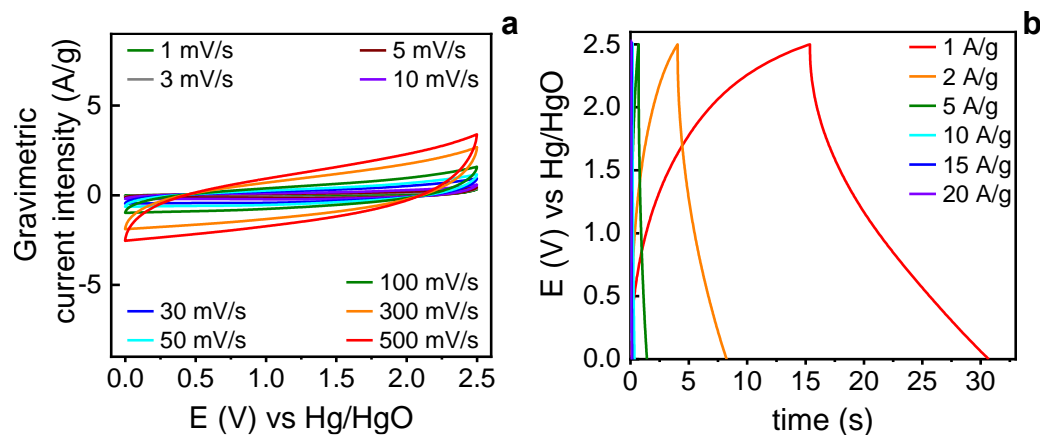


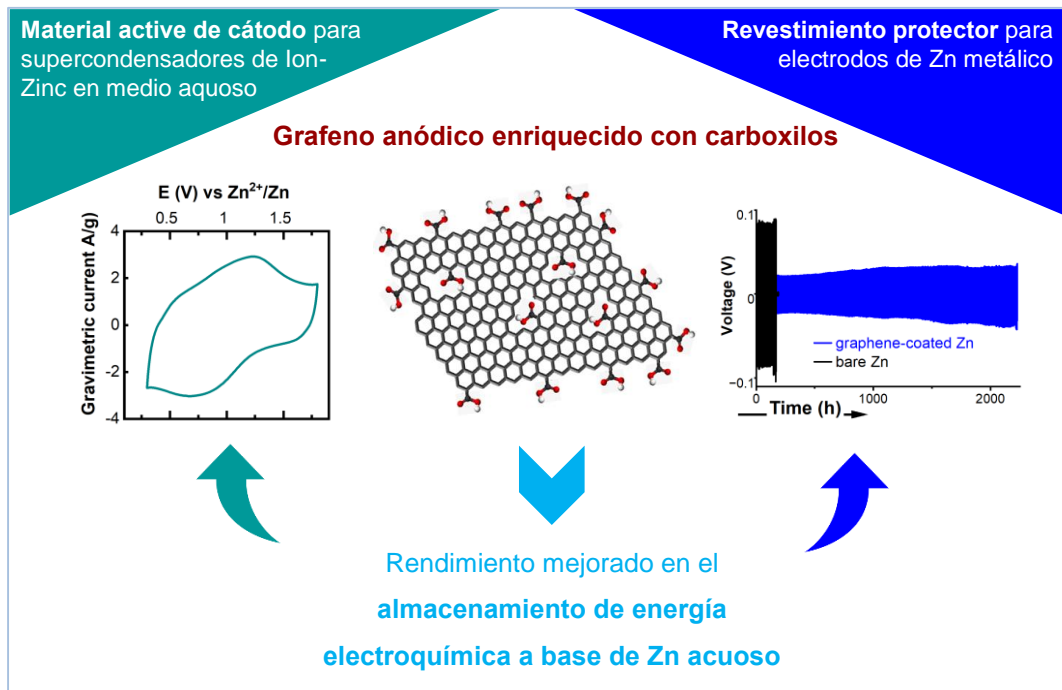
Figure S10. **(a)** Cyclic voltammograms and **(b)** galvanostatic charge-discharge profiles for EOG-H symmetric devices in a concentrated water-in-salt electrolyte (14 m NaClO₄).

References

- [1] M.J. Fernández-Merino, L. Guardia, J.I. Paredes, S. Villar-Rodil, P. Solís-Fernández, A. Martínez-Alonso, J.M.D. Tascón, Vitamin C is an ideal substitute for hydrazine in the reduction of graphene oxide suspensions, *Journal of Physical Chemistry C* 114 (2010) 6426–6432.
- [2] J.I. Paredes, S. Villar-Rodil, P. Solís-Fernández, A. Martínez-Alonso, J. M. D. Tascón, Atomic Force and Scanning Tunneling Microscopy Imaging of Graphene Nanosheets Derived from Graphite Oxide, *Langmuir* 25 (2009) 5957–5968.
- [3] R.P. Panmand, P. Patil, Y. Sethi, S. R. Kadam, M. V. Kulkarni, S. W. Gosavi, N. Munirathnam, B. B. Kale. Unique perforated graphene derived from Bougainvillea flowers for high-power supercapacitors: a green approach, *Nanoscale* 9 (2017) 4801–4809.
- [4] L. Sun , C. Tian, M. Li, X. Meng, L. Wang, R. Wang, J. Yin, H. Fu. From coconut shell to porous graphene-like nanosheets for high-power supercapacitors. *Journal of Materials Chemistry A* 1 (2013) 6462–6470.
- [5] C. Long, X. Chen, L. Jiang, L. Zhi, Z. Fan, Porous layer-stacking carbon derived from in-built template in biomass for high volumetric performance supercapacitors, *Nano Energy* 12 (2015) 141–151.
- [6] J.H. Chang, Y.-H. Hung, X.F. Luo, C.-H. Huang, S. Jung, J.-K. Chang, J. Kong, C.-Y. Su. The hierarchical porosity of a three-dimensional graphene electrode for binder-free and high performance supercapacitors. *RSC Advances* 6 (2016) 8384–8394.
- [7] Y. Song, H. Wang, W. Liu, H. Wang, L. Yan, Na₂MoO₄ as both etcher for three-dimensional holey graphene hydrogel and pseudo-capacitive feedstock for asymmetric supercapacitors, *Journal of Alloys and Compounds*, 780 (2019) 55–64.
- [8] P. Zang, S. Gao, L. Dang, Z. Liu, Z. Lei. Green synthesis of holey graphene sheets and their assembly into aerogel with improved ion transport property, *Electrochimica Acta*, 210 (2016) 171–178
- [9] C. H. Yang, P. L. Huang, X. F. Luo, C. H. Wang, C. Li, Y. H. Wu, J. K. Chang, Holey graphene nanosheets with surface functional groups as high-performance supercapacitors in ionic-liquid electrolyte, *ChemSusChem* 8 (2015) 1779–1786.
- [10] Y. Xu, C. Y. Chen, Z. Zhao, Z. Lin, C. Lee, X. Xu, C. Wang, Y. Huang, M. I. Shakir, X. Duan, Solution Processable Holey Graphene Oxide and Its Derived Macrostructures for High-Performance Supercapacitors *Nano Letters* 15 (2015) 4605–4610.
- [11] Y. Lin, X. Han, C. J. Campbell, J.-W. Kim, B. Zhao, W. Luo, J. Dai, L. Hu, J. W. Connell. Holey Graphene Nanomanufacturing: Structure, Composition, and Electrochemical Properties. *Advanced Functional Materils* 25 (2015) 2920–2927.
- [12] J. Wang, T. Park, J. W. Yi, B. Ding, J. Henzie, Z. Chang, H. Dou, X. Zhang, Y. Yamauchi. Scalable synthesis of holey graphite nanosheets for supercapacitors with high volumetric capacitance. *Nanoscale Horizons*, 4 (2019) 526–530.
- [13] K. Xia, Q. Li, L. Zheng, K. You, X. Tian, B. Han, Q. Gao, Z. Huang, G. Chen, C. Zhou, Controllable fabrication of 2D and 3D porous graphene architectures using identical thermally exfoliated graphene oxides as precursors and their application as supercapacitor electrodes *Microporous and Mesoporous Materials* 237, (2017), 228-236.

- [14] X. Dong, N. Hu, L. Wei, Y. Su, H. Wei, L. Yao, X. Li, Y. Zhang *Journal of Materials Chemistry A*, 4 (2016) 9739–9743.
- [15] Y. Bai, X. Yang, Y. He, J. Zhang, L. Kang, H. Xu, F. Shi, Z. Lei, Z.-H. Liu, Formation process of holey graphene and its assembled binder-free film electrode with high volumetric capacitance. *Electrochimica Acta* 187 (2016) 543–551
- [16] Y. Y. Peng, Y.-M. Liu, J.-K. Chang, C.-H. Wu, M.-D. Ger, N.-W. Pu, C.-L. Chang, A facile approach to produce holey graphene and its application in supercapacitors. *Carbon*, 81 (2015) 347–356.
- [17] S. K. Jhajharia, K. Selvaraj, Non-templated ambient nanoperforation of graphene: a novel scalable process and its exploitation for energy and environmental applications, *Nanoscale*, 7 (2015) 19705–19713.

Resumen artículo II



Los supercondensadores son dispositivos que poseen altas densidades de potencia, pero suelen estar limitados en términos de densidad de energía, quedando en este último aspecto muy por detrás de las baterías. Por esta razón, se están desarrollando los denominados condensadores híbridos, que combinan un electrodo tipo batería con un electrodo tipo condensador, como dispositivos cuyas prestaciones suponen un compromiso entre las de las baterías y las de los supercondensadores. En concreto, en la última década ha tenido lugar un fuerte desarrollo de los condensadores híbridos de ion zinc acuoso (AZICs, *aqueous zinc ion hybrid capacitors*), en los que los materiales grafénicos juegan un importante papel, por ejemplo, como materiales activos de cátodo o en forma de capas protectoras del ánodo metálico de zinc, en este último caso con utilidad también en baterías de ion zinc acuoso (AZIBs, *aqueous zinc ion batteries*).

Resumen Artículo II

Tradicionalmente, los materiales grafénicos para estos fines se obtienen a partir de óxidos de grafito mediante metodologías convencionales (por ejemplo, método de Hummers). Estos materiales se caracterizan por presentar un contenido elevado en grupos funcionales oxigenados como hidroxilo y epóxido, con una cierta presencia también de grupos carboxilo. Sin embargo, se piensa que estos últimos pueden ser los más relevantes para las aplicaciones mencionadas. En el artículo II se presenta una estrategia basada en exfoliación electroquímica para preparar grafeno oxidado con control sobre las proporciones de grupos funcionales oxigenados específicos, en particular grupos carboxilo. Mediante exfoliación electroquímica anódica en medio acuoso con una mezcla de Na₂SO₄, NaCl y NaOH como electrolitos y aditivos de electrolito, se obtuvieron grafenos (denominados AGBE, AGBE+1 y AGBE+2) con cantidades totales de oxígeno similares (relaciones atómicas O/C ~0.26) pero distintas proporciones de grupos funcionales oxigenados. El análisis por XPS confirmó la presencia de distintas poblaciones de tales grupos, de manera que las muestras AGBE y AGBE+2 mostraron proporciones similares de grupos en estado de oxidación 1 (epóxidos e hidroxilos) pero mayor proporción de grupos carboxilo para AGBE+2. Por otro lado, AGBE+1 presentó una mayor proporción de hidroxilos respecto a epóxidos en comparación con los otros dos grafenos.

Las diferencias en las poblaciones de grupos funcionales oxigenados de los grafenos obtenidos se reflejaron en la estabilidad coloidal (menores valores de potencial Z para las muestras con mayor proporción de grupos oxigenados) y la mojabilidad (ángulo de contacto) de las muestras, siendo AGBE+2 la que presentó los mejores valores de mojabilidad (menor ángulo de contacto). En base a los resultados de caracterización fisicoquímica, se determinó que AGBE+2 era el candidato más prometedor para uso como material activo de cátodo en AZICs. De hecho, las medidas con este material mostraron valores de capacidad comparables

a los de otros materiales grafénicos estudiados previamente y una retención de capacidad a corrientes altas superior al resto de los materiales obtenidos. Por otro lado, con el fin de comparar los grafenos obtenidos mediante exfoliación electroquímica con los grafenos utilizados habitualmente como material activo de cátodo (obtenidos a partir de óxido de grafito), se obtuvieron dos grafenos mediante reducción química (NaBH_4) utilizando óxido de grafito (Hummers) como precursor. Uno de estos dos grafenos poseía un grado de oxidación similar al de AGBE+2 (rGO-0.26) y el otro una menor oxidación, pero mayor conductividad eléctrica (rGO-0.21). En ambos casos, el comportamiento como cátodo en dispositivo AZIC fue inferior al del grafeno anódico.

Pese a que los resultados obtenidos para AGBE+2 era comparables a los de grafenos usados como cátodos en AZICs, los valores eran limitados en términos absolutos, probablemente debido al reapilamiento de las láminas que tiene lugar durante el proceso de preparación del electrodo. Para mitigar este efecto, se utilizó mononucleótido de flavina (FMN, *flavin mononucleotide*) como molécula espaciadora anfifílica y con actividad redox que puede contribuir a la capacidad del electrodo. Se estudiaron varias relaciones másicas FMN/AGBE+2 (1:6, 2:6, 3:6 y 6:6), observándose mayores valores de capacidad en todos los casos respecto al grafeno son FMN, con un valor óptimo para la relación 6:6 ($\sim 75 \text{ mAh cm}^{-3}$ a 0.1 A g^{-1}).

Se investigó también el comportamiento de los grafenos obtenidos como recubrimientos protectores para el ánodo de zinc. Se recubrió la superficie de zinc pulido con el material correspondiente hasta varios micrómetros de grosor, el cual fue sometido a ciclos de depósito y decapado de zinc (*plating/stripping*) en dispositivos simétricos Zn//Zn a distintas densidades de corriente, observándose el mejor comportamiento para recubiertos con grafeno AGBE+2. Los resultados de cronoamperometría sugirieron que la protección del electrodo de zinc por parte de

Resumen Artículo II

AGBE+2 se debe a una nucleación y crecimiento mucho más uniformes del metal sobre la superficie del electrodo, atribuible a centros con alta afinidad por el zinc (p.e., grupos carboxílo) presentes en las láminas del grafeno ABGE+2. Finalmente, los electrodos de zinc protegidos por grafeno se evaluaron en dispositivos reales utilizando como material activo de cátodo MoS₂ nanoestructurado con fase 1T predominante y preparado mediante síntesis hidrotérmica. Se observó una mejora en la ciclabilidad del dispositivo en comparación con un ánodo de zinc sin recubrir.

Finalmente, es de prever que la modulación de los grupos funcionales oxigenados introducidos en grafeno mediante un proceso anódico sencillo como el aquí descrito ofrezca oportunidades de aplicación no sólo en el campo del almacenamiento electroquímico de energía, sino también en áreas como la purificación de agua mediante nanofiltración o la administración de fármacos, facilitada por la derivatización selectiva de grupos oxigenados específicos.

ARTÍCULO II

Chemically tuning graphene via anodic exfoliation for enhanced performance in aqueous zinc-based electrochemical energy storage applications

D.F. Carrasco, E. Álvarez-Rubiera, S. Villar-Rodil*, A. Martínez-Jódar,
J.M.D. Tascón, F. Suárez-García, J.I. Paredes*

*Instituto de Ciencia y Tecnología del Carbono, INCAR-CSIC,
C/Francisco Pintado Fe 26, 33011 Oviedo, Spain*

*Corresponding authors.

E-mail address: silvia@incar.csic.es (S. Villar-Rodil),

E-mail address: paredes@incar.csic.es (J. I. Paredes).

Abstract

Graphene materials are attractive for use in novel aqueous electrochemical energy storage devices, including aqueous zinc-ion batteries (AZIBs) and hybrid capacitors (AZICs). Ideally, such materials should be readily accessible by eco-friendly routes and possess physicochemical features beneficial for the intended application. Here, we propose an anodic exfoliation strategy, using a proper combination of common salts/bases as the aqueous electrolyte, for the preparation of highly oxidized graphenes with some control over the populations of their oxygen groups and retention of electrical conductivity ($\sim 10^2\text{--}10^3 \text{ S m}^{-1}$). As an active cathode material for AZIC cells, the hydrophilic, carboxyl-enriched anodic graphene processed into a compact film outperformed reduced graphene oxides derived from common routes (e.g., Hummers' method), in terms of capacity and rate capability. Furthermore, the performance of this new anodic graphene was enhanced by combining it with a multifunctional biomolecule (flavin mononucleotide), which promoted the cathode wettability and provided extra capacity due to its redox-active center, particularly at higher currents. The carboxyl-enriched graphene was also shown to act as an effective coating layer for the protection of the zinc metal electrode in AZICs/AZIBs, extending its cycle life for longer than is usually attained with carbon-based protective coatings.

Keywords: graphene, anodic exfoliation, tunable oxygen groups, aqueous zinc-ion batteries (AZIBs), aqueous zinc-ion hybrid capacitors (AZICs), zinc metal anode stabilization

1. Introduction

Lithium-ion batteries currently dominate the market of electrochemical energy storage (EES) systems owing to their considerable energy density, long calendar/cycle life and high round-trip efficiency, among other merits [1,2]. However, they also suffer from significant drawbacks, such as a relatively high cost, safety risks associated to the use of organic electrolytes and a limited supply of lithium resources and other metals that is unlikely to cope with the increasing demand of both mobile and stationary applications projected for the coming decades. In the pursuit of alternatives, aqueous EES devices based on widely available multivalent metals (e.g., Zn, Ca, Mg or Al), including multivalent metal-ion batteries [3] and hybrid capacitors [4], have become in recent years a research hotspot. Among them, aqueous zinc-ion batteries (AZIBs) [5,6] and hybrid capacitors (AZICs) [7] are considered especially attractive, mainly as a result of the combination of advantageous features that this metal exhibits: (1) a high specific capacity (820 mAh g^{-1} , 5855 mAh cm^{-3}), (2) a suitable redox potential (-0.76 V vs standard hydrogen electrode for the Zn/Zn^{2+} couple), together with a relative stability in mildly acidic to alkaline electrolytes, implying that metallic zinc can be directly used as an anode in aqueous EES devices, and (3) a reasonable abundance and broad distribution in the Earth's crust, combined with modest production costs and mature recycling technologies. Consequently, intensive efforts are being directed at present towards the development of several types of AZIBs and AZICs, with an emphasis on advances in electrode materials, electrolytes and other components aimed at improving different performance metrics of the devices [8–12].

Due to their wide availability, lightweight, versatility in terms of morphology and heteroatom doping, high electrical and thermal conductivity, as well as good mechanical and chemical stability, sp^2 -based carbon materials are

being explored as key components of AZIBs and AZICs, where they can play very different roles [13]. For example, on the cathode side, they are potentially useful as the active material in AZICs (capacitor-type electrode) [14,15], and in AZIBs they are investigated as a conductive supporting substrate/matrix or as an encapsulating layer to prevent degradation and buffer volume variations of the active material [16,17]. On the anode side, carbon materials can serve as a host scaffold for zinc plating/stripping or as an artificial protective interphase to extend the cycle life of metallic zinc [16–18]. Also, with the latter purpose, a few carbons have been investigated as a separator coating or as a colloidal additive for the electrolyte [18]. Carbon-based current collectors are also a subject of exploration [15,16]. The range of carbon materials explored for these purposes includes porous carbons of different origins (biomass, synthetic polymers, metal-organic frameworks, etc), carbon nanotubes (CNTs) and (nano)fibers, carbon black, graphene and graphene derivatives, as well as graphdiynes. Graphene derivatives, in particular, are the focus of considerable attention as a result of some specific attributes of theirs, e.g., two-dimensional nanosheet morphology, high mechanical flexibility and propensity to assemble into useful macroscopic objects, such as thin films, fibers or aerogels. Here, nanosheets derived from graphite oxide, i.e., graphene oxide (GO) and reduced graphene oxide (rGO) nanosheets, are usually the graphene-based materials of choice for studies of AZICs, AZIBs and other types of aqueous zinc-based batteries [15–19]. This is mainly because GO and rGO are readily accessible, cost-effective materials and exhibit a rich surface chemistry in the form of oxygen functional groups that can be beneficial to some of their roles in these aqueous EES devices.

Still, the use of standard GO/rGO is not without its own drawbacks and limitations. First, the production of the corresponding precursor graphite oxides by the classical (Hummers, Brodie) methods or some of their recent variants involves the consumption of large amounts of concentrated acids and harsh oxidants, which

compromises the environmental friendliness of the process [20,21]. Second, the particular surface chemistry of standard GO/rGO nanosheets is not necessarily the most appropriate for their role in AZIBs/AZICs. Such a surface chemistry is generally dominated by the presence of large numbers of hydroxyl and epoxy groups [22,23]. However, other oxygen moieties might be more relevant in this context, such as carboxylic acids and their ionized counterpart (i.e., carboxylates), which are also present in GO/rGO, although only in relatively small proportions [24]. The interaction of water molecules with carboxylic groups on carbon-based surfaces is generally stronger than their interaction with other oxygen functional groups [25,26]. Hence, graphenes enriched with the former moieties are expected to be more readily wettable by the aqueous electrolyte when used as an electrode material (either in an active or supporting role) in AZIBs/AZICs, which could lead to a better performance of the device. Likewise, carboxylic acids have been shown to interact quite strongly with aqueous Zn^{2+} ions from the electrolyte of AZIBs/AZICs (i.e., they are zincophilic) [27]. Indeed, their presence in the zinc anode-electrolyte interphase (e.g., as part of artificial protective layers) favors ion desolvation and a more uniform plating of the metal, thus alleviating the issue of dendrite formation and extending the anode life. From these considerations, it is clear that the availability of milder, more sustainable routes to graphenes that exhibit improved characteristics for their intended purpose in AZIBs/AZICs, as well as in other applications, would be an important asset from a practical perspective.

Over the last decade, the electrochemical exfoliation of graphite, particularly under aqueous anodic conditions, has emerged as an appealing alternative to the graphite oxide and other common top-down routes to graphene and its derivatives, with promising prospects of application in different areas including EES [28–30]. The attractions of the anodic route are varied, such as simplicity and celerity of operation, use of mild chemical reagents (aqueous

electrolytes based on conventional salts of low environmental impact) and high delamination efficiency, both in terms of yield and exfoliation degree (nanosheets made up of single to few graphene layers). Further, the aqueous anodic process is intrinsically oxidative due to the generation of highly reactive oxygen radicals (mainly, the hydroxyl radical) from the electrolytic oxidation of water molecules [31]. This implies that the resulting graphene nanosheets are usually decorated with oxygen functional groups to levels comparable to those of standard rGO materials [32,33]. More significantly, by leveraging the versatility of this method as regards electrolyte composition, the overall oxidation degree of the nanosheets can be tuned within a broad range, from very low or almost no oxidation [34,35] to a degree close to that of unreduced standard GO [36–38]. Nonetheless, the anodic oxidation process generally affords nanosheets with carbon atoms in a low oxidation state, i.e., associated to hydroxyl or epoxy moieties, which is similar to the case of standard GO. Indeed, oxygen groups involving carbon atoms in high oxidation states (carboxyls, carbonyls) are usually present in very low proportions even in extensively oxidized anodic graphenes [36–38]. The availability of straightforward protocols that allow tuning the type of oxygen groups, especially to afford the introduction of carboxyls, could be highly relevant to enhance the performance of anodic graphenes in aqueous zinc-based EES devices and other applications (e.g., filtration membranes [39]). However, such electrochemical protocols have not been explored.

In the present work, we introduce a simple strategy for the preparation of electrochemically exfoliated graphene that is enriched with carboxyl moieties and exhibits increased hydrophilicity. Such a strategy relies on a proper modulation of the aqueous electrolyte by means of common inorganic additives, yielding nanosheets where carboxyls/carbonyls make up about 33% of the total oxygen groups, compared to 22% for standard anodic graphenes. When tested as an active cathode material in AZICs, the carboxyl-enriched nanosheets outperformed their

standard anodic graphene and rGO counterparts in terms of capacity and rate capability, thus highlighting the benefits of finely tuning the graphene chemistry for this application. Further, in the pursuit of more environmentally benign and nature-based strategies for the development of EES devices, we demonstrate that the cathode performance of this new anodic graphene can be enhanced by combining it with a redox-active amphiphilic biomolecule (flavin mononucleotide). Finally, the carboxyl-enriched anodic graphene was also used as a protective layer for the zinc anode, extending its cycle life for longer than is usually achieved with most carbon-based materials. Taken together, the present results attest to the versatility of this newly developed anodic graphene for aqueous EES.

2. Experimental

2.1. Materials and reagents

High purity graphite rods (3.05 mm in diameter, 30.5 cm in length) were purchased from Thermo Scientific. Graphite foil (Papyex I980, 0.5 mm in thickness) was acquired from Mersen. Na₂SO₄, NaCl, NaOH, 2 M ZnSO₄ solution, flavin mononucleotide (FMN, in sodium salt form) and zinc foil (dimensions: 100×100×0.25 mm³) were acquired from Sigma-Aldrich. Carbon paper sheets (dimensions: 300×230×0.2 mm³) were obtained from QuinTech. Hydrophilic polytetrafluoroethylene (PTFE) membrane filters (47 mm in diameter, 0.2 µm of pore size) and nylon membrane filters (25 mm in diameter, 0.2 µm of pore size) were purchased from Sterlitech. Ultrapure deionized water (resistivity: 18.2 MΩ cm) was used throughout the study and obtained from a Milli-Q Reference water purification system (Millipore Corporation).

2.2. Preparation of anodically exfoliated graphenes

A two-electrode setup was used to prepare different graphene samples by electrochemical (anodic) exfoliation of graphite rod. To this end, two graphite rod pieces about 5 cm long were vertically immersed in 80 mL of the aqueous electrolytic solution at a distance of ~2 cm from each other and connected to a DC power supply (E3633A apparatus, from Keysight Technologies) via crocodile clips. Only around 80% of the graphite rod length was actually submerged in the electrolyte. Then, a bias voltage of 10 V was applied between the two electrodes for 1 h. During this time, very small fragments were seen to slowly detach from the positively biased graphite electrode (anode) and to remain suspended in the electrolytic solution, whereas its counter electrode (cathode) remained unchanged. After the bias voltage was turned off, the electrolytic solution was passed through filter paper to collect the detached graphitic particles, which were subsequently washed with copious amounts of water until the pH of the filtrate was around 6–7 (this typically required between 0.5 and 1 L of water). The collected particles were then gently removed from the filter paper and bath-sonicated in water for 3 h (Ultrasons bath sonicator, from J.P. Selecta) to extract individual nanosheets, which became suspended in the aqueous medium. Finally, the individualized nanosheets were separated from the non/poorly exfoliated material by sedimenting the latter via low speed centrifugation (200 g, 20 min; Eppendorf 5430 microcentrifuge), retaining the former in the supernatant as a stable colloidal suspension for further use. Different anodic graphene samples were prepared according to the actual composition of the electrolyte, namely, samples AG-BE (0.1 M Na₂SO₄ as the electrolyte), AG-BE+1 (0.1 M Na₂SO₄ and 0.1 M NaOH), and AG-BE+2 (0.1 M Na₂SO₄, 0.1 M NaOH and 0.1 M NaCl). For comparison, graphene samples were also obtained using graphite foil in the anodic exfoliation experiments instead of graphite rod.

2.3. Characterization techniques

The materials were characterized by UV-vis absorption spectroscopy, X-ray photoelectron spectroscopy (XPS), Raman spectroscopy, field-emission scanning electron microscopy (FE-SEM), scanning transmission electron microscopy (STEM), atomic force microscopy (AFM), X-ray diffraction (XRD), as well as by zeta potential, dynamic light scattering (DLS), water contact angle and electrical conductivity measurements. UV-vis absorption spectra were recorded on a double-beam Genesys 180 spectrophotometer (Thermo Fischer Scientific). XPS was accomplished on a SPECS apparatus equipped with a Phoibos 100 hemispherical electron energy analyzer, recording spectra at a take-off angle of 90° and working at a pressure $<10^{-7}$ Pa with a monochromatic Al K α X-ray source (14.00 KV, 175 W). The photoexcited electrons were analyzed in the constant pass energy mode, at a pass energy of 50 and 10 eV for survey and high-resolution core-level spectra, respectively. Fitting of the core-level spectra into different components was performed by means of a standard least squares algorithm after subtraction of the Shirley background. Each fitted component was taken as a convolution of a Gaussian and a Lorentzian function (80:20), except for the main component of the C 1s envelope (C=C component, located at \sim 284.5 eV), for which an asymmetric function with a long tail on the high binding energy side was taken as a more realistic depiction [40]. Raman spectroscopy was carried out with a Renishaw in Via Qontor apparatus, working at a laser excitation wavelength of 532 nm (green line) and using an incident laser power (< 0.5 mW) sufficiently low so as to minimize sample damage. The Raman spectra were measured at 20 different locations in each sample, the integrated intensity ratios of Raman bands being calculated as the average of such parameter for the 20 spectra. Graphene samples for XPS and Raman spectroscopy were prepared from their colloidal dispersions by sequentially drop-casting small volumes of dispersion onto circular stainless-steel

discs (12 mm in diameter) that were pre-heated at 50–60 °C, until a black film was seen to uniformly cover the whole disc. FE-SEM and STEM imaging was performed on a Quanta FEG instrument (FEI Company) that worked at a bias voltage of 20–25 kV. To prepare graphene specimens for STEM, a few microliters of their aqueous suspensions were dropped onto copper grids (200 square mesh) covered with a thin continuous carbon film (Micro to Nano Innovative Microscopy Supplies) and then allowed to dry under ambient conditions. AFM images of the anodic graphene nanosheets were recorded with a Nanoscope IIIa Multimode apparatus (Veeco Instruments) working in the tapping mode of operation. To this end, rectangular, gold-coated silicon cantilevers with nominal spring constant of 40 N m⁻¹ and resonance frequencies in the 250–300 kHz range were used. For proper AFM imaging, the graphene nanosheets were supported onto atomically flat highly oriented pyrolytic graphite (HOPG) substrates. This was accomplished by drop-casting a few tens of microliters of aqueous graphene dispersion onto a freshly cleaved HOPG substrate pre-heated at 50–60 °C. XRD patterns of the hydrothermally synthesized MoS₂ materials were acquired with a Bruker D8 Advance diffractometer in the 2θ range between 5° and 80°, with a step size/time of 0.02°/2 s and a Cu K_α anode. Zeta potential and DLS measurements of aqueous graphene dispersions were carried out on a Litesizer DLS 500 instrument (Anton Paar), equipped with a 658 nm wavelength laser. The experiments were done in quintuplicate at an angle of 15° for zeta potential and 90° for DLS. The zeta potential was derived using the Smoluchowski equation. Contact angles of neat water and aqueous electrolyte (2 M ZnSO₄) on thin graphene films were determined with a DSA25S Drop Shape Analyzer, from Krüss. The films were obtained following the same procedure as that used to prepare specimens for XPS and Raman spectroscopy (see above). The electrical conductivity of paper-like graphene films was evaluated by the four-point probe method. To this end, paper-like films were prepared by vacuum filtration of aqueous graphene dispersions (250 mL, 0.1 mg mL⁻¹) through

hydrophilic PTFE membrane filters. The film thickness (typically in the range of a few tens of micrometers) was estimated with a digital micrometer.

2.4. Electrochemical measurements

All the electrochemical experiments were carried out in a VSP potentiostat (BioLogic Science Instruments) and, unless stated otherwise, using aqueous 2 M ZnSO₄ solution as the electrolyte. The anodic graphenes were tested as a cathode material of AZIC cells. The graphene cathodes were prepared in the form of thin (~6–8 µm) compact films supported onto carbon paper. To this end, a relatively concentrated aqueous graphene dispersion (~1–2 mg mL⁻¹) was drop-cast (~200 µL) onto a circular piece of carbon paper (diameter: 10 mm) and then allowed to dry at 50–60 °C under ambient pressure. This process was repeated an additional 2–3 times until a graphene mass loading of 1.0–1.2 mg cm⁻² was reached. Discs 10 mm in diameter were punched from the zinc foil for use as the AZIC anode, whereas circular pieces of nylon membrane filter (13 mm in diameter) acted as the separator. Before mounting the cell, the cathode and separator were individually soaked in the electrolyte overnight, and the zinc metal anode was manually polished twice with fine sandpaper (first with P1200 grit and then with P4000 grit). The cells were assembled in a Swagelok-type configuration with stainless steel current collectors. Both cyclic voltammograms (CVs) at different potential scan rates and galvanostatic charge/discharge (GCD) curves at different gravimetric currents were recorded (voltage range between 0.3 and 1.8 V vs Zn/Zn²⁺). Electrochemical impedance spectroscopy (EIS) tests were conducted at the open circuit voltage, with a voltage amplitude of 10 mV and frequencies between 100 kHz and 10 mHz. Cyclability studies were performed by continuously recording GCD profiles at a gravimetric density of 1 A g⁻¹. To test the anodic graphenes as a protective coating for the zinc metal electrode, graphene films were deposited on the latter by a simple drop-casting procedure. Specifically, a fixed volume (200 µL) of an aqueous

graphene dispersion ($\sim 1 \text{ mg mL}^{-1}$) was dropped onto a previously polished zinc foil disc (10 mm in diameter) and allowed to dry at 50–60 °C under ambient pressure. This process was then repeated once, so that 400 μL of dispersion were finally deposited on the zinc disc. The electrochemical tests were conducted in Swagelok-type cells, with nylon membrane filter as the separator (circular pieces 13 mm in diameter). The cyclability of the zinc plating/stripping processes was probed by recording consecutive GCD profiles in symmetric cells at different areal currents (e.g., 0.5, 2 and 5 mA cm^{-2}) for 1 h. Linear sweep voltammograms (LSVs) were obtained for symmetric cells in a three-electrode configuration (Ag/AgCl as the reference electrode) using 2 M Na_2SO_4 as the electrolyte. Chronoamperometric curves were also recorded in symmetric cells, applying a bias voltage of -150 mV for a few minutes. Coulombic efficiency (CE) measurements were carried out in asymmetric cells, where a (bare or graphene-coated) zinc electrode was coupled with a titanium counter electrode.

3. Results and discussion

3.1. Strategy and rationale for the preparation of carboxyl-enriched anodic graphene

The aqueous anodic exfoliation of graphite to give graphene nanosheets is typically carried out using sulfate-based electrolytes, such as H_2SO_4 , $(\text{NH}_4)_2\text{SO}_4$ or Na_2SO_4 [41–43]. This is mainly due to the higher propensity of the sulfate anion to intercalate into graphite compared to other common anions (nitrate, perchlorate, phosphate, etc.), which in turn favors a more efficient delamination of the bulk material [44]. It is also known that anodic graphenes coming from more compact, denser graphites (e.g., graphite rod, highly oriented pyrolytic graphite) tend to be more oxidized than graphenes derived from graphites having a relatively loose, void-rich morphology (e.g., graphite foil obtained from roll pressing of expanded

graphite) [45,46]. Such a distinct outcome based on graphite type is attributed to a slower exfoliation rate taking place in denser graphites. Here, the highly compact stacking of graphite layers makes anion insertion to be more sluggish and more reliant on layer oxidation (the latter facilitates intercalation by locally increasing the interlayer distance) [42,45]. Consequently, graphite fragments require more time to expand and detach from the graphite electrode, and are therefore exposed to the oxidizing conditions of the anodic treatment for longer times, which finally results in exfoliated graphene nanosheets with higher levels of oxidation. Thus, to promote the formation of oxygen-containing groups in the anodically derived nanosheets, a compact graphite (graphite rod) was selected for the exfoliation experiments with 0.1 M Na₂SO₄. Details of the anodic delamination procedure followed here are given in the Experimental section. Briefly, a two-electrode setup was implemented, where two graphite rods acted as the anode and cathode. After being immersed in the electrolytic solution, a bias voltage of 10 V was applied between the two graphite electrodes for 1 h. During this process, small expanded fragments were seen to slowly detach from the anode [see field-emission scanning electron microscopy (FE-SEM) images of the material before and after expansion in Fig. S1 [section S1 of the Electronic Supplementary Material (ESM)], while the cathode remained unchanged. At the end of the treatment, these fragments were collected, washed with deionized water and sonicated to extract individual graphene nanosheets into the aqueous medium. Finally, the sonicated product was centrifuged to separate the well-exfoliated nanosheets remaining in the supernatant as an aqueous colloidal dispersion from the non/poorly exfoliated material (sediment), with the former being kept for further use.

Fig. 1a shows the high-resolution C 1s core-level spectrum, recorded by X-ray photoelectron spectroscopy (XPS), for the graphene sample obtained by anodic exfoliation of graphite rod with the sulfate salt (sample referred to as AG-BE, denoting Anodic Graphene obtained with the Base Electrolyte, where “base

“electrolyte” is used in the sense that this electrolyte will be common to the different aqueous electrolyte media tested in this work). For comparison, the corresponding spectrum of graphene prepared with graphite foil under the same conditions is shown in Fig. S2 (section S2, ESM). The spectra were peak-fitted to several components, centered at about 284.6 eV (carbon atoms in unoxidized, graphitic/graphenic sp^2 -hybridized structures), 286.5 eV (carbon atoms from hydroxyl groups), 287.0 eV (carbon atoms from epoxy groups), 288.0 eV (carbon atoms from carbonyl and carboxylate groups), 289.0 eV (carbon atoms from carboxylic acid groups) and 290.5 eV ($\pi \rightarrow \pi^*$ shake-up satellite) [47,48]. It should be noted that the contributions of hydroxyl and epoxy groups are frequently fitted to a single C 1s component (carbon atoms in an oxidation state of +1), rather than to two distinct components. However, the actual binding energy of the C 1s level is known to differ slightly (~0.5 eV) for hydroxyl and epoxy groups [47]. Further, in the present case the position of the single component was seen to vary to a comparable extent depending on the specific anodic graphene under scrutiny. Such an observation suggested the presence of different relative populations of hydroxyl and epoxy groups, thus warranting a peak-fitting procedure with distinct, explicit components for these two oxygen functional groups. Likewise, the assignment of carboxylic and carboxylate groups to distinct components of the fitting was made according to a recent report, where deprotonation of carboxylic acids in carbon materials was demonstrated to lead to a down-shifting of the binding energy of the corresponding C 1s level [47].

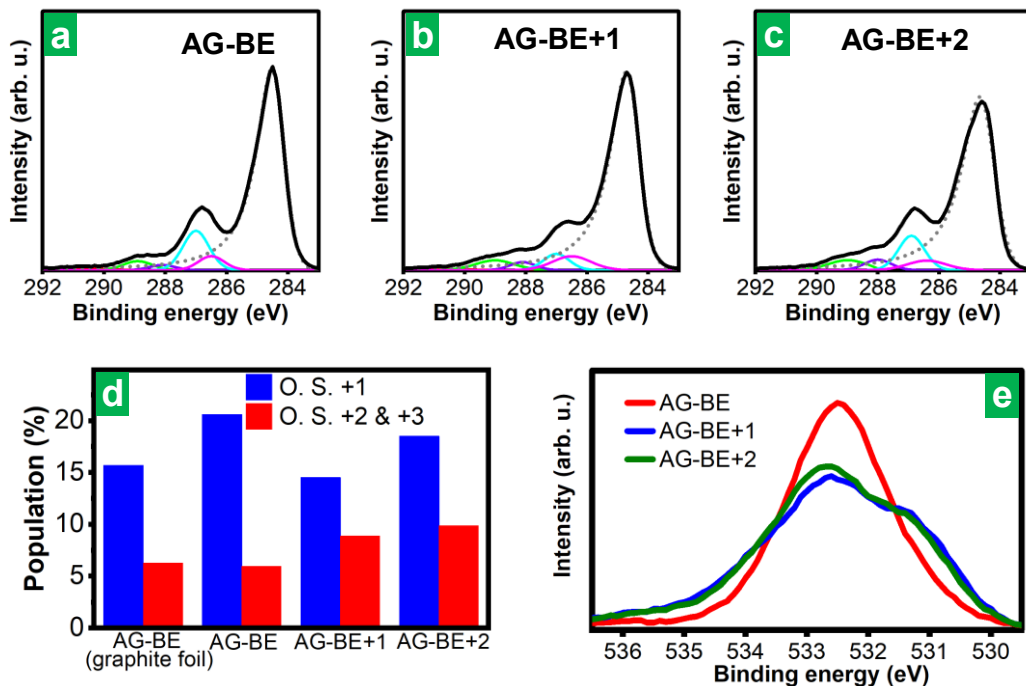


Figure 1. (a) High resolution C 1s XPS core-level spectra of graphene obtained by anodic exfoliation of graphite rod with (a) 0.1 M Na₂SO₄ (AG-BE), (b) 0.1 M Na₂SO₄ with 0.1 M NaOH as a single additive (AG-BE+1) and (c) 0.1 M Na₂SO₄ with 0.1 M NaOH and 0.1 M NaCl as a dual additive. The C 1s signal has been peak-fitted into 6 components: graphitic/graphenic carbon (dotted gray trace), carbon bonded to hydroxyl (magenta trace), epoxy (cyan), carbonyl and carboxylate (violet trace) and carboxyl (green) groups, and $\pi-\pi^*$ shake-up satellite (red). (d) Populations of carbon atoms from oxygen-containing groups in low (+1; i.e., hydroxyl, epoxy groups) and high (+2/+3; i.e., carbonyl, carboxylate, carboxyl groups) oxidation states (O. S.), calculated as the sum of the percentages of the corresponding C 1s components versus the total C 1s signal for each graphene material. (e) High resolution O 1s spectra for AG-BE (red trace), AG-BE+1 (blue trace), AG-BE+2 (green trace).

Comparison of the C 1s spectra of the anodic graphenes obtained from graphite rod (Fig. 1a) and graphite foil (Fig. S2) revealed that the graphite rod-derived graphene was, as expected, more oxidized than its graphite foil-derived counterpart, i.e., the components associated to oxidized carbon atoms were more intense in the former material. Indeed, the overall O/C atomic ratio calculated from the XPS survey spectra (Fig. S3 in section S2 of the ESM) was substantially higher

for the former graphene (0.24 vs 0.17 for the graphite foil-derived graphene). The populations of carbon atoms from oxygen-containing groups in low and high oxidation states, i.e., +1 oxidation state (hydroxyl, epoxy groups) and +2/+3 oxidation states (carbonyl, carboxylate, carboxyl groups), respectively, were quantified from the relative areas of the corresponding C 1s components and are presented in Fig. 1d. The main difference between the graphite rod- and foil-derived samples lay in the proportion of carbon atoms in a low oxidation state (+1), which was significantly larger in the former (20.6 vs. 15.7%). By contrast, the amount of carbon atoms in high oxidation states (+2/+3) was very similar for both materials (~6% for both). Such a result indicated that anodic graphenes with larger oxidation extents overall do not necessarily contain larger populations of carbon atoms in higher oxidation states.

Aimed at increasing the amount of carbon atoms in high oxidation states in the anodic graphenes, exfoliation experiments were carried out using graphite rod together with a modified electrolyte. The latter incorporated NaOH as an additive to the 0.1 M Na₂SO₄ base electrolyte. The rationale for selecting such an additive was the following. It is well known from prior studies that hydroxide ions (OH⁻) trigger some reduction of standard (e.g., Hummers-derived) GOs in aqueous medium, even at room temperature [49–51]. Reduction is thought to take place via attack of epoxides (ring opening) and hydroxyl groups by OH⁻, which also results in the breaking of carbon-carbon bonds and the generation of vacancy defects within the carbon lattice. Because these defects are (internal) edges in the graphene nanosheet, they are amenable to being decorated with carbonyl and carboxylic/carboxylate groups upon their subsequent oxidation; indeed, such groups cannot form unless carbon-carbon bonds are broken. Decoration of internal edges with this type of oxygen groups has been previously demonstrated for holey graphene generated by oxidative attack of standard and anodic GO [52]. Moreover, many strategies developed to boost the population of carboxylic/carboxylate groups

in standard GOs rely on the use of NaOH or alternative bases, either alone or in combination with other reagents [39,53–55]. However, this approach has not been tested under electrolytic exfoliation conditions.

Fig. 1b shows the C 1s XPS spectrum of the graphene product that was anodically exfoliated in 0.1 M Na₂SO₄ with 0.1 M NaOH as an additive. This material was referred to as AG-BE+1 (anodic graphene with base electrolyte plus single additive). As anticipated from the previous reasoning, the fraction of carbon atoms in a low oxidation state decreased somewhat (14.5 vs 20.6 %) and that of carbon atoms in high oxidation states increased (8.8 vs 5.8 %) compared to the AG-BE sample (see also Fig. 1d), while the overall O/C atomic ratio only increased slightly (0.26 vs 0.24). Using higher concentrations of the NaOH additive (e.g., 0.2 or 0.5 M) did not lead to further significant changes in the populations of oxidized carbons atoms in the corresponding graphenes. Such a result could be due to the fact that, under the electrolytic exfoliation conditions, the hydroxide ion should also anodically oxidize at the graphite electrode, to give highly reactive hydroxyl radicals ($\cdot\text{OH}$) as an intermediate product, i.e., $\text{OH}^- \rightarrow \text{e}^- + \cdot\text{OH}$ [56]. Thus, a competition between the reducing ability of the hydroxide ions and the oxidizing power of hydroxyl radicals, the latter also coming from the oxidation of water molecules, would be expected. At any given concentration of the NaOH additive, OH⁻ ions will attack epoxy and hydroxyl groups on the surface of the graphite electrode in a multistep process that in some cases will end up in the creation of an internal edge. The latter can then be oxidized by $\cdot\text{OH}$ radicals derived from water molecules and OH⁻ ions, to finally give carbonyl and carboxylic/carboxylate groups. However, it is reasonable to assume that the generation of internal edges in the graphene planes will be limited not only by the availability of OH⁻ ions but also by the concurrent presence of $\cdot\text{OH}$ radicals. These radicals should be able to reverse the reductive attack of epoxy/hydroxyl groups on the graphene surface by the OH⁻ ions, thus hindering the formation of internal edges. Therefore, higher NaOH

concentrations in the electrolyte do not necessarily imply larger numbers of internal edges in the exfoliated material, as the effect of a greater amount of OH⁻ ions in the medium will be counteracted by that of an increased local concentration of ·OH radicals derived from the former.

In an attempt to tune the relative proportion of OH⁻ ions and ·OH radicals, and thus further modulate the populations of oxidized carbon atoms in the anodic graphenes, a second electrolyte additive (NaCl) was used concurrently with NaOH. It has long been known that Cl⁻ ions readily react with ·OH radicals to first give an intermediate complex (ClOH⁻) and then OH⁻ ions, i.e., $\text{Cl}^- + \cdot\text{OH} \rightarrow \text{ClOH}^- \rightarrow \frac{1}{2}\text{Cl}_2 + \text{OH}^-$ [57], and such a reactivity has been previously exploited to modulate the oxidation extent of anodic graphenes [35]. Consequently, the presence of the halide ion is expected to decrease the amount of ·OH radicals and to increase that of OH⁻ ions in the electrolyte, which likely has an impact on the populations of oxygen functional groups in the anodically exfoliated graphenes. In fact, the XPS results for the graphene material obtained with 0.1 M NaOH and 0.1 M NaCl as a dual additive to 0.1 M Na₂SO₄ (material referred to as AG-BE+2: anodic graphene with base electrolyte plus dual additive; O/C atomic ratio of 0.27) indicated a somewhat higher proportion of carbon atoms in a low oxidation state (18.5 %) compared to the AG-BE+1 sample (14.5 %). However, the amount of carbon atoms in high oxidation states only experienced a small increment, i.e., up to 9.5 % from 8.8 % for AG-BE+1 [see Fig. 1c and d]. For reasons that will be explained below, the AG-BE+2 graphene, rather than AG-BE+1, was taken as the optimum material to be used in aqueous zinc-based EES applications. In comparison, GO made by the standard Hummers method, as mentioned above, would contain larger numbers of hydroxyl and epoxy groups (29.2 %), but smaller proportion of carboxyl groups (4.9 %) [39]. In a recent report, the percentage of carboxylic groups in GO was increased to 15.4 % by an 8 h treatment in 0.7 M KOH at 80 °C [39]. Still, as will

be explained below, anodic exfoliation, a much simpler, faster and environmentally-friendly process than Hummer's method can lead to graphenes with an ideal combination of electrical conductivity and extensive oxidation, which is not available in the case of standard GO or rGO.

Further evidence supporting the conclusion that the AG-BE+1 and AG-BE+2 graphenes were enriched in carboxyl/carboxylate/carbonyl groups compared with the standard anodic AG-BE graphene was obtained from their high-resolution O 1s core-level spectra, which are shown in Fig. 1e. Although the assignment of particular O 1s components to specific oxygen functional groups on carbon materials is far less obvious than in the case of the C 1s spectrum, components at ~531 and 534 eV are generally ascribed to carbonyl and carboxyl/carboxylate groups, respectively [47]. As noticed from Fig. 1e, the O 1s envelope of the AG-BE+1 and AG-BE+2 samples appeared to incorporate stronger components at both 531 and 534 eV than those of their AG-BE counterpart. This implied the presence of larger populations of carboxyl/carboxylate and carbonyl groups in the two former graphenes.

Even though no large increase in the amount of carboxyl/carboxylate groups was possible with the dual NaOH/NaCl additive compared to NaOH alone, the use of the dual additive did allow tuning the types of oxygen groups associated to carbon atoms in a low oxidation state (epoxy, hydroxyl groups). Indeed, from the peak-fitting of the C 1s spectra in Fig. 1a-c, it was concluded that a relatively balanced population of epoxides and hydroxyls was present in both AG-BE and AG-BE+2 (hydroxyl/epoxy ratio of 0.7 and 0.8, respectively), whereas hydroxyls were much more abundant than epoxides in AG-BE+1 (hydroxyl/epoxy ratio of 2.5). While some selectivity in the populations of these two oxygen functional groups has been previously achieved by chemical means for standard GO/rGO [58–60], to the best of our knowledge such a selectivity has so far not been reported for electrochemically derived graphenes.

As to the mechanism behind the ability to modulate the relative epoxy/hydroxyl populations, we note that definitive conclusions are difficult to come by due to the complex and dynamic nature of the (electro)chemical processes taking place at the anode. Nonetheless, some educated guess can be made. First, it is reasonable to assume that the generation of hydroxyl groups on the anodic graphene nanosheets can well take place through a straightforward route (i.e., direct grafting of ·OH radicals), although the formation of epoxy groups is less obvious. Epoxides could be produced via H⁺-catalyzed dehydration of vicinal hydroxyls [61], but they could also result from attack of the graphene lattice by oxidizing species other than ·OH radicals, such as ozone [62], which are also assumed to be produced during the high anodic polarization of the carbon electrode in aqueous medium [63]. Thus, in a neutral or very slightly acidic electrolyte (i.e., 0.1 M Na₂SO₄), protons generated by the anodic oxidation of water molecules would favor the presence of epoxy groups in the resulting graphene (sample AG-BE) by way of dehydration reactions of hydroxyls. When the electrolytic medium is basified through addition of NaOH, dehydration reactions would be hindered by the lack of available protons, slowing down the formation of epoxides and leading to graphene with lower proportions of such groups (sample AG-BE+1). Finally, when the dual NaOH/NaCl additive is used, even more complex processes are to be expected due to the involvement of chlorine-based species. For one thing, reaction of Cl⁻ ions with ·OH radicals to give OH⁻ ions (see above) would promote the generation of hydroxyl groups in graphene over epoxides. For another, Cl₂ molecules arising from such a reaction as well as from direct anodic oxidation of Cl⁻ ions [44] would react with OH⁻ to form hypochlorite ions (OCl⁻), i.e., $\frac{1}{2}\text{Cl}_2 + \text{OH}^- \rightarrow \text{OCl}^- + \frac{1}{2}\text{H}_2$ [63], which have been shown to oxidize graphene and CNTs to give epoxy groups on their basal surface [64,65]. These two processes would thus compete to generate either hydroxyl or epoxy groups on the carbon surface, with the latter probably

winning out, as the hydroxyl/epoxy ratio was much lower in sample AG-BE+2 compared to its AG-BE+1 counterpart (see above). Whatever the actual mechanisms, these results allow tuning the relative populations of the different oxygen groups in anodic graphenes for different target applications by resorting to proper electrolyte additives.

3.2. Physicochemical characterization of the anodic graphenes

Fig. 2a (left) shows a photograph of the dried AG-BE+2 product right after the anodic exfoliation step. This material could be readily dispersed in neutral or slightly basic water ($\text{pH} \sim 7\text{--}8$) at considerable concentrations ($> 5 \text{ mg mL}^{-1}$) with the aid of sonication, yielding stable colloidal suspensions (Fig. 2a, right) that endured high-speed centrifugation (e.g., $5,000 \text{ g}$ for 20 min) with most of the material being kept in the supernatant ($\sim 75 \text{ wt.\%}$). Samples AG-BE+1 and AG-BE were also readily dispersible in water. Because the aqueous colloidal stability of oxidized graphenes relies for the most part on the presence of negative electrostatic charges arising from ionizable groups (including carboxyls) [66], zeta potential measurements were used as a quantitative proxy for such charges. Fig. 2b (solid traces) plots the zeta potential profiles recorded at a pH of ~ 8 for these anodic graphenes. For comparison, the profile of a standard, Hummers-derived GO (denoted as HGO) is also shown. The average zeta potential value was the largest for AG-BE+1 (-70 mV) and AG-BE+2 (-58 mV), although it was also considerable for the other graphenes: -48 (AG-BE) and -48 (HGO) mV, the latter being very similar to previous results from the literature [66]. Being highly ionizable oxygen groups, carboxylic acids are expected to contribute very significantly to the zeta potential of oxidized graphenes, provided they are present in sizable amounts. As the pK_a value of such acids is typically around 5, virtually all of them would be deprotonated and thus would contribute, in the form of carboxylate groups, to the negative charge and to the zeta potential measured at pH 8. Hence, the larger

negative values recorded for AG-BE+1 and AG-BE+2 could in principle be related to the higher abundance of carboxyl/carboxylate groups in these two graphenes. Moreover, if this was actually the case, we would expect a considerable shift of the zeta potential profiles towards less negative values at pH 5 compared to pH 8, due to a limited deprotonation of the carboxylic acids at the former pH, and the magnitude of this shift to be larger for those graphenes with larger amounts of carboxyls (AG-BE+1 and AG-BE+2). Fig. 2b (dotted traces) shows the profiles recorded at pH 5 for the oxidized graphenes, where a much larger positive shift (~25 mV) was indeed noticed for the two mentioned graphenes when going from pH 8 to pH 5, compared to the case of AG-BE and HGO (<12 mV). We also note that carboxyls/carboxylates could not be the only source of negative charges in these graphenes. This was apparent from the fact that AG-BE+1 exhibited a somewhat larger (more negative) zeta potential than that of its AG-BE+2 counterpart. Obviously, other functional groups can contribute to the nanosheet charge. In the case of AG-BE+1, we hypothesize that the higher abundance of hydroxyl groups compared to AG-BE+2 discussed above may provide some extra charges and, consequently, a larger zeta potential (in absolute value). Indeed, in aromatic compounds, the presence of hydroxyl groups in close proximity to carboxyl ($pK_a \sim 4-5$) and hydroxyl groups ($pK_a \sim 9-10$) is generally known to lower their respective pK_a by 1-2 units though stabilization of the corresponding deprotonated forms. These shifts in the pK_a of carboxylic groups and aromatic hydroxyl groups will increase the number of deprotonated groups at both pH 5 and 8, respectively, and explain the more negative zeta potential of AG-BE+1. The lowering of the pK_a of carboxylic groups by the presence of hydroxyl groups has been demonstrated in the particular case of GO [67]. We note that the effect of the proximity of hydroxyl groups on the dissociation of hydroxyl or carboxylic groups is expected to be even more pronounced in anodic graphenes than in standard

GO/rGO, given that oxygen functional groups tend to be more densely packed in the oxidized domains of anodic graphenes [52].

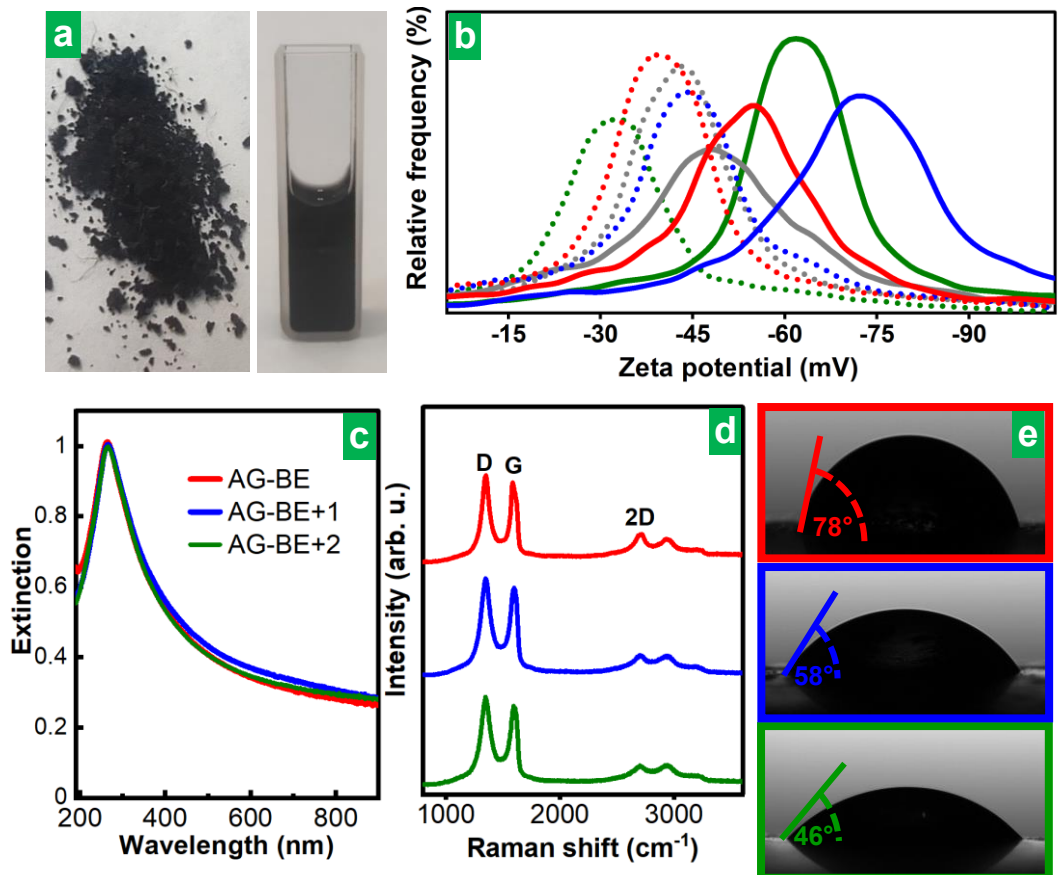


Figure 2. (a) Digital photographs of the dried AG-BE+2 graphene product right after the anodic exfoliation step (left) and following its dispersion in water via sonication (right). (b) Zeta potential profiles for AG-BE (red trace), AG-BE+1 (blue trace), AG-BE+2 (green trace) and a Hummers-derived graphene oxide (HGO, gray trace), measured at a pH of ~ 8 (solid traces) and pH of ~ 5 (dotted traces). (c) UV-vis absorption and (d) Raman spectra of AG-BE, AG-BE+1 and AG-BE+2, with the color code indicated in (c). (e) Water contact angles measured on AG-BE (top), AG-BE+1 (middle) and AG-BE+2 (bottom) thin graphene films processed from their corresponding aqueous dispersions.

The UV-vis absorption spectra of the different anodic graphenes were very much alike (Fig. 2c), all exhibiting a peak at $\sim 266\text{--}267$ nm together with strong,

slowly decaying absorbance at longer wavelengths up to 1000 nm. The absorption peak can be ascribed to $\pi\rightarrow\pi^*$ transitions in the small unoxidized, electronically conjugated domains present in oxidized graphenes, and its actual position is known to upshift as the domain size is increased within the few nanometer range [66,68]. The peak position for the present anodic graphenes was almost identical to that previously reported for well-reduced GOs [69] and even unoxidized graphene derived by direct, liquid-phase exfoliation of pristine graphite [70], i.e., 268 nm, even though the former (O/C ratios of 0.24-0.27) were obviously much more oxidized than the latter (O/C ratios < 0.10). This apparently conflicting result can be explained by noting that, as mentioned before, oxygen functional groups tend to be more densely packed in the oxidized domains of anodic graphenes than they are in standard GO/rGO [52]. As a result, the size of the unoxidized domains and so the absorption peak position of the former can easily be the same as those of the latter, even if their nanosheets are considerably more oxidized overall (higher O/C ratio). The more compact distribution of oxygen groups in anodic graphenes also implies that they should retain higher values of electrical conductivity despite their relatively extensive oxidation. Thin, paper-like films of anodic graphene were prepared by vacuum filtration of their aqueous dispersions and their electrical conductivity measured by the four-point probe method, yielding values of 2260 (AG-BE), 1220 (AG-BE+1) and 220 (AG-BE+2) S m⁻¹. Remarkably, these figures were at least two orders of magnitude larger than those determined for standard rGOs with the same overall extent of oxidation [69], and were sufficiently high to allow the use of the oxidized anodic graphenes as electrodes for EES without the need to resort to reduction treatments (see below).

The relatively large oxidation extent of the present anodic graphenes was expected to lead to correspondingly high levels of structural disorder in their carbon lattice, which would take the form of, e.g., broken C-C bonds, vacancies and sp³ sites. This was corroborated by Raman spectroscopy (Fig. 2d). The first-order

region of the spectra ($1100\text{--}1700\text{ cm}^{-1}$) included the defect-related D band ($\sim 1350\text{ cm}^{-1}$) as well as the G band ($\sim 1580\text{ cm}^{-1}$) [71,72]. The integrated intensity ratio of these two bands (I_D/I_G ratio), which is usually taken as a quantitative proxy for the amount of structural disorder in graphitic/graphenic materials, was quite high and essentially identical (~ 1.1) for the three anodic graphenes. Such a result was reasonable, considering that the AG-BE, AG-BE+1 and AG-BE+2 materials possessed very similar overall degrees of oxidation (O/C ratios between 0.24 and 0.27). The fact that the previously reported electrical conductivity values highlight the difference in the structural disorder in the series can be put down the much wider range of variation of these physical quantity (27 orders of magnitude from a metal to a good electrical insulator) in relation to the just two units of variation of the I_D/I_G ratio in graphitic materials [73]. The fingerprint of disorder was also clearly noticed from the second-order features of the spectra ($2300\text{--}3500\text{ cm}^{-1}$ region), in particular from observation of a rather weak 2D band ($\sim 2700\text{ cm}^{-1}$). The latter appears as a strong band in defect-free graphites/graphenes (comparable in intensity to the G band), but becomes progressively weaker as defects as introduced in the lattice [71]. Differences in hydrophilicity between the anodic graphenes were apparent from the measurement of their water contact angle (Fig. 2e). The values recorded for thin films processed from their aqueous dispersions were about 78° (AG-BE), 58° (AG-BE+1) and 46° (AG-BE+2). Such a result indicated the latter two graphene materials to be more hydrophilic than the former, which was mostly ascribed to their higher abundance of carboxylic groups [39]. We note that the fact that AG-BE+2 exhibits a lower contact angle compared to AG-BE+1 is not necessarily in contradiction with AG-BE+2 having a lower zeta potential value (Fig. 2b).

Indeed, while the zeta potential value of the anodic graphenes depends on the amount of deprotonated oxygen-containing functional groups, the value of the water contact angle depends on the interactions of all their functional groups – deprotonated or not – with water. Although the number of deprotonated groups is

higher for AG-BE+1 than for AG-BE+2, the total number of oxygen-containing groups is higher in AG-BE+2. Certainly, the O/C ratio is slightly higher for AG-BE+2 (0.27) than for AG-BE+1 (0.26) and the percentages of carbon atoms in oxygen-containing groups in both low and high oxidation states are also larger for AG-BE+2 than for AG-BE+1 (18.5% vs. 14.5% and 9.5 % vs. 8.8 %, respectively). In fact, although there is not a large difference in the carboxylic group content between the two materials, it could have a marked effect on hydrophilicity, as carboxylic groups are considered the functional groups that contribute the most, at least in the case of GO [74].

The morphology of the exfoliated anodic nanosheets was directly visualized by scanning transmission electron microscopy (STEM) and atomic force microscopy (AFM). Fig. 3a and b(i) shows representative STEM and AFM images, respectively, of the AG-BE+2 nanosheets. Similar results were obtained for the AG-BE and AG-BE+1 samples (see Fig. S4 in section S3 of the ESM). The nanosheets displayed irregular polygonal shapes, with lateral sizes typically in the range of several hundreds of nanometers. This conclusion was supported by dynamic light scattering (DLS) measurements, which yielded hydrodynamic diameters for the colloidally dispersed objects roughly between 300–400 and 700–800 nm, with relatively small differences being observed between the three anodic graphenes (Fig. 3c). Using the quantitative relationship between hydrodynamic diameter and nanosheet lateral size previously developed for graphene and other 2D materials [75], the actual lateral size of the anodic graphenes was estimated to stretch between 300 and 1600 nm, which was in reasonable agreement with the microscopy results. Estimates of apparent nanosheet thickness derived from the AFM images mostly ranged between 1.5 and 3 nanometers (see histogram in Fig. 3d). Owing to their relatively high degree of oxidation, the actual thickness of a single layer of these anodic graphenes was not expected to be that of pristine graphene (~0.34 nm), but rather to be close to that of standard GO/rGO, i.e., ~0.7–1 nm [76], implying that

they were typically single- to few-layer objects. Indeed, these nanosheets were not atomically flat structures, even though they were supported onto atomically flat highly oriented pyrolytic graphite (HOPG) for AFM imaging, but exhibited a smooth roughness similar to that observed in GO/rGO [see Fig. 3b(ii)] [77]. Such a roughness stems from structural disorder (broken carbon-carbon bonds, carbon vacancies, sp^3 sites) and grafted oxygen groups in the oxidized nanosheets, which inevitably leads to their larger effective thickness.

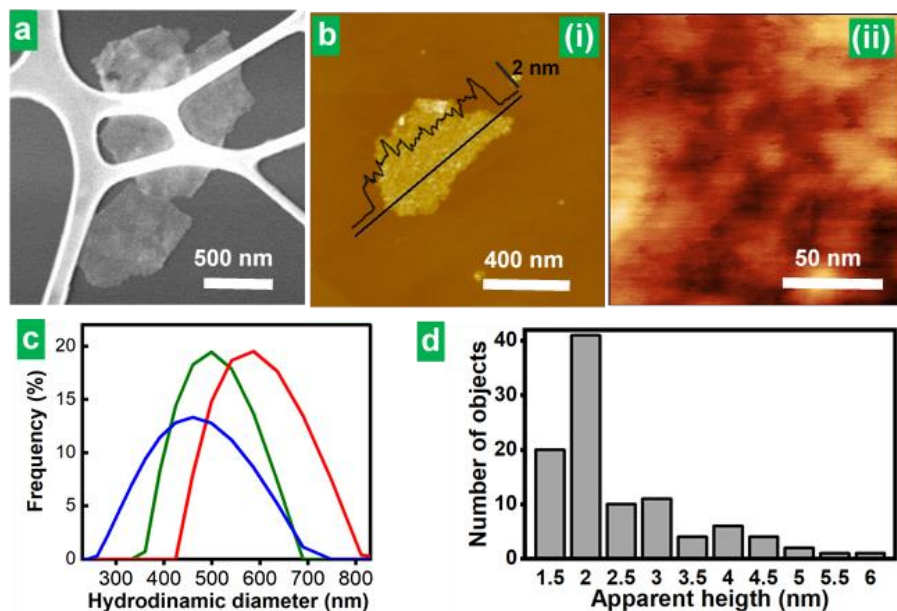


Figure 3. Representative STEM (**a**) and AFM (**b**) images of AG-BE+2 graphene nanosheets. In (**b**), both general view (**i**) and detailed (**ii**) images of a nanosheet are shown. (**c**) Number-weighted distribution of hydrodynamic diameters of aqueous dispersions of AG-BE (red), AG-BE+1 (blue) and AG-BE+2 (green) graphene measured by dynamic light scattering (DLS). (**d**) Histogram of AG-BE+2 graphene nanosheet thickness derived from a pool of 100 objects measured from AFM images.

3.3. Carboxyl-enriched anodic graphene as a cathode material for aqueous zinc-based EES

The single/few-layer nature and enhanced hydrophilicity of the carboxyl-enriched anodic graphene described above make it a potentially attractive cathode material for AZICs. Specifically, these features are expected to provide electrodes with large accessible surface area and good wettability by the aqueous electrolyte, which in turn should favor charge storage [14]. Here, graphene-based electrodes were prepared simply by drop-casting an aqueous suspension of the corresponding graphene nanosheets onto commercial carbon paper, which resulted in the formation of a compact thin film after a drying step (see FE-SEM images in Fig. 4a and b; typical film thickness \sim 6–8 μm). These carbon paper-supported graphene films were then assembled as the cathode of AZIC devices, using polished Zn metal foil as the anode and aqueous 2 M ZnSO_4 solution as the electrolyte. Fig. 4c plots typical cyclic voltammograms (CVs) recorded at a potential scan rate of 30 mV s^{-1} for the AG-BE and AG-BE+2 cathode materials, where a somewhat higher gravimetric current was measured with the latter graphene, indicative of a better performance for the carboxyl-enriched sample. These CVs were roughly rectangular in shape but included some prominent bumps at \sim 0.8–1.2 V vs. Zn/Zn^{2+} , which were ascribed to redox reactions of certain oxygen-containing groups (e.g., quinone-type moieties) present in oxidized carbon materials, including porous carbons [78] and rGOs [79,80]. The occurrence of oxygen-related redox processes in the present anodic graphenes was not surprising, considering their substantial degree of oxidation (O/C ratios in the range of 0.25). CVs obtained at different potential scan rates between 1 and 500 mV s^{-1} for these two samples are shown in Fig. S5a (AG-BE) and b (AG-BE+2) in section S4 of the ESM. While at the lower scan rates the CVs of both graphenes exhibited the approximately rectangular shape described above, which denoted a good (pseudo)capacitive behavior, at high rates

their CV profiles became increasingly distorted, and this effect was somewhat more noticeable for the AG-BE cathode. Such a result implied that the latter graphene possessed a poorer rate capability than that of AG-BE+2, a conclusion that was confirmed by recording the corresponding galvanostatic charge-discharge (GCD) profiles. Fig. 4d shows GCD profiles measured at two representative gravimetric currents (0.5 and 5 A g^{-1}) for the AG-BE+2 (solid lines) and AG-BE (dotted lines) samples. At 0.5 A g^{-1} , the capacity of AG-BE was about 70 % of the AG-BE+2 value, but at 5 A g^{-1} that ratio decreased to $\sim 50\text{ %}$.

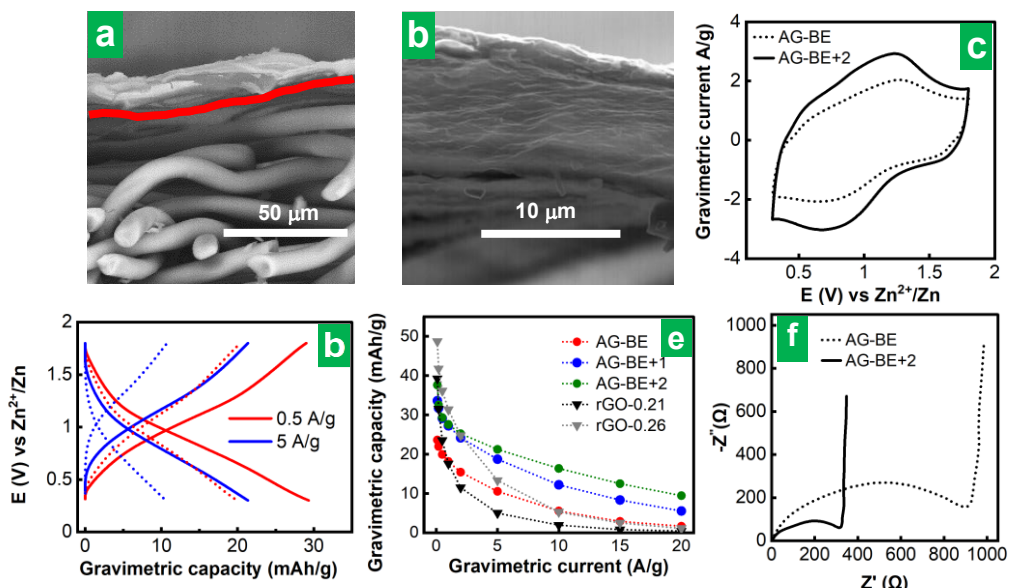


Figure 4. **(a,b)** Representative FE-SEM images of carbon paper-supported AG-BE+2 graphene film electrode at different magnifications ($1600\times$ and $12000\times$, respectively). In (a), the interface between the graphene film and the carbon paper is shown by a red line, with the graphene film (carbon paper) shown above (below) the red line. **(c)** Typical cyclic voltammograms (CVs) for AG-BE (dotted line) and AG-BE+2 (solid line) graphene film AZIC cathodes at a potential scan rate of 30 mV s^{-1} . **(d)** Galvanostatic charge-discharge (GCD) profiles recorded for AG-BE (dotted lines) and AG-BE+2 graphene film AZIC cathodes at 0.5 (red) and 5 (blue) A g^{-1} . **(e)** Gravimetric capacity values measured at different currents for several graphene film-based AZIC cathodes: AG-BE (red circles), AG-BE+1 (blue circles), AG-BE+2 (green circles), rGO-0.21 (black triangles) and rGO-0.26 (gray triangles). **(f)** Nyquist plots recorded for AZIC cells with AG-BE (dotted lines) and AG-BE+2 (solid lines) graphene film as the cathode.

A more detailed depiction of the effect of applied current on the measured gravimetric capacities for a range of graphene-based AZIC cathodes is given in Fig. 4e. The capacity retention at 20 A g^{-1} , determined with respect to the capacity obtained at 0.1 A g^{-1} , was about 25% with the AG-BE+2 cathode, but only 7% with AG-BE. The rate capability of carbon materials as (pseudo)capacitive electrodes in EES devices is largely dictated by their electrical conductivity and the accessibility of electrolyte ions to their adsorption sites [12,14]. In the present case, the inferior rate capability of the AG-BE cathode relative to its AG-BE+2 counterpart could not be due to electrical conductivity limitations in the former graphene, as it was more electrically conductive than AG-BE+2. We therefore conclude that a more sluggish access of electrolyte ions to the adsorption sites of AG-BE, compared to the case of AG-BE+2, was the main reason behind its lower rate capability. Support for this outcome was obtained from electrochemical impedance spectroscopy (EIS) measurements. Fig. 4f shows Nyquist plots recorded with the AG-BE and AG-BE+2 materials, which displayed the well-known features expected for this type of devices, i.e., a semi-circle at high to medium frequencies followed by a more or less vertical, straight line at low frequencies [81]. It can be noticed that the diameter of the semi-circle was smaller and the subsequent straight line was slightly more vertical for the AG-BE+2 graphene, demonstrating a smaller charge transfer resistance and a better ion transport dynamics in this material [80,82]. Moreover, quantitative information on the kinetics of the AZIC cathodes could be derived by analysis of their CVs at different potential scan rates, on the basis of the following equation:

$$i = a \cdot v^b \quad (1)$$

, where i is the measured current, v is the potential scan rate, and a and b are adjustable parameters. A b value of 0.5 denotes charge storage processes that are fully controlled by diffusion (typical of batteries), a value of 1 indicates fully

capacitive (i.e., non-diffusion-controlled) processes, whereas b values in-between these two extremes imply the occurrence of both diffusion-controlled and capacitive processes to different extents [81]. Fitting of the anodic and cathodic peak currents in the CVs of Fig. S5 to eq. (1) yielded b values of 0.75 (anodic)/0.68 (cathodic) for AG-BE and 0.80 (anodic)/0.72 (cathodic) for AG-BE+2. This result proved that the charge storage kinetics was somewhat less dominated by sluggish, diffusion-controlled processes in the carboxyl-enriched AG-BE+2 graphene, which in turn was consistent with the higher rate capability observed for this material. As to the origin of the better accessibility of electrolyte ions to the AG-BE+2 graphene, its higher hydrophilicity (lower water contact angle; see Fig. 2e) was very likely a major driver. This feature should lead to a better wettability of the graphene-based cathode by the aqueous electrolyte, and thus to an improved shuttling of hydrated ions between the electrolyte bulk and adsorption sites located at very narrow slits or pores (i.e., graphene interlayer spaces in the present case) [83]. Contact angles of the anodic graphenes with the aqueous 2 M ZnSO₄ electrolyte were also measured (Fig. S6, section S4 of ESM), yielding values of 88° (AG-BE), 77° (AG-BE+1) and 63° (AG-BE+2), which confirmed that the carboxyl-enriched graphenes exhibited a stronger interaction not just with neat water but also with the electrolyte.

Fig. 4e also shows the rate capability behavior of some graphene-derived AZIC cathodes other than those based on AG-BE and AG-BE+2, including the AG-BE+1 material. The latter displayed a somewhat lower performance than that of AG-BE+2 (e.g., capacity retention of 17% at 20 A g⁻¹), even though their physicochemical traits were very similar, the main difference lying in the relative proportions of hydroxyl and epoxy groups. Consequently, AG-BE+2 was selected as the optimum anodic graphene for this application. For comparison, two oxidized graphenes obtained via partial reduction of standard, Hummers-derived GO were tested as well. By adjusting the amount of reductant used (sodium borohydride in the present case), the overall oxidation level of the resulting rGOs could be tuned

[69]. Sample denoted as rGO-0.26 had an overall O/C atomic ratio of 0.26, i.e., it was almost identical to that of AG-BE+2, but its performance as an AZIC cathode (capacity retention of ~2%) was much worse than that of the anodic graphene. In principle, this could be due to differences in the electrical conductivity of both graphenes (6 S m^{-1} for rGO-0.26 vs 220 S m^{-1} for AG-BE+2). Hence, another rGO sample with a somewhat higher conductivity (35 S m^{-1}) was prepared by reducing GO to a moderately greater extent (O/C ratio of 0.21; sample rGO-0.21) using a larger amount of reductant and tested as an AZIC cathode. However, its rate performance was also much lower than that of the AG-BE+2 graphene. Further, the capacity values attained here for the rGO materials were comparable to those of other as-prepared, rGO-only cathodes previously reported in the literature (without including specific strategies toward capacity enhancement) [82,84]. It thus appears that anodic graphene affords a more effective route to tune the characteristics of oxidized graphenes for improved performance, compared to graphenes derived from standard GO. We believe such an outcome to be probably due to subtle structural differences between anodic graphenes and standard GO/rGO, related to the size and/or density of their oxidized/electronically conjugated domains, even if both graphene types exhibit the same overall level of oxidation [52]. Nevertheless, attaining firm conclusions in this regard will require further in-depth studies. We also note that the AG-BE+2 material boasted a good cycling stability with high coulombic efficiency, showing a capacity retention of 95% after 20,000 GCD cycles at a current of 1 A g^{-1} (Fig. S7 in section S4 of the ESM).

While exhibiting a better rate performance than that of rGOs, the overall gravimetric capacity values of the anodic graphenes developed here were still somewhat limited. This could be due, at least in part, to the rather compact stacking of the nanosheets when processed into films. Although such a compact configuration might be beneficial for the volumetric performance of the device, it usually comes at the expense of its gravimetric efficiency, especially at high

currents. To address this issue, a recent strategy has relied on intercalating rGO nanosheets with crumpled graphene, the latter also coming from standard GO [82]. As an alternative, and to keep on with the spirit of reducing the environmental footprint in the production of materials, we explored the use of biomolecules as an intercalant. More to the point, flavin mononucleotide (FMN) was selected for this purpose. FMN is an amphiphilic molecule comprising a hydrophobic nucleobase (dimethylated isoalloxazine) appended with a hydrophilic phosphorylated sugar moiety (see chemical structure in Fig. S8, section S4 of the ESM). Its nucleobase is known to strongly adsorb on the graphene surface, with the hydrophilic segment pointing outwards [85,86]. Thus, FMN can be expected to act as a spacer between graphene nanosheets, while contributing at the same time to provide a hydrophilic interlayer environment that promotes electrolyte accessibility to the electrode. Moreover, the isoalloxazine nucleobase of FMN has a redox center (highlighted in blue in Fig. S8) [87], thereby potentially also adding to the capacity of the electrode.

FMN-graphene hybrid films to be tested as AZIC cathodes were prepared by the same strategy used to obtain their graphene-only counterparts, but with prior addition of the biomolecule to the starting aqueous graphene dispersion (AG-BE+2) in different FMN:graphene mass ratios (1:6, 2:6, 3:6 and 6:6). Fig. S9 (section S4 of the ESM) shows FE-SEM images of a typical FMN-anodic graphene film (FMN:graphene mass ratio of 3:6), which displayed essentially the same morphology and appearance as that of the graphene-only film (Fig. 4a and b). CVs recorded at different potential scan rates for this particular hybrid film as a representative example are shown in Fig. 5a and b for different ranges of potential scan rate, where oxidation and reduction peaks at 0.5-0.8 V vs. Zn/Zn²⁺ associated to the redox center of the nucleotide were clearly noticed. The contribution of FMN to the cathode capacity was also apparent from the emergence of charge and discharge plateaus in the corresponding GCD profiles, especially at low currents (Fig. 5c). Fig. 5d plots the gravimetric capacity values measured at different

currents between 0.1 and 20 A g⁻¹ for hybrid films prepared with the different FMN:graphene mass ratios (data for the graphene-only film are also plotted for comparison). The presence of FMN in the graphene-based cathode was seen to be clearly beneficial. For the three hybrid films with the lowest FMN ratios (i.e., 1:6, 2:6 and 3:6), the biomolecule contributed to progressively increase the rate capability of the device, up to ~64 % in the 3:6 film (starting from 25 % in the graphene-only cathode), although the capacity values at 0.1 A g⁻¹ were not significantly changed. An estimation of the contributions of anodic graphene and FMN to the capacity of the resulting FMN-graphene hybrid film yielded ~55% and 45%, respectively (see Fig. S10a in section S4 of the ESM). This was calculated by difference of the integrated areas of the experimental CV of the hybrid and a CV with the shape of anodic graphene alone at the same scan rate fitted to its capacitive part. As for the contributions of (pseudo)capacitive and diffusion-controlled processes to the measured current in the CVs, an analysis on the basis of Eq. (1) concluded the former to be dominant, contributing ~92% (Fig. S10b, section S4 of the ESM). This is a reasonable conclusion, given that the redox peaks are associated to FMN adsorbed on the surface of anodic graphene and are consequently not expected to be very diffusion-limited. In contrast with the other hybrids, the 6:6 FMN-graphene hybrid film the capacity at the lowest current was appreciably larger than that of any of the other films, albeit this happened at the expense of a relatively modest rate capability (~47 %). Nonetheless, the 6:6 hybrid cathode exhibited the best performance overall. The Nyquist plot recorded with this cathode was not very different to that of the graphene-only device, displaying just a slightly larger semi-circle and a somewhat less vertical straight line (Fig. S11, section S4 in the ESM). This suggested that the presence of even a relatively large amount of FMN in the graphene-based cathode did not seriously affect the cell behavior. Rather, the negative aspects of including this molecule in the cathode (e.g., decrease of

electrical conductivity) were probably offset by its beneficial contributions (role as a spacer, extra capacity, etc).

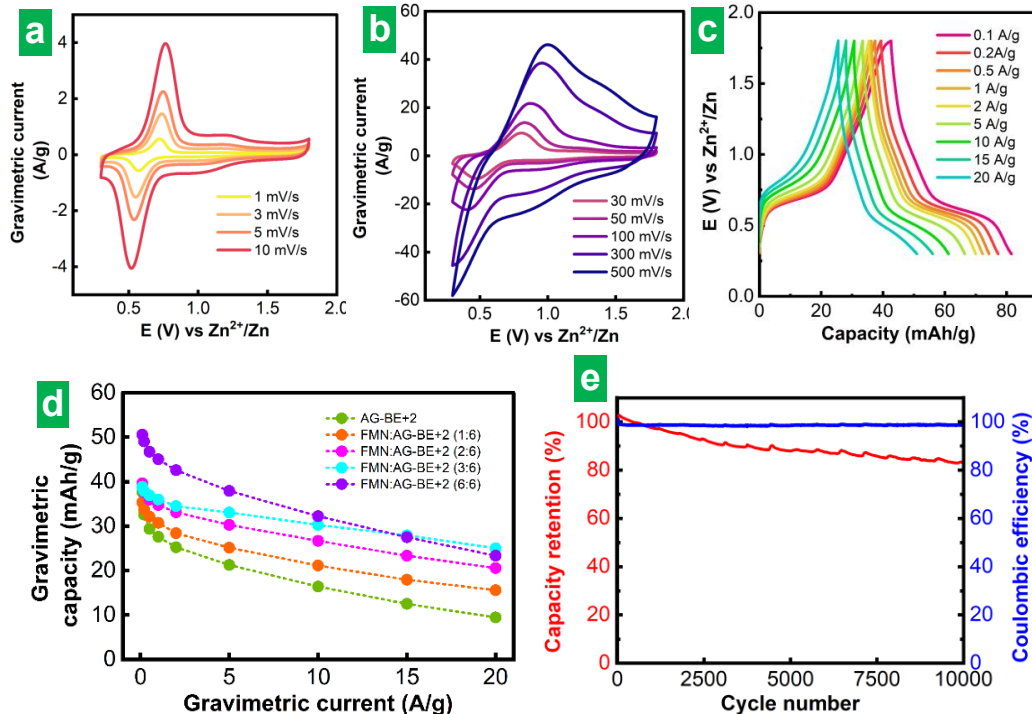


Figure 5. (a,b) CVs recorded for AZIC cathodes based on FMN-anodic graphene (AG-BE+2) hybrid film (FMN:graphene mass ratio of 3:6) at potential scan rates between 1 and 10 mV s⁻¹ (a) and between 30 and 500 mV s⁻¹ (b). **(c)** GCD profiles for the FMN-anodic graphene (3:6) hybrid film as AZIC cathode recorded at different gravimetric currents between 0.1 and 20 A g⁻¹. **(d)** Gravimetric capacity values measured at different currents for FMN-anodic graphene hybrid films with various FMN:graphene mass ratios: 1:6 (orange circles), 2:6 (magenta), 3:6 (cyan) and 6:6 (violet). Data for the graphene-only film are shown for comparison (green circles). **(e)** Cycling performance of AZIC cell with FMN-anodic graphene hybrid film (6:6) as the cathode measured at a gravimetric current of 2 A g⁻¹.

The volumetric capacity of the 6:6 hybrid film was ~ 75 mAh cm⁻³ at 0.1 A g⁻¹ (film density ~ 1.5 g cm⁻³). This figure was very similar to that reported for compact graphene films derived from standard GO that incorporated crumpled

nanosheets as an intercalant ($\sim 72 \text{ mAh cm}^{-3}$ at 0.1 A g^{-1}) [82]. Still, the AZIC cathodes developed here relied on an innocuous biomolecule and a graphene obtained by a milder approach that circumvented the need of harsh chemical reagents, and therefore were particularly attractive from an environmental standpoint. As can be seen in Fig. 5e, this hybrid cathode exhibited a reasonably good cycling stability with high coulombic efficiency (e.g., capacity retention of 83 % after 10,000 cycles at 2 A g^{-1}). Such a result was significant as it implied that FMN molecules did not desorb from the graphene film to a very large extent during AZIC operation, which is frequently a challenging issue when using small molecules as electrode components in liquid electrolytes [10]. In the present case, this problem was very likely mitigated by the strong adsorption of FMN to the electronically conjugated domains of graphene. According to this line of reasoning, using hybrid cathodes with lower FMN:graphene ratios should lead to better cycling stabilities, as the graphene nanosheets are expected to provide a more efficient confinement for smaller numbers of FMN molecules. Indeed, the 3:6 hybrid cathode showed a slightly larger capacity retention of 85 % under the same testing conditions (data not shown). Finally, in addition to compact films, AZIC cathodes were also prepared from relatively loose anodic graphene particles obtained by freeze-drying of aqueous dispersions. The freeze-dried particles were mixed with carbon black (90:10 wt ratio) in *N*-methyl-2-pyrrolidone and deposited onto carbon paper. Here, the effect of FMN addition (3:6 ratio) was not so much an improvement of the rate capability, which was already high in the graphene-only cathode ($\sim 65\%$), but a substantial increase of capacity values in the whole current range, including the lowest currents (Fig. S12, section S4 of the ESM). This demonstrated that the electrochemical performance of graphene-based AZIC cathodes is markedly influenced by the actual processing of the material.

3.4. Carboxyl-enriched anodic graphene for protecting the zinc anode in aqueous EES

The anodic graphene developed here was also tested for the protection of the metal anode in aqueous zinc-based EES systems. Metallic zinc acting as the anode in AZIBs and AZICs is known to suffer from several problems, such as propensity to dendrite formation, occurrence of hydrogen evolution and generation of by-products, which can compromise the cycle life of the device [9]. To address this issue and extend the anode life, different strategies are currently being explored, including coating the zinc metal surface with proper materials acting as a protective interphase layer. Indeed, carbon materials of different types (graphene and others) have already shown their utility in such a role [16–18]. Moreover, the present carboxyl-enriched graphene was an attractive candidate for this purpose, as carboxylate groups are thought to favor the nucleation of zinc and thus a more uniform plating of the metal, thereby easing the problem of dendrite formation [27]. Here, anodic graphene films were deposited onto the surface of polished zinc metal foil by a simple drop-casting procedure. Fig. 6a shows photographs of the bare (top) and AG-BE+2 graphene-coated (bottom) foils cut into circular discs 12 mm in diameter, where the lustrous, mirror-like appearance of the former was replaced, after nanosheet deposition, by the characteristic opaque black tone of graphene films. Further, FE-SEM imaging revealed that the bare zinc foil exhibited a smooth, largely featureless surface (Fig. 6b). By contrast, a rougher appearance that is common for graphene films formed by the irregular stacking of nanosheets was seen for the anodic graphene-coated counterpart (Fig. 6c). Such an irregular stacking was confirmed by cross-sectional imaging of the film (Fig. 6d), where voids that should expedite the shuttling of Zn^{2+} ions between the electrolyte and the metal interface were noticed. The typical film thickness determined from these FE-

SEM images was around 8-12 μm , which was corroborated by measurements with a digital micrometer.

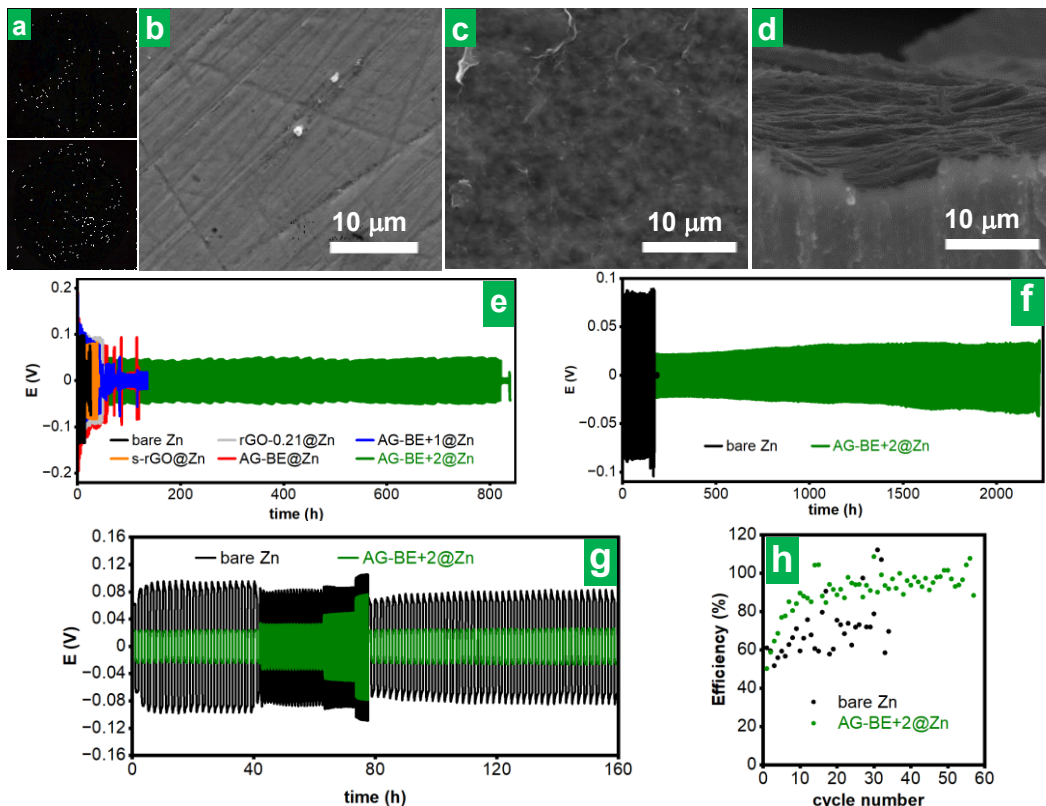


Figure 6. (a) Photographs of bare (top) and AG-BE+2 anodic graphene-coated (bottom) zinc foil electrode. (b-d) FE-SEM images of bare (b) and anodic graphene-coated (c: top view; d: cross-sectional view) zinc foil electrode. (e) Cyclic zinc plating/stripping behavior recorded for symmetric cells at a current density of 5 mA cm^{-2} for a capacity of 5 mAh cm^{-2} with the following electrodes: bare Zn (black trace), AG-BE@Zn (red), AG-BE+1@Zn (blue), AG-BE+2@Zn (green), rGO-0.21@Zn (gray) and s-rGO@Zn (orange). (f) Cyclic zinc plating/stripping behavior recorded for bare Zn (black trace) and AG-BE+2@Zn (green trace) symmetric cells at a current density of 0.5 mA cm^{-2} for a capacity of 0.5 mAh cm^{-2} . (g) Rate performance of bare Zn (black traces) and AG-BE+2@Zn (green traces) symmetric cells at different current densities between 0.5 and 5 mA cm^{-2} for a capacity of 0.5 mAh cm^{-2} . (h) Coulombic efficiency (CE) measured on bare Zn//Ti (black circles) and AG-BE+2@Zn//Ti (green circles) asymmetric cells at a current density of 5 mA cm^{-2} for a capacity of 1 mAh cm^{-2} .

To explore the effect of anodic graphene on the plating/stripping behavior and electrode life of the zinc metal foil, both symmetric and asymmetric cells were electrochemically characterized, using graphene-coated zinc foil electrodes (denoted as, e.g., “AG-BE+2@Zn”) as well as the bare zinc foil electrode (denoted as “bare Zn”). Fig. 6e shows cyclic plating/stripping profiles for a number of symmetric cells (bare Zn and different graphene@Zn electrodes) at a current density of 5 mA cm^{-2} for a capacity of 5 mAh cm^{-2} , which are relatively stringent conditions. It can be seen that the bare Zn electrode could be cycled stably for only a few tens of hours, after which fluctuations in the polarization voltage indicative of short-circuit formation emerged, suggesting cell failure due to zinc dendrite growth [88]. On the other hand, the AG-BE+2@Zn electrode afforded a much longer stable cycling ($>800 \text{ h}$, corresponding to >400 cycles) before cell failure took place, working at a relatively low and constant polarization voltage of $\sim 50 \text{ mV}$. Such a result provided direct evidence of the effective protection that the anodic graphene coating imparted on the zinc anode. For comparison, the performance of zinc electrodes coated with graphenes other than the AG-BE+2 sample is also shown in Fig. 6e. These comprised the AG-BE and AG-BE+1 anodic graphenes, the rGO-0.21 sample described above, as well as an rGO material that formed a coating layer on zinc foil via a previously reported spontaneous reduction and assembly process (electrode denoted as s-rGO@Zn) [89]. Cycle lives much shorter than that of AG-BE+2@Zn were observed with all these graphene-coated electrodes, including AG-BE+1@Zn. The low performance of the latter electrode could be *a priori* a bit surprising, because AG-BE+1 and AG-BE+2 were quite similar materials that differed mainly in their relative populations of epoxy and hydroxyl groups. However, AG-BE+1 was seen to exhibit a rather poor film-forming ability on the zinc surface, which was not the case of AG-BE+2 and probably compromised its role as a protective barrier (an equally poor ability was noticed for s-rGO). It was thus concluded that AG-BE+2 was a better option for

anode protection than the other examined graphenes, and so AG-BE+2@Zn electrodes were further tested at other current densities/capacities, including $0.5 \text{ mA cm}^{-2}/0.5 \text{ mAh cm}^{-2}$ (Fig. 6f) and $2 \text{ mA cm}^{-2}/2 \text{ mAh cm}^{-2}$ (Fig. S13 in section S5 of the ESM). Again, the measured cycle lives (>2200 and 1200 h, respectively) were much longer than those obtained with the bare Zn electrodes (~ 170 and 30 h, respectively). Moreover, these results generally compared favorably with figures reported in the literature for zinc electrodes coated by different types of carbon materials (see Table S1, section S5 in ESM), including graphenes of different origins and characteristics [89–94]. Fig. 6g compares the rate performance of symmetric cells with the bare Zn and AG-BE+2@Zn electrodes recorded at different current densities between 0.5 and 5 mA cm^{-2} for a fixed capacity of 0.5 mAh cm^{-2} . It is noticed that plating/stripping processes tended to occur at somewhat lower polarization voltages with the latter electrode, suggesting faster, more favorable ion transport and metal deposition on the anodic graphene-coated anode [91]. Fig. 6h plots the coulombic efficiency (CE) measured at current density/plating capacity of $1 \text{ mA cm}^{-2}/0.5 \text{ mAh cm}^{-2}$ for asymmetric cells where a bare Zn or AG-BE+2@Zn electrode was paired with a Ti metal counter electrode. While the bare Zn/Ti cell exhibited low coulombic efficiency values around 70%, those of its AG-BE+2@Zn/Ti counterpart were typically $>95\%$, demonstrating the improved reversibility of the plating/stripping process afforded by the protective anodic graphene coating.

The improved stability of the zinc electrode upon AG-BE+2 graphene coating should be in principle the result of mitigating one or several of the problems that plague its operation: hydrogen evolution by reduction of water molecules/protons, precipitation of passivating by-products derived from hydrogen evolution [e.g., $\text{Zn}_4\text{SO}_4(\text{OH})_6 \cdot x\text{H}_2\text{O}$] and uneven deposition of zinc giving rise to dendrite development [9]. We believe that hydrogen evolution was not alleviated by the use of the present anodic graphene. With the aim of averting this problem,

protective coatings should be hydrophobic, to prevent water molecules from reaching the metal surface, as well as non-catalytic, to avoid the coating itself from acting a promoter of hydrogen evolution [88]. Still, as noted above, the AG-BE+2 graphene was quite hydrophilic and decorated with a significant amount of edge defects (where carboxyl groups are accommodated), which are known to have some catalytic activity towards hydrogen evolution [95,96]. To compare their propensity towards promoting hydrogen evolution, linear sweep voltammograms (LSVs) were recorded for the bare Zn and AG-BE+2@Zn electrodes in 2 M Na₂SO₄ electrolyte (Fig. 7a). Indeed, somewhat higher polarization currents were measured with the latter electrode, which demonstrated that this anodic graphene did not inhibit hydrogen evolution, but rather it appeared to promote it to some extent. For this reason, the formation of passivating by-products was neither thought to be substantially diminished, although the negative charges in the anodic graphenes could have had some tempering effect in this regard by repelling sulfate anions [88].

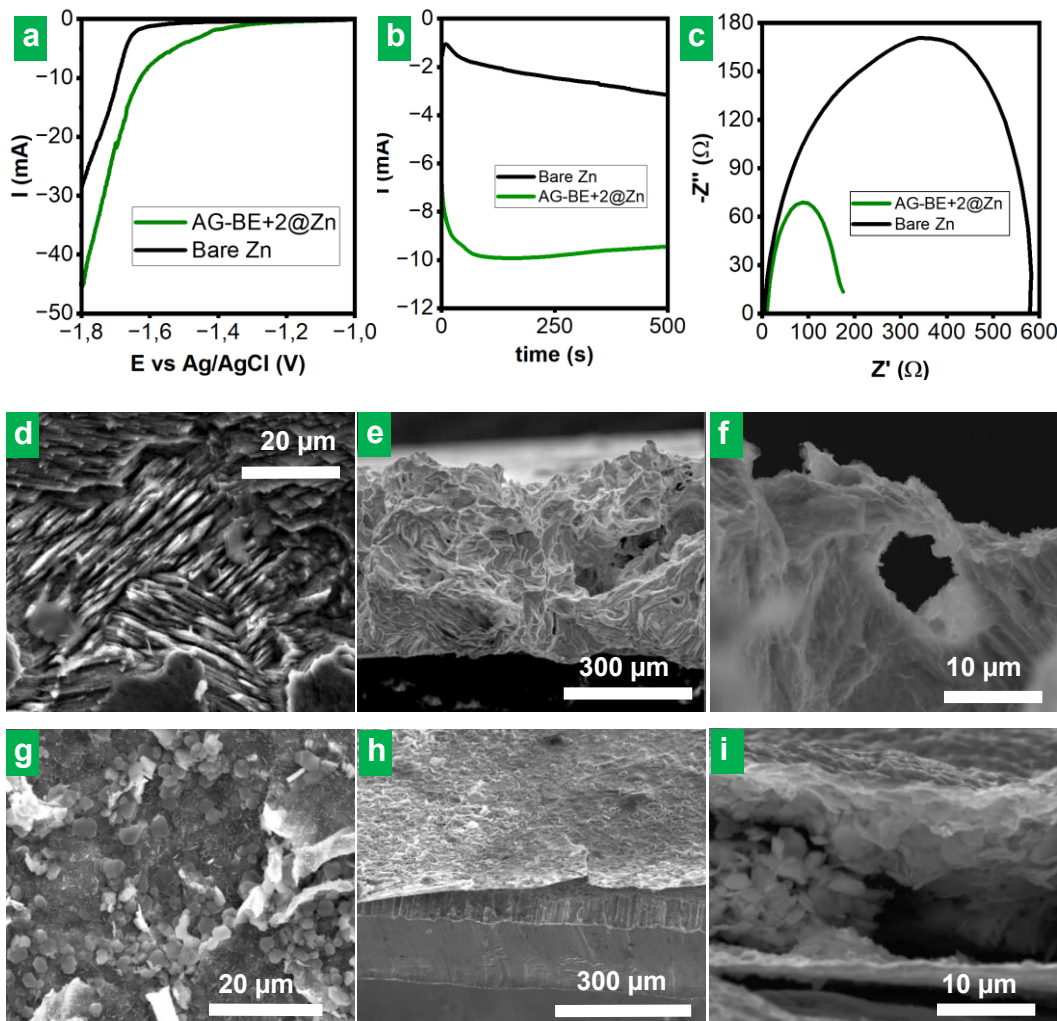


Figure 7. (a) Linear sweep voltammograms (LSVs) recorded for the bare Zn (black trace) and AG-BE+2@Zn (green trace) electrodes in aqueous 2 M Na_2SO_4 electrolyte at a potential scan rate of 50 mV s⁻¹ and using Ag/AgCl (3 M KCl) as a reference electrode. (b) Chronoamperometric curves measured at a polarization voltage of -150 mV for symmetric cells with bare Zn (black trace) and AG-BE+2@Zn (green) electrodes. (c) Nyquist plots obtained for symmetric cells with bare Zn (black trace) and AG-BE+2@Zn (green) electrodes. (d-i) FE-SEM images of bare Zn (d-f) and AG-BE+2@Zn (g-i) electrodes after being tested at a current density of 2 mA cm⁻² for a capacity of 2 mAh cm⁻² for 30 cycles in symmetric cells. Both top (d,g) and side (e,f,h,i) views are shown.

Mitigation of dendrite development was thus inferred to be the main mechanism behind the enhanced stability of the graphene-coated electrode. Such a conclusion was corroborated by means of chronoamperometric tests carried out on the symmetric cells at a polarization voltage of -150 mV (Fig. 7b). For the bare Zn electrode, the measured current was seen to increase steadily with time, which indicated that the surface area available for zinc nucleation and growth was continuously enlarging. In turn, the latter was a clear sign of dendrite development driven by the 2D diffusion and non-uniform deposition of zinc on the electrode surface [88,93]. By contrast, the recorded current reached a plateau very rapidly with the AG-BE+2@Zn electrode, implying a much more restricted diffusion of zinc across the electrode surface and a more uniform deposition of the metal, leading up to little dendrite generation. This behavior was ascribed to the abundance of zincophilic sites on the anodic graphene nanosheets in the form of carboxylic groups, which were thought to favor nucleation processes and thus a more uniform plating of the metal by curtailing 2D diffusion [27,93]. Further support for the kinetically enhanced deposition of zinc on the AG-BE+2@Zn electrode relative to its bare Zn counterpart was obtained from EIS data. Fig. 7c shows Nyquist plots recorded on symmetric cells with these two electrodes, where the substantially lower interfacial charge-transfer resistance (smaller diameter of the semicircular feature) noticed for the AG-BE+2@Zn electrode revealed more favorable zinc deposition processes. The different propensity of the two electrodes towards dendrite development was confirmed by direct imaging of cycled electrodes. Fig. 7d-i shows FE-SEM images of the bare Zn (d-f) and AG-BE+2@Zn (g-i) electrodes after being tested at a current density/capacity of 2 mA cm⁻²/2 mAh cm⁻² for 30 cycles in symmetric cells, where both top (d,g) and cross-sectional (e,f,h,i) views are provided. An uneven and rough morphology indicative of non-uniform zinc deposition and considerable dendrite formation was observed for the cycled bare Zn electrode. On the other hand, the surface morphology was smoother and more

compact in the case of the AG-BE+2@Zn electrode, consistent with a more uniform deposition of the metal that alleviated the generation of dendrites.

Finally, full cells were tested and compared using the bare Zn and AG-BE+2@Zn electrodes as AZIB anodes. To this end, nanostructured MoS₂ (n-MoS₂) was employed as the cathode material. Specifically, n-MoS₂ was prepared in the form of nanometer-thick flakes vertically grown onto a carbon paper substrate via hydrothermal synthesis strategies previously reported in the literature (see Experimental section for details) [97,98]. Fig. S14a and b (section S5, ESM) shows FE-SEM images of the n-MoS₂ material, where vertically arranged nanosheets were seen to uniformly decorate the individual carbon fibers that make up the carbon paper substrate. As deduced from X-ray diffraction (Fig. S14c) and XPS (Fig. S14d and e) measurements, these MoS₂ nanosheets exhibited an enlarged interlayer spacing (~9.5 Å vs 6.7 Å for standard bulk or nanostructured MoS₂) and were mostly in the metallic 1T phase rather than in the thermodynamically stable, semiconducting 2H phase of this transition metal dichalcogenide [99]. Fig. 8a plots typical CVs recorded for the bare Zn//n-MoS₂ and AG-BE+2@Zn//n-MoS₂ cells at a potential scan rate of 0.1 mV s⁻¹. Both CVs were very much alike and displayed the characteristic features of MoS₂-based AZIBs, most prominently a pair of broad redox peaks at ~0.70 (cathodic branch) and 0.95 (anodic branch) V vs. Zn/Zn²⁺, associated to Zn²⁺ intercalation into/deintercalation from the MoS₂ lattice, respectively [97]. The rate capability of both cells for gravimetric currents in the range between 0.1 and 3 A g⁻¹ was very similar, as shown in Fig. 8b (representative GCD profiles where these data were taken from are shown in Fig. S15, section S5 of ESM). Fig. 8c shows the long-term cyclic behavior of the two cells at 1 A g⁻¹, where the improved stability of the device incorporating the anodic graphene-coated zinc anode in terms of capacity retention was made apparent.

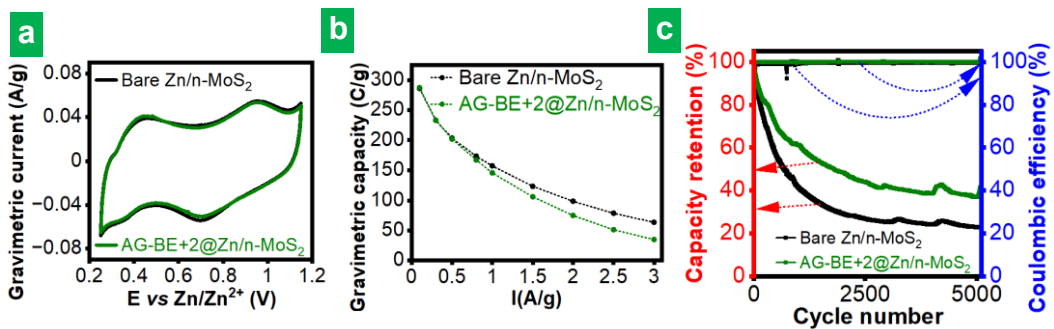


Figure 8. Electrochemical performance of full cells: bare Zn//n-MoS₂ (black traces/circles), AG-BE+2@Zn//n-MoS₂ (green traces/circles). **(a)** CVs recorded at a potential scan rate of 0.1 mV s⁻¹. **(b)** Rate capability behavior tested at gravimetric currents between 0.1 and 3 A g⁻¹. **(c)** Cycling performance measured at a gravimetric current of 1 A g⁻¹.

4. Conclusions

We have demonstrated a straightforward and mild route for the preparation of hydrophilic, carboxyl-enriched graphene nanosheets based on the aqueous anodic exfoliation of graphite and resorting to proper combinations of common electrolytes. More specifically, starting from Na₂SO₄ solution as the base electrolyte, inclusion of NaOH and NaCl as electrolyte additives allowed some tunability in the populations of oxygen functional groups generated in the resulting oxidized anodic graphenes, not only of carboxyls but also of hydroxyls and epoxides. Such a tunability was ultimately ascribed to the reactivity of OH⁻ and Cl⁻ ions with oxygen functional groups on the carbon surface and/or with oxygen radicals and other chemical species brought about by the anodic process. Even though the produced anodic graphenes were highly oxidized (O/C atomic ratios of ~0.25–0.27), they exhibited a considerable electrical conductivity, in the range of 10²–10³ S m⁻¹. This allowed their direct use as electrode materials for electrochemical energy storage without the need to apply reduction treatments that are prevalent for standard graphene oxides. Indeed, the carboxyl-enriched anodic

graphene was processed into compact films and tested as the active cathode material in aqueous zinc-ion hybrid capacitors, where it generally exhibited a higher capacity and rate capability than those of standard anodic graphene and reduced graphene oxides obtained by common routes (Hummers' method). Moreover, the cathode performance of this new anodic graphene was improved via hybridization with a multifunctional biomolecule, namely, flavin mononucleotide, which enhanced the electrode wettability and contributed additional capacity, especially at high currents. The carboxyl-enriched anodic graphene was also shown to act as an efficient protective coating for the zinc metal electrode of aqueous energy storage devices, affording cycle lives that were for the most part longer than those typical of coatings based on carbon materials. The protective effect of this anodic graphene was concluded to derive mainly from the inhibition of dendrite generation and attributed to the zincophilic nature of its carboxyl groups. Finally, we believe that modulation of the types of oxygen groups in graphene demonstrated here by a simple and environmentally friendly anodic route provides opportunities for application not only in the broader field of aqueous batteries and hybrid capacitors, but also in other areas. The latter include water purification via nanofiltration and drug delivery, which may be facilitated by chemoselective derivatization of specific oxygen groups.

Electronic Supplementary Material. The Supplementary Material is available free of charge on the Elsevier website at <https://doi.org/10.1016/j.carbon.2024.119293>.

SEM images of starting and anodically treated graphite. Additional XPS data. Additional STEM and AFM results. Additional results and data on the use of anodic graphene as an AZIC cathode. Additional results and data on the use of anodic graphene for the protection of zinc metal anodes.

Acknowledgements

Funding by the Spanish Ministerio de Ciencia e Innovación and Agencia Estatal de Investigación (MCIN/AEI/10.13039/501100011033) as well as the European Regional Development Fund (ERDF, A way of making Europe) through grant PID2021-125246OB-I00, by MCIN/AEI/10.13039/501100011033 and the European Union NextGenerationEU/PRTR through grant TED2021-131517B-C22, as well as by Plan de Ciencia, Tecnología e Innovación (PCTI) 2018-2022 del Principado de Asturias and the ERDF through grant IDI/2021/000037. E.A-R. and A.M-J. are grateful to the Spanish MCIN for their pre-doctoral contracts (PRE2022-104458 and PRE2019-087583, respectively).

Reference

- [1] M. Li, J. Lu, Z. Chen, K. Amine, 30 years of lithium-ion batteries, *Advanced Materials* 30 (2018), 1800561.
- [2] G. Zubi, R. Dufo-López, M. Carvalho, G. Pasaoglu, The lithium-ion battery: state of the art and future perspectives, *Renewable and Sustainable Energy Reviews* 89 (2018), 292-308.
- [3] Z. Pan, X. Liu, J. Yang, X. Li, Z. Liu, X.J. Lo, J. Wang, Aqueous rechargeable multivalent metal-ion batteries: advances and challenges, *Advanced Energy Materials* 11 (2021), 2100608.
- [4] L. Dong, W. Yang, W. Yang, Y. Li, W. Wu, G. Wang, Multivalent metal ion hybrid capacitors: a review with a focus on zinc-ion hybrid capacitors, *Journal of Materials Chemistry A* 7 (2019), 13810-13832.
- [5] B. Tang, L. Shan, S. Liang, J. Zhou, Issues and opportunities facing aqueous zinc-ion batteries, *Energy & Environmental Science* 12 (2019), 3288-3304.
- [6] H. Liu, J.-G. Wang, Z. You, C. Wei, F. Kang, B. Wei, Rechargeable aqueous zinc-ion batteries: mechanism, design strategies and future perspectives, *Materials Today* 42 (2021), 73-98.
- [7] H. Tang, J. Yao, Y. Zhu, Recent developments and future prospects for zinc-ion hybrid capacitors: a review, *Advanced Energy Materials* 11 (2021), 2003994.
- [8] C. Liu, X. Xie, B. Lu, J. Zhou, S. Liang, Electrolyte strategies toward better zinc-ion batteries, *ACS Energy Letters* 6 (2021), 1015-1033.
- [9] C. Nie, G. Wang, D. Wang, M. Wang, X. Gao, Z. Ba, N. Wang, J. Yang, Z. Xing, S. Dou, Recent progress on Zn anodes for advanced aqueous zinc-ion batteries, *Advanced Energy Materials* 13 (2023), 2300606.
- [10] G. Li, L. Sun, S. Zhang, C. Zhang, H. Jin, K. Dave, G. Liang, S. Liu, J. Mao, Z. Guo, Developing cathode materials for aqueous zinc ion batteries: challenges and practical prospects, *Advanced Functional Materials* 34 (2023), 2301291.
- [11] M. Devi, B. Moorthy, R. Thangavel, Recent developments in zinc metal anodes, cathodes, and electrolytes for zinc-ion hybrid capacitors, *Sustainable Energy & Fuels* 7 (2023), 3776-3795.
- [12] Y. Liu, L. Wu, Recent advances of cathode materials for zinc-ion hybrid capacitors, *Nano Energy* 109 (2023), 108290.
- [13] Z. Wang, M. Zhang, W. Ma, J. Zhu, W. Song, Application of carbon materials in aqueous zinc ion energy storage devices, *Small* 17 (2021), 2100219.
- [14] D. Sui, M. Wu, K. Shi, C. Li, J. Lang, Y. Yang, X. Zhang, X. Yan, Y. Chen, Recent progress of cathode materials for aqueous zinc-ion capacitors: carbon-based materials and beyond, *Carbon* 185 (2021), 126-151.

- [15] Y. Wang, S. Sun, X. Wu, H. Liang, W. Zhang, Status and opportunities of zinc ion hybrid capacitors: focus on carbon materials, current collectors, and separators, *Nano-Micro Letters* 15 (2023), 78.
- [16] L. Wu, Y. Dong, Recent progress of carbon nanomaterials for high-performance cathodes and anodes in aqueous zinc ion batteries, *Energy Storage Materials* 41 (2021), 715-737.
- [17] M. Xue, J. Bai, M. Wu, Q. He, Q. Zhang, L. Chen, Carbon-assisted anodes and cathodes for zinc ion batteries: from basic science to specific applications, opportunities and challenges, *Energy Storage Materials* 62 (2023), 102940.
- [18] C. Mao, Y. Chang, X. Zhao, X. Dong, Y. Geng, N. Zhang, L. Dai, X. Wu, L. Wang, Z. He, Functional carbon materials for high-performance Zn metal anodes, *Journal Energy Chemistry* 75 (2022), 135-153.
- [19] M. Aizudin, W. Fu, R.P. Pottammel, Z. Dai, H. Wang, X. Rui, J. Zhu, C. C. Li, X. L. Wu, E. H. Ang, Recent advancements of graphene-based materials for zinc-based batteries: beyond lithium-ion batteries, *Small* 20 (2023), 2305217.
- [20] R. Arvidsson, D. Kushnir, B.A. Sandén, S. Molander, Prospective life cycle assessment of graphene production by ultrasonication and chemical reduction, *Environmental Science & Technology* 48 (2014), 4529-4536.
- [21] J. Munuera, L. Britnell, C. Santoro, R. Cuéllar-Franca, C. Casiraghi, A review on sustainable production of graphene and related life cycle assessment, *2D Materials* 9 (2022), 012002.
- [22] W. Cai, R.D. Piner, F.J. Stadermann, S. Park, M.A. Shaibat, Y. Ishii, D. Yang, A. Velamakanni, S. J. An, M. Stoller, D. Chen, R. S. Ruoff, Synthesis and solid-state NMR structural characterization of 13C-labeled graphite oxide, *Science* 321 (2008), 1815-1817.
- [23] W. Gao, L.B. Alemany, L. Ci, P.M. Ajayan, New insights into the structure and reduction of graphite oxide, *Nature Chemistry* 1 (2009), 403-408.
- [24] S. Guo, S. Garaj, A. Bianco, C. Ménard-Moyon, Controlling covalent chemistry on graphene oxide, *Nature Reviews Physics* 4 (2022), 247-262.
- [25] Y. Zeng, L. Prasetyo, V.T. Nguyen, T. Horikawa, D.D. Do, D. Nicholson, Characterization of oxygen functional groups on carbon surfaces with water and methanol adsorption, *Carbon* 81 (2015), 447-457.
- [26] Y. Xu, B. Tian, S. Fang, W. Guo, Z. Zhang, Probing the interaction of water molecules with oxidized graphene by first principles, *Journal of Physical Chemistry C* 125 (2021), 4580-4587.
- [27] Y. Yang, H. Hua, Z. Lv, M. Zhang, C. Liu, Z. Wen, H. Xie, W. He, J. Zhao, C. C. Li, Reconstruction of electric double layer for long-life aqueous zinc metal batteries, *Advanced Functional Materials* 33 (2023), 2212446.
- [28] S. Yang, M.R. Lohe, K. Müllen, X. Feng, New-generation graphene from electrochemical approaches: production and applications, *Advanced Materials* 28 (2016), 6213-6221.
- [29] F. Liu, C. Wang, X. Sui, M.A. Riaz, M. Xu, L. Wei, Y. Chen, Synthesis of graphene materials by electrochemical exfoliation: recent progress and future potential, *Carbon Energy* 1 (2019), 173-199.

Artículo II

- [30] N.S. Mankge, M.J. Madito, N.W. Hlongwa, A.T. Kuvarega, Review of electrochemical production of doped graphene for energy storage applications, *Journal of Energy Storage* 46 (2022), 103527.
- [31] W. Li, M. Wojcik, K. Xu, Optical microscopy unveils rapid, reversible electrochemical oxidation and reduction of graphene, *Nano Letters* 19 (2019), 983-989.
- [32] A.M. Abdelkader, A.J. Cooper, R.A.W. Dryfe, I.A. Kinloch, How to get between the sheets: a review of recent works on the electrochemical exfoliation of graphene materials from bulk graphite, *Nanoscale* 7 (2015), 6944-6956.
- [33] J.I. Paredes, J.M. Munuera, Recent advances and energy-related applications of high quality/chemically doped graphenes obtained by electrochemical exfoliation methods, *Journal of Materials Chemistry A* 5 (2017), 7228-7242.
- [34] S. Yang, S. Brüller, Z. S. Wu, Z. Liu, K. Parvez, R. Dong, F. Richard, P. Samori, X. Feng, K. Müllen, Organic radical-assisted electrochemical exfoliation for the scalable production of high-quality graphene, *Journal of the American Chemical Society* 137 (2015), 13927-13932.
- [35] J.M. Munuera, J.I. Paredes, S. Villar-Rodil, A. Castro-Muñiz, A. Martínez-Alonso, J.M.D. Tascón, High quality, low-oxidized graphene via anodic exfoliation with table salt as an efficient oxidation-preventing co-electrolyte for water/oil remediation and capacitive energy storage applications, *Applied Materials Today* 11 (2018), 246-254.
- [36] J. Cao, P. He, M.A. Mohammed, X. Zhao, R.J. Young, B. Derby, I. A. Kinloch, R. A. Dryfe, Two-step electrochemical intercalation and oxidation of graphite for the mass production of graphene oxide, *Journal of the American Chemical Society* 139 (2017), 17446-17456.
- [37] S. Pei, Q. Wei, K. Huang, H.M. Cheng, W. Ren, Green synthesis of graphene oxide by seconds timescale water electrolytic oxidation, *Nature Communications* 9 (2018), 145.
- [38] D. Chen, Z. Lin, M.M. Sartin, T. X. Huang, J. Liu, Q. Zhang, L. Han, J. F. Li, Z. Q. Tian, D. Zhan, Photosynergetic electrochemical synthesis of graphene oxide, *Journal of the American Chemical Society* 142 (2020), 6516-6520.
- [39] D. Wu, M. Sun, W. Zhang, W. Zhang, Simultaneous regulation of surface properties and microstructure of graphene oxide membranes for enhanced nanofiltration performance, *ACS Applied Materials & Interfaces* 15 (2023), 52029-52037.
- [40] A. Kovtun, D. Jones, S. Dell'Elce, E. Treossi, A. Liscio, V. Palermo, Accurate chemical analysis of oxygenated graphene-based materials using X-ray photoelectron spectroscopy, *Carbon* 143 (2019), 268-275.
- [41] C.-Y. Su, A. Y. Lu, Y. Xu, F.-R. Chen, A.N. Khlobystov, L. J. Li, High-quality thin graphene films from fast electrochemical exfoliation, *ACS Nano* 5 (2011), 2332-2339.
- [42] K. Parvez, Z. S. Wu, R. Li, X. Liu, R. Graf, X. Feng, K. Müllen, Exfoliation of graphite into graphene in aqueous solutions of inorganic salts, *Journal of American Chemical Society* 136 (2014), 6083-6091.
- [43] A. Ambrosi, M. Pumera, Electrochemically exfoliated graphene and graphene oxide for energy storage and electrochemistry applications, *Chemistry A European Journal* 22 (2016), 153-159.

- [44] H. Lee, J.I. Choi, J. Park, S.S. Jang, S.W. Lee, Role of anions on electrochemical exfoliation of graphite into graphene in aqueous acids, *Carbon* 167 (2020), 816-820.
- [45] J.M. Munuera, J.I. Paredes, S. Villar-Rodil, M. Ayán-Varela, A. Pagán, S.D. Aznar-Cervantes, J.L. Cenis, A. Martínez-Alonso, J.M.D. Tascón, High quality, low oxygen content and biocompatible graphene nanosheets obtained by anodic exfoliation of different graphite types, *Carbon* 94 (2015), 729-739.
- [46] M. Sevilla, G.A. Ferrero, A.B. Fuertes, Aqueous dispersions of graphene from electrochemically exfoliated graphite, *Chemistry Europe Journal* 22 (2016), 17351-17358.
- [47] I. Ferrari, A. Motta, R. Zanoni, F.A. Scaramuzzo, F. Amato, E.A. Dalchiele, A.G. Marrani, Understanding the nature of graphene oxide functional groups by modulation of the electrochemical reduction: a combined experimental and theoretical approach, *Carbon* 203 (2023), 29-38.
- [48] A. Kovtun, D. Jones, S. Dell'Elce, E. Treossi, A. Liscio, V. Palermo, Accurate chemical analysis of oxygenated graphene-based materials using X-ray photoelectron spectroscopy, *Carbon* 143 (2019), 268-275.
- [49] X. Fan, W. Peng, Y. Li, X. Li, S. Wang, G. Zhang, F. Zhang, Deoxygenation of exfoliated graphite oxide under alkaline conditions: a green route to graphene preparation, *Advanced Materials* 20 (2008), 4490-4493.
- [50] A. Dimiev, L.B. Alemany, J.M. Tour, Graphene oxide. Origin of acidity, its instability in water, and a new dynamic structural model, *ACS Nano* 7 (2013), 576-588.
- [51] C. Chen, W. Kong, H.-M. Duan, J. Zhang, Theoretical simulation of reduction mechanism of graphene oxide in sodium hydroxide solution, *Physical Chemistry Chemical Physics* 16 (2014), 12858-12864.
- [52] D.F. Carrasco, J.I. Paredes, S. Villar-Rodil, F. Suárez-García, A. Martínez-Alonso, J.M.D. Tascón, An electrochemical route to holey graphene nanosheets for charge storage applications, *Carbon* 195 (2022), 57-68.
- [53] Y. Kuang, J. Chen, X. Zheng, X. Zhang, Q. Zhou, C. Lu, Synthesis of carboxylate-functionalized graphene nanosheets for high dispersion of platinum nanoparticles based on the reduction of graphene oxide via 1-pyrenecarboxaldehyde, *Nanotechnology* 24 (2013), 395604.
- [54] N. Pan, D. Guan, Y. Yang, Z. Huang, R. Wang, Y. Jin, C. Xia, A rapid low-temperature synthetic method leading to large-scale carboxyl graphene, *Chemical Engineering Journal* 236 (2014), 471-479.
- [55] S. Guo, J. Raya, D. Ji, Y. Nishina, C. Ménard-Moyon, A. Bianco, Is carboxylation an effective method for graphene oxide functionalization?, *Nanoscale Advances* 2 (2020), 4085-4092.
- [56] Irkham, Y. Einaga, Oxidation of hydroxide ions in weak basic solutions using boron-doped diamond electrodes: effect of the buffer capacity, *Analyst* 144 (2019), 4499-4504.
- [57] G.G. Jayson, B.J. Parsons, A.J. Swallow, Some simple, highly reactive, inorganic chlorine derivatives in aqueous solution. Their formation using pulses of radiation and their role in the mechanism of the Fricke dosimeter, *Journal of the Chemical Society, Faraday Transactions 1* 69 (1973), 1597-1607.

Artículo II

- [58] C.K. Chua, M. Pumera, Selective removal of hydroxyl groups from graphene oxide, *Chemistry A European Journal* 19 (2013), 2005-2011.
- [59] Y. Zheng, S. Li, D. Han, L. Kong, J. Wang, M. Zhao, W. Cheng, H. Ju, Z. Yang, S. Ding, Eco-friendly preparation of epoxy-rich graphene oxide for wound healing, *ACS Biomaterials Science & Engineering Journal* 7 (2021), 752-763.
- [60] C. H. Kim, S.I. Kim, F.N. Ju, Y. W. Cho, H. Kim, J. H. Park, K.-H. Lee, H. Son, Z. Luo, T. H. Kim, Fabrication of hydroxyl-group-rich reduced graphene oxide film and its application for electrochemical detection of hydrogen peroxide, *Advanced Materials Technologies* 8 (2023), 2300470.
- [61] S. Choudhary, H.P. Mungse, O.P. Khatri, Hydrothermal deoxygenation of graphene oxide: chemical and structural evolution, *Chemistry An Asian Journal* 8 (2013), 2070-2078.
- [62] G. Lee, B. Lee, J. Kim, K. Cho, Ozone adsorption on graphene: ab initio study and experimental validation, *The Journal of Physical Chemistry C* 113 (2009), 14225-14229.
- [63] M.E.H. Bergmann, J. Rollin, Product and by-product formation in laboratory studies on disinfection electrolysis of water using boron-doped diamond anodes, *Catalysis Today* 124 (2007), 198-203.
- [64] M. Zhang, M. Yang, Y. Okigawa, T. Yamada, H. Nakajima, Y. Iizumi, T. Okazaki, Patterning of graphene using wet etching with hypochlorite and UV light, *Scientific Reports* 12 (2022), 4541.
- [65] M. Yang, Y. Iizumi, L. Chen, T. Okazaki, D. Futaba, M. Zhang, Rapid room temperature degradation of carbon nanotubes by sodium hypochlorite and UV-light irradiation, *Carbon* 208 (2023), 238-246.
- [66] D. Li, M.B. Müller, S. Gilje, R.B. Kaner, G.G. Wallace, Processable aqueous dispersions of graphene nanosheets, *Nature Nanotechnology* 3 (2008), 101-105.
- [67] B. Konkena, S. Vasudevan. Understanding aqueous dispersibility of graphene oxide and reduced graphene oxide through pKa measurements, *The Journal of Physical Chemistry Letters* 3 (2012), 867-872.
- [68] J. Hu, H. Zeng, C. Wang, Z. Li, C. Kan, Y. Liu, Interband π plasmon of graphene: strong small-size and field-enhancement effects, *Physical Chemistry Chemical Physics* 16 (2014), 23483-23491.
- [69] M.J. Fernández-Merino, L. Guardia, J.I. Paredes, S. Villar-Rodil, P. Solís-Fernández, A. Martínez-Alonso, J.M.D. Tascón, Vitamin C is an ideal substitute for hydrazine in the reduction of graphene oxide suspensions, *The Journal of Physical Chemistry C* 114 (2010), 6426-6432.
- [70] L. Guardia, M.J. Fernández-Merino, J.I. Paredes, P. Solís-Fernández, S. Villar-Rodil, A. Martínez-Alonso, J.M.D. Tascón, High-throughput production of pristine graphene in an aqueous dispersion assisted by non-ionic surfactants, *Carbon* 49 (2011), 1653-1662.
- [71] M.A. Pimenta, G. Dresselhaus, M.S. Dresselhaus, L.G. Cançado, A. Jorio, R. Saito, Studying disorder in graphite-based systems by Raman spectroscopy, *Physical Chemistry Chemical Physics* 9 (2007), 1276-1290.
- [72] J.B. Wu, M.L. Lin, X. Cong, H.N. Liu, P.H. Tan, Raman spectroscopy of graphene-based materials and its applications in related devices, *Chemical Society Reviews* 47 (2018), 1822-1873.

- [73] A. C. Ferrari, J. Robertson, Interpretation of Raman spectra of disordered and amorphous carbon, *Physical Reviews B* 61 (2000), 14095-14107.
- [74] R. Rasuli, Z. Mokarian, R. Karimi, H. Shabanzadeh, Y. Abedin, Wettability modification of graphene oxide by removal of carboxyl functional groups using non-thermal effects of microwave, *Thin Solid Films* 589 (2015), 364–368.
- [75] M. Lotya, A. Rakovich, J.F. Donegan, J.N. Coleman, Measuring the lateral size of liquid-exfoliated nanosheets with dynamic light scattering, *Nanotechnology* 24 (2013), 265703.
- [76] P. Solís-Fernández, J.I. Paredes, S. Villar-Rodil, A. Martínez-Alonso, J.M.D. Tascón, Determining the thickness of chemically modified graphenes by scanning probe microscopy, *Carbon* 48 (2010), 2657-2660.
- [77] J.I. Paredes, S. Villar-Rodil, P. Solís-Fernández, A. Martínez-Alonso, J.M.D. Tascón, Atomic force and scanning tunneling microscopy imaging of graphene nanosheets derived from graphite oxide, *Langmuir* 25 (2009), 5957-5968.
- [78] J. Yin, W. Zhang, W. Wang, N.A. Alhebshi, N. Salah, H.N. Alshareef, Electrochemical zinc ion capacitors enhanced by redox reactions of porous carbon cathodes, *Advanced Energy Materials* 10 (2020), 2001705.
- [79] Y. Shao, Z. Sun, Z. Tian, S. Li, G. Wu, M. Wang, X. Tong, F. Shen, Z. Xia, V. Tung, J. Sun, Y. Shao, Regulating oxygen substituents with optimized redox activity in chemically reduced graphene oxide for aqueous Zn-ion hybrid capacitor, *Advanced Functional Materials* 31 (2021), 2007843.
- [80] H. Xu, W. He, Z. Li, J. Chi, J. Jiang, K. Huang, S. Li, G. Sun, H. Dou, X. Zhang, Revisiting charge storage mechanism of reduced graphene oxide in zinc ion hybrid capacitor beyond the contribution of oxygen-containing groups, *Advanced Functional Materials* 32 (2022), 2111131.
- [81] A. Noori, M.F. El-Kady, M.S. Rahmanifar, R.B. Kaner, M.F. Mousavi, Toward establishing standard performance metrics for batteries, supercapacitors and beyond, *Chemical Society Reviews* 48 (2019), 1272-1341.
- [82] J. Luo, L. Xu, H. Liu, Y. Wang, Q. Wang, Y. Shao, M. Wang, D. Yang, S. Li, L. Zhang, Z. Xia, T. Chang, Y. Shao, Harmonizing graphene laminate spacing and zinc-ion solvated structure toward efficient compact capacitive charge storage, *Advanced Functional Materials* 32 (2022), 2112151.
- [83] J. Zhao, H. Lai, Z. Lyu, Y. Jiang, K. Xie, X. Wang, Q. Wu, L. Yang, Z. Jin, Y. Ma, J. Liu, Z. Hu, Hydrophilic hierarchical nitrogen-doped carbon nanocages for ultrahigh supercapacitive performance, *Advanced Materials* 27 (2015), 3541-3545.
- [84] Y. Lu, Z. Li, Z. Bai, H. Mi, C. Ji, H. Pang, C. Yu, J. Qiu, High energy-power Zn-ion hybrid supercapacitors enabled by layered B/N co-doped carbon cathode, *Nano Energy* 66 (2019), 104132.
- [85] M. Ayán-Varela, J.I. Paredes, L. Guardia, S. Villar-Rodil, J.M. Munuera, M. Díaz-González, C.F. Sánchez, A.M. Alonso, J.M.D. Tascón, Achieving extremely concentrated aqueous dispersions of graphene flakes and catalytically efficient graphene-metal nanoparticle hybrids with flavin mononucleotide as a high-performance stabilizer, *ACS Applied Materials & Interfaces Journal* 7 (2015), 10293-10307.

Artículo II

- [86] S. Huang, A. Croy, V. Bezugly, G. Cuniberti, Stabilization of aqueous graphene dispersions utilizing a biocompatible dispersant: a molecular dynamics study, *Physical Chemistry Chemical Physics* 21 (2019), 24007-24016.
- [87] Q. Yu, Z. Xue, M. Li, P. Qiu, C. Li, S. Wang, J. Yu, H. Nara, J. Na, Y. Yamauchi, Electrochemical activity of nitrogen-containing groups in organic electrode materials and related improvement strategies, *Advanced Energy Materials* 11 (2021), 2002523.
- [88] X. Peng, Y. Li, F. Kang, X. Li, Z. Zheng, L. Dong, Negatively charged hydrophobic carbon nano-onion interfacial layer enabling high-rate and ultralong-life Zn-based energy storage, *Small* 20 (2023), 2305547.
- [89] C. Shen, X. Li, N. Li, K. Xie, J. Wang, X. Liu, B. Wei, Graphene-boosted, high-performance aqueous Zn-ion battery, *ACS Applied Materials & Interfaces Journal* 10 (2018), 25446-25453.
- [90] A. Xia, X. Pu, Y. Tao, H. Liu, Y. Wang, Graphene oxide spontaneous reduction and self-assembly on the zinc metal surface enabling a dendrite-free anode for long-life zinc rechargeable aqueous batteries, *Applied Surface Science* 481 (2019), 852-859.
- [91] J. Zhou, M. Xie, F. Wu, Y. Mei, Y. Hao, R. Huang, G. Wei, A. Liu, L. Li, R. Chen, Ultrathin surface coating of nitrogen-doped graphene enables stable zinc anodes for aqueous zinc-ion batteries, *Advanced Materials* 33 (2021), 2101649.
- [92] X. Yang, J. Lv, C. Cheng, Z. Shi, J. Peng, Z. Chen, X. Lian, W. Li, Y. Zou, Y. Zhao, M. H. Rümmeli, S. Dou, J. Sun, Mosaic nanocrystalline graphene skin empowers highly reversible Zn metal anodes, *Advanced Science* 10 (2023), 2206077.
- [93] L. Hu, K. Yang, Y. Zhang, N. Wang, M. Sun, Z. Li, X. You, C. Jia, Interface engineering with porous graphene as deposition regulator of stable Zn metal anode for long-life Zn-ion capacitor, *Journal of Colloid and Interface Science* 631 (2023), 135-146.
- [94] M. Sun, K. Yang, N. Wang, L. Hu, X. Ren, Z. Li, C. Jia, X. Yao, Nitrogen-doped graphene enables stable zinc anode for long-term cycling aqueous Zn-ion batteries, *Applied Surface Science* 648 (2024), 159008.
- [95] G.B. Choi, S. Hong, J. H. Wee, D.-W. Kim, T.H. Seo, K. Nomura, H. Nishihara, Y. A. Kim, Quantifying carbon edge sites on depressing hydrogen evolution reaction activity, *Nano Letters* 20 (2020), 5885-5892.
- [96] R.M. Kluge, R.W. Haid, I.E.L. Stephens, F. Calle-Vallejo, A.S. Bandarenka, Monitoring the active sites for the hydrogen evolution reaction at model carbon surfaces, *Physical Chemistry Chemical Physics* 23 (2021), 10051-10058.
- [97] H. Liang, Z. Cao, F. Ming, W. Zhang, D.H. Anjum, Y. Cui, H.N. Alshareef, Aqueous zinc-ion storage in MoS₂ by tuning the intercalation energy, *Nano Letters* 19 (2019), 3199-3206.
- [98] H. Liu, J. G. Wang, W. Hua, Z. You, Z. Hou, J. Yang, C. Yang, C. Wei, F. Kang, Boosting zinc-ion intercalated in hydrated MoS₂ nanosheets toward substantially improved performance, *Energy Storage Materials* 35 (2021), 731-738.
- [99] S. Shi, Z. Sun, Y.H. Hu, Synthesis, stabilization and applications of 2-dimensional 1T metallic MoS₂, *Journal of Materials Chemistry A* 6 (2018), 23932-23977.

Electronic Supplementary Material for

Chemically tuning graphene via anodic exfoliation for enhanced performance in aqueous zinc-based electrochemical energy storage applications

D.F. Carrasco, E. Álvarez-Rubiera, S. Villar-Rodil*, A. Martínez-Jódar, J.M.D. Tascón, F. Suárez-García, J.I. Paredes*

Instituto de Ciencia y Tecnología del Carbono, INCAR-CSIC, C/Francisco Pintado Fe 26, 33011 Oviedo, Spain

*Corresponding authors' e-mail addresses: paredes@incar.csic.es (J. I. Paredes),
silvia@incar.csic.es (S. Villar-Rodil).

S1. SEM images of starting and anodically treated graphite

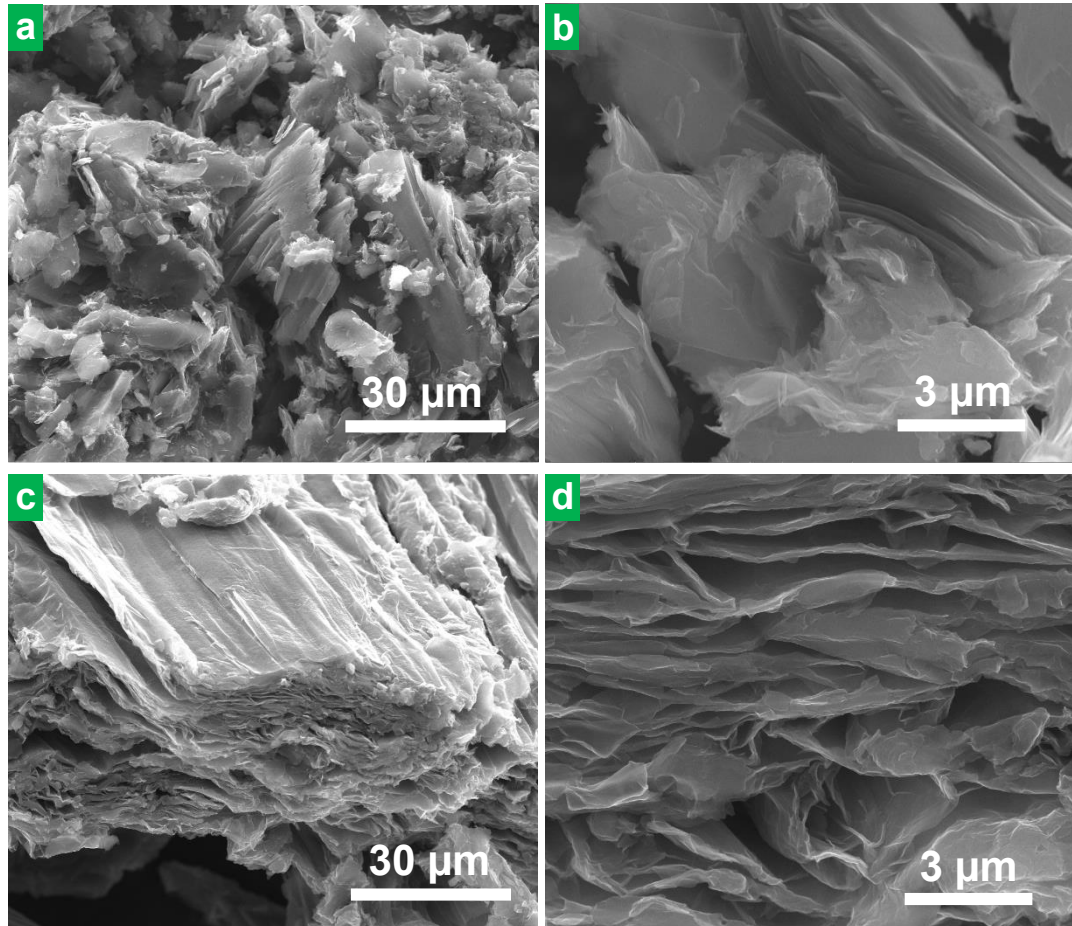


Figure S1. FE-SEM images of the starting graphite rod material (**a,b**) and the material right after anodic treatment in 0.1 M Na_2SO_4 electrolyte, i.e., before sonication (**c,d**). The starting graphite rod was gently rubbed with a spatula to pull off small particles for imaging.

S2. Additional XPS data

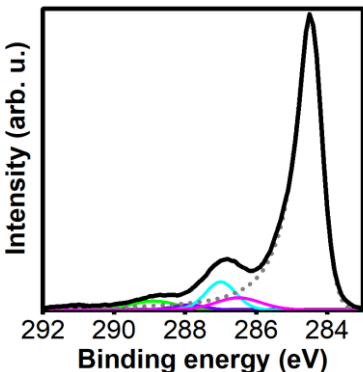


Figure S2. High resolution C 1s XPS core-level spectra of graphene obtained by anodic exfoliation of graphite foil with the base electrolyte (0.1 M Na₂SO₄). The C1s signal has been peak-fitted into 6 components: graphitic/graphenic carbon (dotted gray trace) and carbon in hydroxyl (magenta trace), epoxy (cyan), carbonyl/carboxylate (violet) and carboxyl (green) groups. The $\pi \rightarrow \pi^*$ shake-up satellite component is shown in red trace.

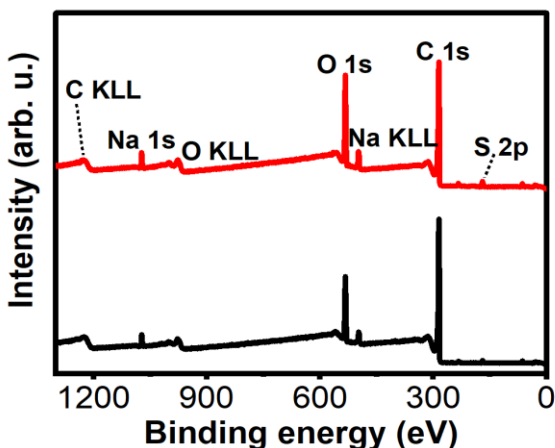


Figure S3. XPS survey spectra for graphene obtained by anodic exfoliation of graphite rod with the base electrolyte (AG-BE, top red trace) and graphite foil under the same conditions (bottom black trace). The main XPS and Auger bands for each element have been labeled for clarity. Apart from carbon and oxygen, some sodium and sulfur from residual electrolyte remaining on the surface of the materials have been detected.

S3. Additional STEM and AFM results

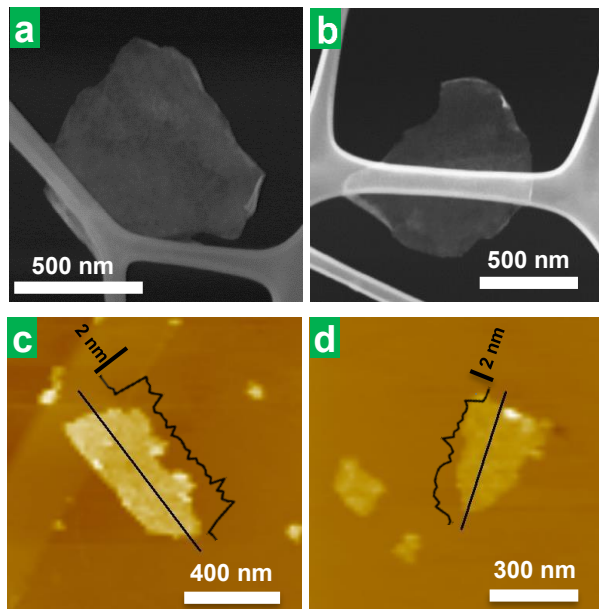


Figure S4. Representative (a,b) STEM and (c,d) AFM images of (a,c) AG-BE and (b,d) AG-BE+1 anodic graphene nanosheets.

S4. Additional results and data on the use of anodic graphene as an AZIC cathode

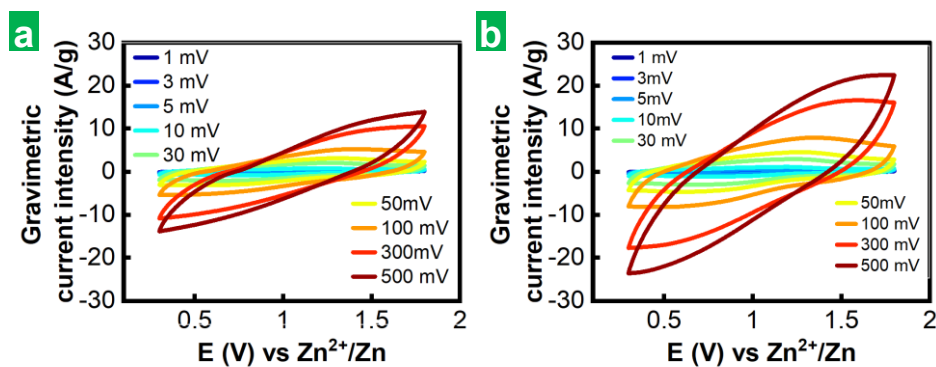


Figure S5. CVs obtained at different potential scan rates between 1 and 500 $mV\ s^{-1}$ for (a) AG-BE and (b) AG-BE+2 graphene films.

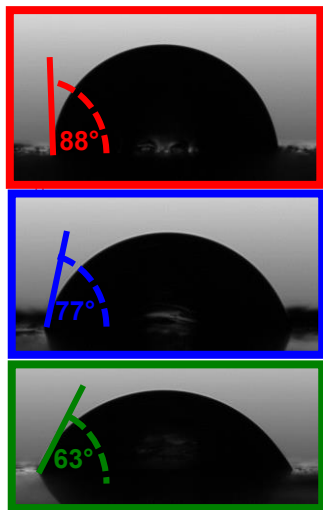


Figure S6. Contact angles of AG-BE (red), AG-BE+1 (blue) and AG-BE+2 (green) anodic graphenes with aqueous 2 M ZnSO_4 electrolyte.

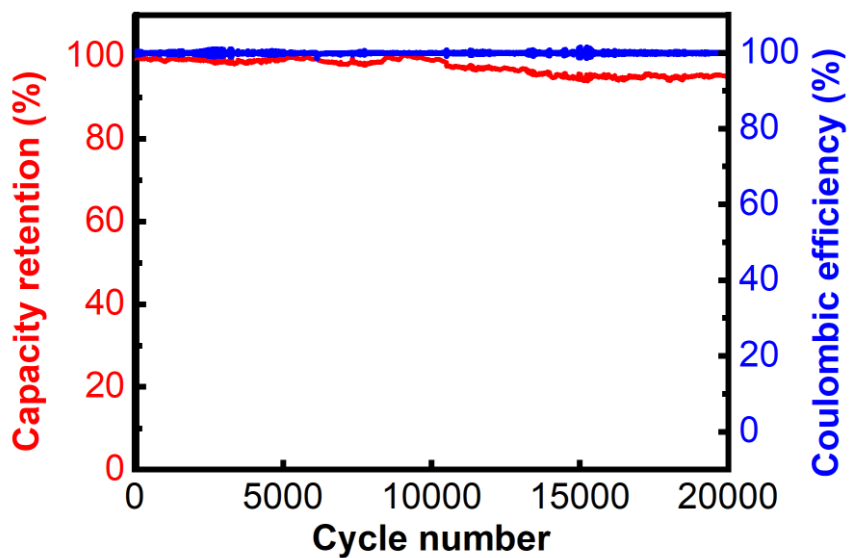


Figure S7. Cycling performance of AZIC cell recorded at a current of 1 A g^{-1} with AG-BE+2 anodic graphene film as the cathode: coulombic efficiency (blue trace), capacity retention (red trace).

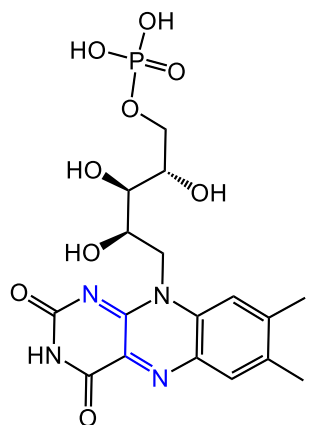


Figure S8. Chemical structure of flavin mononucleotide (FMN) with its redox center highlighted in blue.

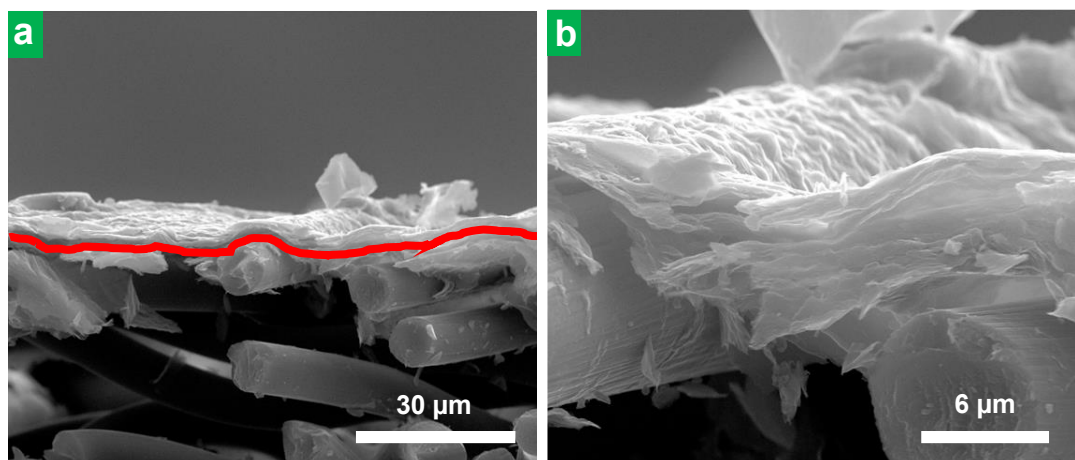


Figure S9. (a,b) FE-SEM images of carbon paper-supported FMN-anodic graphene (AG-BE+2) film (FMN:graphene mass ratio of 3:6) at different magnifications.

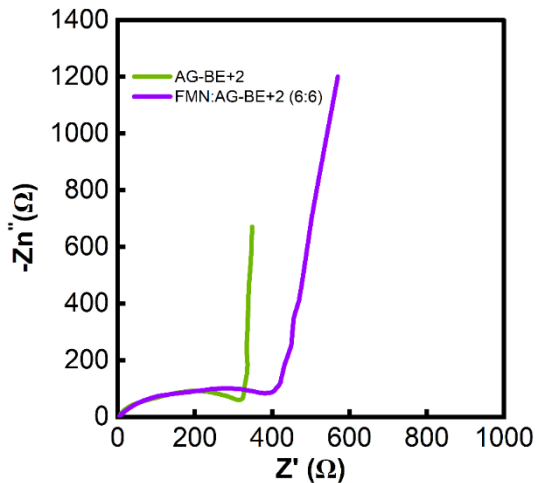


Figure S10. Nyquist plot recorded for AZIC cell with FMN-anodic AG-BE+2 graphene hybrid film (FMN:graphene mass ratio of 6:6) as the cathode (violet trace). The corresponding plot for the AG-BE+2 graphene-only film as the AZIC cathode is also shown for comparison (green)

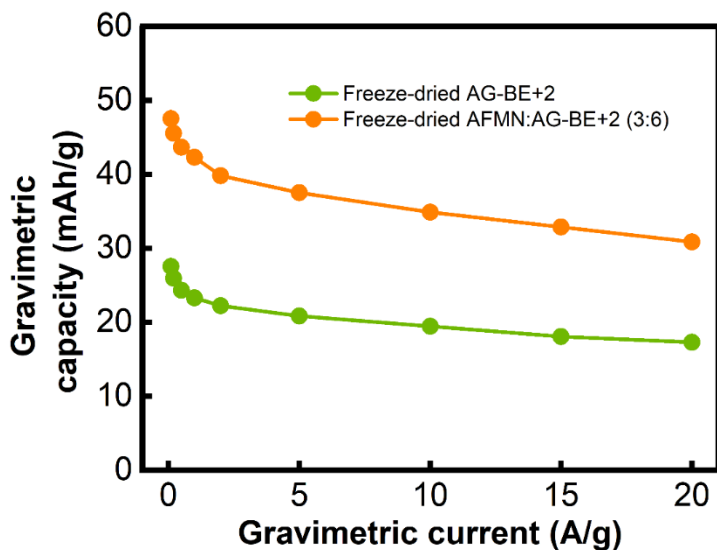


Figure S11. Gravimetric capacity values measured at different currents for AZIC cathodes based on freeze-dried anodic graphene material (AG-BE+2; green circles) and FMN-anodic graphene hybrid material (FMN:graphene mass ratio of 3:6; orange circles).

S5. Additional results and data on the use of anodic graphene for the protection of zinc metal anodes

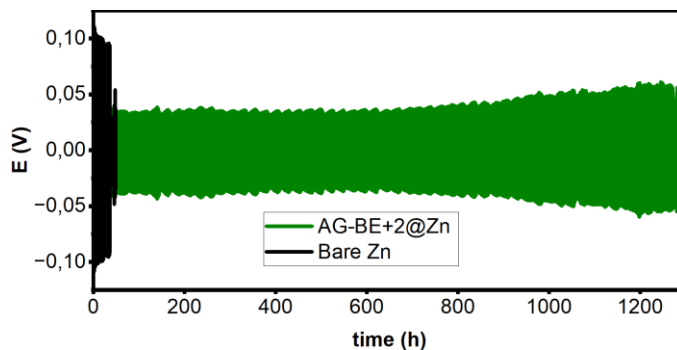


Figure S12. Cyclic zinc plating/stripping behavior recorded for bare Zn (black trace) and AG-BE+2@Zn (green trace) symmetric cells at a current density of 2 mA cm^{-2} for a capacity of 2 mAh cm^{-2} .

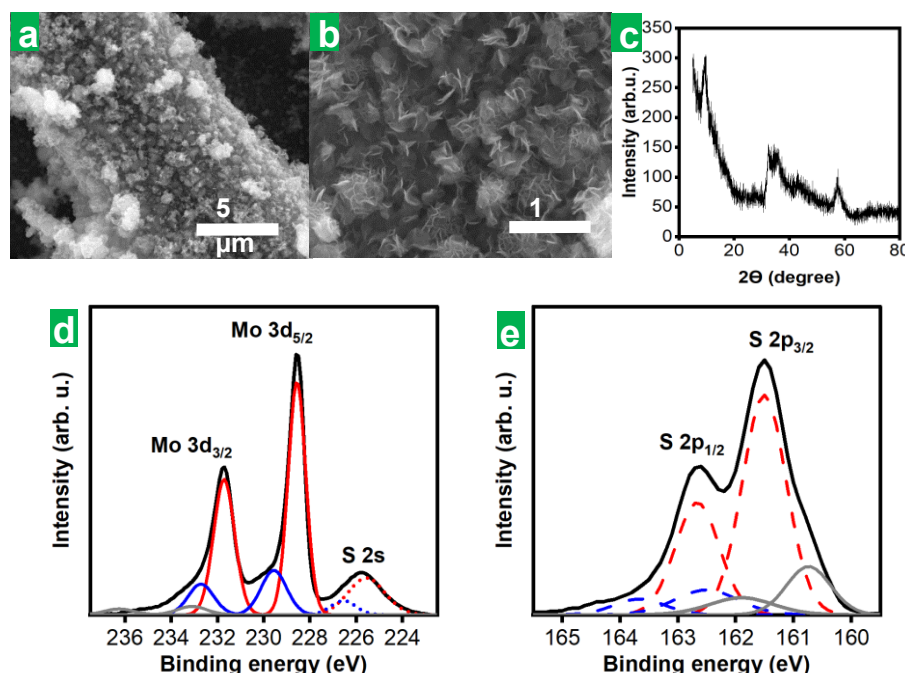


Figure S13. (a,b) FE-SEM images of nanostructured MoS₂ (n-MoS₂) hydrothermally synthesized on carbon paper substrate. (c) X-ray diffractogram of n-MoS₂. (d,e) High resolution core-level Mo 3d (d) and S 2p (e) XPS spectra of n-MoS₂.

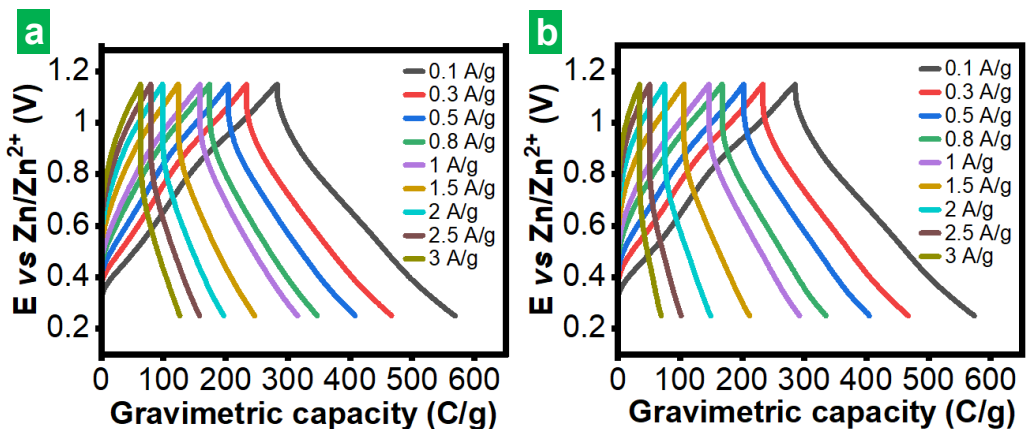


Figure S14. GCD profiles recorded for full (a) bare $Zn//n\text{-MoS}_2$ and (b) $AG\text{-BE}+2@Zn//n\text{-MoS}_2$ cells at different currents between 0.1 and 3 A g^{-1} .

Supporting Artículo II

Table S1. Cycling performance of symmetric cells based on zinc metal electrodes coated with different carbon-based materials as a protective barrier. In each case, the performance of the bare Zn electrode is also given for comparison.

Carbon Material	Current (mA cm ⁻²)	Capacity (mAh cm ⁻²)	Bare Zn lifespan (h)	Coated Zn lifespan (h)	Ref.
<i>AG-BE+2 anodic graphene</i>	0.5	0.5	140	2220	This work
	2	2	35	1270	
	5	5	15	820	
<i>Carbon nano-onions</i>	1	0.5	<50	2000	S1
	5	1	1	750	
<i>Self-assembled rGO (10 min)</i>	2	2	>400	>400	S2
<i>Self-assembled rGO (0.5-3h)</i>	0.4	0.4	92	2000	S3
	1	1	108	1200	
<i>N-doped graphene</i>	1	1	200	1200	S4
	5	5	20	300	
<i>N/O co-doped carbon</i>	1	1	45	3040	S5
<i>Flame-reduced GO</i>	2	1	100	750	S6
	5	5	50	410	
<i>N-doped rGO</i>	1	1	100	1200	S7
	5	5	55	140	
<i>N-doped hollow carbon spheres with Sn nanoparticles</i>	1	1	140	380	S8
<i>N-doped carbon</i>	1	1	72	>1000	S9
	2	2	30	800	
<i>Graphite</i>	0.1	0.1	70	200	S10
<i>Carbon nanotubes</i>	0.1	0.5	50	1800	S11
<i>N-rich carbon</i>	1	1	350	1350	S12
	5	5	50	220	
	20	1	150	>900	
<i>O,N-codoped carbon microflowers</i>	0.5	0.25	150	2000	S13
<i>F-doped carbon</i>	0.5	0.25	360	2200	S14
<i>Bifunctional N-doped carbon</i>	1	1	55	4000	S15
<i>Melamine foam-derived carbon</i>	2	1	400	650	S16
<i>Hydroxylated carbon nanotube film</i>	1	1	100	500	S17
<i>N-doped vertical graphene</i>	0.5	0.5	50	150	S18
<i>O,N-dual functionalized carbon cloth</i>	2	2	45	240	S19
<i>Conductive graphite fiber</i>	1	1	300	700	S20
<i>Zinc microspheres/carbon nanotubes/nanocellulose composite</i>	5	5	40	400	S21
<i>MOF-derived carbon</i>	1	1	25	50	S22

S7. References

- [1] X. Peng, Y. Li, F. Kang, X. Li, Z. Zheng, L. Dong, Negatively charged hydrophobic carbon nano-onion interfacial layer enabling high-rate and ultralong-life Zn-based energy storage, *Small* 20 (2023), 202305547.
- [2] C. Shen, X. Li, N. Li, K. Xie, J. Wang, X. Liu, B. Wei, Graphene-boosted, high-performance aqueous Zn-ion battery, *ACS Applied Materials & Interfaces* 10 (2018), 25446-25453.
- [3] A. Xia, X. Pu, Y. Tao, H. Liu, Y. Wang, Graphene oxide spontaneous reduction and self-assembly on the zinc metal surface enabling a dendrite-free anode for long-life zinc rechargeable aqueous batteries, *Applied Surface Science* 481 (2019), 852-859.
- [4] J. Zhou, M. Xie, F. Wu, Y. Mei, Y. Hao, R. Huang, G. Wei, A. Liu, L. Li, R. Chen, Ultrathin surface coating of nitrogen-doped graphene enables stable zinc anodes for aqueous zinc-ion batteries, *Advanced Materials* 33 (2021), 2101649.
- [5] X. Yang, J. Lv, C. Cheng, Z. Shi, J. Peng, Z. Chen, X. Lian, W. Li, Y. Zou, Y. Zhao, M.H. Rümmeli, S. Dou, J. Sun, Mosaic nanocrystalline graphene skin empowers highly reversible Zn metal anodes, *Advances. Science* 10 (2023), 2206077.
- [6] L. Hu, K. Yang, Y. Zhang, N. Wang, M. Sun, Z. Li, X. Yao, C. Jia, Interface engineering with porous graphene as deposition regulator of stable Zn metal anode for long-life Zn-ion capacitor, *Journal of Colloid and Interface Science* 631 (2023), 135-146.
- [7] M. Sun, K. Yang, N. Wang, L. Hu, X. Ren, Z. Li, C. Jia, X. Yao, Nitrogen-doped graphene enables stable zinc anode for long-term cycling aqueous Zn-ion batteries, *Applied Surface Science* 648 (2024), 159008.
- [8] H. Yu, Y. Zeng, N. W. Li, D. Luan, L. Yu, X. W. Lou, Confining Sn nanoparticles in interconnected N-doped hollow carbon spheres as hierarchical zincophilic fibers for dendrite-free Zn metal anodes, *Science Advances* 8 (2022), eabm5766.
- [9] C. Wu, K. Xie, K. Ren, S. Yang, Q. Wang, Dendrite-free Zn anodes enabled by functional nitrogen-doped carbon protective layers for aqueous zinc-ion batteries, *Dalton Transactions* 49 (2020), 17629-17634.
- [10] Z. Li, L. Wu, S. Dong, T. Xu, S. Li, Y. An, J. Jiang, X. Zhang, Pencil Drawing Stable Interface for Reversible and Durable Aqueous Zinc-Ion Batteries, *Advanced Functional Materials* 31 (2021), 2006495.
- [11] L. Dong, W. Yang, W. Yang, H. Tian, Y. Huang, X. Wang, C. Xu, C. Wang, F. Kang, G. Wang, Flexible and conductive scaffold-stabilized zinc metal anodes for ultralong-life zinc-ion batteries and zinc-ion hybrid capacitors, *Chemical Engineering Journal* 384 (2020), 123355.
- [12] X. Wang, K. Yang, C. Ma, W. Lu, N. Chen, M. Yao, Z. Li, C. Liu, H. Yue, D. Zhang, F. Du, N-Rich carbon as Zn²⁺ modulation layers for dendrite-free, highly reversible zinc anodes, *Chemical Engineering Journal* 452 (2023), 139257.
- [13] Z. Xu, S. Jin, N. Zhang, W. Deng, M. H. Seo, X. Wang, Efficient Zn Metal Anode Enabled by O,N-Codoped Carbon Microflowers, *Nano Letters* 22 (2022), 1350-1357.

Supporting Artículo II

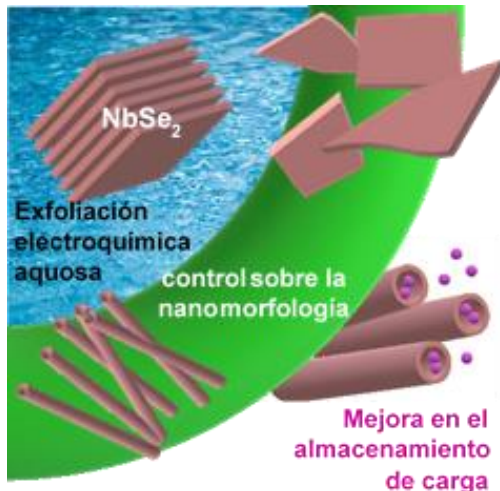
- [14] H. Wang, Y. Chen, H. Yu, W. Liu, G. Kuang, L. Mei, Z. Wu, W. Wei, X. Ji, B. Qu, L. Chen, A Multifunctional Artificial Interphase with Fluorine-Doped Amorphous Carbon layer for Ultra-Stable Zn Anode, *Advanced Functional Materials* 32 (2022), 2205600.
- [15] Y. Li, D. Zhao, J. Cheng, Y. Lei, Z. Zhang, W. Zhang, Q. Zhu, Abifunctional nitrogen doped carbon network as the interlayer for dendrite-free Zn anode, *Chemical Engineering Journal* 452 (2023), 139264.
- [16] Y. Liu, F. Tao, Y. Xing, Y. Pei, F. Ren, Melamine Foam-Derived Carbon Scaffold for Dendrite-Free and Stable Zinc Metal Anode, *Molecules* 28 (2023), 1742.
- [17] J. Q. Huang, Z. Hou, P. Gao, X. Yan, X. Lin, B. Zhang, A freestanding hydroxylated carbon nanotube film boosting the stability of Zn metal anodes, *Materials Today Communications* 32 (2022), 103939.
- [18] Q. Cao, H. Gao, Y. Gao, J. Yang, C. Li, J. Pu, J. Du, J. Yang, D. Cai, Z. Pan, C. Guan, W. Huang, Regulating Dendrite-Free Zinc Deposition by 3D Zincopilic Nitrogen-Doped Vertical Graphene for High-Performance Flexible Zn-Ion Batteries, *Advanced Functional Materials* 31 (2021), 2103922.
- [19] M. Zhou, G. Sun, S. Q. Zang, Uniform zinc deposition on O,N-dual functionalized carbon cloth current collector, *Journal of Energy Chemistry* 69 (2022), 76-83.
- [20] L. P. Wang, N. W. Li, T. S. Wang, Y. X. Yin, Y. G. Guo, C. R. Wang, Conductive graphite fiber as a stable host for zinc metal anodes, *Electrochimica Acta* 244 (2017), 172-177.
- [21] A. Wang, W. Zhou, M. Chen, A. Huang, Q. Tian, X. Xu, J. Chen, Integrated design of aqueous zinc-ion batteries based on dendrite-free zinc microspheres/carbon nanotubes/nanocellulose composite film anode, *Journal of Colloid and Interface Science* 594 (2021), 389-397.
- [22] Z. Wang, J. Huang, Z. Guo, X. Dong, Y. Liu, Y. Wang, Y. Xia, A Metal-Organic Framework Host for Highly Reversible Dendrite-free Zinc Metal Anodes, *Joule* 3 (2019), 1289-1300.

5.2. Obtención de dicalcogenuros de metales de transición mediante exfoliación electroquímica catódica

Artículo III

NbSe₂ nanosheets/nanorolls obtained via fast and direct aqueous electrochemical exfoliation for high capacity lithium storage, Daniel Fernández Carrasco, Sergio García-Dalí, Silvia Villar-Rodil, José M. Munuera, Encarnación Raymundo-Piñero, Juan Ignacio Paredes, *ACS Applied Energy Materials* 6 (2023), 7180-7193.

Resumen artículo III



Como se ha discutido en los artículos I y II, los grafenos y sus derivados son materiales atractivos para su aplicación como electrodos en almacenamiento electroquímico de energía. Pese a que éstos son los materiales 2D más ampliamente investigados para dicha aplicación, otros materiales 2D también presentan características que los hacen interesantes para el mismo tipo de uso. Entre ellos se encuentran los dicalcogenuros de metales de transición laminares. En concreto, MoS₂, WSe₂ y MoSe₂ son los más estudiados como materiales activos. Sin embargo, estos últimos son sólidos semiconductores en su fase termodinámicamente estable, lo que implica que su conductividad eléctrica es relativamente limitada. Otros dicalcogenuros menos estudiados, como el NbSe₂, poseen un carácter metálico y, por tanto, más eléctricamente conductor, lo que los hace potencialmente buenos candidatos para almacenamiento electroquímico de energía.

No obstante, hasta la fecha, la obtención de NbSe₂ 2D por métodos de exfoliación ha sido relativamente poco explorada más allá de las estrategias genéricas aplicadas al conjunto de materiales laminares. En el artículo III, se estudia la obtención de NbSe₂ exfoliado mediante una estrategia singular de deslaminación

Resumen Artículo III

electroquímica catódica en medio acuoso. Junto con la exfoliación propiamente dicha, se consigue un control sobre la morfología del material resultante (nanolámina, nanorollo) en base a la elección del disolvente en que se dispersa dicho material.

Como material de partida, se usó NbSe₂ *bulk* en polvo, que fue prensado sobre un soporte de grafito flexible para obtener una pastilla compacta usada como cátodo en una celda electrolítica de dos electrodos. Como electrolito, se usó una disolución acuosa de KNO₃. Tras aplicar una diferencia de potencial de 10 V entre los electrodos de la celda, en pocos segundos se observa el desprendimiento de material de color marrón rojizo del cátodo, que permanece en dispersión, junto con material de color negro, que precipita al fondo de la celda. Tras su secado, el sólido suspendido era dispersable tanto en agua como en isopropanol, y estaba formado por objetos nanoestructurados cuya morfología dominante dependía del disolvente empleado, tal y como se pudo observar por microscopía electrónica: nanorrollos para la dispersión en agua y nanoláminas para la dispersión en isopropanol. Estos resultados fueron corroborados por microscopía de fuerza atómica.

Los materiales se caracterizaron por difracción de rayos X (XRD, espectroscopía fotoelectrónica de rayos X (XPS) y espectroscopía Raman. Al tratarse de técnicas que sondean los materiales hasta profundidades muy diferentes, los resultados que se obtienen proporcionan información sobre la totalidad de los nano-objetos (XRD y espectroscopía Raman) o sobre sus capas más superficiales (XPS). Los resultados obtenidos mediante XRD mostraron la presencia de selenio elemental y NbSe₂ tanto en el material de partida como en los productos exfoliados. Por espectroscopía Raman se observaron las bandas atribuibles a NbSe₂ en el material exfoliado, aunque con una variación en la relación de intensidades entre ellas respecto al material *bulk* de partida. Dicho resultado se atribuyó a la presencia de selenio elemental, más presente en el producto exfoliado debido a procesos

superficiales de oxidación durante la exfoliación. De hecho, el espectro de Nb 3d obtenido por XPS apenas mostraba señal correspondiente a Nb(IV), es decir, a NbSe₂, sino que estaba completamente dominado por componentes asociadas a Nb(V) que indicaban la presencia de óxidos de niobio en la superficie de los nano-objetos. Estos resultados, junto con el grosor de las nanoláminas obtenidas (4-12 nm) y la constatación en base a datos de la literatura de que la oxidación de una monocapa de NbSe₂ aumenta su grosor en aproximadamente un factor de 3, permitieron concluir que el material exfoliado contiene un filme superficial originado a partir de una o dos monoláminas de NbSe₂ transformadas en óxido de niobio, que a su vez encierran un núcleo de varias monoláminas de NbSe₂ inalteradas.

Asimismo, se observó que la exfoliación del material ocurría de forma muy rápida y daba lugar directamente a material completamente exfoliado, cuando habitualmente los tratamientos de exfoliación electroquímica de materiales laminares dan lugar a una expansión del material, cuya exfoliación se completa normalmente con un tratamiento adicional por ultrasonidos. Esta rápida exfoliación, junto con el hecho de que no se generaban partículas expandidas durante el proceso electrolítico, indicó que la exfoliación electroquímica no tenía lugar a través del proceso habitual de expansión simultánea de partículas por intercalación, sino más bien mediante la separación de nano-objetos de las partículas uno a uno. En base a experimentos de control, se concluyó que la exfoliación del NbSe₂ tenía lugar mediante la generación de especies moleculares oxidadas (polioxoniobatos) inducida por el medio localmente básico creado bajo las condiciones de tratamiento catódico. Estas especies moleculares, fuertemente cargadas, se adsorben sobre la superficie y en los intersticios entre láminas, favoreciendo su rápida exfoliación por repulsión electrostática. Este tipo singular de exfoliación electroquímica se demostró también con otros dicalcogenuros de carácter metálico, como NbS₂ y VSe₂.

Resumen Artículo III

El comportamiento de los nanorrollos y nanoláminas de NbSe₂ generados catódicamente como materiales para almacenamiento de litio se evaluó en una configuración de semicelda. Los voltamperogramas cíclicos iniciales para ambos materiales presentaron características cualitativamente similares, consistentes con una combinación de procesos de intercalación y conversión. No obstante, la intensidad de los correspondientes picos disminuyó tras el primer ciclo, indicando una reversibilidad parcial de estos procesos. Cuantitativamente, los nanorrollos exhibieron corrientes más altas que las medidas con las nanoláminas, lo que sugería una mayor actividad electroquímica en los primeros. Ello se atribuyó a su morfología tubular, que debería facilitar el acceso del electrolito al material activo en comparación con el caso de las nanoláminas. En los ciclos de inserción-desinserción, los nanorrollos mostraron también un mejor rendimiento inicial, pero perdieron capacidad tras 900 ciclos, mientras que las nanoláminas mantuvieron valores razonables de capacidad hasta los 1600 ciclos. Esta diferencia se atribuyó igualmente a la mayor accesibilidad del electrolito a los nanorrollos, lo que se esperaría que también acelerase su deterioro. En cualquier caso, los nanorrollos alcanzaron capacidades máximas ($>700 \text{ mAh g}^{-1}$) superiores a las teóricamente esperadas en el NbSe₂ (427 mAh g^{-1}), lo que subraya su potencial para aplicaciones de almacenamiento de energía.

En resumen, se ha desarrollado un método sencillo y rápido para exfoliar NbSe₂ y otros dicalcogenuros de carácter metálico, con control sobre la nanomorfología de los productos obtenidos. Dicho control ha permitido propiedades electroquímicas mejoradas que son atractivas en almacenamiento de energía, como se ha demostrado en el caso del litio, y que presentan también un gran potencial en otros campos.

ARTÍCULO III

NbSe₂ nanosheets/nanorolls obtained via fast and direct aqueous electrochemical exfoliation for high capacity lithium storage

Daniel F. Carrasco^a, Sergio García-Dalí^{a,b}, Silvia Villar-Rodil^{a,*}, José M. Munuera^a,
Encarnación Raymundo-Piñero^b, Juan I. Paredes^{a,*}

^a*Instituto de Ciencia y Tecnología del Carbono, INCAR-CSIC,
Francisco Pintado Fe, 26, 33011 Oviedo, Spain*

^b*CNRS, CEMHTI UPR3079, Univ. Orléans, 1D avenue de la Recherche Scientifique,
45071, Orléans, France*

* Corresponding author: silvia@incar.csic.es (S. Villar-Rodil),

* Corresponding author: paredes@incar.csic.es (J. I. Paredes)

Abstract

Layered transition metal dichalcogenides (LTMDs) in two-dimensional (2D) form are attractive for electrochemical energy storage, but research efforts in this realm have so far largely focused on the best-known members of such a family of materials, mainly MoS₂, MoSe₂ and WS₂. To exploit the potential of further, currently less studied 2D LTMDs, targeted methods for their production, preferably by cost-effective and sustainable means, as well as control over their nanomorphology, are highly desirable. Here, we report a quick and straightforward route for the preparation of 2D NbSe₂ and other metallic 2D LTMDs that relies on delaminating its bulk parent solid under aqueous cathodic conditions. Unlike typical electrochemical exfoliation methods for 2D materials, which generally require an additional processing step (e.g., sonication) to complete delamination, the present electrolytic strategy yielded directly exfoliated nano-objects, in a very short time (1-2 min) and with significant yields (~16 wt%). Moreover, the dominant morphology of the exfoliated 2D NbSe₂ products could be tuned between rolled-up nanosheets (nanorolls) and unfolded nanosheets, depending on the solvent where the nano-objects were dispersed (water or isopropanol). This rather unusual delamination behavior of NbSe₂ was explored and concluded to occur via a redox mechanism that involves some degree of hydrolytic oxidation of the material triggered by the cathodic treatment. The delamination strategy could be extended to other metallic LTMDs, such as NbS₂ and VSe₂. When tested toward electrochemical lithium storage, electrodes based on the exfoliated NbSe₂ products delivered very high capacity values, up to 750-800 mAh g⁻¹ at 0.5 A g⁻¹, where the positive effect of the nanoroll morphology, associated to increased accessibility of the lithium storage sites, was made apparent. Overall, these results are expected to expand the availability of fit-for-purpose 2D LTMDs by resorting to simple and expeditious production strategies of low environmental impact.

Keywords: Layered transition metal dichalcogenides (LTMDs); NbSe₂; VSe₂, electrochemical exfoliation; nanorolls; energy storage

1. Introduction

The emergence of graphene in 2004 signaled the beginning of the now vast field of two-dimensional (2D) materials, the breadth of which pertains to the large number of different known 2D systems, their possible combinations (2D heterostructures) and the exotic physical phenomena they can give rise to, as well as to the variety of technological domains where they can be potentially applied [1,2]. One such relevant domain is that of electrochemical energy storage (EES), where many 2D materials (typically, those having sufficient electrical conductivity) can be used as efficient electrodes for various types of supercapacitors [2] and batteries [3], including metal-ion, metal-sulfur and metal-air batteries. In addition to the distinct advantages that a given 2D system might exhibit on account of its particular chemical composition and structural configuration, 2D materials possess some overarching features that make them especially attractive for EES applications, most notably, high specific surface areas and extremely thin (usually <10 nm) sheet-like morphologies [3]. Such features are expected to be conducive to promoting charge storage by facilitating extensive interactions with, e.g., ions and redox-active species, as well as by expediting mass transport through the electrode, particularly when the thin sheets are of limited lateral dimensions (e.g., below a few micrometers).

Over the last decade, intensive research efforts have been made to unlock the full potential and advance the implementation prospects of 2D materials in EES devices [2–4]. However, these efforts have preferentially, although not exclusively, focused on a small subset of 2D materials, which mainly includes graphene and its

Artículo III

derivatives [5], a few layered transition metal dichalcogenides (LTMDs), MXenes and Xenes (mostly MoS₂, Ti₃C₂T_x and phosphorene, respectively) [6–8], as well as some 2D metal oxides and hydroxides [9]. Not surprisingly, many of them are readily accessible materials, with techniques for their production and processing in significant amounts being already relatively mature. Thus, to uncover the possibilities and exploit the promise of other, currently less explored 2D materials for EES, suitable targeted preparation methods should be developed in parallel [4]. Another relevant issue in the use of 2D materials as electrodes for EES concerns their actual nanomorphology and aggregation state in the electrode. 2D materials are often obtained in the form of stand-alone, largely unfolded nanosheets, e.g., in colloidal dispersion, but their processing into electrodes can easily lead to widespread nanosheet re-stacking and, consequently, to a dramatic decrease in the available surface area and to a deterioration of the ion diffusion kinetics [10]. This issue can be alleviated by, among other strategies, assembling the nanosheets into suitable nanomorphologies, such as loose aggregates (e.g., nanoflowers), hollow/porous structures (nanorolls, nanospheres, porous gels, etc), or highly crumpled films [11]. Therefore, straightforward approaches that allow access to these types of nanomorphologies with 2D materials are also highly desirable.

As a member of the 2D LTMD family, NbSe₂ nanosheets are a very attractive material for EES applications. Different to the case of the most commonly studied LTMDs, such as MoS₂, WS₂ and MoSe₂, which are electrically semiconducting compounds in their thermodynamically stable phase (2H phase), NbSe₂ exhibits a metallic nature that should favor its use in such applications [12]. Indeed, although still rather limited in number, some reports have in recent years disclosed the potential of NbSe₂ nanosheets/nanostructures, either alone or in combination with other materials, as a suitable electrode for Li-ion [13–15], Na/K-ion [16–18] and multivalent-ion [13,19] storage in batteries, as well as for Li-S batteries [20] and supercapacitors [21,22]. However, also in contrast with the most

widespread LTMDs, the pool of available methods for producing NbSe₂ nanosheets in significant amounts has so far remained quite small, which in turn has limited the range of practically available 2D NbSe₂ materials. For example, top-down methods essentially boil down to the well-known, generic exfoliation of the bulk material in proper organic solvents driven by ultrasound [23], and to electrochemical exfoliation with electrolytes based on lithium or alkylammonium salts, also in organic solvents [24–26]. Likewise, control over the nanomorphology of 2D NbSe₂ has been mainly restricted to nanoflower-like structures obtained by solvothermal synthesis [14]. Hence, strategies that allow access to NbSe₂ nanosheets as well as some control of their nanomorphology without resorting to the use of organic media (e.g., more sustainable, water-based strategies) would be an important asset to further the prospects of this material in EES and other applications.

Here, we report a straightforward approach for the production of NbSe₂ nanosheets via an electrochemical delamination route carried out in an aqueous electrolyte. We also show that, depending on the specific solvent where the exfoliated product is dispersed (water or isopropanol), the obtained nanosheets can be preferentially rolled-up into 1D nano-objects (nanorolls) or kept in an unfolded state. A mechanism based on redox processes is proposed to account for the somewhat unusual, smooth electrolytic delamination of the starting bulk NbSe₂ material. Such mechanism applies to other metallic LTMDs, allowing their straightforward delamination, as shown here for NbS₂ and VSe₂. Likewise, the 2D NbSe₂ nanorolls and unfolded nanosheets are both investigated as an electrode material for Li-ion storage, thus affording a direct comparison of the effect of nanomorphology on the EES performance. In particular, the nanorolls are seen to reach quite high Li-ion storage capacity values, making them a competitive anode material for Li-ion batteries. Thus, by introducing a simple, water-based method for producing 2D NbSe₂ with controlled nanomorphology, the present results should expand the scope of less studied LTMDs in EES and beyond.

2. Results and discussion

2.1. General Aspects of the Cathodic Delamination of NbSe₂ in Aqueous Medium

An electrochemical delamination route was implemented for the preparation of NbSe₂ nanosheets from their corresponding bulk material in powder form [details of the procedure are given in the Experimental Section (see Supporting Information)]. In an optimized procedure, a certain amount of commercial NbSe₂ powder (Fig. 1a), made up of micrometer- and submicrometer-sized particles [see field emission scanning electron microscopy (FE-SEM) image in Figure 1b], was compacted onto a circular piece of graphite foil by means of a hydraulic press (Figure 1c). The graphite foil served as an electrically conductive supporting substrate for the LTMD and acted as the cathode in an electrolytic set-up that made use of platinum foil as the anode. Both electrodes were immersed in an aqueous 0.3 M KNO₃ solution in a parallel configuration and kept at a distance of ~2 cm from each other (Figure 1d). The side of the graphite foil coated with NbSe₂ was directly facing the platinum counter electrode. Upon application of a negative voltage (-10 V) to the NbSe₂-graphite foil electrode for a few minutes, lustrous gray particles were seen to detach from it and to quickly sediment at the bottom of the electrolytic cell. At the same time, a reddish-brown substance was also released from the cathode surface, but this remained suspended in the electrolyte instead (Figure 1e; see also Movie 1 in the Supporting Information). Such a substance, as well as the gray particles, necessarily originated from the NbSe₂ component of the cathode because they were not observed when the naked graphite foil was negatively biased. The latter only underwent a slight swelling and released just a few black particles that floated atop the electrolytic solution (see Movie S2 in the Supporting Information). Indeed, aqueous cathodic delamination of graphite in significant extent is known to require treatments on the scale of hours, rather than minutes, and the use of more complex, specific electrolytes [27]. Moreover, both the reddish-

brown substance and the gray particles were also generated when stand-alone, pressed NbSe₂ pellets were used as the cathode, i.e., in the absence of the graphite foil support (see Movie 3 in the Supporting Information). However, such stand-alone pellets were relatively brittle and thus more difficult to handle than their graphite foil-supported counterparts. After completion of the cathodic treatment in just a few minutes, the reddish-brown substance in the electrolyte was collected (the gray sediment discarded), washed with deionized water [three cycles of (i) sedimentation via centrifugation or overnight resting and (ii) resuspension in water], dried under a vacuum at room temperature, and then stored for further use. This product could be colloidally dispersed in isopropanol and water (Figure 1f) with the aid of a vortex mixer or a brief (1 or 2 min) sonication step, although its stability was generally rather limited, with most of the material sedimenting in several hours. Nonetheless, the sediment could be easily re-suspended for an indefinite number of times, indicating that an irreversible agglomeration of the colloidally dispersed product was not taking place.

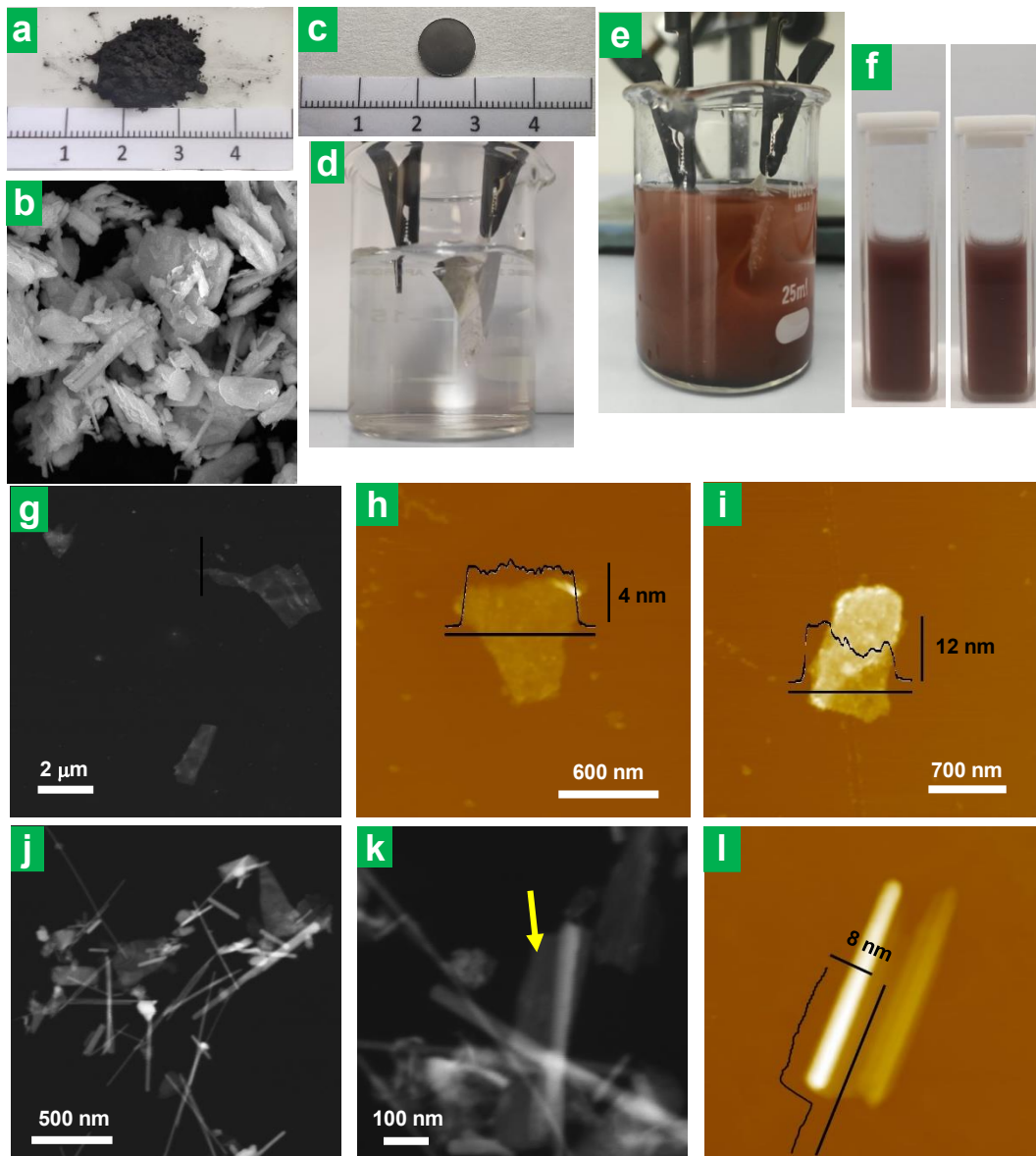


Figure 1. (a) Digital photograph and (b) FE-SEM micrograph of commercial NbSe₂ powder. Digital photographs of (c) the NbSe₂-graphite foil cathode and the experimental set-up for electrolytic exfoliation (d) before and (e) after application of a negative voltage (-10 V) to the NbSe₂-graphite foil cathode. (f) Digital photographs of the cathodic exfoliation product colloidally dispersed in isopropanol (left) and water (right). Typical STEM (g) and AFM images (h,i) and of the cathodically derived product deposited from its dispersion in isopropanol. (j,k) STEM images of the cathodic product deposited from its dispersion in water. The arrow in k points to a site where the sheet is incompletely rolled-up. (l) AFM image of a partially unfolded nanoroll.

Figure 1g shows a typical scanning transmission electron microscopy (STEM) image of the cathodically derived product from its dispersion in isopropanol, where it can be noticed that the material was made up of submicrometer-sized nanosheets of irregular polygonal profile, showing lengths mostly in the ~300–600 nm range. As determined by atomic force microscopy (AFM; Figure. 1h,i), the nanosheets were typically between 4 and 12 nm in thickness. Based on the above observations, it is reasonable to conclude that these 2D objects were obtained from the delamination of bulk NbSe₂ during the cathodic treatment. If we assume 0.628 nm to be the thickness of a NbSe₂ monolayer [28], then the present nanosheets would be nominally several (~6–19) monolayers thick, according to the above AFM results (Figs. 1h and 1i). Nonetheless, this result will need to be refined in the light of further data, as discussed below. However, the actual morphology of the delaminated nano-objects could also be modulated by a proper selection of the dispersing solvent. Figure 1j presents a STEM image of the cathodic product deposited from its dispersion in water, instead of isopropanol. In this case, while nanosheets were still spotted in significant numbers, the sample was largely dominated by 1D entities that were about 500–700 nm long and ~20 nm wide. Closer inspection of the 1D objects (Figure 1k) revealed them to possess a tubular morphology and suggested that they were formed by the rolling-up of nanosheets to give nanorolls (note the incompletely rolled-up sheet at the site marked by an arrow in Figure 1k). Further evidence of this point is given in the AFM image of Figure 1l, where a partially unrolled nanoroll can be noticed. The two ends of the corresponding nanosheet appeared to be rolled up, with only its middle section unrolled. From the unrolled section, the thickness of the nanosheet was estimated to be ~7–8 nm. It is worth noting that this nanosheet was initially fully rolled up (a single 1D object was seen during the first AFM scan, image not shown), but a partial unrolling apparently took place at some point of the

measurement, likely as a result of perturbations induced by interaction with the AFM tip.

The transformation between unfolded nanosheet and nanoroll morphology of the present cathodically delaminated materials appeared to be reversible through solvent exchange. For example, the as-obtained, dried cathodic product first dispersed in isopropanol yielded unfolded nanosheets, but if isopropanol was exchanged by water (via several cycles of sedimentation by centrifugation and re-suspension in water), nanorolls became the dominant nanomorphology, and vice versa (see Figure S1 in the Supporting Information). Not surprisingly, nanorolls were prevalent in the as-obtained, dried cathodic product that was not subsequently dispersed in any solvent (Figure S2), given that this product was originally processed in water. It is also worth noting that such a solvent-driven control of the nanomorphology was not exclusive of the cathodically derived material. Indeed, direct sonication of bulk NbSe₂ powder in isopropanol and water also afforded suspensions made up of unfolded nanosheets and rolled-up nanotubes, respectively (Fig. S3). However, the cathodic delamination strategy turned out to be a much more efficient process than direct sonication. For instance, a delamination yield of ~16 wt% could be obtained with the cathodic process in just a few minutes (at the expense of just ~0.7 A h /g), whereas direct sonication only gave a yield of ~6 wt% after 6 hours. Generally speaking, it is not possible to establish a comparison in terms of delamination yield with previous examples of NbSe₂ electrochemical exfoliation in the literature, as this data is not usually reported [24,26]. In some instances, the efficiency of the exfoliation is discussed in terms of exfoliation degree, i. e., the percentage of monolayers obtained over the whole exfoliated material [26] but, of course, this does not allow to know which wt% of the starting material has been exfoliated. We note that the delamination yield of ~16 wt% found here could be further increased if, instead of discarding the gray sediment from the electrolytic exfoliation of NbSe₂ (which is none other but non-exfoliated NbSe₂), it

was recovered and pressed again onto a graphite foil disc to be reused as an anode in successive exfoliation cycles.

The effect of different electrolytic parameters on the amount of delaminated product was also investigated. Taking the 0.3 M KNO₃ electrolyte and bias voltage of -10 V as the benchmark treatment conditions, we observed that both lower (e.g., 0.1 M) and higher (e.g., 1 M) electrolyte concentrations clearly led to smaller amounts of delaminated products. In the former case, delamination was relatively slow and generated little reddish-brown substance in the aqueous solution. In the latter, a much more vigorous process was noticed, but this only resulted in a very quick detachment of gray particles that sedimented at the bottom of the solution, with no or very little reddish-brown substance being released. Under such conditions, the detaching particles probably loose their electrical contact to the cathode so quickly that there is virtually no time for them to delaminate to any significant extent. The magnitude of the bias voltage had a similar effect, so that both smaller (e.g., -5 V) and larger (e.g., -20 V) voltages gave rise to lower delamination efficiencies. The amount of delaminated product also decreased when changing the cation in the electrolyte from K⁺ to Na⁺ or Li⁺, which was ascribed to the reduced ability of the latter ions in hydrated form to reach and intercalate the LTMD due to their lower ionic conductivity and larger size [27]. Changing the electrolyte anion to, e.g., Cl⁻ had no apparent effect on the delamination efficiency. However, the use of anions that are highly oxidizing or can readily generate highly oxidizing species in the electrolyte should be avoided, as these could then attack the oxidation-prone NbSe₂ (see below). In this regard, the Cl⁻ anion can be expected to anodically oxidize during the electrolytic treatment, to give Cl₂ and then hypochlorous acid (HOCl) upon reaction with water, which is a rather oxidizing species. By contrast, the reduction potential of the NO₃⁻ anion is lower than that of HOCl (0.96 vs. 1.48 V, relative to the standard hydrogen electrode) [29], making it

a weaker oxidizing species and thus a better choice as the electrolyte anion for NbSe₂ exfoliation.

2.2. Physicochemical characterization of cathodically delaminated NbSe₂

The identity of the delaminated products was assessed by X-ray diffraction (XRD), Raman spectroscopy and X-ray photoelectron spectroscopy (XPS). Possessing different probing depths, each of these characterization techniques gathers partial information on the material, which must be combined to generate a global picture (see Figure S4). The XRD pattern of the starting bulk NbSe₂ powder (Figure 2a, black trace) exhibited an array of well-defined, sharp diffraction peaks that was consistent with the material being 2H-phase NbSe₂ (hexagonal crystal structure with space group *P63/mmc*) [30]. A couple of additional peaks, marked with an asterisk in the diffractogram, indicated the presence of elemental selenium of trigonal phase (t-Se) as an impurity in the material [31,32]. For NbSe₂, the strong (002) reflection located at ~14.10° (2θ) indicated the interlayer distance in the LTMD to be of 0.628 nm. Most, if not all, of the diffraction peaks characteristic of 2H-phase NbSe₂ were also present in the cathodically delaminated product, whether the latter was predominantly in the form of nanorolls (i.e., processed in water only; Figure 2a, orange trace) or of unfolded nanosheets (upon processing in isopropanol; Figure 2a, red trace). Some t-Se was also noticed in the XRD patterns of some of the delaminated products. As will be explained below, although elemental Se is indeed present in the exfoliated products, it is not necessarily in crystalline t-Se form. It can be in amorphous, S8 form, which is not detectable by XRD. Although the intensity of the (002) peak could be maybe expected to decrease relative to that of the other peaks upon exfoliation [30] (and finally disappear in the complete exfoliation, down to monolayer), the simultaneous decrease in the lateral size of the NbSe₂ entities will also diminish the intensity of the XRD peaks corresponding to

other spatial directions, and thus the final effect in the relative intensities is uncertain.

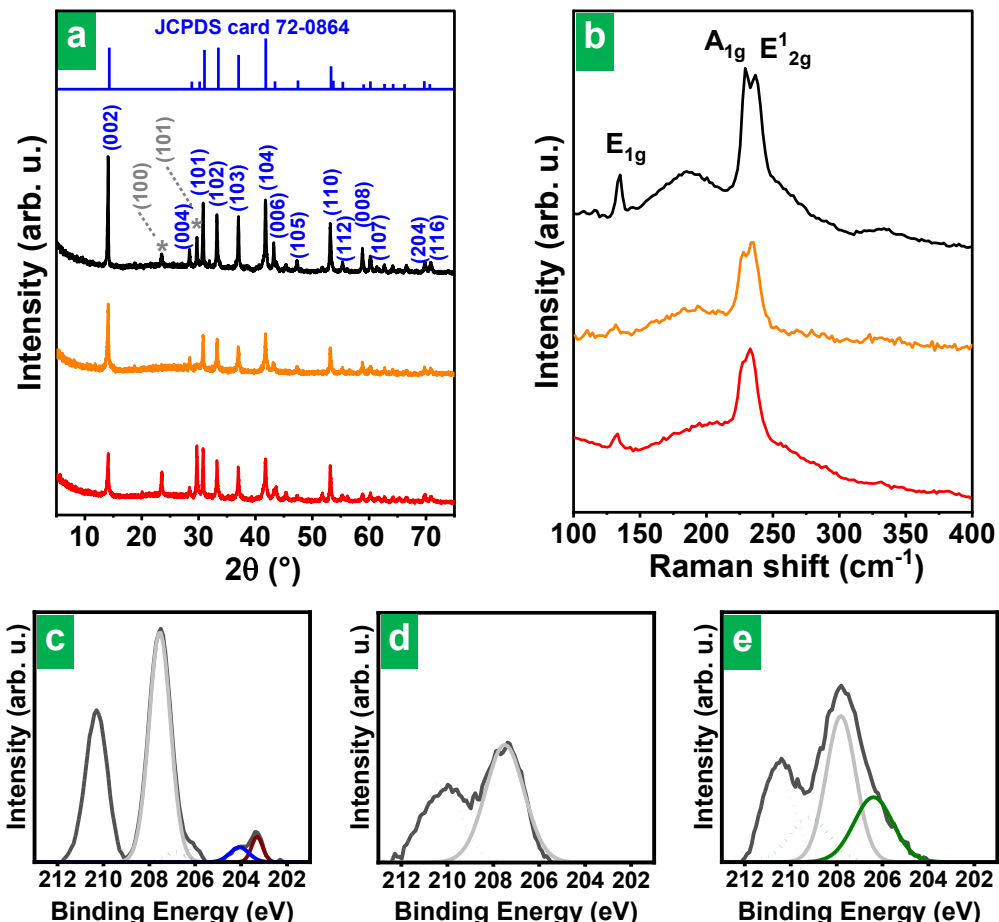


Figure 2. XRD pattern (a) and Raman spectrum (b) of the starting bulk NbSe₂ powder (black trace) and the cathodically delaminated product processed in water only (orange trace) and in isopropanol (red trace). 2H-NbSe₂ XRD peaks have been labelled according to JCPDS card 72-0864 (blue trace and labels) while the peaks labeled in gray and marked with an asterisk correspond to crystalline selenium in trigonal phase, namely, to 2θ values of 23.5° and 29.7° corresponding to the crystal planes (100) and (101), respectively. Background-subtracted high-resolution Nb 3d XPS spectrum of (c) the starting bulk NbSe₂ powder and the cathodically delaminated product processed in (d) water only and (e) in isopropanol. Niobium appears in different oxidation states and/or chemical environments: Nb(V) from orthoniobates or polyoxoniobates (gray trace); Nb(IV) from NbSe₂ (wine trace) and in NbO₂ (green trace); Nb(II) in NbO (blue trace). The Nb 3d_{3/2} and Nb 3d_{5/2} components are graphed with solid and dotted lines, respectively.

Figure 2b (black trace) shows a typical Raman spectrum of bulk NbSe₂ powder in the 100-400 cm⁻¹ wavenumber range, where the characteristic bands (signature peaks) for the 2H phase of this LTMD are known to be located [33,34]. These include the intense and sharp A1g (~230 cm⁻¹) and E12g (~240 cm⁻¹) peaks, which correspond, respectively, to an out-of-plane phonon of the chalcogen atoms and an in-plane phonon of both the metal and chalcogen atoms. The weaker E1g peak (~135 cm⁻¹) is an in-plane vibrational mode of the chalcogen atoms that is thought to be activated only at edge planes. In addition, a broad band that could be assigned to the so-called soft mode was noticed at about 180 cm⁻¹. The latter is a second-order feature involving two-phonon scattering processes, and its relatively high intensity is connected to the fact that NbSe₂ exhibits charge density wave states at low temperatures [35,36]. These Raman bands have been shown to be also present, with very minor variations (e.g., a shift in peak positions of just a few inverse centimeters, if any), in atomically thin NbSe₂ [37,38]. In fact, such bands were clearly noticed in the cathodically delaminated product obtained here, whether it was processed in water only or transferred to isopropanol (Figure 2b, orange and red traces, respectively). Nonetheless, the Raman features of this product were largely but not totally coincident with those expected for (bulk or atomically thin) NbSe₂. Specifically, in the delaminated material, the peak at ~240 cm⁻¹ (i.e., the E12g band frequency of 2H-NbSe₂) was somewhat more intense than its 230 cm⁻¹ counterpart (A1g band frequency of 2H-NbSe₂), whereas this is not usually the case with the E12g and A1g bands for pure NbSe₂ (e.g., see the spectrum of bulk NbSe₂ in Figure 2b) [33,35,37,38]. We interpret such distinct Raman feature of cathodically delaminated NbSe₂, relative to those expected for the pure LTMD, to arise from a partial oxidation of the obtained nanosheets/nanorolls. The surface of bulk NbSe₂ is known to slowly oxidize under ambient conditions, giving Nb(V) species, which are mainly thought to be amorphous Nb₂O₅, and elemental Se [39,40]. This reaction can be accelerated with external stimuli, such as heat or light

[41,42]. Surface oxidation readily develops on 2D NbSe₂ nanosheets as well [22,43]. Moreover, as will be shown below, the present cathodic treatment of NbSe₂ leads to the surface oxidation of the delaminated objects. However, the unusual Raman features of the delaminated products cannot be ascribed to the presence of Nb₂O₅, either in crystalline or in amorphous form (see Figure S5). In fact, Nb₂O₅ exhibits other intense features outside the 100–400 cm⁻¹ range, particularly strong bands at around 600–700 cm⁻¹ [44], which we detected in commercial samples of both crystalline and amorphous Nb₂O₅, but totally absent in the cathodically delaminated NbSe₂ material (see Fig. S5). Instead, the unusual Raman features of the delaminated products most likely arise from the presence of elemental Se species as the other product of NbSe₂ oxidation. In fact, the Raman spectrum of t-Se, which was detected here by XRD (Figure 2a), is known to be dominated by a band at 235–240 cm⁻¹ (A1 phonon), whereas Se₈ rings in amorphous Se (a-Se) give rise to a peak at around 260 cm⁻¹ (intra-ring stretching vibrations) [45,46]. Elemental Se, both in crystalline and amorphous form, was therefore very likely responsible for the slightly altered Raman features of cathodically delaminated NbSe₂ (a Raman spectrum of elemental selenium will be shown below regarding the discussion of the exfoliation mechanism).

Some (native) surface oxidation was also expected on the starting bulk NbSe₂ particles, but the thickness of the corresponding layer of oxidation products was probably small compared to the probing depth of the Raman technique (a few tens of nanometers for NbSe₂ [33]). For this reason, the intensity of the Raman features resulting from such products (i.e., those of elemental Se) in bulk NbSe₂ was negligible relative to those coming from the LTMD proper (Figure 2b, black trace). In the delaminated materials, the amount of surface oxidation products probed relative to that of (non-oxidized) NbSe₂ should be considerably larger due to the nanometric thickness of the nanosheets/nanorolls. Hence, their Raman bands should be easier to detect (Figure 2b, orange and red plots). In agreement with previous

work [47], further oxidation of the delaminated nanosheets/nanorolls could be triggered by repeatedly measuring a given area with the Raman laser beam. This effect was clearly noticed from the progressive rise of the 240 and 260 cm⁻¹ peaks when spectra were consecutively recorded on the same spot (not shown). In consequence, to avoid altering the exfoliated samples throughout the measurements, the spectra were obtained with low laser powers (below 0.5 mW) and short measurement times (a few tens of seconds).

The presence of a surface layer of oxidation products both on the starting bulk NbSe₂ powder and on its cathodically delaminated counterpart was disclosed by a much more surface-sensitive technique (smaller probing depth), namely, XPS (see Figure S4). The high-resolution core-level Nb 3d spectra of the bulk powder as well as of the exfoliated nanorolls and nanosheets are presented in Figure 2c-e, respectively. In all cases, the spectral envelopes were dominated by components located at ~207.5 and ~210.2 eV (gray traces in Figure 2c–e), which can be assigned to the 3d5/2 and 3d3/2 levels of Nb(V), respectively, and were thus indicative of Nb oxide species on the surface of the samples [19]. Much weaker features consistent with 2H-phase NbSe₂, i.e., the components located at about 203.2 [Nb(IV) 3d5/2] and 206.0 [Nb(IV) 3d3/2] eV [19], were observed in the spectrum of the bulk powder (wine traces in Figure 2c). Niobium oxides with oxidation states lower than V were also detected (blue and green traces in Figure 2c and e, respectively). This result agrees with previous reports in the literature on XPS characterization of NbSe₂ nanosheets where Nb(V) is either the only [14] or the majoritarian component detected [24] in the Nb 3d spectrum. The core-level O 1s spectra of these materials were consistent with most of the surface Nb being in the form of oxide, e.g., orthoniobates, polyoxoniobates, or Nb₂O₅ (Figure S6). In agreement with the detection of elemental Se by XRD and Raman spectroscopy (Figure 2a,b), XPS also revealed the presence of this species in the bulk and delaminated materials (see Se 2p core-level spectra in Figure S7).

In the case of the delaminated nanosheets/nanorolls, we assume that the surface layer of oxidation products mostly formed during their preparation by the cathodic treatment (see below). Moreover, it can be inferred that just one or two of the outermost monolayers in the NbSe₂ nanosheets (as well as their rolled-up counterparts) eventually got oxidized to give Nb oxide and elemental Se species on the surface. These oxidized layers would sandwich an inner section containing a few or several non-oxidized NbSe₂ monolayers. Such a conclusion was mainly supported by two facts. First, the thickness of the delaminated nanosheets was in the 4–12 nm range. Second, upon oxidation, the thickness of NbSe₂ slabs/nanosheets has been shown to increase substantially, up to a factor of ~3 [41,47]. Hence, considering that a pristine NbSe₂ monolayer is ~0.6 nm thick [28], the layer of oxidation products in the delaminated nanosheets should not have originated from, e.g., the three outermost NbSe₂ monolayers, as these would have led to nanosheets considerably thicker than those actually measured here. Rather, the nanosheet thickness would be consistent with such an oxidation layer coming from one or two NbSe₂ monolayers. Moreover, the thickness of this oxidation layer (i.e., a few nanometers) would be similar to values given in the literature for the native oxide in 2D NbSe₂ and NbS₂ nanostructures [48,49], as well as to the typical probing depth of the XPS technique [50], implying that most, if not all, of the XPS signal should originate from the oxidation layer (see Figure S4), as demonstrated in Figure 2c–e and reported in previous works on NbSe₂ nanosheets [14,24]. However, as explained above, the deeper probe depth of a few tens of nanometers of Raman spectroscopy will allow detecting both the oxide layer and the 2H-NbSe₂ core of a number of thin nanosheets (4–12 nm thick, see Figure 1h,i) constituting the probed films (see Figure S4), while less proportion of the oxide layer (presumably only one oxidized surface) will contribute to the Raman signal for thicker, unexfoliated starting NbSe₂ powder (Figure 2b). The larger probe depth of XRD will allow detecting the surface oxide layer and the unmodified 2H-NbSe₂ core for both the

exfoliated objects and the starting powders (Fig. 2a and S4). We note that the appearance of an oxidation layer is not avoided by using lower voltages for the electrochemical delamination as the layer is present even in the case of the starting, non-electrochemically treated material. In fact, in previous reports in the literature for the case of electrochemical exfoliation of NbSe₂ in organic media, even when the electrochemical parameters were adjusted to minimize structure degradation, the main Nb species detected by XPS was still Nb (V) [24].

2.3. Rationalizing the aqueous cathodic delamination of NbSe₂ and the morphology of the delaminated products

The above results demonstrate that bulk NbSe₂ can be readily exfoliated by electrochemical means based on a simple and expeditious aqueous process to give nanometer-thick sheets that can be switched between unfolded and rolled-up morphologies. We note that, while the protocols reported in the literature for the preparation of nanostructured NbSe₂ take hours [13,14,16–19] or even days [15], the duration of the present methodology is in the order of minutes (see Table S1 in the Supporting Information). Indeed, after just 2 min of cathodic treatment, bulk NbSe₂ is transformed into well-exfoliated 2D NbSe₂ nano-objects (Figure 1) with high structural quality (Figure 2). Furthermore, unlike other methodologies, the present protocol is performed at room temperature and under ambient conditions, not involving high temperatures [14,16–19], inert atmosphere [14,16,17,19] or complex or scarce reagents or solvents [18] (see Table S1 in the Supporting Information). Significantly, the final individual exfoliated nano-objects could be directly obtained from the electrochemical treatment without the need of any further substantial energy input (e.g., sonication). Such an outcome was quite different to that found for typical electrochemical exfoliation methods of most layered

materials, such as graphite, black phosphorus, and LTMDs, including NbSe₂ itself. In those cases, the electrolytic treatment usually affords just a bulk expanded material (e.g., worm-like expanded particles or accordion-like expanded crystals), from which individual nanosheets need to be subsequently extracted in the liquid phase via, e.g., sonication or shear forces [51,52]. In contrast, no expanded particles were generated by the present electrochemical treatment of the bulk NbSe₂ powder. Indeed, FE-SEM imaging of the gray particles that sedimented at the bottom of the electrolytic cell during the treatment (not shown) showed them to be as compact as those of the starting material (Figure 1b). This suggested that delamination in the present case did not proceed through simultaneous intercalation/expansion of many interlayer galleries in the NbSe₂ particles, which is the expected exfoliation pattern for common electrochemical methods, but rather via a sequential, layer-by-layer peeling process. The latter would be more similar, although probably not identical, to the exfoliation behavior brought about by direct sonication of the bulk material. However, as noted above, the electrolytic exfoliation rate of NbSe₂ was much faster than that afforded by direct sonication. These observations pointed to an unusual exfoliation mechanism taking place here, which was thus worth examining.

We hypothesize that the present electrolytic exfoliation of NbSe₂ proceeded via a singular path akin to the redox mechanism of LTMD exfoliation proposed in recent years [53,54]. Such a redox exfoliation has been shown to rely on the generation of soluble molecular metal oxide precursors (e.g., orthometalates) on the surface of the LTMD particles, including NbSe₂, either via naturally occurring oxidation processes under ambient air or by purposeful oxidation with a chemical oxidant. Subsequent reduction of these soluble orthometalates yields the corresponding polyoxometalates. The latter are highly charged polyatomic anions that adsorb on the surface and at the interlayer gaps of the LTMD, triggering its sequential delamination through Coulombic repulsions with just a very small energy input (e.g., stirring) being required. This mechanism provides a priori a

consistent conceptual framework to understand the aqueous electrolytic exfoliation of NbSe₂. Specifically, oxidation-prone NbSe₂ could certainly provide an abundant source of naturally occurring orthoniobate anions when the starting bulk material has been stored in ambient air, as it was the case here. Indeed, the XPS results shown in Figure 2c provided evidence of the presence of oxidized Nb species in the starting NbSe₂ powder. It could be argued that, under the intrinsically reductive conditions of the present cathodic treatment, the orthoniobate anions would assemble into polyoxoniobates, and then the latter would drive the sequential exfoliation of the NbSe₂ particles as discussed above. This delamination process would be assisted by the intercalation of K⁺ ions at NbSe₂ edges [27], affording a wedge effect that would facilitate the adsorption of orthoniobates and polyoxoniobates at interlayer gaps.

It should be noted, however, that the redox mechanism of LTMD exfoliation was not originally proposed in the context of either electrolytic or aqueous systems [53,54]. Consequently, different aqueous electrochemical processes that were previously not contemplated may have contributed to the currently observed outcome. In fact, we believe that during the aqueous cathodic treatment of NbSe₂, new oxidized Nb species are continuously generated *in situ*, facilitating the sequential delamination of the material. In such a scenario, the native Nb oxides already present in the starting bulk powder would not be strictly necessary to make exfoliation possible. To show evidence of this point, the starting NbSe₂ powder was subjected to reflux in acetonitrile with the aim of removing its native molecular Nb oxide species (this solvent is known to solubilize molecular metal oxide precursors present in LTMDs, including NbSe₂ [53,54]). Then, the refluxed NbSe₂ material was tested in an aqueous cathodic delamination experiment. If the native molecular Nb oxide species were strictly required for delamination to occur, the yield of exfoliated products obtained with the acetonitrile-treated NbSe₂ powder should be substantially lower, if not negligible, relative to that attained with its non-treated

counterpart. Nonetheless, essentially the same yield was obtained in both cases (i.e., ~16 wt%), suggesting that *in situ* generated Nb oxide species are indeed central to the exfoliation process.

The generation of Nb oxide species during cathodic delamination most likely resulted from the pH-dependent hydrolytic oxidation of NbSe₂, and more specifically hydrolysis under basic conditions. We note that due to the high bias voltage applied to the electrolytic cell, water molecules are expected to be reduced at the cathode side, yielding hydrogen molecules and hydroxide anions that raise the local pH of the aqueous electrolyte around the cathode. To demonstrate that a basic medium triggers the hydrolytic oxidation of NbSe₂, a control experiment was carried out whereby bulk NbSe₂ powder was stirred in a 3 M KOH solution (pH ~14) at 90 °C for 30 min. Upon completion of the treatment, a very small amount of gray particles were seen to sediment at the bottom of the beaker and the supernatant solution developed a transparent dark red tone. The material in the supernatant was recovered by flocculation induced by the addition of HCl, washed through several cycles of centrifugation and re-suspension in water, and finally dried under vacuum. The resulting material was a dark red powder with a small amount of brilliant gray particles (see the digital photograph in the inset to Figure 3a and FE-SEM image in the same figure) with a weight that amounted to ~92–94 % of that of the starting bulk NbSe₂ powder. The gray particles that made up the sediment were also collected and washed, but their weight was just a few percent of the initial mass of NbSe₂ used for the treatment with alkali. XRD confirmed the presence of NbSe₂ in the gray particles (pattern not shown). In contrast, no sign of the LTMD was noticed in the XRD pattern of the powder coming from the supernatant, where just elemental Se could be detected (Figure 3b). We note that the XRD pattern should come from the gray, crystalline Se allotrope as the red allotrope is amorphous and is thus not detected by XRD. The latter result was supported by Raman spectroscopy (Figure 3c), as only the characteristic peaks of

(crystalline gray and amorphous red) elemental Se were seen in this material but not those typical of NbSe_2 . Still, Se was not the sole element present in the dark red powder: energy-dispersive X-ray (EDX) spectroscopy (Figure 3d) revealed that it also contained substantial amounts of Nb (9–24 at%) and O (19–40 at%), together with some residual K and Cl (~1–2 at%) from the KOH and HCl solutions. Because Se was only found in its elemental form, we infer that O must be combined with Nb, thus forming Nb oxide species.

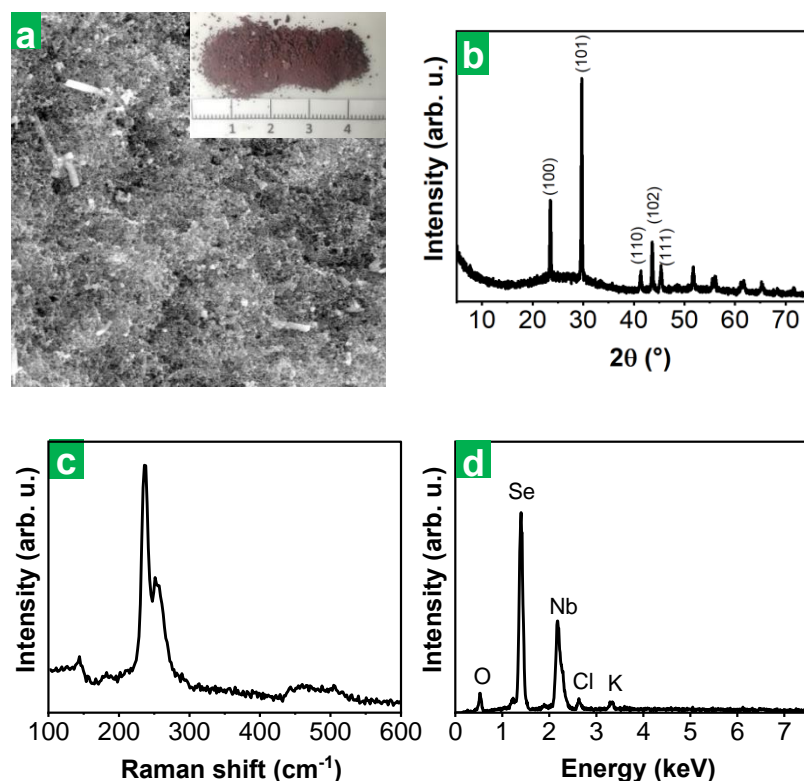


Figure 3. Characterization of the product of the treatment of bulk NbSe_2 powder with 3 M KOH solution ($\text{pH} \sim 14$) at 90°C for 30 min: (a) FE-SEM image with digital photograph in the inset, (b) XRD, (c) Raman, and (d) EDX. The XRD patterns obtained show the main peaks characteristic of crystalline t-Se at 2θ values of 23.5° , 29.7° , 41.4° , 43.7° and 45.4° corresponding to the crystal planes (100), (101), (110), (102) and (111), respectively, which have been labelled for clarity.

The above results demonstrate that, under basic conditions, NbSe₂ undergoes hydrolytic oxidation to give elemental Se and Nb oxide species. Moreover, the alkaline treatment can be made harsh enough to induce an almost complete decomposition of the material. Further hydrolysis experiments carried out at lower KOH concentrations indicated that substantial decomposition of NbSe₂ only occurred above a threshold pH value of about 10.5. Based on this new understanding and the general mechanism of redox exfoliation of LTMDs, the following course of events can be proposed for the aqueous cathodic delamination of NbSe₂: (1) under the applied cathodic potential (-10 V), water molecules are reduced at the NbSe₂ electrode, thus raising the local pH of the electrolyte in a region close to the electrode surface, from an initial value of ~6 (pH of 0.3 M KNO₃ solution). (2) The local basic medium induces some degree of hydrolytic oxidation of the NbSe₂ surfaces that are in contact with the electrolyte, if they were not previously oxidized. Such an oxidation generates molecular Nb oxide species, most likely in the form of polyoxoniobates [e.g., the hexaniobate anion (Nb₆O₁₉)⁸⁻ referred to as the Lindqvist ion], rather than the monomeric orthoniobate anion, NbO₄³⁻. This is because the latter is not stable in aqueous medium, whereas polyoxoniobates like the Lindqvist ion are known to readily form under alkaline conditions (pH > 10.5) [55]. (3) An initial cathodic intercalation of K⁺ ions, probably as hydrated entities ([K(H₂O)_n]⁺ [27]), takes place at layer edges of the NbSe₂ particles, making the interlayer space at such edges to become exposed to the aqueous electrolyte, which triggers its oxidation. The resulting highly charged polyoxoniobates adsorb on the two opposite surfaces of the interlayer space, generating a strong electrostatic repulsion between them that causes their separation [53,54]. This event initiates delamination proper of a sheet at its edges. The assisting role of K⁺ ions in the process explains the previously reported influence of KNO₃ concentration in the delamination yield (Section 2.1). (4) The incipient delamination of the sheet favors the ensuing intercalation of K⁺ ions and the

Artículo III

oxidation of the interlayer space at locations increasingly farther away from the edges. As a result, the sheet is progressively delaminated. (5) When delamination is completed, the sheet is released into the aqueous medium and a freshly exposed surface is ready for new exfoliation events. The very nature of the process entails the oxidation of both surfaces of the exfoliated sheets.

The delamination mechanism proposed here implies that the yield of exfoliation should be dependent, in a non-monotonous way, on the local pH of the electrolyte in the region close to the NbSe₂ cathode. Although this local pH could not be measured, its actual value during the cathodic treatment was probably not very far from the threshold of 10.5 that was shown above to trigger the hydrolytic oxidation of NbSe₂ and is also known to allow the solubilization of polyoxoniobates [55]. If it had been much lower than 10.5, no or little hydrolytic oxidation of NbSe₂ would have occurred, and so not many polyoxoniobates would have formed to support sheet delamination. As a result, a low exfoliation yield would have been expected. On the other hand, an exceedingly basic local pH would have likely driven a much too aggressive oxidation of the exposed NbSe₂ sheets, which would have extensively decomposed into elemental Se and Nb oxide species. Consequently, smaller amounts of NbSe₂ would have been available for delamination, thus leading to lower exfoliation yields. To test this prediction, the local pH around the NbSe₂ cathode should be controlled. While this is not possible by direct means, some indirect control should be feasible by tuning the pH of the starting electrolyte. To that effect, we conducted additional cathodic delamination experiments using purposefully acidified and basified electrolytes. More specifically, we prepared an acidic (pH ~1) and a basic (pH ~11) electrolyte by adding a proper amount of HNO₃ and KOH, respectively, to the standard 0.3 M KNO₃ neutral electrolyte, which gave exfoliation yields of ~6 wt% (acidic) and ~11 wt% (basic). This result is to be compared with the yield of ~16 wt% obtained with

the standard KNO_3 electrolyte ($\text{pH} \sim 6$) and is therefore consistent with the predictions derived from the proposed delamination mechanism.

The second relevant feature of the exfoliated NbSe_2 material was the fact that it could be obtained in the form of rolled-up nanosheets (nanorolls). This feature was not exclusive of the present electrolytic delamination process: as noted above, nanorolls could be generated as well just by sonicating the starting NbSe_2 powder in water, albeit at much lower yields. Moreover, different 1D NbSe_2 nanostructures, such as nanorods and nanowhiskers, have been previously generated by the processing of bulk NbSe_2 via, e.g., sonication or ball milling [56,57]. However, the origin of such a behavior is not clear. Nanoscrolls of several other LTMDs (MoS_2 , MoSe_2 , WS_2 , etc) have been reported in recent years [58–61], but their preparation typically relies on the post-processing of the LTMD already in 2D form, not in bulk form. Indeed, the attainment of 1D nano-objects directly from the exfoliation of the bulk material has been rarely documented for LTMDs other than NbSe_2 [62,63]. It is thus reasonable to conclude that the ability of bulk NbSe_2 to yield 1D nano-objects directly upon exfoliation should be connected to some particular traits of this LTMD. We believe that the relatively strong tendency of NbSe_2 to oxidize (stronger than that of many other LTMDs) plays a central role. Specifically, the surface oxidation of the exfoliated NbSe_2 nanosheets is thought to generate stress in their structure in a way similar to the surface stress brought about by the adsorption of organic molecules (ligands) onto colloidal nanoplatelets, including LTMD nanosheets, which drives their folding into curved morphologies [61,64]. In this scenario, it is reasonable to assume that such a surface stress may be affected by the interaction of the oxide layer with its surrounding medium, and so that the induction of curvature in the nanosheets depends on the solvent where they are dispersed. For the cathodically delaminated material, the required surface oxide species would be generated *in situ*, as discussed above. On the other hand, for the material obtained by direct sonication, only the native surface oxides would

be in principle available to support exfoliation and folding into 1D nanorolls, which would explain its lower yield. However, it should be possible to increase the exfoliation yield by generating oxide species *in situ* in this case as well, provided that the sonication treatment is carried out under proper alkaline conditions. To this end, we sonicated bulk NbSe₂ powder at different basic pH values, controlled by the addition of KOH. As could be anticipated, the exfoliation yield increased substantially when working at pH values of ~10–11, once again confirming the key part played by hydrolytic oxidation in the delamination behavior of this LTMD.

Finally, we demonstrated that the cathodic exfoliation route developed here for NbSe₂ could be extended to other LTMDs. To this end, metallic LTMDs such as NbS₂ or VSe₂ seemed to be better candidates than their semiconducting counterparts (MoS₂, WS₂, MoSe₂, etc.) for two reasons. First, for the present exfoliation strategy to succeed, the LTMD should be highly reactive toward oxidation, particularly alkaline hydrolytic oxidation. By their own nature, metallic LTMDs are generally expected to be more prone to oxidation than semiconducting ones [65]. Second, the higher electrical conductivity of metallic LTMDs should favor the occurrence of the processes that lead to their exfoliation under electrolytic conditions. Such processes should be much more limited for semiconducting LTMDs as a result of their lower conductivity. Indeed, upon application of a negative voltage (-10 V), bulk NbS₂ and VSe₂ resulted in, respectively, gray and brownish-red colloidal dispersions (see Movie S4 and Figure S8a for NbS₂, and Movie S5 and Figure S8b for VSe₂ in the Supporting Information) of micrometer- and submicrometer-sized 2D NbS₂ and VSe₂ nanosheets (see Figure S8c,d in the Supporting Information, respectively). Thus, we have shown that the present simple and fast exfoliation strategy of low environmental impact is applicable to metallic LTMDs, making metallic 2D LTMDs available for, e. g., EES.

2.4. Lithium Storage performance of the Cathodically Delaminated NbSe₂

Materials

The Li storage performance of the two cathodically delaminated NbSe₂ products, i.e., nanorolls and unfolded nanosheets, was evaluated in a half-cell configuration, with the NbSe₂ material combined with a conductive additive (a mixture of carbon black and carbon nanotubes) and a binder as the working electrode, Li metal foil as the counter and reference electrode, and 1 M LiPF₆ solution in an ethylene carbonate/diethylene carbonate solvent mixture (1/1 weight ratio) as the electrolyte (see the Experimental Section in the Supporting Information for details). We note that the two cathodically delaminated NbSe₂ products were not dispersed as individual objects in any solvent after their preparation and were thus expected to retain their different morphology through their testing as electrodes. Indeed, as will be seen below, their dissimilar electrochemical performance gave experimental indication of the persistence of such morphological difference. Figure 4a,b shows the first four cyclic voltammograms (CVs) recorded for the rolled-up nanotubes and unfolded nanosheets, respectively, at a scan rate of 0.1 mV s⁻¹ in the potential range 0.01–3.00 V vs Li/Li⁺. The CVs of both samples were qualitatively identical and, in agreement with previous reports, they were dominated by a number of redox features characteristic of NbSe₂ materials, where Li storage is thought to arise from a combination of intercalation and conversion processes [13–15]. Specifically, in the first cathodic scan (red trace, negative current range), the peaks located at ~1.64–1.67 and 1.47 V vs. Li/Li⁺ have been ascribed to a transition of the NbSe₂ lattice from the starting H phase to the H' phase upon Li intercalation (i.e., $x\text{Li} + \text{H-NbSe}_2 \rightarrow \text{Li}_x\text{H}'\text{-NbSe}_2$), as well as to the conversion of NbSe₂ into Li₂Se and metallic Nb ($4\text{Li} + \text{H-NbSe}_2 \rightarrow 2\text{Li}_2\text{Se} + \text{Nb}$). Furthermore, the relatively broad cathodic peak at 0.63 V vs. Li/Li⁺ is thought to result from the conversion reaction of H'-phase NbSe₂ [$\text{Li}_x\text{H}'\text{-NbSe}_2 + (4-x)\text{Li} \rightarrow 2\text{Li}_2\text{Se} + \text{Nb}$], whereas the sharp,

intense peak at ~0.15 V vs Li/Li⁺ can be traced to the irreversible formation of a solid-electrolyte interphase (SEI) at the NbSe₂ electrode. In the ensuing anodic scan (red trace, positive current range), the relatively featureless, low-current ~0.05–1.50 V vs. Li/Li⁺ region can be attributed to the conversion of Li₂Se and Nb back to Li-intercalated NbSe₂ [2Li₂Se + Nb → Li_xH' - NbSe₂ + (4-x)Li], while the sharp peaks at 1.86–1.88 and 2.23–2.25 V vs. Li/Li⁺ have been attributed, respectively, to delithiation of NbSe₂ [Li_xH' - NbSe₂ → H' - NbSe₂ + xLi] and to oxidation of Li₂Se to give lithium polyselenides and/or elemental Se [e.g., nLi₂Se → Li₂Se_n + 2(n-1)Li, with 4 ≤ n ≤ 8]. The latter chemical species are then expected to reduce back to Li₂Se during the following cathodic scan (orange trace), which was indeed reflected in the peak appearing at 2.00–2.02 V vs. Li/Li⁺. Significantly, this peak was already noticed in the first cathodic run of both samples, thus supporting the above conclusion that some elemental Se was present in the as-prepared delaminated NbSe₂ materials. The intensity of the peaks associated to intercalation/conversion processes in NbSe₂ decreased after the first CV, which suggested that such processes were not totally reversible.

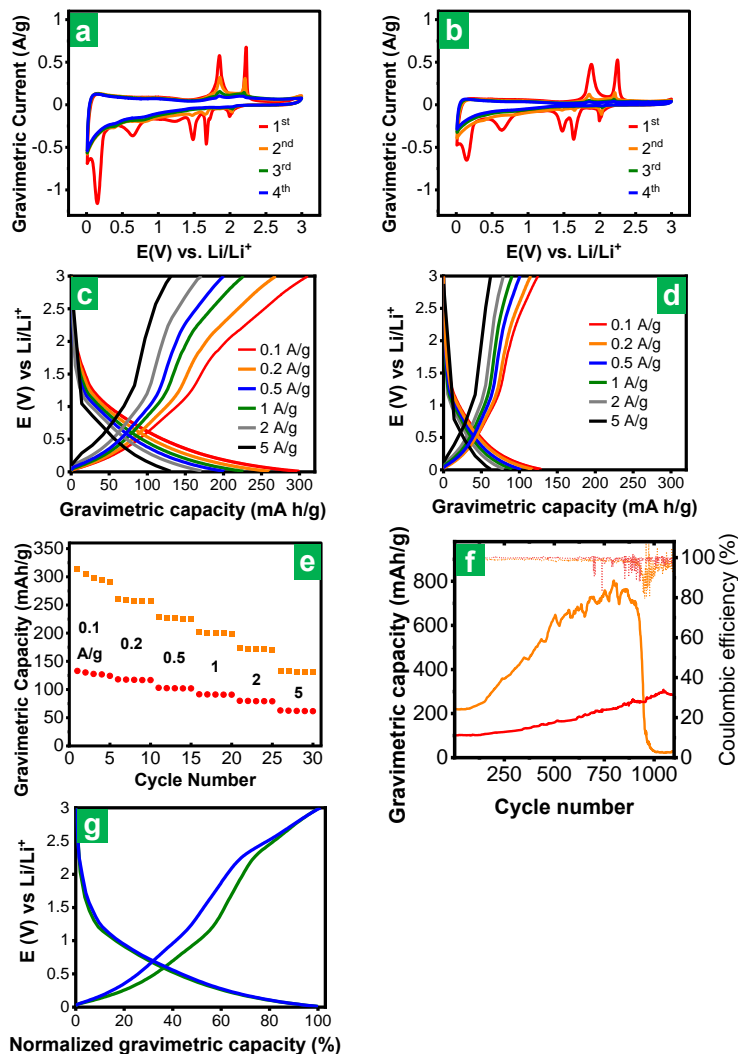


Figure 4. First four CVs for NbSe₂ nanorolls (**a**) and unfolded nanosheets (**b**) at a scan rate of 0.1 mV s⁻¹: 1st (red trace), 2nd (orange), 3rd (green), and 4th (blue). Typical GCD profiles for NbSe₂ nanorolls (**c**) and nanosheets (**d**) at current densities between 0.1 and 5 A g⁻¹. (**e**) Gravimetric capacity values for NbSe₂ nanorolls (orange squares) and nanosheets (red circles) determined at different current densities from the discharge curves in **c** and **e**, respectively. The gravimetric capacity and current density values are given relative to the total mass of the NbSe₂-based electrode; the figures would be a factor of ~1.85 larger if given relative to the mass of active material (i.e., mass of NbSe₂ only). (**f**) Cyclability of NbSe₂ nanorolls (orange trace) and nanosheets (red trace) in terms of capacity (solid trace) and Coulombic efficiency (dotted trace) at a current density of 0.5 A g⁻¹. (**g**) Typical GCD for the early stages of cycling of the NbSe₂ nanorolls (green traces) and for the electrode with increased capacity after several hundred cycles (blue traces). For ease of comparison, the profiles have been normalized to their full discharge capacity.

Quantitative comparison of the CVs for the nanorolls and unfolded nanosheets revealed that consistently higher currents were measured with the former material, implying its higher electrochemical activity (the mass loading of both samples was the same, i.e., $\sim 0.65 \text{ mg cm}^{-2}$). Such a result was consistent with the idea that tubular morphologies should be more conducive to facilitating access of the electrolyte to the active material, compared to the case of unfolded nanosheets [66,67]: the strong tendency of the latter to re-stack upon processing should be substantially alleviated when the nanosheets are rolled-up into nanorolls. The larger electrode-electrolyte contact area expected for the rolled-up nano-objects was reflected in the much more intense current associated to the generation of the SEI layer (i.e., the cathodic peak at $\sim 0.15 \text{ V}$ vs. Li/Li^+ of the first CV) in this sample relative to that of the unfolded nanosheets, as can be noticed in Figure 4a,b. Due to the irreversible formation of the SEI layer as well as to the partial irreversibility of the intercalation and conversion events in NbSe_2 , the Coulombic efficiency of the first voltammetric cycle was rather low, and even more so for the nanorolls ($\sim 58\%$ vs 62% for the unfolded nanosheets), but in both cases, the efficiency tended to approach 100 % upon subsequent cycles.

Typical galvanostatic charge-discharge (GCD) profiles recorded at different current densities between 0.1 and 5 A g^{-1} after the first few initial cycles are presented in Figure 4c,d and d for the nanorolls and unfolded nanosheets, respectively. As expected, larger capacity values were obtained with the rolled-up nano-objects both at low and high current densities. For example, capacities of ~ 300 (nanorolls) and ~ 130 (unfolded nanosheets) mAh g^{-1} at 0.1 A g^{-1} , as well as ~ 130 (nanorolls) and ~ 60 (unfolded nanosheets) mAh g^{-1} at 5 A g^{-1} were measured. More detailed data of the rate capability of the samples are given in Figure 4e. In both cases, about $\sim 45\%$ of the capacity could be retained when the current density was increased from 0.1 to 5 A g^{-1} . We note that these gravimetric capacity and current density figures are given relative to the total mass of the NbSe_2 -based electrode. If

given relative to the mass of active material (i.e., mass of NbSe₂ only), the capacities/current densities would be a factor of ~1.85 larger. Taking this point into account is important when making comparisons with results from the literature, where the distinction between total mass of the electrode and mass of active material in gravimetric data is not always explicitly stated. When such comparisons were possible on an equal footing, the present cathodically delaminated NbSe₂ material was seen to exhibit a very good performance. Specifically, the Li storage capacities for the rolled-up nano-objects were competitive with recent excellent results from a few-layer NbSe₂@graphene heterostructure obtained by a wet ball milling technique [15]. Relative to the mass of active material, the NbSe₂@graphene heterostructure yielded capacities of 492 and 416 mAh g⁻¹ at 0.1 and 3 A g⁻¹, respectively, to be compared with values of 545 and 325 mAh g⁻¹ at 0.18 and 3.7 A g⁻¹, respectively, measured for the present NbSe₂ nanoroll sample (see Table S1 in the Supporting Information for a comparison of the electrochemical performance of the materials prepared here with the very few examples reported in the literature for NbSe₂-based materials applied to Li storage).

The cyclic behavior of the delaminated NbSe₂ materials was also investigated, and the corresponding results (capacity and Coulombic efficiency values) are shown in Figure 4f for tests carried out at a current density of 0.5 A g⁻¹ (relative to the total mass of the electrode). Remarkably, the capacity was seen to increase to a large extent after several hundred charge-discharge cycles, especially in the case of the nanorolls (orange solid trace), e.g., it was a factor of ~3 times higher (up to 750–800 mAh g⁻¹) for this sample upon 700–800 cycles, compared to a factor of ~2 (up to 200–220 mAh g⁻¹) for the unfolded nanosheets (red solid trace). Nonetheless, after about 900 cycles, the capacity of the nanorolls plummeted to values below 50 mAh g⁻¹ over the course of several tens of cycles (~0.1% of capacity decrease per cycle), which was indicative of severe cell failure. By contrast, the capacity of the unfolded nanosheets continued to rise up to ~320 mAh

Artículo III

g^{-1} for some additional 300 cycles, reaching a plateau subsequently and starting to decline slowly ($\sim 0.06\%$ per cycle) after 1600 cycles (see Figure S9). The steady increase in capacity upon repeated cycling would appear to suggest that not all of the active materials in the electrode were initially available for Li storage. This could be due to the barrier effect of the binder and/or conductive additive, the contact of which with particles of the active material would hamper access of the electrolyte to the latter, thus compromising their activity [15]. The local volume changes associated to recurrent lithiation/delithiation of the active particles would likely promote the opening of gaps between such particles and the binder/conductive additive, which in turn would facilitate a more extensive infiltration of the electrolyte. The fact that no such an improvement in rate capability was observed between nanoroll and nanosheet morphology (see Figure 4e) must be related to the protocol used to prepare the electrodes, i. e., casting a mixture of lyophilized powder with additives onto copper foil (see the Experimental Section in the Supporting Information for details), which must favor re-stacking of the nanosheets, but to a limited extent. If a method more prone to re-stacking of the nanosheets, such as, e. g., filtering dispersions of the active material to yield films, had been used, the lower tendency to re-stack of the nanorolls would be expected to lead to a relatively better performance in the rate capability tests as well.

It is worth noting, however, that the maximum capacities measured here relative to the mass of NbSe_2 , i.e., $\sim 1450 \text{ mAh g}^{-1}$ for the nanorolls and $\sim 600 \text{ mAh g}^{-1}$ for the unfolded nanosheets, were much larger than the theoretical capacity calculated for this LTMD in bulk form, i.e., $\sim 427 \text{ mAh g}^{-1}$, which was obtained assuming a full conversion to Li_2Se and Nb. This suggests that Li storage mechanisms other than those described above must contribute heavily to the measured capacities. Similar to the case of graphene with respect to graphite [68], the present large excess capacity likely arises from the formation of Li multilayers on the surface of the NbSe_2 nano-objects, and maybe also on the surface of the

carbon particles used as a conductive additive. Such a Li storage process would be expected to occur at very low potentials (e.g., below 0.3 V vs Li/Li⁺). Indeed, a large fraction of the measured capacities was seen to come from that potential range (Figure 4c,d). To further explore this question, Figure 4g plots two GCD profiles from the rolled-up nano-objects, one of them typical of the early stages of cycling (cycle no. 20, green traces) and the other one typical of the electrode with increased capacity after several hundred cycles (cycle no. 700, blue traces). An equivalent plot for the unfolded nanosheets is shown in Figure S10. To facilitate comparisons, the profiles have been normalized to their respective capacity, that is, with the full discharge capacity equaling to 100%. If the large excess capacity built up steadily over several hundred cycles was only due to the progressive formation of Li multilayers, we would expect the corresponding discharge profile to be considerably skewed toward very low potentials compared to that obtained during the initial cycles. Nevertheless, as noticed from Figures 4g and S10, that was not the case. Rather, the two discharge profiles were very similar to each other in the two samples. This result implied that the active material in the electrode became increasingly available as a whole upon cycling, i.e., not just the outer surface of the particles for the formation of Li multilayers but also simultaneously the interior of the NbSe₂ nano-objects for intercalation/conversion reactions.

On the other hand, as also noticed in Figures 4g and S10, the normalized charge profiles skewed toward higher potentials upon prolonged cycling, particularly in the case of the nanorolls, indicative of an increased polarization of the cell. Although the origin of this effect is currently unclear, we believe it may be related to Ohmic processes (Ohmic polarization) [69]. As the gaps between active NbSe₂ particles and binder/conductive additive progressively open, the quality of the electrical contacts between the electrode components can be expected to decrease, which would be possibly further promoted by the formation of additional SEI layers in the new gaps. This would result in an electrode with poorer electrical

conductivity and, consequently, with increased polarization of Ohmic nature. The increasingly poor electrical contacts within the electrode could also be responsible for the capacity decay noticed in the cells. Specifically, the larger surface area associated to the NbSe₂ nanoscrolls compared to the unfolded nanosheets, while attractive for promoting higher Li storage capacities, would also be conducive to a more extensive opening of gaps. In turn, this would lead to a more drastic deterioration of the electrical contacts within the electrode and thus to a faster capacity decay in the former sample, as is actually seen in Figures 4f and S9. The abrupt morphological changes during charge/discharge would also lead to sudden changes in the electrical contacts, yielding a zigzagging curve, as seen in the latter figures. A more in-depth investigation of the failure mechanisms of this electrode material will be provided in future work, with the aim of proposing strategies that improve its cycle life performance.

3. Conclusions

We have demonstrated a simple and expeditious method for the preparation of 2D NbSe₂ predominantly in the form of either rolled-up nanosheets (nanorolls) or unfolded nanosheets. This method relies on the direct cathodic exfoliation of bulk NbSe₂ powder in an aqueous solution of a readily available salt, which makes it especially attractive from a practical standpoint. The fact that the exfoliated nano-objects could be directly obtained by the present electrolytic treatment in a very short time (1–2 min) with substantial yields (~16 wt%) sets this strategy apart from most other top-down methods previously used for the production of 2D NbSe₂, such as direct liquid-phase exfoliation via sonication (longer processing times, lower yields) and typical electrochemical exfoliation techniques (use of organic electrolytes, post-treatment required to complete delamination). An inquiry into the cathodic exfoliation mechanism suggested that delamination is driven by a partial hydrolytic oxidation of the material in the locally alkaline environment around the

NbSe₂ cathode. This reaction is expected to generate molecular niobium oxide species (e.g., highly charged polyoxoniobates) that prompt the cleavage of thin NbSe₂ layers from their bulk parent solid, in a process that resembles the redox exfoliation mechanism of LTMDs. As expected from the particulars of the exfoliation mechanism, the methodology could be extended to other metallic LTMDs, such as NbS₂ and VSe₂. As an active material for electrochemical lithium storage, the cathodically delaminated products were seen to exhibit very high capacity values, particularly the material with dominant nanoroll morphology. This can be ascribed to a higher accessibility of the lithium storage sites afforded by such a morphology (larger electrode-electrolyte contact area) compared to the material with unfolded nanosheet morphology, where re-stacking issues probably constitute a barrier in that respect. Overall, the present results make metallic 2D LTMDs available by a simple and fast preparation strategy of low environmental impact, which is expected to expedite their uses in EES and beyond.

Supporting Information: The Supporting Information is available free of charge at <https://pubs.acs.org/doi/10.1021/acsaem.3c00893>.

- Experimental section; evidence on the reversibility of the folding of the NbSe₂ nanosheets into nanoroll morphology through solvent exchange; further physicochemical characterization of cathodically delaminated NbSe₂; cathodical delamination of other LTMDs (NbS₂ and VSe₂); comparison of the electrochemical performance for Li storage of the cathodically delaminated NbSe₂ with other NbSe₂-based materials; additional information of the cyclability of the cathodically delaminated NbSe₂ materials for lithium storage (PDF).

Artículo III

- Movie 1 demonstrating the electrochemical delamination of NbSe₂ bulk material pressed on flexible graphite for the preparation of NbSe₂ nanosheets (MP4).
- Movie 2 demonstrating the change undergone by flexible graphite alone under the same conditions (MP4).
- Movie 3 demonstrating the electrochemical delamination of a pellet NbSe₂ bulk material (MP4).
- Movie 4 demonstrating the electrochemical delamination of NbS₂ into of NbS₂ nanosheets (MP4).
- Movie 5 demonstrating the electrochemical delamination of VSe₂ into of VSe₂ nanosheets (MP4).

Acknowledgements

D. F. C., S. G. D, S. V. R., J. M. M., J. I. P. gratefully acknowledge funding by the Spanish Ministerio de Ciencia e Innovación and Agencia Estatal de Investigación (MCIN/AEI/ 10.13039/501100011033) as well as the European Regional Development Fund (ERDF, A way of making Europe) through grant PID2021-125246OB-I00, and by Plan de Ciencia, Tecnología e Innovación (PCTI) 2018-2022 del Principado de Asturias and the ERDF through grant IDI/2021/000037. S.G.D. is grateful to the Spanish MINECO for his pre-doctoral contract [BES/2016 077830]. E. R. P. thanks the Région Centre val de Loire in France [Project APR-IR SCAP-3D, convention n°2017-00117284] for financial support.

References

- [1] K.S. Novoselov, A. Mishchenko, A. Carvalho, A.H. Castro Neto, 2D materials and van der Waals heterostructures, *Science* 353 (2016), 6298.
- [2] K.S Kumar, N. Choudhary, Y. Jung, J. Thomas, Recent advances in two-dimensional nanomaterials for supercapacitor electrode applications, *ACS Energy Letters* 3 (2018), 482-495.
- [3] D. Yuan, Y. Dou, Z. Wu, Y. Tian, K.-H. Ye, Z. Lin, S.X. Dou, S. Zhang, Atomically thin materials for next-generation rechargeable batteries, *Chemical Reviews* 122 (2022), 957-999.
- [4] H. Cui, Y. Guo, W. Ma, Z. Zhou, 2D materials for electrochemical energy storage: design, preparation, and application, *ChemSusChem* 13 (2020), 1155-1171.
- [5] M.F. El-Kady, Y. Shao, R.B. Kaner, Graphene for batteries, supercapacitors and beyond, *Nature Reviews Materials* 1 (2016), 16033.
- [6] J. Wu, F. Ciucci, J.-K Kim, Molybdenum disulfide based nanomaterials for rechargeable batteries, *Chemistry: A European Journal* 26 (2020), 6296-6319.
- [7] D. Xiong, X. Li, Z. Bai, S. Lu, Recent advances in layered Ti₃C₂T_xMXene for electrochemical energy storage, *Small* 14 (2018), 1703419.
- [8] Y. Tao, T. Huang, C. Ding, F. Yu, D. Tan, F. Wang, Q. Xie, S. Yao, Few-layer phosphorene: an emerging electrode material for electrochemical energy storage, *Applied Materials Today* 15 (2019), 18-33.
- [9] H. T. Tan, W. Sun, L. Wang, Q. Yan, 2D transition metal oxides/hydroxides for energy-storage applications, *ChemNanoMat* (2015) 562-577.
- [10] E. Pomerantseva, F. Bonaccorso, X. Feng, Y. Cui, Y. Gogotsi, Energy storage: the future enabled by nanomaterials, *Science* 366 (2019) 6468.
- [11] G.H. Jeong, S.P. Sasikala, T. Yun, G.Y. Lee, W.J. Lee, S.O. Kim, Nanoscale assembly of 2D materials for energy and environmental applications, *Advanced Materials* 32 (2020), 1907006.
- [12] B. Zhao, D. Shen, Z. Zhang, P. Lu, M. Hossain, J. Li, B. Li, X. Duan, 2D metallic transition metal dichalcogenides: structures, synthesis, properties, and applications, *Advanced Functional Materials* 31 (2021), 2105132.
- [13] C. Peng, C. H. Lyu, L. Wu, T. Xiong, F. Xiong, Z. Liu, Q. An, L. Mai, Lithium- and magnesium-storage mechanisms of novel hexagonal NbSe₂, *ACS Applied Materials & Interfaces* 10 (2018), 36988-36995.
- [14] J. Zhang, C. Du, J. Zhao, H. Ren, Q. Liang, Y. Zheng, S. Madhavi, X. Wang, J. Zhu, Q. Yan, CoSe₂-decorated NbSe₂ nanosheets fabricated via cation exchange for Li storage, *ACS Applied Materials & Interfaces* 10 (2018), 37773-37778.
- [15] Q. H. Nguyen, H. Kim, I.T. Kim, W. Choi, J. Hur, Few-layer NbSe₂@graphene heterostructures as anodes for lithium-ion half- and full-cell batteries, *Chemical Engineering Journal* 382 (2020), 122981.

Artículo III

- [16] Y. Luo, J. Han, Q. Ma, R. Zhan, Y. Zhang, Q. Xu, M. Xu, Exploration of NbSe₂ flakes as reversible host materials for sodium-ion and potassium-ion batteries, *ChemistrySelect* 3 (2018), 9807-9811.
- [17] B. Xu, X. Ma, J. Tian, F. Zhao, Y. Liu, B. Wang, H. Yang, Y. Xia, Layer-structured NbSe₂ anode material for sodium-ion and potassium-ion batteries, *Ionics* 25 (2019), 4171-4177.
- [18] Q. Peng, F. Ling, H. Yang, P. Duan, R. Xu, Q. Wang, Y. Yu, Boosting potassium storage performance via construction of NbSe₂-based misfit layered chalcogenides, *Energy Storage Materials* 39 (2021), 265-270.
- [19] M.J. Park, H. Y. Asl, A. Manthiram, Understanding Zn-ion insertion chemistry through nonaqueous electrochemical investigation of 2H-NbSe₂, *Advanced Materials Interfaces* 8 (2021), 2100878.
- [20] D. Yang, Z. Liang, C. Zhang, J.J. Biendicho, M. Botifoll, M.C. Spadaro, Q. Chen, M. Li, A. Ramon, A.O. Moghaddam, J. Llorca, J. Wang, J.R. Morante, J. Arbiol, S.-L. Chou, A. Cabot, NbSe₂ meets C2N: a 2D-2D heterostructure catalysts as multifunctional polysulfide mediator in ultra-long-life lithium-sulfur batteries, *Advanced Energy Materials* 11 (2021), 2101250.
- [21] G. Sun, J. Liu, X. Zhang, X. Wang, H. Li, Y. Yu, W. Huang, H. Zhang, P. Chen, Fabrication of ultralong hybrid microfibers from nanosheets of reduced graphene oxide and transition-metal dichalcogenides and their application as supercapacitors, *Angewandte Chemie International Edition* 53 (2014), 12576-12580.
- [22] H.M.N. Ahmad, S. Ghosh, G. Dutta, A.G. Maddaus, J.G. Tsavalas, S. Hollen, E. Song, Effects of impurities on the electrochemical characterization of liquid-phase exfoliated niobium diselenide nanosheets, *The Journal of Physical Chemistry C* 123 (2019), 8671-8680.
- [23] J.N. Coleman, M. Lotya, A. O'Neill, S.D. Bergin, P.J. King, U. Khan, K. Young, A. Gaucher, S. De, R.J. Smith, I.V. Shvets, S.K. Arora, G. Stanton, H.-Y. Kim, K. Lee, G.T. Kim, G.S. Duesberg, T. Hallam, J.J. Boland, J.J. Wang, J.F. Donegan, J.C. Grunlan, G. Moriarty, A. Shmeliov, R.J. Nicholls, J.M. Perkins, E.M. Grievson, K. Theuwissen, D.W. McComb, P.D. Nellist, V. Nicolosi, Two-dimensional nanosheets produced by liquid exfoliation of layered materials, *Science* 331 (2011), 568-571.
- [24] Z. Zeng, T. Sun, J. Zhu, X. Huang, Z. Yin, G. Lu, Z. Fan, Q. Yan, H.H. Hang, H. Zhang, An effective method for the fabrication of few-layer-thick inorganic nanosheets, *Angewandte Chemie International Edition* 51 (2012), 9052-9056.
- [25] Z. Lin, Y. Liu, U. Halim, M. Ding, Y. Liu, Y. Wang, C. Jia, P. Chen, X. Duan, C. Wang, F. Song, M. Li, C. Wan, Y. Huang, X. Duan, Solution-processable 2D semiconductors for high-performance large-area electronics, *Nature* 562 (2018), 254-258.
- [26] J. Li, P. Song, J. Zhao, K. Vaklinova, X. Zhao, Z. Li, Z. Qiu, Z. Wang, L. Lin, M. Zhao, T.S. Herring, Y. Zuo, W. Jonhson, W. Yu, X. Hai, P. Lyu, H. Xu, H. Yang, C. Chen, S.J. Pennycook, J. Ding, J. Teng, A.H.C. Neto, K.S. Novoselov, J. Lu, Printable two-dimensional superconducting monolayers, *Nature Material* 20 (2021), 181-187.
- [27] S. García-Dalí, J.I. Paredes, J.M. Munuera, S. Villar-Rodil, A. Adawy, A. Martínez-Alonso, J.M.D. Tascón, Aqueous cathodic exfoliation strategy toward solution-processable and phase-preserved MoS₂ nanosheets for energy storage and catalytic applications, *ACS Applied Materials & Interfaces* 11 (2019), 36991-37003.

- [28] F. Calavalle, P. Dreher, A.P. Surdendran, W. Wan, M. Timpel, R. Verucchi, C. Rogero, T. Bauch, F. Lombardi, F. Casanova, M.V. Nardi, M.M. Ugeda, L.E. Hueso, M. Gobbi, Tailoring superconductivity in large-area single-layer NbSe₂ via self-assembled molecular adlayers, *Nano Letters* 21 (2021), 136-143.
- [29] CRC Handbook of Chemistry and Physics, Lide, D. R. (Ed.), 87th Ed. 2006, pp. 8-21 & 8-22.
- [30] J. Chen, J. Yang, B. Chen, S. Liu, J. Dong, C. Li, Large-scale synthesis of NbSe₂ nanosheets and their use as nanofillers for improving the tribological properties of epoxy coatings, *Surface and Coatings Technology* 305 (2016), 23-28.
- [31] B. Gates, B. Mayers, B. Cattle, Y. Xia, Synthesis and characterization of uniform nanowires of trigonal selenium, *Advanced Functional Materials* 12 (2002), 219-227.
- [32] M.A.R. Fresneda, J.D. Martín, J.G. Bolívar, M.V.F. Cantos, G. Bosch-Estévez, M.F.M. Moreno, M.L. Merroun, Green synthesis and biotransformation of amorphous Se nanospheres to trigonal 1D Se nanostructures: impact on Se mobility within the concept of radioactive waste disposal, *Environmental Science: Nano* 5 (2018), 2103-2116.
- [33] C.S. Wang, J.M. Chen, Raman spectrum of metallic layered compound NbSe₂, *Solid State Communications* 14 (1974), 1145-1148.
- [34] C.M. Pereira, W.Y. Liang, Raman studies of the normal phase of 2H-NbSe₂, *Journal of Physics C: Solid State Physics* 15 (1982), L991-L995.
- [35] J.C. Tsang, J.E. Smith, M.W. Shafer, Raman spectroscopy of soft modes at the charge-density-wave phase transition in 2H-NbSe₂, *Physical Review Letters* 37 (1976), 1407-1410.
- [36] J.C. Tsang, J.E. Smith, M.W. Shafer, Effect of charge density wave fluctuations on the frequencies of optic phonons in 2H-TaSe₂ and -NbSe₂, *Solid State Communications* 27 (1978), 145-149.
- [37] N.E. Staley, J. Wu, P. Eklund, Y. Liu, L. Li, Z. Xu, Electric field effect on superconductivity in atomically thin flakes of NbSe₂, *Physical Review B* 80 (2009), 184505.
- [38] H.M. Hill, A.F. Rigos, S. Krylyuk, J. Tian, N.V. Nguyen, A.V. Davydov, D.B. Newell, A.R.H. Walker, Comprehensive optical characterization of atomically thin NbSe₂, *Physical Review B* 98 (2018), 165109.
- [39] G. Vacquier, A. Casalot, A. Rolland, Superficial characterization of NbSe₂ single crystals: an Auger electron spectroscopy study, *Materials Science and Engineering* 85 (1987), L9-L12.
- [40] S. Naik, S. Kalaiarasan, R.C. Nath, S.N. Sarangi, A.K. Sahu, D. Samal, H.S. Biswal, S.L. Samal, Nominal effect of Mg intercalation on the superconducting properties of 2H-NbSe₂, *Inorganic Chemistry Journal* 60 (2021), 4588-4598.
- [41] G. E. Myers, G.L. Montet, Light-induced oxidation of NbSe₂ single crystals, *Journal of Physics and Chemistry of Solids* 32 (1971), 2645-2646.
- [42] Y. Kim, J.-L Huang, C.M. Lieber, Characterization of nanometer scale wear and oxidation of transition metal dichalcogenide lubricants by atomic force microscopy, *Applied Physics Letters* 59 (1991), 3404-3406.

Artículo III

- [43] L. Nguyen, H.-P. Komsa, E. Khestanova, R.J. Kashtiban, J.J.P. Peters, S. Lawlor, A.M. Sanchez, J. Sloan, R.V. Gorbachev, I.V. Grigorieva, A.V. Krasheninnikov, S.J. Haigh, Atomic defects and doping of monolayer NbSe₂, *ACS Nano* 11 (2017), 2894-2904.
- [44] B.X. Huang, K. Wang, J.S. Church, Y.-S. Li, Characterization of oxides on niobium by Raman and infrared spectroscopy, *Electrochimica Acta* 44 (1999), 2571-2577.
- [45] A.E. Raevskaya, A.L. Stroyuk, S.Y. Kuchmiy, V.M. Dzhagan, D.R.T. Zahn, S. Schulze, Annealing-induced structural transformation of gelatin-capped Se nanoparticles, *Solid State Communications* 145 (2008), 288-292.
- [46] W.-Y. Tzeng, Y.-H Tseng, T.-T Yeh, C.-M Tu, R. Sankar, Y.-H. Chen, B.-H. Huang, F.-C. Chou, C.-W. Luo, Selenium nanoparticle prepared by femtosecond laser-induced plasma shock wave, *Optics Express* 28 (2020), 685-694.
- [47] M.S. El-Bana, D. Wolverson, S. Russo, G. Balakrishnan, D.M. Paul, Bending, S.J. Superconductivity in two-dimensional NbSe₂ field effect transistors, *Superconductor Science and Technology* 26 (2013), 125020.
- [48] J.E. Kim, V.T. Vu, T.T.H. Vu, T.L. Phan, Y.R. Kim, W.T. Kang, K. Kim, Y.H. Lee, W.J. Yu, A non-volatile memory based on NbO_x/NbSe₂ van der Waals heterostructures, *Applied Sciences* 10 (2020), 7598.
- [49] B. Wang, H. Luo, X. Wang, E. Wang, Y. Sun, Y.-C Tsai, H. Zhu, P. Liu, K. Jiang, K.; Liu, Bifunctional NbS₂-based asymmetric heterostructure for lateral and vertical electronic devices, *ACS Nano* 14 (2020), 175-184.
- [50] Surface Analysis –The Principal Techniques. Vickerman, J. C.; Gilmore, I. S. Ch. 3: Electron Spectroscopy for Chemical Analysis, B: Ratner, D.; Castner, D. G. p.89, 2nd Ed. 2009, John Wiley & Sons.
- [51] A. Ambrosi, M. Pumera, Exfoliation of layered materials using electrochemistry, *Chemical Society Reviews* 47 (2018), 7213-7224.
- [52] Y. Fang, X. Li, J. Li, C. Yao, H.Y. Hoh, X. Hai, J. Lu, C. Su, Janus electrochemical exfoliation of two-dimensional materials, *Journal of Materials Chemistry A* 7 (2019), 25691-25711.
- [53] A. Jawaid, J. Che, L.F. Drummy, J. Bultman, A. Waite, A.-S. Hsiao, R.A. Vaia, Redox exfoliation of layered transition metal dichalcogenides, *ACS Nano* 11 (2017), 635-646.
- [54] A. M. Jawaid, A.J. Ritter, R.A. Vaia, Mechanism for redox exfoliation of layered transition metal dichalcogenides, *Chemistry of Materials Journal* 32 (2020), 6550-6565.
- [55] M. Nyman, Polyoxoniobate chemistry in the 21st century, *Dalton Transactions* 40 (2011), 8049-8058.
- [56] M.A. Ibrahim, W.-C. Huang, T. Lan, K.M. Boopathi, Y.-C Hsiao, C.-H Chen, W. Budiawan, Y.-Y. Chen, C.-S. Chang, L.-J. Li, C.-H. Tsai, C.W. Chu, Controlled mechanical cleavage of bulk niobium diselenide to nanoscaled sheet, rod, and particle structures for Pt-free dye-sensitized solar cells, *Journal of Materials Chemistry A* 2 (2014), 11382-11390.
- [57] R. Qu, X. Wen, Y. Zhao, T. Wang, R. Yao, J. Lu, Ultrasonic-assisted top-down preparation of NbSe₂ micro/nanoparticles and hybrid material as solid lubricant for sliding electrical contact, *Ultrasonics Sonochemistry* 73 (2021), 105491.

- [58] J. Meng, G. Wang, X. Li, X. Lu, J. Zhang, H. Yu, W. Chen, L. Du, M. Liao, J. Zhao, P. Chen, J. Zhu, X. Bai, D. Shi, G. Zhang, Rolling up a monolayer MoS₂ sheet, *Small* 12 (2016), 3770-3774.
- [59] X. Cui, Z. Kong, E. Gao, D. Huang, Y. Hao, H. Shen, C. Di, Z. Xu, J. Zheng, D. Zhu, Rolling up transition metal dichalcogenide nanoscrolls via one drop of ethanol, *Nature Communications* 9 (2018), 1301.
- [60] W. Wang, Y. Gai, D. Xiao, Y. Zhao, A facile and general approach for production of nanoscrolls with high-yield from two-dimensional nanosheets, *Scientific Reports* 8 (2018), 15262.
- [61] D. Y. Hwang, K.H. Choi, D.H. Suh, A vacancy-driven phase transition in MoX₂ (X: S, Se and Te) nanoscrolls, *Nanoscale* 10 (2018), 7918-7926.
- [62] P. Thangasamy, M. Sathish, Rapid, one-pot synthesis of luminescent MoS₂ nanoscrolls using supercritical fluid processing, *Journal of Materials Chemistry C* 4 (2016), 1165-1169.
- [63] T.M.D. Alharbi, S. Elmas, A.S. Alotabi, M.R. Andersson, C.L. Raston, Continuous flow fabrication of MoS₂ scrolls for electrocatalytic hydrogen evolution, *ACS Sustainable Chemistry & Engineering Journal* 10 (2022), 9325-9333.
- [64] L. Guillemeney, L. Lermusiaux, G. Landaburu, B. Wagnon, B. Abécassis, Curvature and self-assembly of semi-conducting nanoplatelets, *Communications Chemistry* 5 (2022), 7.
- [65] Q. Li, Q. Zhou, L. Shi, Q. Chen, J. Wang, Recent advances in oxidation and degradation mechanisms of ultrathin 2D materials under ambient conditions and their passivation strategies, *Journal of Materials Chemistry A* 7 (2019), 4291-4312.
- [66] Y. Lian, N. Yang, D. Wang, Y. Zheng, C. Ban, J. Zhao, H. Zhang, Optimization design and application of niobium-based materials in electrochemical energy storage, *Advanced Energy and Sustainability Research* 1 (2020), 2000038.
- [67] Z. Zou, Q. Wang, K. Zhu, K. Ye, G. Wang, D. Cao, J. Yan, Ultrathin-walled Bi₂S₃nanoroll/MXene composite toward high capacity and fast lithium storage, *Small* 18 (2022), 2106673.
- [68] F.J. Sonia, M.K. Jangid, B. Ananthoju, M. Aslam, P. Johari, A. Mukhopadhyay, Understanding the Li-storage in few layers graphene with respect to bulk graphite: experimental, analytical and computational study, *Journal of Materials Chemistry A* 5 (2017), 8662-8679.
- [69] J. Zheng, J. Lu, K. Amine, F. Pan, Depolarization effect to enhance the performance of lithium ions batteries, *Nano Energy* 33 (2017), 497-507.

Supporting Information.

NbSe₂ nanosheets/nanorolls obtained via fast and direct aqueous electrochemical exfoliation for high capacity lithium storage

Daniel F. Carrasco^a, Sergio García-Dalí^{a,b}, Silvia Villar-Rodil^{a,*}, José M. Munuera^a, Encarnación Raymundo-Piñero^b, Juan I. Paredes^{a,*}

^a*Instituto de Ciencia y Tecnología del Carbono, INCAR-CSIC, Francisco Pintado Fe 26, 33011 Oviedo, Spain*

^b*CNRS, CEMHTI UPR3079, Univ. Orléans, 1D avenue de la Recherche Scientifique, 45071, Orléans, France*

*Corresponding authors' e-mail addresses: paredes@incar.csic.es (J. I. Paredes), silvia@incar.csic.es (S. Villar-Rodil).

S1. Experimental section

S1.1. Materials and reagents

Bulk NbSe₂ in powder form was acquired from American Elements. Graphite foil (Papyex I980, thickness ~0.5 mm, mass density ~1.1 g cm⁻³) was obtained from Mersen. Platinum foil (dimensions: 25×25×0.025 mm³), lithium foil, copper foil, potassium nitrate (KNO₃), nitric acid (HNO₃, 65-67 wt% solution), potassium hydroxide (KOH), potassium chloride (KCl), hydrochloric acid (HCl, 37 wt% solution), N-methyl-2-pyrrolidone (NMP) and isopropanol were purchased from Sigma-Aldrich. 1 M lithium hexafluorophosphate solution in ethylene carbonate/dimethyl carbonate (1/1 weight ratio) (LP30) was procured from Solvionic whereas carbon nanotubes (CNTs) and carbon black (Super C65) were bought from Arkema and Timcal, respectively. Polyvinylidene difluoride (PVDF, Solef) and glass fiber paper (thickness 670 µm) were acquired from Solvay and Whatman®, respectively. Milli-Q deionized water (Millipore Sigma, resistivity: 18.2 MΩ·cm) was used throughout the experiments.

S1.2. Cathodic exfoliation experiments

The electrolytic delamination of NbSe₂ was carried out in a two-electrode set-up under aqueous cathodic conditions, using a platinum foil piece as the counter electrode (anode). In a typical experiment, 100 mg of bulk NbSe₂ powder were compacted onto a circular piece of graphite foil (10 mm in diameter) by means of a hydraulic press (5 tons applied for 1 min). The resulting NbSe₂/graphite foil electrode and the platinum foil piece were immersed in an aqueous 0.3 M KNO₃ solution (25 mL) at a distance of ~2 cm from each other and connected to a DC power supply (E3633A apparatus, from Keysight Technologies) via crocodile clips. Only about one half of the NbSe₂/graphite foil piece was actually immersed in the

aqueous electrolyte, the emerged half being held with the crocodile clip. Almost immediately upon application of a negative voltage (-10 V) to the NbSe₂/graphite foil electrode, a reddish-brown substance was seen to release from it and to get dispersed in the electrolyte. At the same time, gray particles also detached from the cathode and sedimented at the bottom of the electrolytic cell (see Movie S1 in The Supporting Information). After one minute of cathodic treatment, the bias voltage was turned off and the previously emerged half of the NbSe₂/graphite foil piece was immersed in the electrolyte to treat the corresponding fraction of NbSe₂ material (again, a bias voltage of -10 V applied for one minute). Finally, the electrolytic solution containing the reddish-brown dispersion was collected (the sedimented gray particles were discarded) and processed to recover this material for subsequent use. To this end, the dispersion was first sedimented either by allowing it to rest undisturbed overnight or by centrifuging it at 100 g for 10 min. Centrifugation was conducted with the electrolytic dispersion in glass vials that in turn were inserted into 50 mL centrifuge tubes. This was done to avoid direct contact of the dispersion with the polypropylene material of the centrifuge tubes, as sedimentation of the reddish-brown product caused it to strongly adhere to the latter, which prevented its recovery. Then, the sedimented material was re-suspended in pure water by a brief treatment with a vortex mixer. Following three consecutive sedimentation/re-suspension cycles, the reddish-brown product was subjected to a final sedimentation step, and the sediment was finally collected and dried under a vacuum. For the subsequent studies, this dried product could be readily dispersed in water and isopropanol via a brief treatment (1–2 min) with a vortex mixer or a bath sonicator.

S1.3. Characterization techniques

The materials were characterized by X-ray diffraction (XRD), field emission scanning electron microscopy (FE-SEM), scanning transmission electron microscopy (STEM), atomic force microscopy (AFM), energy-dispersive X-ray (EDX) spectroscopy, Raman spectroscopy and X-ray photoelectron spectroscopy (XPS). XRD patterns were recorded with a D5000 diffractometer (Siemens), using Cu K α radiation, a step size of 0.015° and a step time of 1 s. FE-SEM, STEM and EDX spectroscopy measurements were accomplished with a Quanta FEG apparatus (FEI Company) working at a bias voltage of 20–25 kV. Specimens for FE-SEM and EDX spectroscopy were prepared by mounting the sample (dry powder) onto the sample-holder by means of double-sided carbon adhesive tape, while those for STEM were procured by drop-casting a dispersion of the sample in water or isopropanol (10–20 μ L) onto a copper grid covered with a thin continuous carbon film (200 square mesh, MicrotoNano), and allowing it to dry under ambient conditions. AFM images were obtained with a Nanoscope IIIa Multimode microscope (Veeco Instruments) working in the tapping mode of operation. Rectangular silicon cantilevers with a nominal spring constant of 40 N m $^{-1}$ and resonance frequency of 250-300 kHz were employed. To image exfoliated NbSe₂ nano-objects by AFM, the delaminated material was dispersed in isopropanol, drop-cast (10–20 μ L) onto a freshly cleaved highly oriented pyrolytic graphite (HOPG) substrate and dried under vacuum at room temperature overnight (drying under ambient conditions led to molecularly thin islands of the alcohol on the HOPG surface, which could be largely removed under vacuum conditions). The recorded AFM images were analyzed with SPIP software (Image Metrology). Raman spectra were acquired with a Renishaw inVia Qontor instrument, working at a laser excitation wavelength of 532 nm (green line). To minimize damage to the sample, the incident laser power was set below 0.5 mW. XPS was carried out on a SPECS

system equipped with a Phoibos 100 hemispherical electron energy analyzer. The spectra were recorded at a take-off angle of 90°, working at a pressure below 10⁻⁷ Pa and using a monochromatic aluminum X-ray source operated at a voltage of 14.00 kV and a power of 175 W. The photoexcited electrons were analyzed in the constant pass energy mode, using a pass energy of 50 eV for survey spectra and 10 eV for high resolution core-level spectra. The surface charging effect was compensated by the use of an electron flood gun operated at 0.4 eV and 0.10 mA. CasaXPS software was used for data processing. Specimens for both XPS and Raman spectroscopy were prepared in the form of continuous, thin films by drop-casting NbSe₂ dispersions onto stainless steel discs, which were allowed to dry at room temperature. In the case of the commercial NbSe₂ powder, a pellet was prepared by means of a hydraulic press.

S1.4. Electrochemical measurements

The cathodically delaminated NbSe₂ materials were tested as electrodes for lithium storage in a coin cell configuration. The working electrodes were prepared by mixing 54 wt% of delaminated NbSe₂ as the active material, 16 wt% CNTs and 20 wt% Super C65 as the conductive additives, and 10 wt% PVDF as the binder. A small volume of NMP was added to the latter components and the mixture was transformed into a homogeneous slurry with the aid of a high-shear mixer. The slurry was then cast onto a 24 cm² sheet of copper foil and dried at 120 °C for 3 h. Circular discs 10 mm in diameter were finally cut from the coated copper foil. The total mass loading of the working electrode (i.e., the combined mass of NbSe₂, CNTs, Super C65 and PVDF) on the foil was 0.65 ± 0.03 mg cm⁻². A piece of lithium foil was used as both the counter and reference electrode. The coin cells were assembled in a glove box under argon atmosphere, with LP30 as the electrolyte and two stacked glass fiber filters as the separator. The measurements were carried out

with a VMP3 potentiostat (BioLogic), recording cyclic voltammograms at different potential scan rates and galvanostatic charge-discharge profiles at different current densities.

S2. Evidence for the reversibility of the folding of the NbSe₂ nanosheets into nanoroll morphology through solvent exchange

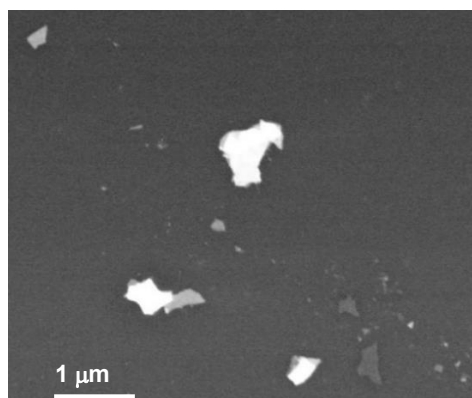


Figure S1. Typical STEM image of the objects coming from a dispersion prepared by suspension of the as-obtained, dried cathodic product first in water followed by transference of the aqueous dispersion to isopropanol (via several cycles of sedimentation by centrifugation and re-suspension in isopropanol).

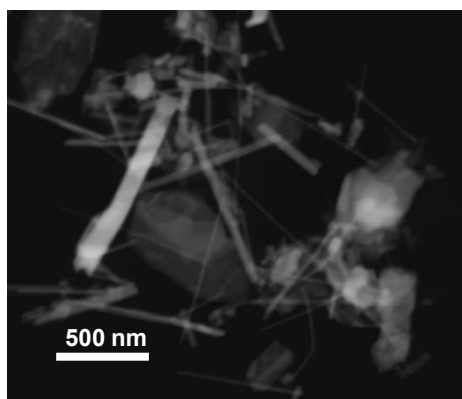


Figure S2. Typical STEM image of the as-obtained, dried cathodic product.

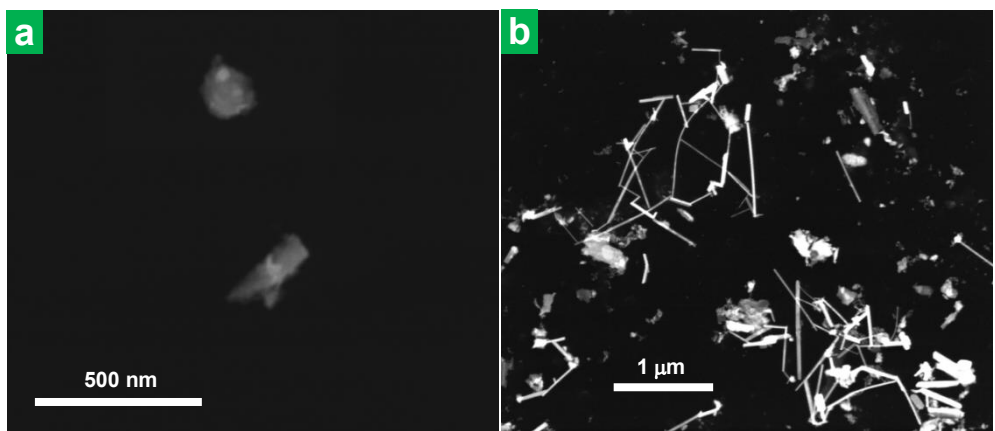


Figure S3. Typical STEM images of the nano-objects obtained by direct sonication of the bulk NbSe₂ powder in (a) isopropanol and (b) water.

S3. Further physicochemical characterization of cathodically delaminated NbSe₂

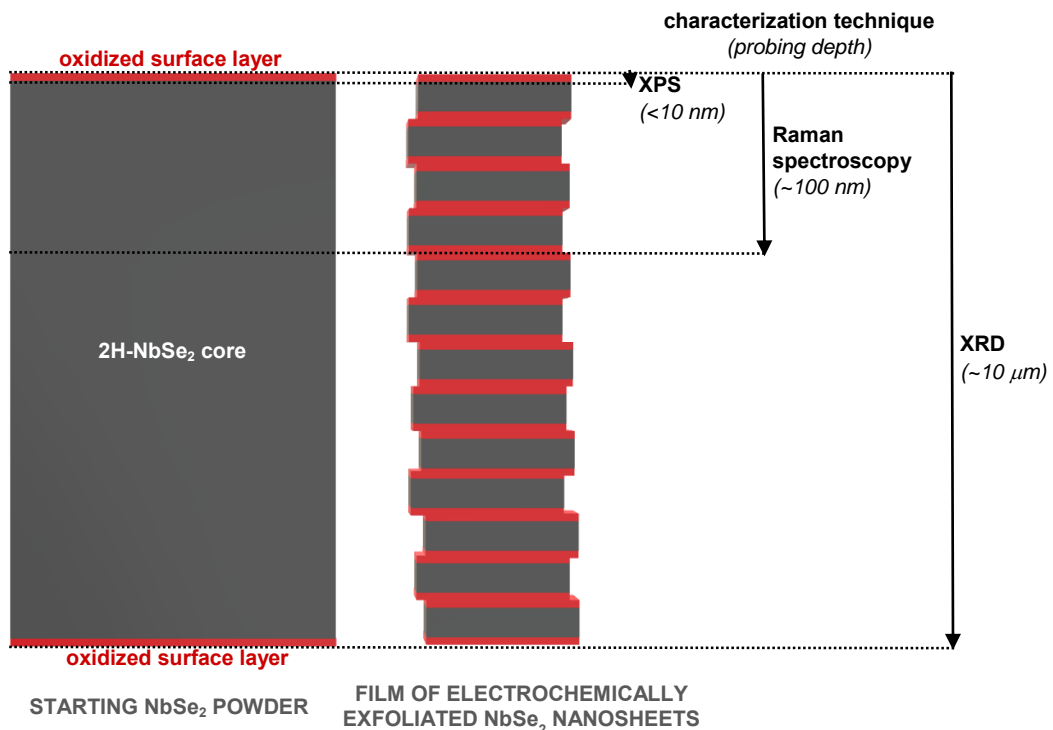


Figure S4. Schematic representation of the structure of the starting NbSe₂ powder and that of films of electrochemically exfoliated NbSe₂ showing which parts of the structures are probed by different techniques depending on their respective probe depths.

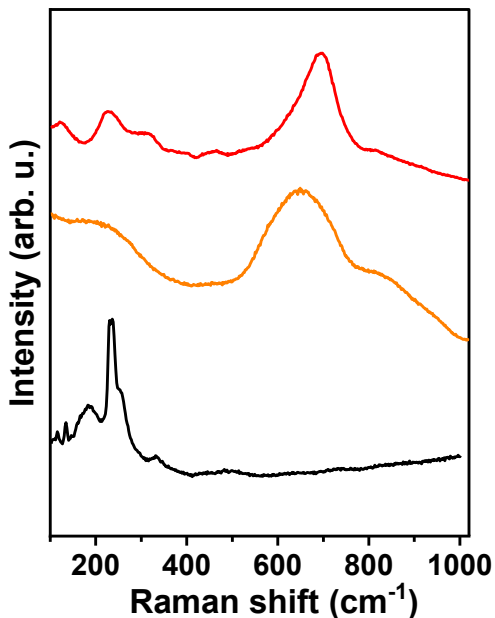


Figure S5. Raman spectra of commercial samples of crystalline (red trace) and amorphous Nb_2O_5 (orange trace), and of cathodically delaminated NbSe_2 (black trace).

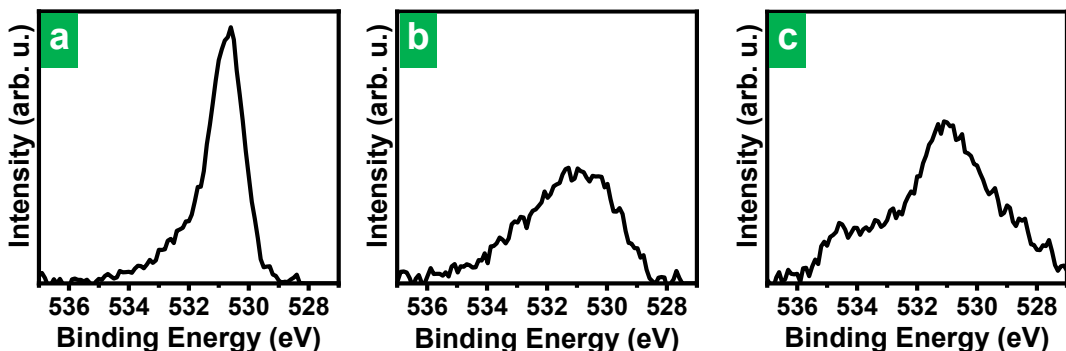


Figure S6. Background-subtracted high-resolution O 1s XPS spectrum of (a) the starting bulk NbSe_2 powder and the cathodically delaminated product processed in (b) water only and (c) in isopropanol. The maxima of the O 1s spectra are located ~ 530.7 eV, which is consistent with the presence of metal oxides.

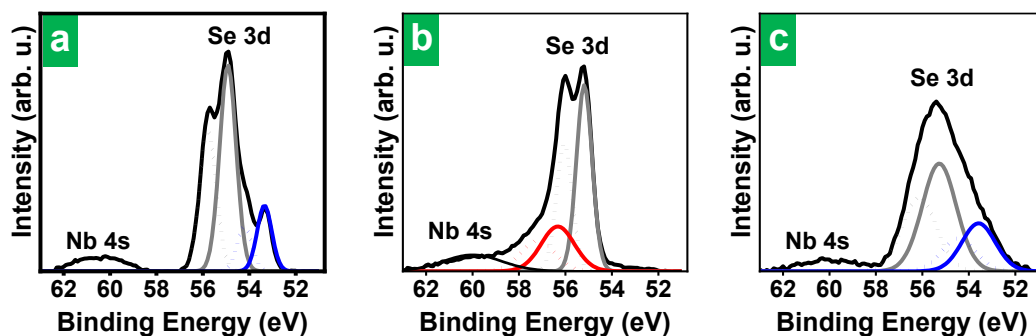


Figure S7. Background-subtracted high-resolution Se 3d XPS spectrum of (a) the starting bulk NbSe₂ powder and the cathodically delaminated product processed (b) in water only and (c) in isopropanol. The weak, wide band at binding energy ~60 eV corresponds to Nb 4s core level. Both XPS core level bands have been labelled for clarity. The Se 3d_{3/2} and Se 3d_{5/2} components are graphed with solid and dotted lines, respectively. Selenium appears in two oxidation states, namely, -2 (blue trace, ~53.3 eV), which is assigned to selenide in NbSe₂ [1] and 0 (gray trace, ~55.2 eV), which corresponds to elemental Se [2]. The red component with maximum at 56.3 eV could be also due to elemental selenium in another less electrically conducting allotropic form, which would become positively charged upon photoemission and consequently shifted to higher binding energy. Indeed, selenium shows different allotropic forms; most of them are non-conducting while the most thermodynamically stable one is electrically conductive [3]. According to the Raman results (see main text) both conducting (crystalline, gray t-Se) and non-conducting (amorphous, red Se) are detected in the surface of the NbSe₂ materials.

The fact that some Se in NbSe₂ form is detected in the material processed in isopropanol from the Se 3d spectrum (Fig. S7c) but not from the Nb 3d spectrum (Fig. 2e in the main text) can be explained by the difference in the probing depths of the corresponding XPS signals (see Fig. S4). As the kinetic energy of the Se 3d XPS electrons is ~150 eV higher than that of those ejected from Nb 3d core level, the latter band is more surface-specific, and thus more suitable for the detection of surface oxides, while the NbSe₂ material underneath is better detected in the Se 3d band.

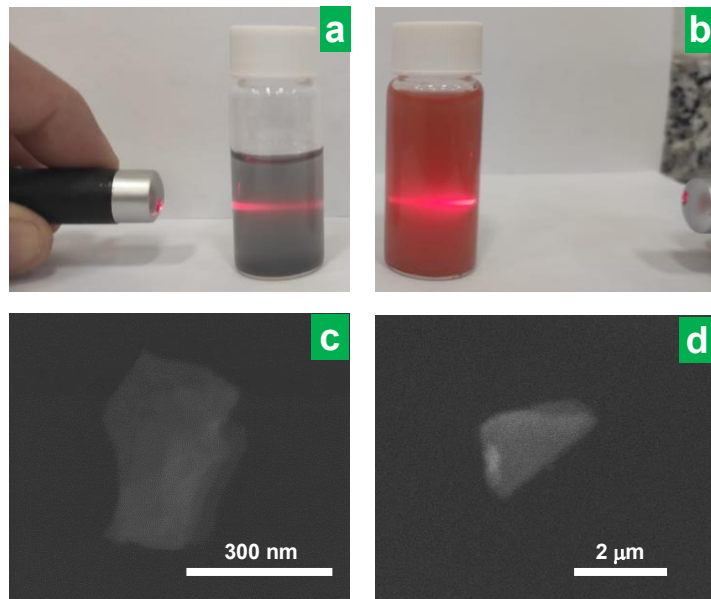
S4. Cathodic delamination of other LTMDs (NbS_2 and VSe_2)

Figure S8. Digital photographs of cathodically delaminated (a) NbS_2 and (b) VSe_2 in aqueous dispersion showing the Tyndall effect (by which the objects present in colloidal dispersion make the laser beam visible by light scattering). STEM micrographs of (c) NbS_2 and (b) VSe_2 nanosheets drop-cast from aqueous dispersion on continuous carbon supports.

S5. Comparison of the electrochemical performance for Li storage of the cathodically delaminated NbSe_2 with other NbSe_2 -based materials

There are very few examples in the literature of NbSe_2 materials experimentally applied to Li storage. Some other works related to Li storage in NbSe_2 in the literature just give proof of the possibility of the intercalation of Li in NbSe_2 [4] or deal with theoretical calculations and thus the capacity values provided are not experimental [5–7] and have not been included in the comparison below.

Table S1. A comparison of the performance of different NbSe₂-materials for Li storage applications. The gravimetric capacity values are given relative to the active material (i. e., mass of NbSe₂ only).

Material	Synthesis method	Cyclic performance	Rate capability	Ref.
NbSe ₂ nanorolls	Cathodic exfoliation for 2 min; dispersion in water via a brief treatment (1–2 min) with a vortex mixer	~1450 mAh g ⁻¹ at 0.9 A g ⁻¹ upon 700–800 cycles	325 mAh g ⁻¹ at 3.7 A g ⁻¹	This work
NbSe ₂ nanosheets	Cathodic exfoliation for 2 min; dispersion in isopropanol via a brief treatment (1–2 min) with a vortex mixer	~600 mAh g ⁻¹ at 0.9 A g ⁻¹ after 1100 cycles	148 mAh g ⁻¹ at 3.7 A g ⁻¹	This work
Nanosized surface hexagonal NbSe ₂	Ultrasonic treatment of bulk NbSe ₂ powder; microwave hydrothermal treatment 180 °C for 12 h	-	313 mA h g ⁻¹ at 0.1 A g ⁻¹	⁸
CoSe ₂ -decorated NbSe ₂ nanosheets	Bottom-up, from molecular precursors; cation exchange at 240 °C for 30 min; annealing in Ar atmosphere at 400 °C for 3 h	364.7 mAh g ⁻¹ at 5 A g ⁻¹ after 1500 cycles (*)	280 mAh g ⁻¹ at 10 A g ⁻¹ (*)	⁹
Few-layer NbSe ₂ @graphene heterostructure	Wet-ball milling of bulk NbSe ₂ powder for 40 h	~700 mAh g ⁻¹ at 1 A g ⁻¹ after 1000 cycles	416 mAh g ⁻¹ at 3 A g ⁻¹	¹⁰

(*) It is not clear whether the reported values are calculated with respect to the active material or to the complete electrode. In case they were given per mass of electrode, the values would have to be multiplied by a factor of 1.43 to express them as relative to the active material.

S6. Additional information of the cyclability of the cathodically delaminated NbSe₂ materials for lithium storage

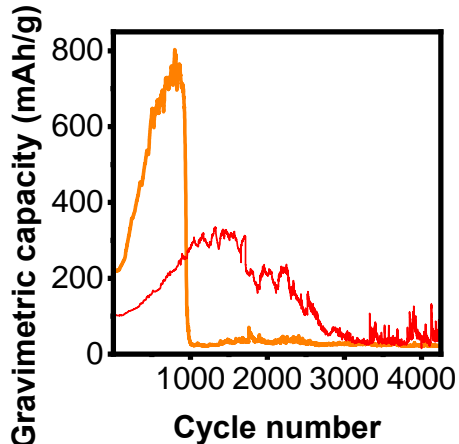


Figure S9. Cyclability of NbSe₂ nanorolls (orange trace) and nanosheets (red trace) in terms of capacity at a current density of 0.5 A g⁻¹, including a greater number of cycles (more than 3000) than in the main text. The gravimetric capacity figures are given relative to the total mass of the NbSe₂-based electrode; they would be a factor of ~1.85 larger if given relative to the mass of active material (i.e., mass of NbSe₂ only).

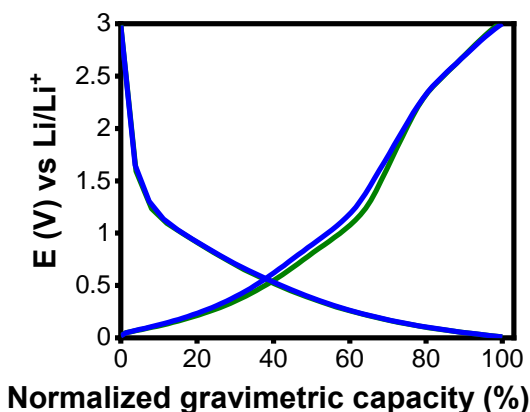


Figure S10. Typical GCD for the early stages of cycling of the NbSe₂ unfolded nanosheets (green traces) and for the electrode with increased capacity after several hundred cycles (blue traces). For ease of comparison, the profiles have been normalized to the full discharge capacity.

References

- [1] H. Wang, X. Huang, J. Lin, J. Cui, Y. Chen, C. Zhu, F. Liu, Q. Zeng, J. Zhou, P. Yu, X. Wang, H. He, S. H. Tsang, W. Gao, K. Suenaga, F. Ma, C. Yang, L. Lu, T. Yu, E. H. T. Teo, G. Liu, Z. Liu. High-quality monolayer superconductor NbSe₂ grown by chemical vapour deposition, *Nature Communication* 8 (2017) 394.
- [2] B. V. Crist. Handbook of Monochromatic XPS Spectra. The Elements & Native Oxides; XPS International LLC: Mountain View, CA, 2004; Vol. 1. p. 245 (Se0).
- [3] N.N. Greenwood, A. Earnshaw, Chemistry of the elements. Ch. 26: Cobalt, rhodium and iridium, Pergamon Press. Oxford, 1984, pp. 886–888.
- [4] E. Hitz, J. Wan, A. Patel, Y. Xu, L. Meshi, J. Dai, Y. Chen, A. Lu, A. V. Davydov, Li. Hu. Electrochemical Intercalation of Lithium Ions into NbSe₂ Nanosheets, *ACS Applied Materials & Interfaces* 8 (2016) 11390–11395.
- [5] X. Lv, W. Wei, Q. Sun, B. Huang, Y. Dai. A first-principles study of NbSe₂ monolayer as anode materials for rechargeable lithium-ion and sodium-ion batteries. *Journal of Physics D: Applied Physics* 50 (2017) 23.
- [6] H. Liu, Z. Huang, G. Wu, Y. Wu, G. Yuan, C. He, X. Qi, J. Zhong. A novel WS₂/NbSe₂ vdW heterostructure as an ultrafast charging and discharging anode material for lithium-ion batteries. *Journal of Materials Chemistry A* 6 (2018) 17040-17048.
- [7] D. B. Putungan, J. L. Kuo. Lithium and sodium intercalation in a 2D NbSe₂ bilayer-stacked homostructure: comparative study of ionic adsorption and diffusion behavior. *Physical Chemistry Chemical Physics* 23 (2021) 19811-19818.
- [8] C. Peng, H. Lyu, L. Wu, T. Xiong, F. Xiong, Z. Liu, Q. An, L. Mai, Lithium- and magnesium-storage mechanisms of novel hexagonal NbSe₂, *ACS Applied Materials & Interfaces* 10 (2018) 36988-36995.
- [9] J. Zhang, C. Du, J. Zhao, H. Ren, Q. Liang, Y. Zheng, S. Madhavi, X. Wang, J. Zhu, Q. Yan, CoSe₂-decorated NbSe₂ nanosheets fabricated via cation exchange for Li storage, *ACS Applied Materials & Interfaces* 10 (2018) 37773-37778.
- [10] H. Nguyen, H. Kim, I.T. Kim, W. Choi, J. Hur, Few-layer NbSe₂@graphene heterostructures as anodes for lithium-ion half- and full-cell batteries, *Chemical Engineering Journal* 382 (2020) 122981.

6. CONCLUSIONES

6. Conclusiones

Los resultados obtenidos en esta tesis y recogidos en la presente memoria permiten extraer las siguientes conclusiones generales:

- Se ha demostrado que la exfoliación electroquímica en medio acuoso es una técnica eficiente y versátil para la obtención de grafeno y dicalcogenuros de metales de transición. Este método ha permitido superar algunas de las limitaciones de otros métodos, facilitando un control significativo sobre la estructura y funcionalización de los materiales obtenidos.
- El grafeno altamente oxidado obtenido mediante exfoliación anódica presenta una calidad estructural superior a la del óxido de grafeno obtenido por métodos convencionales, caracterizada por la presencia de dominios aromáticos relativamente grandes y dominios oxidados relativamente pequeños, lo que a su vez permite obtener grafeno poroso con poros pequeños y de tamaño uniforme (unos pocos nanómetros).
- El grafeno poroso obtenido a partir de grafeno anódico demostró un mejor desempeño como material de electrodo en almacenamiento electroquímico de energía, en comparación con grafeno poroso obtenido a partir de óxido de grafeno estándar. La mayor conductividad eléctrica (derivada de unos mayores dominios aromáticos) y la porosidad más uniforme mejoran los procesos de transporte de carga eléctrica y masa, lo que se traduce en una mayor capacidad de almacenamiento.
- Se ha desarrollado una metodología simple para producir grafeno anódico con poblaciones ajustables de grupos funcionales oxigenados. Este enfoque, basado en el uso de electrolitos comunes, permite en particular aumentar la población de grupos oxigenados de alto estado de oxidación (carbonilos, carboxilos), generalmente baja en grafeno oxidado obtenido anódicamente.

Conclusiones

- El grafeno anódico enriquecido en grupos carboxilo mostró un rendimiento superior a grafenos convencionales en su uso como cátodo en condensadores híbridos de ion zinc acuoso. En forma de filme delgado, este material también permitió una protección eficaz del ánodo de zinc, inhibiendo la formación de dendritas y prolongando significativamente su vida útil.
- La exfoliación catódica ha demostrado ser una técnica eficaz y rápida para exfoliar NbSe₂ en medio acuoso, siguiendo un mecanismo de deslaminación capa a capa *in situ*, diferente al comúnmente conocido para los materiales laminares (expansión electroquímica con deslaminación completada por tratamiento posterior con ultrasonidos/fuerzas de cizalla). El procedimiento puede ser aplicado a otros dicalcogenuros metálicos, como NbS₂ y VSe₂.
- La morfología del NbSe₂ exfoliado puede controlarse mediante la elección del disolvente de dispersión: el isopropanol permite obtener nanoláminas, mientras que el agua favorece morfologías tubulares.
- El NbSe₂ obtenido por exfoliación catódica presenta un buen comportamiento en almacenamiento de litio. Dicho comportamiento depende de la morfología, obteniéndose mejores resultados para la tubular, lo cual se atribuye a una mejor accesibilidad del electrolito cuando el NbSe₂ presenta tal morfología en comparación con la morfología nanolaminar.

ANEXOS

Anexo I

Artículos

Edgar H. Ramírez-Soria, Sergio García-Dalí, Jose M. Munuera, Daniel F. Carrasco, Silvia Villar-Rodil, Juan M. D. Tascón, Juan I. Paredes, José Bonilla-Cruz, A Simple and Expedited Route to Phosphate-Functionalized, Water-Processable Graphene for Capacitive Energy Storage, *ACS Applied Materials & Interfaces* 13 (2021), 1944-8244.

Alberto Martínez-Jódar, S. Villar-Rodil, M.A. Salavado, D.F. Carrasco, P. Pertierra, J.M. Recio, J.I. Paredes, Two-dimensional transition metal dichalcogenides beyond MoS₂ for the catalytic reduction of nitroarenes: MoSe₂ exhibits enhanced performance, *Applied Catalysis B: Environmental* 339 (2023), 123174.

Sergio García Dalí, Daniel F. Carrasco, Silvia Villar-Rodil, Juan I. Paredes, Juan M.D. Tascón, Electrochemical functionalization of graphene nanosheets with iodoacetic acid towards supercapacitor electrodes, *Flatchem* 47 (2024), 100710.

Comunicaciones orales en congresos

Daniel F. Carrasco, Sergio García-Dalí, S. Villar-Rodil, José M. Munuera, E. Raymundo-Piñero, J. I. Paredes, Electrochemically exfoliated NbSe₂ nanosheets and nanorolls for high capacity lithium storage, *Graphene conference 2024*, Madrid, España, 25/06/2024, Comunicación oral, presentada por Daniel F. Carrasco.

E. Álvarez-Rubiera, D.F. Carrasco, S. Villar-Rodil, A. Martínez-Jódar, J.M.D. Tascón, F. Suárez-García, J.I. Paredes, Chemically tuning graphene for aqueous zinc-based electrochemical energy storage applications, *Graphene conference 2024*, Madrid, España, 25/06/2024, Comunicación oral, presentada por E. Álvarez-Rubiera.

A. Martínez-Jódar, S. Villar-Rodil, M. A. Salvadó, D.F. Carrasco, P. Pertierra, J.M. Recio, J.I. Paredes, Two-dimensional transition metal dichalcogenides as catalysts for organic reduction reactions: rationalizing activity trends, *Graphene conference 2024*, 25/06/2024, Comunicación póster, presentada por A. Martínez-Jódar

Edgar H. Ramírez-Soria, José Bonilla-Cruz, Alfredo Aguilar Elguezabal, Sergio García-Dalí, Jose M. Munuera, Daniel F. Carrasco, Silvia Villar-Rodil, Juan M. D. Tascón, Juan I. Paredes, A simple and circular synthesis process for sustainable and greener energy-storage devices based graphene, *31st International Materials Research Congress*, México, 13/08/2023, Comunicación oral, presentada por Edgar H. Ramírez-Soria.

Daniel F. Carrasco, Juan I. Paredes, Silvia Villar-Rodil, F. Suarez-García, A. Martínez-Alonso, Juan M. D. Tascón, Graphene decorated with uniform nanoholes via an electrochemical route for energy storage applications, *Graphene conference 2023*, Manchester, Gran Bretaña, 27/06/2023, Comunicación oral, presentada por Daniel F. Carrasco.

Anexo I

Daniel F. Carrasco, S. Villar-Rodil, J. I. Paredes, F. Suárez-García, A. Martínez-Alonso, J.M.D. Tascón, Holey graphene derived from an electrochemical strategy for charge storage applicat, *Carbon for energy storage and enviroment protection, (CESEP'23)*, Budapest, Hungía, 24/09/2023, Comunicación póster, presentada por J.M.D. Tascón.

D.F. Carrasco, E.H. Ramírez-Soria, S. García-Dalí, J.M. Munuera, S. Villar-Rodil, J.M.D. Tascón, J.I. Paredes, J. Bonilla-Cruz, Obtención de grafeno funcionalizado con grupos fosfato mediante una ruta electroquímica para su utilización en almacenamiento de energía, *XVI Reunión del Grupo Español del Carbón*, Gijón, Asturias, 22/10/2023, Comunicación póster, presentada por D.F. Carrasco.

E. Álvarez-Rubiera, D.F. Carrasco, S. Villar-Rodil, J.I. Paredes, Ánodos de zinc recubiertos con grafeno para dispositivos de almacenamiento de energía acuosos, *XVI Reunión del Grupo Español del Carbón*, Gijón, Asturias, 22/10/2023, Comunicación póster, presentada por E. Álvarez-Rubiera.

Edgar H. Ramírez-Soria, Sergio García-Dalí, Jose M. Munuera, Daniel F. Carrasco, Silvia Villar-Rodil, Juan M. D. Tascón, Juan I. Paredes, José Bonilla-Cruz, Phosphate-functionalized graphene obtained by a fast, one-step electrochemical strategy for capacitive energy storage, *European forum graphene 2022 (EFG'22)*, Atenas, Grecia, 26/10/2022, Comunicación oral, presentada por Daniel F. Carrasco.

Daniel F. Carrasco, Juan I. Paredes, Silvia Villar-Rodil, Fabián Suárez-García, A. Martínez-Alonso, J. M.D. Tascón, Síntesis mediante una ruta electroquímica de nanoláminas de grafeno porosos para aplicaciones de almacenamiento de carga, *XV Reunión del Grupo Español del Carbón*, Granda, España, 24/04/2022, Comunicación oral, presentada por Daniel F. Carrasco.

Daniel F. Carrasco, Juan I. Paredes, F Suarez-garcía, Silvia Villar-Rodil, A. Martínez-Alonso, Juan M.D. Tascón. Síntesis de Grafeno poroso a partir de óxido de grafeno y estudio de su ampliación como electrodo de trabajo en almacenamiento de energía, *IX Jornadas Internacionales de Doctorado*, Oviedo, España, 16/10/2020. Comunicación oral, presentada por Daniel F. Carrasco.